Analysis of Infiltration and Overland Flow over Sloped Surfaces: Application to Roadside Swales

A DISSERTATION
SUBMITTED TO THE FACULTY OF
UNIVERSITY OF MINNESOTA
BY

María del Carmen García de la Serrana Lozano

IN PARTIAL FULFILLMENT OF THE REQUIREMENTS
FOR THE DEGREE OF
DOCTOR OF PHILOSOPHY

Dr. John S. Gulliver and Dr. John L. Nieber

June 2017

Acknowledgements

This dissertation represents a formal document compiling research findings accomplished in the last four years; however, none of this would have been possible without the support I have received, and I was never alone on this road (or these roadside swales, to be precise). First, I will always be grateful to my advisors Prof. John Gulliver and Prof. John Nieber for their constant guidance, strong support, and constructive criticism. Prof. Gulliver's dedication and determination are inspiring and strongly contagious. I feel utmost respect for him as a mentor in research and life. Prof. Nieber's commitment to my understanding of hydrologic processes and thorough reviews have been key to the completion of this dissertation. I am thankful for the impactful discussions we have had along the way. I would also like to express my gratitude to the other members of my committee, Prof. Bruce Wilson and Prof. Vaughan Voller for their helpful advice and lessons learned in their insightful lectures.

I would like to thank the main funding agencies of this research project: Minnesota Department of Transportation (MnDOT) and Minnesota Local Road Research Board (LRRB) for their support and collaboration. Especially, thanks to Barbara Loida, technical liason, Bruce Holdhusen, project manager, and Beth Neuendorf. Additionally, I would like to acknowledge every person involved with the planning, safety measures, and realization of the field experiments; your help was crucial. The technical guidance on this project from the technical advisory panel (TAP) members, with members from Minnesota Pollution Control Agency (MPCA) and MnDOT, was greatly appreciated.

I also gratefully acknowledge the support from the University of Minnesota–Department of Civil, Environmental and Geo- Engineering (CEGE) and from the Minnesota Supercomputing Institute. My sincere thanks to the families and donors of the: Edward Silberman Fellowship, Heinz G. Stefan Fellowship, and Matthew J. Huber Award. I would not have been able to share my research and expand my knowledge in conferences without the financial support of the Frank and Julie Tsai Travel Award, the American Geophysical Union travel grant, the University of Minnesota–CEGE travel award, the GAPSA travel grant, and the SAFL Student Travel Fund Award.

Prof. Gulliver's research group members have always been supportive, thank you all. Special thanks to Andy Erickson for his help with the swale calculator and his efforts to build and maintain the SAFL Stormwater Research website; his work is the perfect example of how much impact good research can make. I am grateful to Dr. Farzana Ahmed, her previous research work in this topic was extremely helpful to start my project. I would also like to thank all the undergraduate researchers who helped in the laboratory, field experiments, and modeling efforts: David Liddell, Tyler Olsen, Ugonna Ojiaku, and Anthony Vecchi. Additional thanks to Dr. Ali Ebrahimian (coach) and Prof. Peter Weiss.

St. Anthony Falls Laboratory offered me lemons, a juicer, sugar, and water i.e. funding, equipment, caring people, and literally water, making it easier for me to make lemonade. I wish to express a special thank you to all of the SAFL faculty, research, and administrative staff. Chapter 4 would have not been possible without help from Craig Taylor and Jim Mullen. Furthermore, I am profoundly grateful to the SAFL Student Council members and those who have been a catalyst for good times: Abby Tomasek, Alec Petersen, Anne Wilkinson, Gerard Salter, Mirko Musa, ex-president Dr. Jon Schwenk, and former members. An honorable mention to Michael Heisel and Dr. Craig Hill, as well. I feel extremely fortunate to have shared much more than a working space with all of you, my SAFL buddies.

A special recognition goes out to my family and friends in Spain and the U.S.A. Thanks for those friendships that make me feel at home wherever I am. I greatly appreciate all the warmth received from my Minnesota family and for providing me with key equipment for my field tests. I appreciate the mental health time with my favorite person, who always keeps my feet on the ground. Finally, my parents, my brother, and my sister-in-law have shown me during these years that love travels long, long distances.

Dedication

To my parents, Florentina and Fernando, for giving me wings, unconditional support, and the perfect toolbox to do anything I set my mind to. You have dedicated your life to me; this is for and because of you.

Para mis padres, Florentina y Fernando, por darme alas, apoyo incondicional, y las herramientas perfectas para lograr cualquier cosa que me proponga. Habéis dado vuestra vida por mí; esto es por y gracias a vosotros.

To my brother and first mentor, Fernando, I will always look up to you.

To my life partner and personal editor, Erik, for holding my hand through every step of this uncertain and jagged path. Thank you.

To every inspiring woman in science and engineering.

.

Abstract

Environmental impacts and regulatory requirements associated with highway runoff present design challenges. Roadside swales, or drainage ditches, improve water quality by infiltration, filtration, and sedimentation. Road runoff volume reduction through infiltration occurs as the water flows over the side slope, acting as a filter strip, or down the length of the swale channel. Therefore, roadside swales are practical solutions that can mitigate the effect that linear transportation projects have on water bodies. This dissertation advances the understanding of the infiltration performance of roadside swales for design and planning purposes. The main objectives of this thesis are: understanding the overland flow and infiltration processes over a fraction of a slope, relating surface roughness parameters to the fraction of wetted area, and quantifying the effect of equidistant parallel strip water sources on the lateral component of infiltration. Moreover, this research leads to a better understanding of overland flow and infiltration in roadside swales through field experiments, and modeling efforts that can simulate how roadside swales operate.

All the field tests, performed in four different highways, showed that water flow on the side slope of a roadside swale is concentrated in fingers, instead of sheet flow, at the typical road runoff intensities for which infiltration practices are utilized to improve surface water quality. The laboratory experiments aimed to formulate the relevance of fractal parameters, based on the Fourier power spectrum method, for understanding soil surface roughness, overland flow patterns, and erosion.

A model has been developed for coupling a Green-Ampt-Mein-Larson infiltration submodel with kinematic wave submodels for both overland flow down the side slope and open channel flow for flow in the channel. The side slope of a roadside swale is the main part contributing to the loss of runoff by infiltration and the channel primarily conveys the water. Finally, a simplified roadside swale calculator has been developed with a reduced set of input parameters. The calculator can estimate the total percentage of annual volume infiltrated, supporting informed decision-making on how to account for the infiltration benefits of roadside swales.

Table of Contents

List of Tables

List of Figures

Chapter 1

Introduction

1. Background

Urban development has hydrological, physical, and water quality effects on watersheds (Booth and Jackson, 1997; Chabaeva *et al.*, 2009; Ebrahimian *et al.*, 2016). In terms of hydrology, the effects are related to fast runoff response to rainfall, increased runoff rates, volumes, and peaks, and decreased infiltration and baseflow (Fletcher *et al.*, 2012).

In the past, urban drainage systems were designed to transport runoff from impervious areas, like roads and highways, as fast as possible (Holman-Dodds *et al.*, 2003). The increased runoff volumes from roadways, occurring over a shorter period of time, increase erosion and destabilize stream channels (Dupuis and Kobriger, 1985). In addition, highway runoff can contain pollutants, including total suspended solids, oxygen-demanding organic material, nutrients, metals,

and toxic organic compounds (Barrett *et al.*, 1995; McKenzie *et al.*, 2009; LeFevre *et al.*, 2014; Kayhanian *et al.*, 2012). Highway runoff effect on receiving streams and lakes is site specific and usually is not acutely toxic; however, highway runoff has been associated with a decrease in the diversity and productivity of aquatic ecosystems (Barrett *et al.*, 1995; USGS, 2003). On the other hand, there are regulatory requirements to protect the environment from the impact of roadway runoff. The National Pollution Discharge Elimination System (NPDES), enforced by the U.S. Environmental Protection Agency (EPA), requires stormwater discharge permits for highways. Therefore, both the environmental impacts and the regulatory requirements associated with highway runoff support the need for further study of stormwater management practices that can mitigate the effects of transportation projects (Walsh and Barrett, 1997).

A growing trend in stormwater management is to incorporate practices that reduce runoff volumes and peak flow in addition to improving runoff water quality. Such practices are called low impact development (LID) practices or Green Infrastructure (GI) and are typically designed to reduce runoff and to mimic a site's predevelopment hydrology (Fletcher *et al.*, 2012). Some examples of LID or GI are grass strips, bioretention, swales, detention basins, media filters, porous pavement, retention ponds, wetland basins, etc. These practices improve water quality by infiltration, filtration, and sedimentation. In addition to reducing surface runoff, these new approaches may also promote the increase of groundwater recharge, reduce erosion and stream widening, and improve water quality (Holman-Dodds *et al.*, 2003).

Implementing stormwater volume reduction approaches in extremely constrained urban environments is a challenge (Strecker *et al.*, 2014). Traditionally, the main purpose of roadside drainage ditches (Figure 1.1) has been to convey stormwater runoff to prevent road flooding. However, grassed roadside drainage ditches also act as swales, with a filter strip over the side slope and a grassed

channel parallel to the road. Roadside drainage ditches or swales convey and treat water by sedimentation and filtration of solid particles (sediment-bound nutrients) and by infiltration of stormwater and dissolved pollutants (Abida and Sabourin, 2006). In addition, roadside swales require low maintenance (Tourbier, 1994; Lucke *et al.*, 2014) and have been incorporated in transportation projects for decades (Ahmed *et al.*, 2015). As a LID practice or GI for stormwater treatment and control, there is a need to quantify the infiltration performance of roadside swales (Stagge *et al.*, 2012). A better understanding of how effective these practices are at infiltrating runoff from roadways could justify their costs and support informed decision-making in stormwater management (NRC, 2009; Ghimire *et al.*, 2017).

Figure 1.1 Roadside Swale on Hwy 47 in Fridley, MN.

Finally, for roadway runoff flowing into a grassed swale, volume reduction occurs primarily through infiltration into the soil, either as the water flows over the side slope in a direction perpendicular to the roadway and into the swale, or parallel to the roadway and down the length of the swale channel. The process of overland flow and infiltration over a sloped surface is affected by its micro-topography; these processes do not usually take place uniformly. Surface disturbances, micro-topographic variations, and drainage patterns, which develop as a result of the soil erosion processes, can all generate concentrated flows (Hairsine and Rose, 1992). A rill is an incision on the soil surface as a consequence of erosion

that acts like a channel, concentrating the water flow. When the micro-topography of a surface presents rills, sheet flow, which is flow that has constant or irregular depth over the entire width of the slope, does not typically take place. Instead, water tends to flow concentrated in those rills so that only a fraction of the hillslope surface contributes to the overland flow, and therefore infiltration. Having a better understanding of overland flow and infiltration processes over rilled surfaces is important to advance the scientific understanding, to develop simplified models capable of reproducing the effect of erosion processes, and to understand the impact of rills on the performance of stormwater management practices, such as grassed filter strips.

2. Thesis Overview

This research is based on a project funded by the Minnesota Department of Transportation (MnDOT) and the Local Road Research Board (LRRB) to develop a calculator to measure the infiltration performance of roadside swales. The title of the project is “Enhancement and Application of the Minnesota Dry Swale Calculator”. The principal investigators (PIs) were Dr. John S. Gulliver from the Department of Civil, Environmental and Geo- Engineering, and Dr. John L. Nieber from the Department of Bioproducts and Biosystems Engineering, both at the University of Minnesota-Twin Cities.

This thesis is an assembly of several research articles with the common purpose of investigating infiltration and overland flow processes. There are two main topics in this thesis; the first, contained in Chapters 2, 3 and 4, is related to micro-processes; the second topic, contained in Chapters 5, 6, and 7, deals with the quantification of infiltration in roadside swales. Chapter 2 is a critical literature review focused on the features of surface micro-topography and soil infiltration properties that affect surface runoff generation and patterns of overland flow. This work has been submitted for publication.

Chapter 3 describes the two-dimensional infiltration flux from parallel strip water sources. In the study, a relationship between the characteristics of a strip water source, soil texture, and the lateral infiltration from parallel strip sources of water on the soil surface is established. This relationship represents a modification of the previous research on this topic to account for infiltration rates at steady state with multiple parallel strip water sources. Research paper to be submitted.

In Chapter 4, the results of a set of laboratory experiments of simulated runoff tests over a bare soil slope surface are presented. Fractal dimensions of the soil surface are calculated over time and compared to the fraction of wetted area contributing to overland flow and infiltration. In addition, the impact that concentrated flow or fractional wetting of the slope surface has on infiltration and runoff generation is analyzed. Research paper to be submitted.

Chapters 5, 6, and 7 focus on roadside swales' performance as stormwater management practices. Chapter 5 presents the results from a total of thirty-two field tests performed during three seasons on four different highways located in the Minneapolis-St. Paul metropolitan area, MN, to analyze the infiltration performance of roadside filter strips and the effect of fractional coverage of water on infiltration. This work was published in the Journal of Hydrology Vol. 545, (2017), pp. 451-462. Chapter 6 describes the development of an overland flow and infiltration model to quantify the infiltration performance of roadside swales in both the side slope and the channel. The filter strip portion of the model is then validated using the field data from Chapter 5. This work has been submitted for publication and it is currently under review. In Chapter 7, a roadside swale calculator that allows the user to estimate the total percentage of annual volume infiltrated is presented. This calculator is a simplification of the model presented in Chapter 6, with a reduced set of input parameters that have proven to be essential to obtain accurate results based on two global sensitivity analyses. This roadside swale calculator is suitable for design and planning purposes.

A summary and overall conclusions are offered in Chapter 8.

Chapter 2

Influence of Micro-topography on Overland Flow and Infiltration

Summary

This review focuses on the features of surface micro-topography and soil infiltration properties that affect surface runoff generation and patterns of overland flow. Furthermore, the review covers the studies that establish a connection between roughness parameters and hydrological processes, establishing hydraulic connections across the surface and resulting in spatially non-uniform overland flow and infiltration. Micro-topography or roughness can be completely random or be a defined structure with a dominant direction. In general, roughness that has a cross-slope orientation decreases runoff while roughness with a downslope orientation tends to increase runoff. The overall conclusion derived from the literature is that most surfaces with surface depressions tend to enhance infiltration and decrease runoff, although

downsloping rilled surfaces tend to enhance runoff generation. There is a need to find roughness parameters that define the surface sufficiently to be able to determine flow direction and pattern of overland flow under specific flow conditions.

The effect of depressions on runoff generation is more complex than simply the approach where runoff only starts when depression storage capacity is full. Micro-topographic formations and surface sealing and crusting are dynamic processes that have been associated with both surface roughness characteristics and the effect of rainfall intensity and overland flow. To estimate runoff generation on a dynamically changing surface it is necessary to couple the processes of soil erosion, sediment transport, flow pathway, and infiltration. On a fully-developed surface, only the micro-topographic and infiltration features are needed to adequately represent runoff processes. A standard of how to (1) determine the main micro-topographical features and how to (2) use these to predict hydrologic connectivity needs to be researched and developed. Research also is needed to identify parameters derived from micro-topographic mappings that can be used in successful prediction of surface runoff from sloping surfaces.

1. Introduction

A hillslope can be considered a sloping surface with micro-topographic variability consisting of mounds and depressions of different sizes. According to Horton's (1945) infiltration theory, a surface exposed to persistent rainfall can result in a number of different stages as illustrated in Figure 2.1. The first stage (not shown in Figure 2.1) takes place before ponding, when water infiltrates without water redistribution. In the second stage (A), ponding is initiated. Rainfall can produce ponding by two mechanisms: when the rainfall intensity is greater than the infiltration capacity of the soil at the surface; and soil filling, where a soil layer at depth restricts downward flow and the surface layer fills to its available porosity. The third stage (B left and C right) starts when the depressions containing the ponded water overtop. Then, runoff establishes flow and hydrologic connectivity between upslope and downslope locations. This connectivity will link runoff flow paths to the channel if the water depth keeps increasing. The fourth stage (C left) is where some of the micro-topographic features are submerged, and a "mixed flow" regime around emergent micro-topographic mounds is created. Only when water depth is greater than every micro-topographic mound height (stage five, D) will a sheet flow regime be achieved (Thompson *et al.,* 2010).

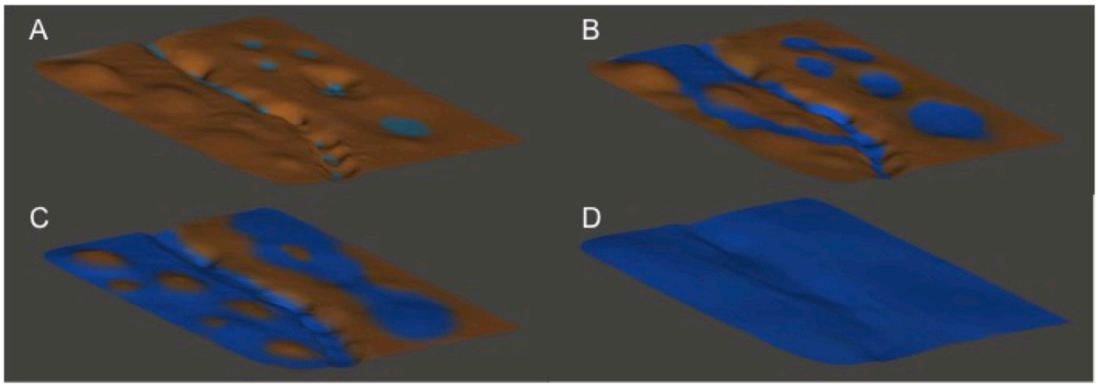

Figure 2.1 Classification of the characteristics of runoff generated during a storm event into multiple flow stages depending on the water depth with respect to the micro-topographic features. **A-** Initial water ponding **B-** Hydrologic connectivity between upslope and downslope locations. **C-** Right: Depressions containing the ponded water overtop; Left: "mixed flow" **D-**Sheet flow regime.

Overland flow is defined as the flow of water over the land surface in excess of the infiltration capacity and depression storage, and is the initial phase of surface runoff generation (Emmet, 1970). In most hydrologic modeling of overland flow the process is simplified by assuming uniform sheet flow (D in Figure 2.1), which is flow that has constant or irregular depth over the entire width of a hillslope and that does not concentrate into micro-channels or rills (Moore and Grayson, 1989; Woolhiser, *et al.,* 1990; Goodrich, *et al.,* 1991). A rill is an incision on the soil surface as a consequence of erosion, compaction, etc., that acts like a channel concentrating the water flow. The uniform sheet flow assumption has been questioned by multiple authors (Emmet 1970; Parsons *et al.,* 1990; Hairsine and Rose*,* 1992; Cerdà, 1995; Bergkamp *et al.,* 1996). Instead, these authors conclude that water more likely flows concentrated in channels so that only a portion of the hillslope surface contributes to the infiltration of overland flow on the hillslope.

An intrinsic feature of hillslopes is spatial variability of slope, soil parameters and infiltration parameters. The characteristics of that variability often have a substantial influence on the hydrologic connectivity of upslope areas to the flow outlet at the base of a hillslope and thus the runoff behavior of the system (Western *et al.,* 2001; Ahmed *et al.,* 2015). Surface disturbances, natural micro-

topographic variation, and drainage patterns, which develop as a result of the soil erosion process, can all generate concentrated flows (Hairsine and Rose, 1992). For instance, Smith *et al.* (2011a,b) conducted an experiment where a constant discharge was supplied at the upper end of three semi-arid hillslope transects each with differing soil properties. Estimates of flow depth were made, and an increase in median depth was observed in the presence of rills, confirming the occurrence of flow concentration and an increase in flow velocity.

This review will focus on the processes and methods in overland flow over the Earth's surface that affect infiltration and runoff on the plot and hillslope scales. Having a better understanding of overland flow and infiltration processes is important to advance the scientific understanding and develop spatially distributed models suitable to estimate surface water hydrology, contaminant transport, erosion processes, and performance of management practices that utilize these processes. The main questions underlying the review are: 1) What roughness features substantially affect overland flow and infiltration? 2) Which techniques to measure surface micro-topography should be used to capture these features? 3) How does micro-topography affect hydrologic connectivity of upslope areas to the outlet at the base of the hillslope? and 4) How do computational models take into account micro-topography to estimate overland flow and infiltration?

2. Micro-Topography

Micro-topographic variations are one of the main reasons why most flows over hillslopes cannot be considered sheet flow. Micro-topography —consisting of small-scale variations in the elevation of the land surface on millimeter to centimeter scales— is omnipresent on hillslopes (Thompson *et al.,* 2010). The definition, factors and measurements that define micro-topography have been investigated, however their connection to overland flow patterns needs to be further researched.

2.1 Micro-topography and Surface Sealing and Crusting

Overland flow processes, and as a consequence the hydrograph shape, can be affected by the micro-topography of the surface. At small-scale, three types of roughness can be distinguished (Römkens and Wang, 1986), (i) micro-relief, (ii) random roughness and (iii) oriented roughness. Micro-relief is related to variations due to grain size and micro-aggregates, and this roughness is not directional. Random roughness is linked to random distribution of aggregates, or clods, on the soil surface at a fine scale and variations resulting from erosion and deposition. Oriented roughness is the result of agricultural or grading and maintenance operations. This paper focuses on the first two types. Overland flow is generated when rainfall rate exceeds the infiltration capacity, but the overland flow process itself affects infiltration by the processes of soil surface sealing and crusting. Roughness plays a significant role in the control of the spatial variability of infiltration, overland flow and of surface sealing and crusting. The effect is most pronounced during hydrograph recession (Woolhiser *et al.,* 1990) and for flows with water depths comparable to the characteristic height of the micro-topography, when the area of soil covered by the flowing water determines the water susceptible to infiltration.

The micro-aggregation of soil particles, forming crusts and seals, is connected with the infiltration capacity of the soil. Overland flow is affected by crust and seal formation and subsequent reduction of infiltration (Freebairn and Gupta, 1990; Singer and Le Bissonnais, 1998). Crusting follows a general pattern: first, the sealing of the soil surface by a structural crust, typically formed due to rain impact or wet-dry cycles; and then development of a depositional crust, formed by sediment transport. Bresson and Boiffin (1990) concluded that the change from a structural crust to a depositional crust is mainly characterized by a decrease in infiltration capacity; the structural crust properties cause micro-runoff and puddling under rainfall. In addition, their research showed that there could be a

relation between microbedding and sorting with the hydrodynamic behavior of the soil surface (abundance, size, and duration of puddles).

In addition, crusting and sealing processes have been related to micro-topographic features, with the most studied being depressions and mounds. Valentin (1991) observed a differentiation in the crust formed in diverse roughness elements: Mounds have a thin structural crust while depressions had a thick depositional crust and do not have a uniform crust over their surface. Fox *et al.* (1998a,b) found that a depositional crust is formed in the depression and a structural crust on the side slope of the depression, the former having lower hydraulic conductivity (Figure 2.2 A). The effect of rill formation, and the subsequence formation of crusts and seals in rills, on hydraulic conductivity of the soil needs to be further researched (Figure 2.2 B).

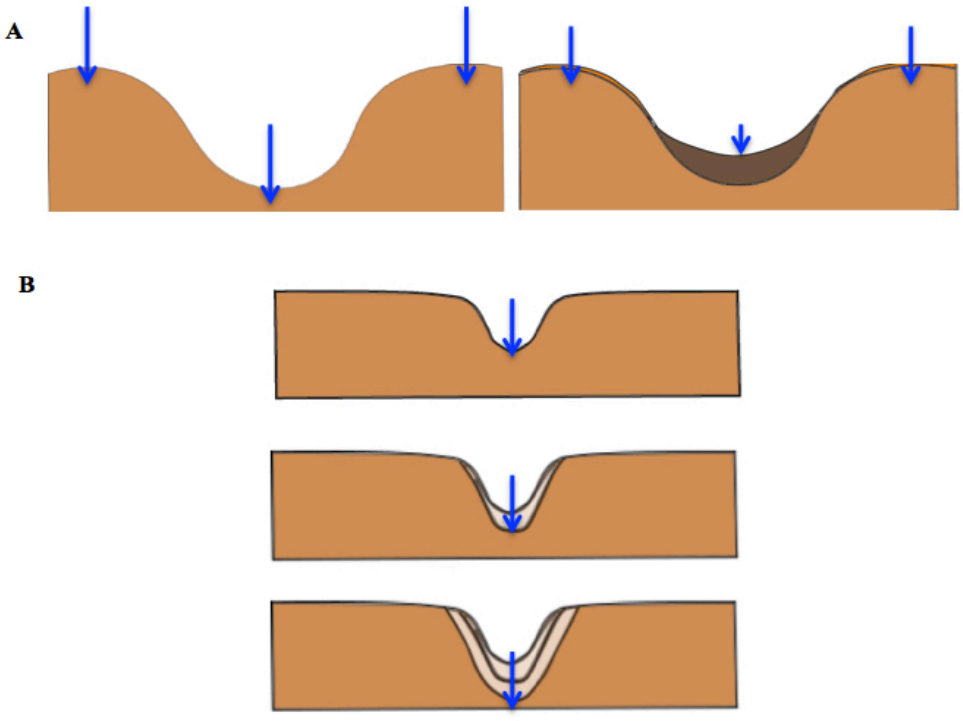

Figure 2.2 Infiltration rates in depressions (A) and rills (B), the blue arrows represent the magnitude of the infiltration rates. A Left- Cross section of a newly formed depression Right- Cross section of a depression with depositional crust at the bottom and structural crust on the mounds. B Cross section of a rill evolving from top to bottom (lighter areas represent erosion zones).

Soil roughness can either decrease or increase during rainfall depending on both the surface condition and processes occurring on the surface (Zheng and Wu, 2014). Surface sealing processes, such as depositional crusts, tend to reduce soil roughness (Vermang *et al.,* 2013). At the same time, erosion processes and seal cracks tend to increase roughness resulting in the formation of rills (Imeson and Verstraten, 1988; Huang and Bradford 1992; Magunda *et al.,* 1997). Vermang *et al.* (2015) related a roughness parameter (RR) with the formation of either thin structural sealing or thick depositional crusts. In their study, they observed a RR threshold under which a thick surface crust was less prone to occur. This was linked to large and more stable aggregates on the soil surface. On the other hand, when RR was greater than the threshold, the creation of a depositional crust was detected, in addition to preferential micro-channels (Figure 2.3). Runoff rates were lower on the surfaces with a RR smaller than the threshold because of the reduced tendency of the crust to form. These experiments were performed using the same precipitation rate for all the surfaces; runoff depths were not recorded. It would be useful to investigate whether the RR threshold where depositional crusts are observed would change with different rainfall intensities and types of soil.

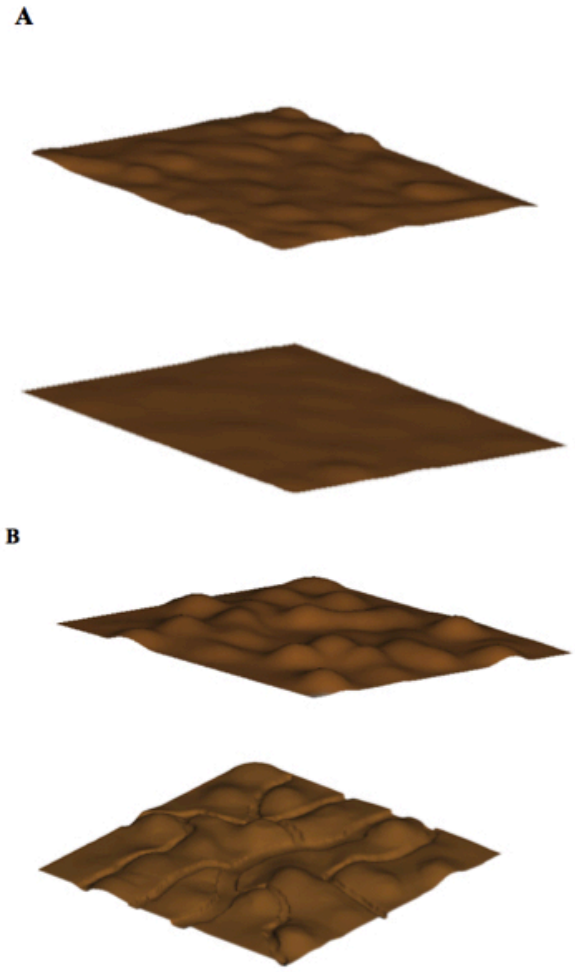

Figure 2.3 Evolution of a surface with an: (A) initially smooth surface and (B) rough surface. The first image in each pair is the initial condition and the second is the surface after runoff/erosion.

Appels *et al.* (2011) found that the fraction of the field that contributes to runoff is unaffected by infiltration if the infiltration parameters are uniform or are spatially distributed at a smaller scale than that of the micro-topography. Moreover, surface sealing and crusting are dynamic processes that have been associated with both surface roughness characteristics and the effect of rainfall intensity and overland flow. A decrease in infiltration capacity of the soil facilitates runoff generation and decreases retention time on a hillslope. Roughness parameters can be applied to map spatial patterns neglecting the evolution of the surface during the process (fully developed surface), however few relationships have been developed to predict the formation of surface geometries (dynamic surface).

The effect of the micro-topography of a soil surface on infiltration/runoff processes is an area that needs further study.

2.2 Quantification of Micro-topography

There have been recent advances in the techniques used to quantify surface micro-topography. Jester and Klik (2005) reviewed the techniques used to acquire the microrelief data of soil surfaces. Measurement techniques can be classified by measurement dimension (2D and 3D) and sensing type (contact and non-contact methods). The most common contact methods are profile or pin meters (Kuipers, 1957; Podmore and Huggins, 1981; Gilley and Kottwitz, 1995) and chain meters (Saleh, 1993; Merrill, 1998), which perform 2D measurements. The disadvantages of contact methods are: that it is a labor-intensive technique, there can be alteration of soil surface (Jester and Klik, 2005), and poor capture of spatial variability. On the other hand, contact methods are inexpensive and easy to implement. The non-contact methods include: stereophotogrammetry (Welch *et al.*, 1984; Warner, 1995; Wegmann *et al.*, 2001; Jester and Klik, 2005; Rossi *et al.*, 2012), infrared thermography (De Lima and Abrantes, 2014), ultrasonic wave reflection (Robichaud and Molnau, 1990), and laser techniques (Helming *et al.*, 1998; Huang and Bradford, 1992; Darboux and Huang, 2003; Legout *et al.*, 2012). Stereophotogrammetry is a suitable technique for the coverage of large areas in the field, since a camera can be easily transported; the ultrasonic wave reflection method and laser techniques usually require a heavy reference frame and the area scanned is limited (Rieke-Zapp, 2002). The ultrasonic wave reflection profiler, reported by Robichaud and Molnau (1990), had a vertical accuracy of ± 3 mm and a horizontal resolution of 30 mm; whereas current laser profilers have vertical resolutions from 0.1 to 0.5 mm and horizontal resolution between 0.1 and 2mm (Jester and Klik, 2005). Although the main advantage of laser scanners is their measuring accuracy, there are some disadvantages linked to them (Verhoest *et al.*, 2008): interference of light from other sources (Huang and Bradford, 1992), measurements affected by external disturbances, such as

wind, and difficulty in differentiating between changes in topography and changes in optical reflectivity of surfaces (Mattia *et al.*, 2003). Finally, when soil surfaces are covered by mulch, infrared thermography is currently the only technique that can estimate soil surface micro-topography with a satisfactory performance (maximum mulch density: 2 ton / ha) (De Lima and Abrantes, 2014).

One of the main challenges of obtaining data about the micro-topography of a soil surface is to capture measured roughness patterns in hydrologically relevant parameters. Smith (2014) presents a comprehensive review of such parameters, classifying them as a representation of a surface property, a flow property (flow resistance) or a model tuning parameter (calibration value without physical connection with roughness). We will mention parameters sporadically throughout this manuscript, but refer to Smith (2014) for detailed definitions. Although there is not a standard roughness measurement protocol, the technique used to obtain a roughness parameter should be justified. Table 2.1 displays a list of important factors and questions to take into account when choosing a measuring technique.

Table 2.1 Factors to determine which technique to use to quantify micro-topography.

	Factors	Questions to analyze
1	**Purpose of Roughness Parameterization**	What are we going to use the roughness parameter for?
2	**Size of the Study Area**	Representative size or entire surface?
3	**Location of the surface**	Is the surface in the laboratory or in the field?
4	**Is the system Static or Dynamic?**	Is the change over time important? What reading speed is necessary?
5	**Is a DEM necessary?**	Is spatial anisotropy relevant? Are the main features enough to represent the surface?
6	**Vertical and Horizontal Accuracy**	Is a minimum precision required?
7	**Restrictions due to Surface Characteristics**	Does the surface have a high slope or mulch/vegetation cover? Is it hard to access? Are the micro-topographic features complex?
8	**Budget**	Does the cost of the technique appropriate for measurement requirements fit the budget? If not, which of the previous requirements can be overlooked?

3. Micro-Topography and Flow Patterns

Despite the connection of micro-topography with the hydrologic system, its effects have rarely been incorporated into hydrological analyses of rainfall-runoff partitioning. The role of micro-topography in concentrating overland flow and its influence on hydraulics is an area where further research is needed. At a watershed scale, the distribution of surface flow (open channel flow) is controlled

by the interactions between surface topography and the hydrologic network. At the plot and hillslope scale, the surface flow (overland flow) is affected by surface roughness elements. These are: ridge-and-furrow geometry created by tilling, random roughness, small depressions, and micro-channels. Flow patterns influenced by macroscopic elements have been studied, but the interactions between water flow at the hillslope scale and micro-topography remain indeterminate (Legout *et al.*, 2012).

3.1 Rainfall-Runoff Partitioning

Surface roughness controls many transfer processes on and across the surface boundary, such as infiltration and runoff (Huang and Bradford, 1992). Helmers and Eisenhauer (2006) observed that roughness as a surface property (micro-topography) had a greater effect on overland flow than roughness as a flow property (resistance) when modeling a vegetative filter. Overlooking micro-topographic variation might lead to significant biases in prediction of hydrological partitioning of rainfall into infiltration and runoff (Thomson *et al.,* 2010). It is more representative to model local flow depths and velocities over the flow surface considering the actual variations of micro-topography (Tayfur *et al.*, 1993); this is particularly important for low inflow rates. There is a broad series of studies (Lane *et al.*, 2005; Thompson *et al.*, 2010; Chi *et al.*, 2012; Chu *et al.* 2013a) that show substantial connections between micro-topography in the shape of mounds, rills and depressions, infiltration, and runoff response.

Soil surface roughness greatly affects surface sealing and runoff generation and distribution; furthermore, surface roughness may evolve as a result of consecutive rainfall events (Helming *et al.*, 1998). The erosion experienced by initially smooth surfaces after several precipitation events significantly affects the runoff pattern; in this case the initial conditions of the soil roughness are not a suitable parameter to represent drainage networks. However, the mounds representing the rough surfaces provide useful information to describe the overland flow distribution over the surface (Helming *et al.*, 1998; Abrahams, *et*

al., 1992; Lane, 2005), where the presence of initial micro-topographic features facilitates the prediction of runoff/infiltration partitioning over time. Smooth surfaces, conversely, are prone to evolve until a predominant geometry forms and the surface stabilizes. In addition, the laboratory experiments of Darboux *et al.* (2001) indicated that the total volume of depressions decreased after successive rainfalls, since scour and sedimentation in interrill areas tend to decrease the roughness amplitude as a result of erosion and sealing. A threshold roughness was observed, where the storage capacity tends to zero below this limit. One characteristic of this threshold was its dependence only on initial soil surface shape. This threshold is another example of an initial roughness characteristic of the soil that can predict the final morphology of the surface.

Thomson *et al.* (2010) introduced the concept of "effective sorptivity," which represents the scaled value of sorptivity, or a measure of a soil's tendency to absorb water due to capillary effects, used when the measurement point has a significant micro-topographic variation. An increase of the sorptivity implies an extension of the time to ponding. These researchers showed that micro-topographic features in the form of elongated depressions running cross-slope increase the infiltration of the total volume of water running onto the surface by 20–200% (relative to an otherwise smooth surface) for short storms on shallow slopes. The increase in infiltration was greater with larger micro-topographic amplitudes. Although Thompson *et al.* focused on features perpendicular to the flow, the micro-topographic features parallel to the flow, such as rills (Figure 2.4), also experience an increment in infiltration rates per unit area due to the effect of lateral infiltration or edge effect (Figure 2.5) (Warrick and Lazarovitch, 2007). However, the total volume infiltrated when micro-channels develop is typically lower than for a flat surface.

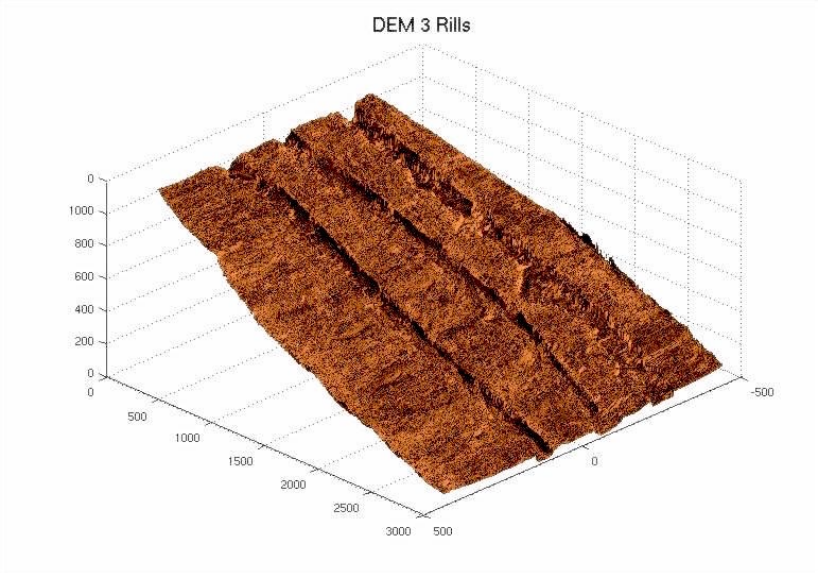

Figure 2.4 Digital Elevation Model (DEM) of a laboratory soil slope with an initial condition of three parallel rills after 20 minutes of flow. Space dimensions are in mm (Chapter 4).

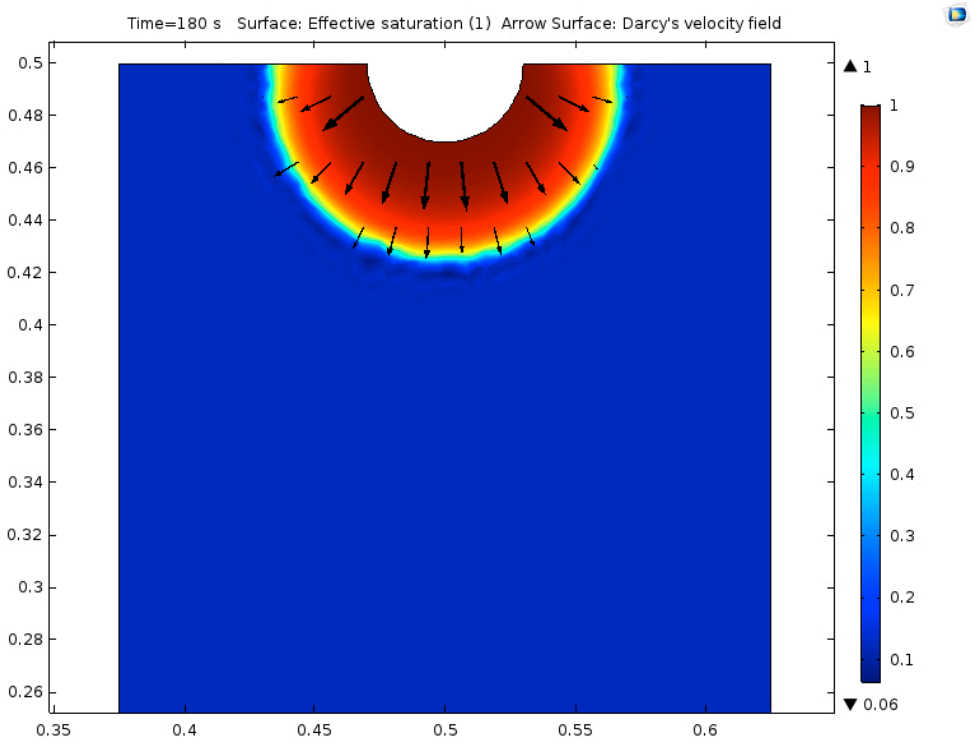

Figure 2.5 Simulation of the effective saturation in a cross-section of a semi-circular rill, with both vertical and lateral infiltration flux into the soil. Simulation space dimensions are in meters. Simulation was accomplished with COMSOL Multiphysics (2016).

The research shows that micro-topography is one of the main factors controlling the drainage network, jointly with the infiltration capacity of the soil (Helmers and Eisenhauer, 2006). Surface roughness affects runoff generation by water retention in depressions, by flow obstruction, and by accommodation of preferential pathways on the surface. Surfaces with cross-slope oriented surface depressions tend to enhance infiltration and decrease runoff while downslope oriented surface depressions (rilled) exhibit an increase of runoff and decrease in infiltration. As a result of consecutive rainfall events affecting surface roughness, infiltration rates of a soil with a fully developed crust are independent of initial soil roughness (Govers *et al.*, 2000); however initial soil roughness can help to predict where the crust will be formed (typically in depressions and interrill areas) and different rainfall intensities can change both the soil roughness and the crusting. Accordingly, both features need to be taken into account to predict the runoff/infiltration processes.

3.2 Erosion and Rill Network

In their laboratory experiments Chu *et al.* (2013a) observed earlier and greater runoff discharge for the surface dominated by downslope oriented roughness (though initially smooth) and lower runoff from the surface governed by depressions. Smooth surfaces will often evolve until a predominant geometry forms and the surface stabilizes. Another illustration of a smooth surface becoming rough after rainfall are the laboratory experiments by Cooper *et al.* (2012), where rills were developed in the downslope direction of an experimental plot. Cooper *et al.* developed a soil-erosion model that could predict the formation of shallow rills, obtaining a good approximation of the observed runoff hydrograph for the plot. This study demonstrated that for surfaces with high potential for dynamic change it is necessary to couple the runoff generation and surface erosion generation processes.

The geometry of rill networks developed during a rainfall event depends on the relative importance of sediment transport mechanisms, along with the initial slope

and magnitude of surface roughness. McGuire *et al.* (2013) developed a numerical model to simulate landscape evolution; where the equations represented three processes: the direct transport of material due to raindrop splash, the fluvial detachment and transport of bed material disturbed by raindrop impact, and the deposition of sediment being advected through overland flow. Micro-topographic formations have been associated with characteristics of the slope and roughness parameters (Helming *et al.*, 1998; Vermang *et al.*, 2015), always in combination with the effect of rainfall and overland flow. Rill morphology has also been associated with flow discharge, median grain size, soil hydraulic conductivity, and slope angle (Imeson and Verstraten, 1988). Ali *et al.* (2012) found that with smaller grain size, fewer rills formed but the rills were wider and with greater grain size, more rills formed but the rills were narrower. In order to characterize rill erosion and reflect the complexity of a rill network, with main and secondary rills, such as seen in Figure 2.6, researchers have used roughness, topological, and rill specific parameters. Zhang *et al.* (2016) established that fractal dimension can reflect the static complexity of the rill network, but not the dynamic changes. In addition, topological parameters, such as bifurcation ratio (the ratio of each channel's order and the higher order channel), can suggest the stability of the rill network structure (Zhang *et al.*, 2016). Shen *et al.* (2015) found that to evaluate rill morphology and erosion, individual rill width was the best basic morphological indicator and degree of rill dissection (rill coverage area per unit drainage area) was the best derivative morphological indicator.

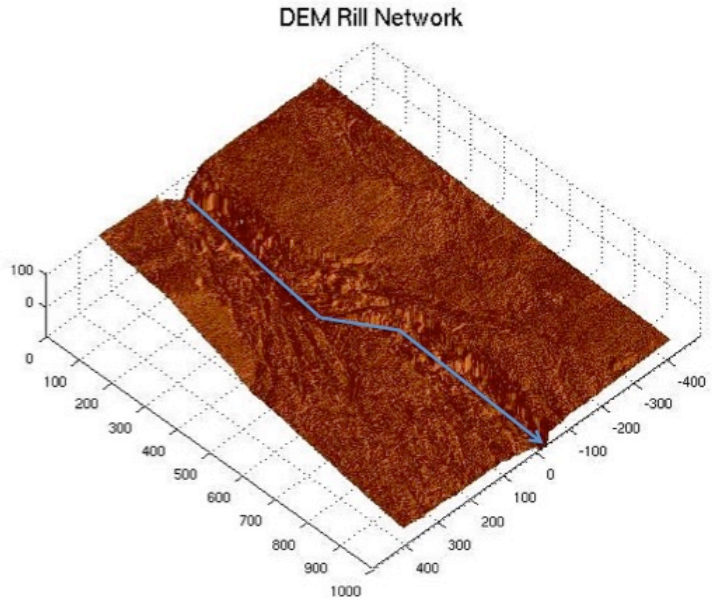

Figure 2.6 Digital Elevation Model (DEM) of a laboratory soil slope with an initially smooth condition that has evolved into a network of rills after 40 minutes of flow. The blue arrow represents the main rill. Space dimensions are in mm (Chapter 4).

Rainfall intensities influence the effect of micro-topography on the runoff partitioning process and sequential precipitation events can generate the formation of micro-channels and rill networks in initially smooth surfaces. To understand the evolution of eroded surfaces, there are roughness parameters that can be used to assess the stability and morphology of rill networks (Zhang *et al.*, 2016; Shen *et al.*, 2015). When a surface still has not reached a stable stage, coupled overland flow-erosion models are necessary to make accurate runoff-infiltration predictions.

3.3 Connectivity

The characteristic spatial patterns of hydrologic processes can range from being completely random (low connectivity) to being highly organized (high connectivity). Bracken and Croke (2007) define connectivity as: “all the former and subsequent positions, and times, associated with the movement of water or sediment passing through a point in the landscape”. Connectivity is important on all scale levels (Cammeraat, 2002). The process of runoff initiation involves the

gradual filling of depressions and the connection of those overflowing at a certain time toward an outflow point (Darboux *et al.*, 2001). Consequently, infiltration efficiency affects hydrological connectivity, and thus runoff.

Functional or process-based (Bracken *et al.*, 2013) hydrologic connectivity analysis is the quantification of the hydrologic responses of micro-topography to the system inputs, while structural hydrologic connectivity represents the connectivity properties of static topographic surfaces (Antoine *et al.*, 2009). Antoine *et al.* (2011) proposed a procedure with what they coined a relative surface connection (RSC) function that integrates the effects of both depression storage and surface detention dynamics. The procedure was found to improve hydrograph prediction compared to the conventional approach where runoff is assumed to start only after depression storage capacity is full. This improvement was considered to be due to the representation of micro-topographic variability within a single grid cell (smallest computational element in a model), which better incorporates the heterogeneity of the soil surface micro-topography. Appels *et al.* (2016) calculated RSC functions from the results of a model of two different fields with different micro-topography and general lack of topographic gradient. A convex RSC function was associated with the well-connected surface and a more pronounced step function was associated with the poorly connected surface with a small number of large puddles. Peñuela *et al.* (2015) characterized the RSC function using three parameters: the surface initially connected to the outlet, connectivity threshold, and maximum depression storage. The connectivity threshold represents the excess of cumulative rainfall volume at which a sharp increase in the runoff is observed as a result of a sudden increase in hydraulic connections over the surface. Peñuela *et al.* found connections between the sill and range of the semi-variograms for a surface's micro-topography, and the parameters used to characterize the RSC function. For low slopes with deep depressions, the RSC function was related to a single parameter (range or sill) of the surface micro-topography, whereas for high slopes and shallow depressions, both variogram characteristics were needed to quantify connectivity.

On surfaces dominated by depressions, the distribution of water is primarily controlled by the correlation of topographic features (Chi *et al.*, 2012). Fractal D, for example, is a direction-dependent parameter, derived from variogram analysis of the topographic surface. A surface with a smaller D value had the potential to retain more water on the surface (in depressions), which in turn redistributed surface water, enhanced infiltration in the depressions, and delayed surface runoff generation. Chi *et al.* (2012) performed overland flow experiments under natural rainfall and observed that relationships established between fractal dimension, D, and infiltration, runoff and hydrologic connectivity (quantified as number of connected areas or depressions) are important to runoff and infiltration. The predominant surface roughness features existed along the directions of smaller D values. Along those directions, surface runoff was prone to be hindered or blocked by continuously distributed ridges. This study is an example of how a roughness parameter (fractal D) can relate to the overland flow process and hydrologic connectivity. Further research is needed in this direction.

Despite the importance of connectivity in overland flow processes, researchers have not agreed on a preferred hydrological connectivity index or evaluation protocol (Bracken *et al.*, 2013). Previous studies have analyzed process-based and structural hydrologic connectivity of surfaces with depressions using a roughness parameter (Fractal D) and a RSC function. More detailed information can be obtained from the RSC function, however it requires either model simulations or field observations of runoff. The rainfall distribution, size and intensity, micro-topography and spatial variation in infiltration should be analyzed to better represent areas of rainfall excess generation on a hillslope and the connections of those areas to accommodate flow downslope.

4. Overland flow models and micro-topography

Traditional physically-based of overland flow have tended to assume plane surfaces, resulting in water distributed over the entire surface. In addition, the

hydraulic properties are usually assumed to be spatially constant (Esteves *et al.*, 2000) and simplified equations, such as kinematic wave and diffuse wave assumptions, are used (Fiedler and Ramírez, 2000). According to Tayfur *et al.* (1993) these simplified models avoided incorporating fine scale topography not only because of the complications arising in the numerical procedures, but also because of the extra effort involved in obtaining the micro-topography data at the grid scale dictated by the numerical model. In addition, computational times were and are a constraint imposed on these models. However, advances in hydrology in the last 30 years have been supported by an exponential increase of the power of computers (Singh and Woolhiser, 2002) and measurement techniques (Bracken *et al.*, 2013). Now we are able to capture micro-topography with advanced measurements techniques, process the data in a fast manner, and use the results as input in models with significant details and improved numerical schemes. The computational models are still limited in scale, but the greater limitation is the lack of research focus on the development of these topography-flow-infiltration models.

Puddle-filling models have been used to predict connectivity and spatial distribution of overland flow from micro-topography. Chu *et al.* (2013b) established puddle delineation by first classifying the puddle types according to the relationship of the lowest elevation in a puddle to the corresponding overflow threshold elevation (pour point) and second by establishing a spatial hierarchy of how the puddles relate to each other. Yang and Chu (2015) included infiltration in their puddle-to-puddle model and found that surface depressions altered the spatio-temporal redistribution and interactions of infiltration and runoff water. However, this model does not represent sealing and crusting processes that are likely to occur in depressions and cause spatial heterogeneity of the infiltration capacity of the soil. In addition, in puddle-to-puddle models depression storage capacity does not change with time.

Physically-based hydrologic models are those that are based upon the

conservation of mass, momentum, and/or energy equations of water flow in various flow domains. The hydrologic variables of interest are forecasted by these models not only at the outlet, but at any spatial location within a catchment. Consequently, they require information on spatially distributed initial conditions and time-space distributed boundary conditions in order to describe the evolution of hydrologic flow processes in time and space (Kavvas *et al.*, 2004). Generating an accurate overland flow model involves knowledge of the water movement at any point of the soil surface, thus a physically-based model is the most suitable. An example of a spatially variable model, for both infiltration and micro-topography is Fiedler and Ramirez (2000) two-dimensional overland flow model that uses the hydrodynamic flow equations solved using a modified McCormack finite difference scheme, and the Green Ampt model solved using Newton-Raphson iteration. Seeking to quantify the combined impact of soil-surface sealing, micro-topography, and vegetation patches on surface hydrologic processes on a semiarid hillslope, Chen *et al.* (2013) developed a two-layer conceptual infiltration model and two-dimensional surface runoff model. They determined that the seal layer controls the initiation of runoff generation; vegetation patches reduce overland flow by enhancing local infiltration rates; and micro-topography has a small impact on the total amount of runoff, but shapes the spatial pattern of overland flow. The cumulative runoff depth in the cases with vegetation and vegetation with micro-topography differed by less than 1mm in the simulations. The Chen *et al.* model did not have the ability to simulate sediment transport as a consequence of the water flowing on the surface, so the evolution of the soil surface was not represented in the simulations. Had they included the evolution of the surface, the magnitude of the preferential channels on the surface would have increased over time, especially on bare soils. Consequently, it is not surprising to find only a slight impact of the micro-topography on the total runoff in their results. Surface sealing has been related to micro-topography; consequently these two processes should not be analyzed independently, but as a combined process. When the soil surface does not experience erosion and

deposition, however, the type of model represented by the model of Chen *et al.* may be a good option. Cea *et al.* (2014) developed and validated a two-dimensional overland flow model capable of accurately reproduce water depths and flow velocities of a 1 m^2 plot with a spatial resolution in the order of 10 mm. No infiltration was included in the experiments for the validation. In surfaces with soil aggregates, as opposed to sand texture, to accurately reproduce the flow hydrodynamic, the bed roughness coefficient must account for the flow resistance associated with the soil aggregates.

An efficient method to reduce model input resolution was presented by Frei and Fleckenstein (2014), based on the fact that surface flows regulated by micro-topography occur in defined micro-channels and extended surface flow networks of interconnected ponded depressions. Frei and Fleckenstein mimicked a complex micro-topographic surface using a planar model with a lower grid resolution and superimposed spatially distributed rill or depression storage height variations. The simplified surface was compared with a highly resolved, three-dimensional numerical grid to explicitly represent micro-topography, and micro-channeling effects and surface flow networks were successfully simulated. Consequently, high-resolution grids can be substituted by lower resolution representations of the surface with the addition of its key micro-topographic features, reducing the required number of computational nodes.

Dynamic distributed models that take into account spatial variability (Morgan *et al.*, 1998) are necessary for representing erosion and overland flow. In contrast with the models discussed previously, Nord and Esteves (2005) developed a two-dimensional infiltration and overland flow model that incorporated erosion and soil crust effects. Erosion and deposition processes affected slope and infiltration parameters. The spatially distributed thickness and hydraulic conductivity of the crust was specified, and the infiltration and roughness parameters were calibrated. The model was not validated in natural slopes and the accuracy in field plots is linked to the effort of collecting micro-topography and infiltration

parameters over the whole area.

What good comes from these detailed computational models? First, to gain full scientific understanding of the infiltration/overland flow/soil erosion processes it is necessary to develop and test these types of models. Thus, the collection of micro-topographic data and the utilization of two-dimensional models are both recommended. Second, subgrid parameterization can be developed and applied to facilitate adequate simulation of the hydrologic responses given by fine-scale models but using coarse grid representations. It is these upscaled models that will be needed to facilitate the practical application of models for prediction of hydrologic response. To date, most research has focused on the first of these two points. In the future, more focus needs to be applied to the second.

5. Conclusions

Micro-topography plays a significant role in the control of the spatial variability of infiltration, overland flow and of surface sealing and crusting. In general, micro-topography that has a cross-slope orientation decreases runoff while micro-topography with a downslope orientation tends to increase runoff (Thomson *et al.* 2010; Kirkby *et al.*, 2014). The overall consensus of the literature is that most surfaces with surface depressions tend to enhance infiltration and decrease runoff, although rilled surfaces (with channels in the flow direction) exhibit an increase of runoff. Rainfall intensities also affect the influence of depressions in runoff-infiltration partitioning and precipitation events can generate the formation of micro-channels in initially smooth surfaces. Additionally, it is particularly important to consider the micro-topography of the surface when water depths are comparable to the characteristic height of the micro-topography due to the possible blockage of the flow.

Determining empirical relationships between micro-topography parameters and flow characteristics simplifies the representation of the latter, avoiding cumbersome measurements of the flow or surface crust. The challenge is to find

characterizations that mean something relative to explaining differences in surface runoff volume, hydrograph shape, and/or surface erosion patterns. There are parameters that have already been successfully used to relate micro-topography to hydrological processes and surface sealing and crusting; e.g. random roughness (RR) (Vermang *et al.*, 2015), fractal D (Chi *et al.*, 2012) and sill, range and slope (Peñuela *et al.*, 2015). However, more research needs to be undertaken in this area to develop a micro-topography descriptor of how water and surface interact. This micro-topography parameter should define the surface well enough to be able to determine flow direction and pattern of overland flow under specific flow conditions. Moreover, the effect that overland flow patterns have on the aggregate runoff generated from a hillslope has not been satisfactorily verified.

The conventional approach where runoff is assumed to start only after depression storage capacity is full does not provide accurate predictions, the alternative puddle-to-puddle models better represent the connectivity of depressions. The rainfall distribution, size and intensity, micro-topography and spatial variation in infiltration should be analyzed to better predict areas of runoff generation on a hillslope and their connections. When calculating connectivity, infiltration should be included in the analysis, because it reduces the water available to contribute to overland flow; particularly, varying spatial distribution of infiltration properties has been postulated to affect connectivity (Appels *et al.*, 2011). A future research need is the effect of varying infiltration properties on the process-based and structural hydrologic connectivity. Previous studies have analyzed process-based and structural hydrologic connectivity of surfaces with depressions using a roughness parameter (Fractal D) and a RSC function. More detailed information can be obtained from the RSC function, however it requires either model simulations or field observations of runoff.

Roughness parameters can be applied to map spatial patterns, neglecting the evolution of the surface during the process (fully developed surface), however

only a few relationships between initial and final micro-topography (Darboux *et al.*, 2001; Vermang *et al.*, 2015) have been established to predict the formation of new surface geometries (dynamic surface). More research is required to determine the conditions under which initial soil roughness of an erodible surface can be used to estimate runoff and infiltration volumes. Once the surface is fully developed, only the main micro-topographic features (channels, mounds and depressions) are needed to adequately represent runoff processes.

To develop accurate spatially distributed models on the plot and hillslope scale, a better understanding of overland flow and infiltration processes is needed. These models will then have the ability to better estimate erosion processes, contaminant transport, and infiltration volume. New measurement techniques and computer power are continually improving our ability to add fine topographic and soil detail to the simulation of the hillslope processes of infiltration, overland flow, and erosion/deposition. These fine details are essential to facilitate the development of scientific understanding of the coupling of these processes. Therefore it is recommended that the collection of fine detailed data and development of more efficient models should continue. However, there is also interest in the relation between the fine details and upscaled representations of the processes, since in the end to facilitate practical application of the models one needs to coarsen the representations. This step of upscaling will require additional research. Implementing a planar model with a lower grid resolution and superimposed spatially distributed rill or depression storage (Frei and Fleckenstein, 2014) is an efficient solution to represent the effect of micro-topographic features on hydrologic processes. The challenge lies in developing meaningful upscaling relationships that will allow adequate representation of observed phenomenon using coarser scale models.

Acknowledgments

The writers are grateful to the Minnesota Department of Transportation and

Minnesota Local Road Research Board for funding this research under Contract No. 99008- 97, with Barbara Loida as Technical Liaison. John Nieber's effort on this project was partially supported by the USDA National Institute of Food and Agriculture, Hatch/Multistate project 12-059.

Chapter 3

Infiltration Flux for Parallel Strip Water Sources

Summary

The importance of the lateral component of flow on the infiltration of water from parallel strip sources of water on the soil surface is evaluated. Infiltration from such sources is two-dimensional, having both a vertical and a lateral component. Warrick and Lazarovitch (2007) developed a method to calculate two-dimensional infiltration from a single strip water source by adding an "edge effect" to the one-dimensional calculations. Since their analysis was for a single strip source they did not account for the impact of parallel strip sources on this edge effect. In our research a finite element model has been used to obtain numerical solutions of the two-dimensional Richards equation and simulate the reduction of lateral infiltration, and therefore the edge effect, of a strip water source due to the influence of adjacent strips. The infiltration from strip water sources was modeled using various strip spacing, widths, flow depths, and soil textural classes.

The interaction between neighboring parallel strips effectively reduces the steady-state infiltration rates through each strip. The effect of the spacing of strip water sources and soil texture on the infiltration from parallel strip sources of water on the soil surface has been studied. This relationship represents a modification of previous work in which the edge effect on infiltration caused by lateral flow from an isolated strip water source was investigated. In general, the relationship shows that for a given strip spacing, wider strips, greater flow depths, and finer-textured soils have more interactions and a greater reduction in edge effect infiltration from parallel strip water sources. For transient flow conditions, the relative edge effect increases over time until, at steady state, it reaches a maximum constant value. The outcomes of this study are applied to two different practical applications of infiltration under steady state conditions using a factor to account for two-dimensional flow with strip sources interactions.

1. Introduction

A better understanding of the processes that control water fluxes in the vadose zone is important to understand the impact of water source geometry on infiltration rates. Models of water fluxes in the vadose zone typically use Richards' equation (Richards, 1931), except for scenarios with preferential flow (Lassabarere *et al.*, 2009; Feddes *et al.*, 1988). Infiltration models of strip sources of water on the soil surface using Richards' equation are computationally intensive and complex for practical use (Subbaiah, 2013; Bautista, 2016). However, there are approximations that can provide reasonably accurate results avoiding intense computational efforts (Warrick and Lazarovitch, 2007; Warrick *et al.*, 2007, Bautista *et al.*, 2014).

Analytical models provide a direct relationship between input parameters and and output variables, require only essential parameters to solve problems, and offer a general framework that simplifies design formulation (Subbaiah, 2013). Historically the multiple dimensional infiltration through the surface has been approximated by a one-dimensional infiltration equation with one or more terms added to account for the accompanying lateral flow component. The general form for infiltration due to two-dimensional flow is expressed as $i_{2D} = i_{1D} + i_{Edge}$, where i_{1D} is the term for vertical flow and $i_{Edge} = \phi\ i_{Horiz}$ is the term for capillary-driven lateral flow, also called the 'edge effect'. The i_{Edge} term is composed of a term for horizontal infiltration (i_{Horiz}; purely capillary-driven flow), and a scale factor ϕ that accounts for the geometry of the flow. The i_{Edge} term is dependent on the capillarity of the soil, and also the actual geometry of the two-dimensional flow. An analytical equation for infiltration from one strip source was developed and presented by Warrick and Lazarovitch (2007). This analysis evaluates the importance of the lateral component of flow on the infiltration of water from multiple parallel strip sources of water on the soil surface, and establishes a comparison with Warrick and Lazarovitch's steady state results from a single

strip. Flows from such sources are two-dimensional, having both a vertical and a lateral component, and thereby the infiltration through the surface will also be affected by the shape of the flow pattern.

There is a need for a simple estimation of two-dimensional water infiltration from parallel strip sources of water on the soil surface in order to simplify computations for practical applications. The applications are diverse, from furrow irrigation to overland flow and infiltration from parallel rills or infiltration over filter strips with shallow concentrated overland flow. The geometry of the flow in these cases is affected by the soil type, the flow depth, width of the strips, and the spacing between strips. The purpose of this research was to develop relationships between the strip water sources and soil type characteristics and the infiltration from parallel strip sources of water on the soil surface. The findings are applied to two different practical applications where the effect in edge infiltration of neighboring parallel strips has been evaluated.

2. Method

Warrick and Lazarovitch (2007) proposed an equation for two-dimensional cumulative infiltration per unit area of a single strip source over a given amount of time, based on previous work from Haverkamp *et al.* (1994):

$$I_{2D} = I_{1D} + \frac{\gamma S_0^2 t}{2x_0(\theta_0 - \theta_i)} \quad (1)$$

where I_{1D} is the one-dimensional cumulative infiltration, t is time, S_o is the sorptivity, x_0 is the semi-width of the strip, θ_0 is the volumetric water content at the source, θ_i is the initial water content in the profile, and γ is a dimensionless calibrated “constant” accounting for flow geometry.

Furthermore, the infiltration rate per unit area of a strip was derived from Eq. 1:

$$i_{2D} = i_{1D} + \frac{\gamma S_0^2}{2x_0(\theta_0 - \theta_i)} \quad (2)$$

where i_{1D} is the one-dimensional infiltration rate. For steady state conditions, i_{1D} equals the saturated hydraulic conductivity (K_{sat}) for the case of a ponded strip source.

In the analysis, the effect of spacing between strip sources on the relative importance of the edge effect term (i_{2D}-i_{1D}) was examined for steady state and transient conditions. It is hypothesized that the edge effect will decrease as the distance between strips decreases. At steady state, the second term in Eq. 2 would be multiplied by an additional constant, from 0 to 1, to account for the effect of multiple strips versus a single strip. For transient conditions, the influence of multiple parallel strip sources of water on the edge-effect term would also depend on time.

For the numerical solution COMSOL Multiphysics® was used, a commercial finite element modeling software capable of solving a wide range of partial differential equations. Three different types of subsurface flow were simulated: vertical flow (one-dimensional flow) from a single strip, two-dimensional flow from a single strip, and two-dimensional flow from multiple parallel strips.

2.1 Governing Equations and Simulation Parameters

COMSOL's Subsurface Flow Module with the time-dependent governing equation given by the two-dimensional Richards' equation (Eq. 3) (Richards, 1931) was used in the simulations, with the following assumptions: homogenous soil, uniform initial soil water content, and shallow water depth at the source.

$$\frac{\partial \theta}{\partial t} = \frac{\partial}{\partial x}\left(K \frac{\partial h}{\partial x}\right) + \frac{\partial}{\partial z}\left(K \frac{\partial h}{\partial z}\right) - \frac{\partial K}{\partial z} \tag{3}$$

The van Genuchten (van Genuchten, 1980) hydraulic model was used to represent the effective saturation and hydraulic conductivity functions of the soils evaluated:

$$S_e = \frac{\theta - \theta_r}{\theta_s - \theta_r} = (1 + |\alpha h|^n)^{-m}; m = 1 - \frac{1}{n} \tag{4}$$

$$K(h) = K_{sat} S_e^l [1 - (1 - S_e^{-m})]^2 \quad (5)$$

where S_e is the effective saturation, θ is the volumetric water content, θ_s is the saturated water content, θ_r is the residual water content, h is water depth, α and n, are empirical shape parameters, $l = 0.5$, and $K(h)$ is the unsaturated hydraulic conductivity.

To estimate sorptivity (S_0) the following method used by Warrick *et al.* (2007) and justified by Bautista *et al.* (2014), based on the Green and Ampt analysis (Green and Ampt, 1911; Warrick, 2003) was applied:

$$S_o = \sqrt{2K_{sat}(\theta_s - \theta_i)(h_0 - h_f)} \quad (6)$$

where h_0 is the water depth at the surface, and h_f is wetting front pressure head.

The wetting front pressure head (h_f) was calculated based on the following equation by Neuman (1976):

$$h_f = -\int_{h_i}^{0} \frac{K(h)}{K_{sat}} \quad (7)$$

where h_i is the pressure head corresponding to the initial water content.

Four soils were selected to perform the simulations: sand, loamy sand, sandy loam, and loam. The input parameters of the soil, presented in Table 3.1, are based on Carsel and Parrish (1988). The modifications of the van Genuchten equations presented in Vogel *et al.* (2001) were used for the loam simulations; the pressure parameter h_s was set to -0.04 m for all the simulations shown here.

Table 3.1 Soil hydraulic properties for four different soils described with the van Genuchten model. Based on Carsel and Parrish (1988). *Parameter estimated using Equation 7.

Soil type	α [1/cm]	n	θ_r	θ_s	K_{sat} [cm/h]	h_f^* [cm]
Sand	0.145	2.68	0.045	0.43	29.7	4.6
Loamy Sand	0.124	2.28	0.057	0.41	14.6	5.0
Sandy Loam	0.075	1.89	0.065	0.41	4.42	7.2
Loam	0.036	1.56	0.078	0.43	1.04	11.9

Four strip widths (1, 3, 10, and 20cm) and multiple distances between strips were tested. The simulations were characterized by a computational domain (Figure 3.1) of 50cm height (A-F and C-D) and varying width (A-C), depending on the semi-width of the strip (A-B) and the semi-distance to the next parallel strip (B-C). The width of the computational domain varied from 2cm (for the 0.5cm semi-width of the strip and 1.5cm semi-distance between strips) to 200cm (for the single strip simulations). The domain was discretized into triangular finite elements forming a fine mesh with the finest elements surrounding the water source. The time step was set to 10s and the calculations were carried out to steady state.

2.2 Initial and Boundary Conditions

The following initial and boundary conditions were used in all the simulations:

1. Specified initial capillary pressure head (H_p) on the flow domain.
2. Specified pressure head on the strip source (h_0) at the soil surface (A-B).
3. Zero flux on the vertical boundaries (symmetry) and the soil surface outside of the strip source (A-F, B-C, and C-D).
4. Specified unit hydraulic gradient (free drainage) at the bottom boundary. This condition represents free drainage at the bottom boundary.

The corresponding initial soil moisture content (θ_i) was determined by the model based on the specified H_p and Eq (4). For the steady state simulations the initial H_p was set to -0.5m for all the soils.

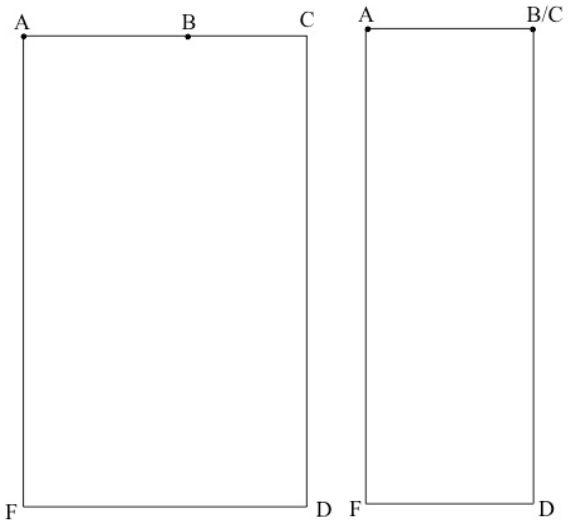

Figure 3.1 Illustrations of the axisymmetric domain for (a) semi-strip (A-B) with parallel strips at a semi-distance B-C. (b) semi-strip A-B with one-dimensional (vertical) infiltration. Symmetry lines were A-F and C-D.

3. Results

3.1 Steady State Conditions

The infiltration from strip water sources was modeled using various strip widths, spacing, flow depths, and soil textural classes. The simulation times was extended until steady state was observed for the selected initial soil moisture content. For θ_i = 0.3 in both sand and loamy sand, steady state was achieved in less than 30min (Figure 3.2). It is observed that, for multiple strip sources, the flow from each of the parallel strips interacts with the adjacent strips (Figure 3.2). The maximum infiltration rate was observed for the two-dimensional single strip water source and the minimum was for the one-dimensional single strip. The infiltration rates from multiple strip sources approached the upper bound as the distance between strips increased, as expected. The case of a single strip with

one-dimensional infiltration represents sheet flow conditions, with zero space between the water sources. The relative importance of the edge effect was quantified by taking the ratio of the infiltration per strip source (with multiple sources) to the infiltration from a single isolated strip source. The results showing a relation between strip spacing and the edge effect (i_{2D}-i_{1D}) at steady state for four soil textures is illustrated in Figure 3.3. The initial soil moisture content does not influence the results at steady state. For a given strip spacing the magnitude of the interaction increases, and the infiltration decreases, for finer soil texture. This interaction effectively reduces the lateral flow beneath the individual strips and, in effect, reduces the vertical flux (infiltration) through each strip. The interaction between strips will be zero for strips spaced an infinite distance apart, and the maximum edge effect and thereby the maximum infiltration through the strip will occur for that case. Figure 3.4 presents the influence of the strip source spacing on the edge effect for four different strip widths in a sandy loam soil. The wider the strip water source, the more interaction between strips, and lower edge effect, at a given distance apart. The results show that there is a specific separation between strips, different for each soil texture class and strip width, where there is no effective interaction between them with respect to the edge effect.

A

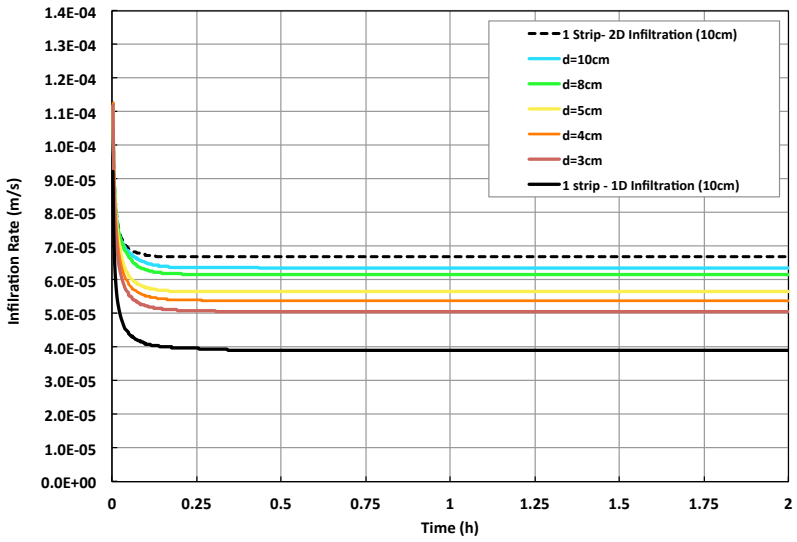

B

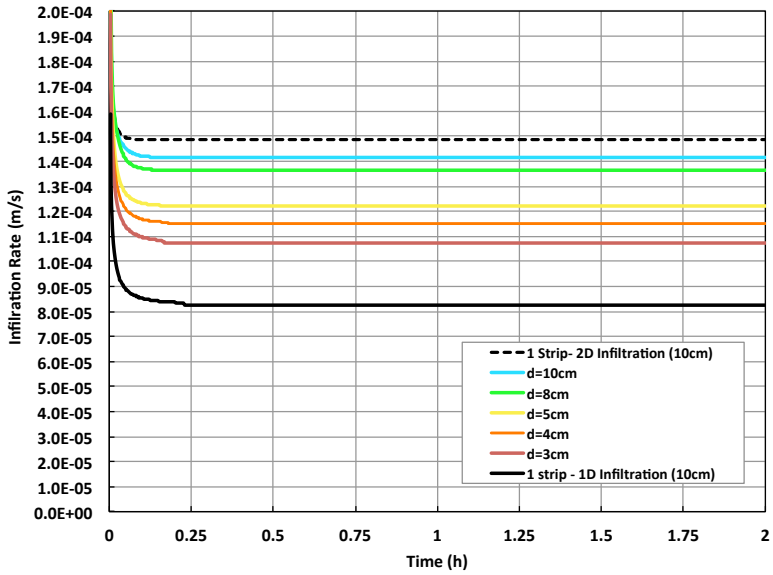

Figure 3.2 Infiltration rated from a single strip and multiple strip water sources with different distances (d) between them are presented. **A**) Loamy sand. **B**) Sand. The width of the strips is 10cm, the water depth 3mm, and θ_i=0.3.

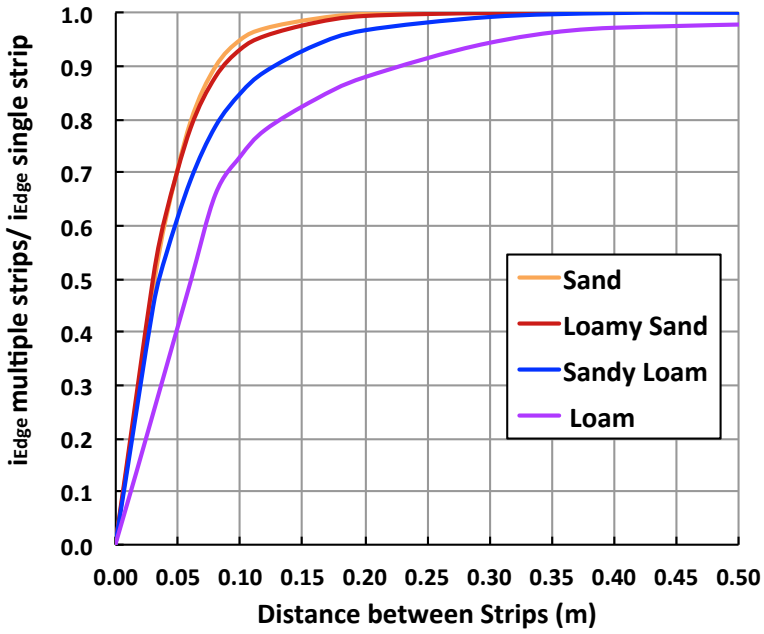

Figure 3.3 The influence of the strip source spacing on the edge effect as impacted by soil texture at steady state conditions for a strip width of 3cm and water depth of 3mm.

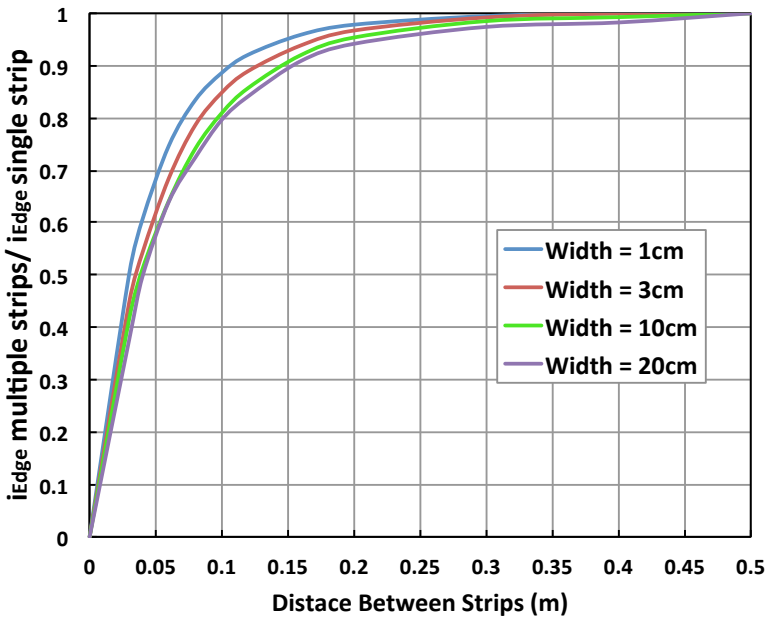

Figure 3.4 The influence of the strip source spacing on the edge effect as impacted by strip width at steady state conditions in a sandy loam soil for a water depth of 3mm.

Following the results presented in Figures 3.3 and 3.4, a modification of Warrick and Lazarovitch (2007) Eq. 2 is proposed to account for infiltration rates at steady state with multiple parallel strip water sources:

$$i_{Edge}=i_{2D}-i_{1D}=\zeta\frac{\gamma S_0^2}{2x_0(\theta_0-\theta_i)} \quad (8)$$

$$\zeta = 1-exp(-CL_\zeta) \quad (9)$$

where ζ is the ratio of edge infiltration rate with multiple sources to the edge infiltration from a single isolated strip, C is a constant that depends on the soil type, width of the strip and water depth at the source (h_0); and L is the distance to the next parallel strip. Rearranging Eq. 9:

$$L_\zeta = -\frac{1}{C}\,ln(1-\zeta) \quad (10)$$

where L_ζ is the distance between strips at which (1-ζ) fraction reduction takes place; for example, L_{90} represents the distance at which the edge effect from a strip water source parallel to other sources is 0.9 times the edge effect of a single strip without interactions, or 10% reduction.

Table 3.2 presents the calculated constant C, values of L_{90} and L_{50}, and γ for three different soil types and strip widths with the same water depth at the source (h_0 =3mm). Figure 3.5 shows the COMSOL simulated i_{Edge} and the predicted i_{Edge} using Eq. 8, Eq.9, and the C value in Table 3.2 for multiple strip water sources of 10cm of width and 3mm water depth in a loamy sand soil. All the R^2 values of the linear fit of predicted i_{Edge} versus simulated i_{Edge} were above 0.98. Within the range of conditions studied, strip width has a greater impact on the value of C than soil type. The L_{90} and L_{50} values for these configurations were computed from Eq. 10. Finally, the values of γ were derived from the COMSOL simulations results of the edge infiltration rate for a single strip water source and Eq. 3 at steady state conditions. Bautista *et al.*, (2014) reported that γ values are time-dependent but eventually tend to a near-constant value, for this reason steady state conditions were used to derive γ vales.

Table 3.2 Values of the fitted parameters C and γ based on COMSOL simulations using three different soil types and widths and the derived values of L_ζ.

Soil Type	Width [cm]	C [1/m]	L_{90} [cm]	L_{50} [cm]	γ
Sand	**1**	32.0	7.2	2.2	0.49
	3	25.1	9.2	2.8	0.62
	10	19.2	12.0	3.6	0.83
	20	17.6	13.1	3.9	0.96
Loamy Sand	**1**	31.2	7.4	2.2	0.40
	3	24.8	9.3	2.8	0.51
	10	20.0	11.5	3.5	0.66
	20	17.2	13.4	4.0	0.75
Sandy Loam	**1**	22.6	10.2	3.1	0.32
	3	19.5	11.8	3.6	0.39
	10	17.1	13.5	4.1	0.48
	20	16.2	14.2	4.3	0.53

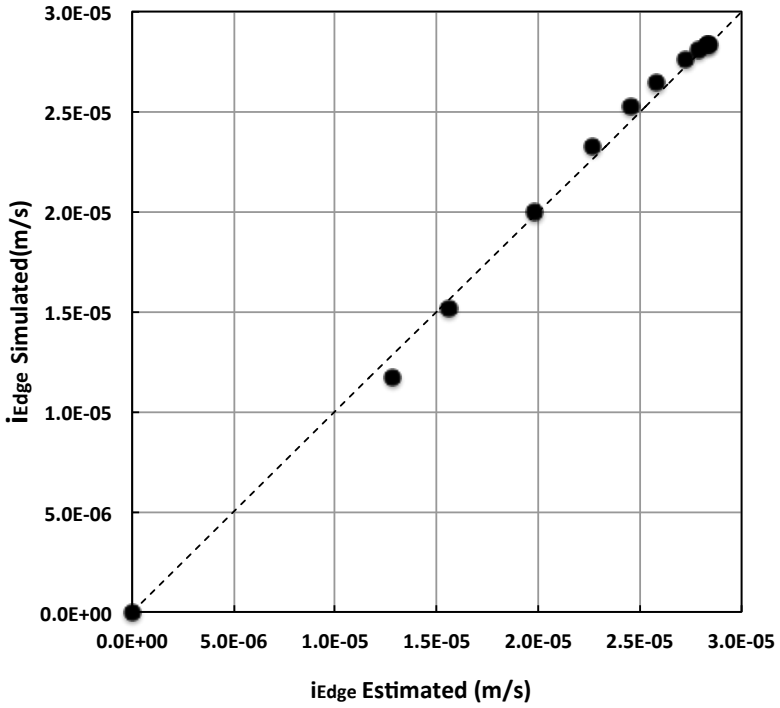

Figure 3.5 Edge infiltration rates simulated with COMSOL (i_{Edge} simulated) and estimated from Eq. 6 and Eq.7 using the C and γ values presented in Table 3.2 for multiple strip water sources of 10cm of width and 3mm water depth in a loamy sand soil. The distances between the multiple equidistant strips ranged from 3 cm to 100cm. The dashed line the 1:1 ratio of the estimated versus simulated i_{Edge} and the R^2 fit to the 1:1 line is 0.99.

L_{50} values for three soil types and four widths of the strip water source for h_0=3mm are shown in Table 3.2. The range of variation of L_{50} is below 2cm for a range of widths of the strip of 1 to 20 cm and a set water depth (3mm). However, the values of C, and consequently L_{50} and L_{90}, also depend on the water depth; an increase in the water depth would result in larger ranges in the L_ζ values. C is inversely proportional to h_0 and their relationship depends on the soil type and width of the strip water source (Figure 3.6). The infiltration predicted with Richards' equation for soils with smaller h_f is more sensitive to changes in the water depths (h_0) (Bautista *et al.*, 2014). This sensitivity is also observed for the edge infiltration rates with multiple parallel filter strips, supported by the greater slopes in Figure 3.6 of the fit of the constant C and h_0 for loamy sand (h_f=5cm)

compared to sandy loam (h_f=7.2cm). In addition, wider strips are more sensitive to changes in h_0.

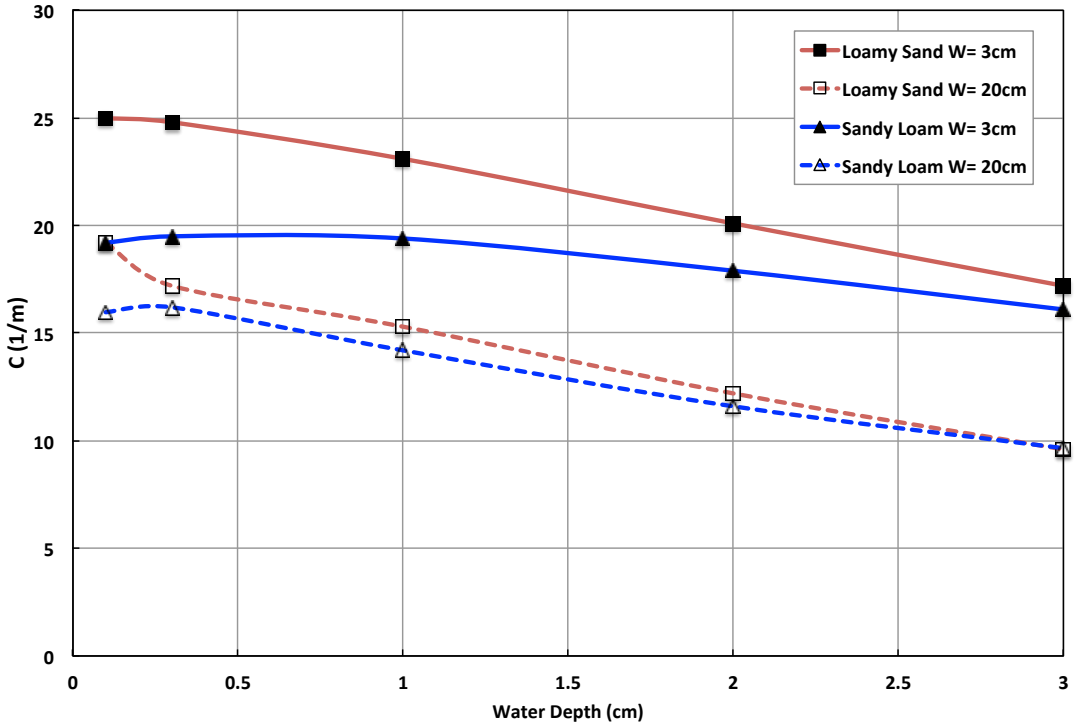

Figure 3.6 Effect of the flow depth of a strip water source in the constant *C* for parallel water strip sources on sandy loam and loamy sand soils of widths of 3 cm and 20 cm.

3.2Transient Flow Conditions

In the last section we examined the effect of strip source spacing, strip width, and water depth on steady-state infiltration rates. In this section we consider the transient phase of the infiltration process and quantify again the effect of strip source spacing. The importance of the lateral component of flow on the infiltration of water from multiple parallel strip sources of water on the soil surface has also been evaluated for transient flow conditions. Figure 3.7 illustrates the flow from a surface strip source of width 10cm equidistant to identical strip water sources at an 8cm distance at 0.05, 0.1, and 1 hour elapsed time. The vectors are close to vertical below the source, but the lateral flow due to capillarity is clearly seen. At

1 hour, capillarity is still seen in the upper two rows of vectors, but at 10 cm depth the flow is primarily vertical and well-distributed across the media.

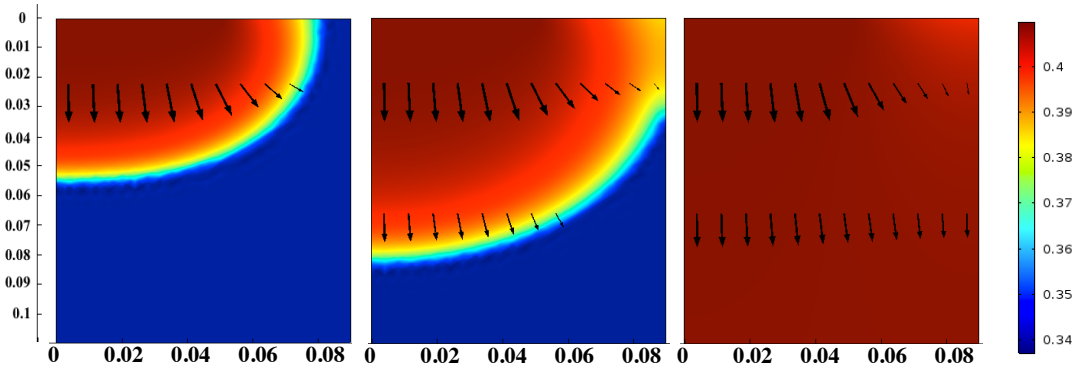

Figure 3.7 Soil moisture content at 180s (0.05h), 360s (0.1h) and 3,600s (1h), from left to right, from the infiltration of a 10cm strip water source (5cm semi-width) of 3mm water depth with parallel strip water sources at a distance of 8cm (4cm semi-distance). The simulations correspond to a loamy sand soil with θ_i=0.3. The arrows represent Darcy's velocity. Dimension is in m, except for the bar to the right, which is soil moisture content.

The cumulative infiltration depth has been evaluated for transient flow conditions. A set of numerical experiments simulating one-dimensional and two-dimensional infiltration of a strip water source was conducted for a constant width of the strip (W=10cm), water depth (h_0=3mm), θ_i= 0.3, and variable distance between parallel strips (d= 3, 4, 5, 8, and 10cm) (Figures 3.8 and 3.9). Warrick and Lazarovitch (2007) found that the cumulative infiltration depth due to the edge effect (I_{2D}-I_{1D}), or the difference in one-dimensional and two-dimensional cumulative infiltration depth, is linear over time. For multiple equidistant strip sources the relationship initially is non-linear, transitioning to a linear relation at larger times (Figure 3.8), with R^2 greater than 0.99 after 0.5h. In addition, the edge effects are dampened the closer the strips are located together tending to the x-axis for the case with sheet flow (no separation between strips). The average reduction in infiltration depth due to edge effects for multiple equidistant strips 3cm apart in sand and loamy sand was 61% and 57% respectively; the impact of the interaction with parallel strips is slightly smaller for finer soils.

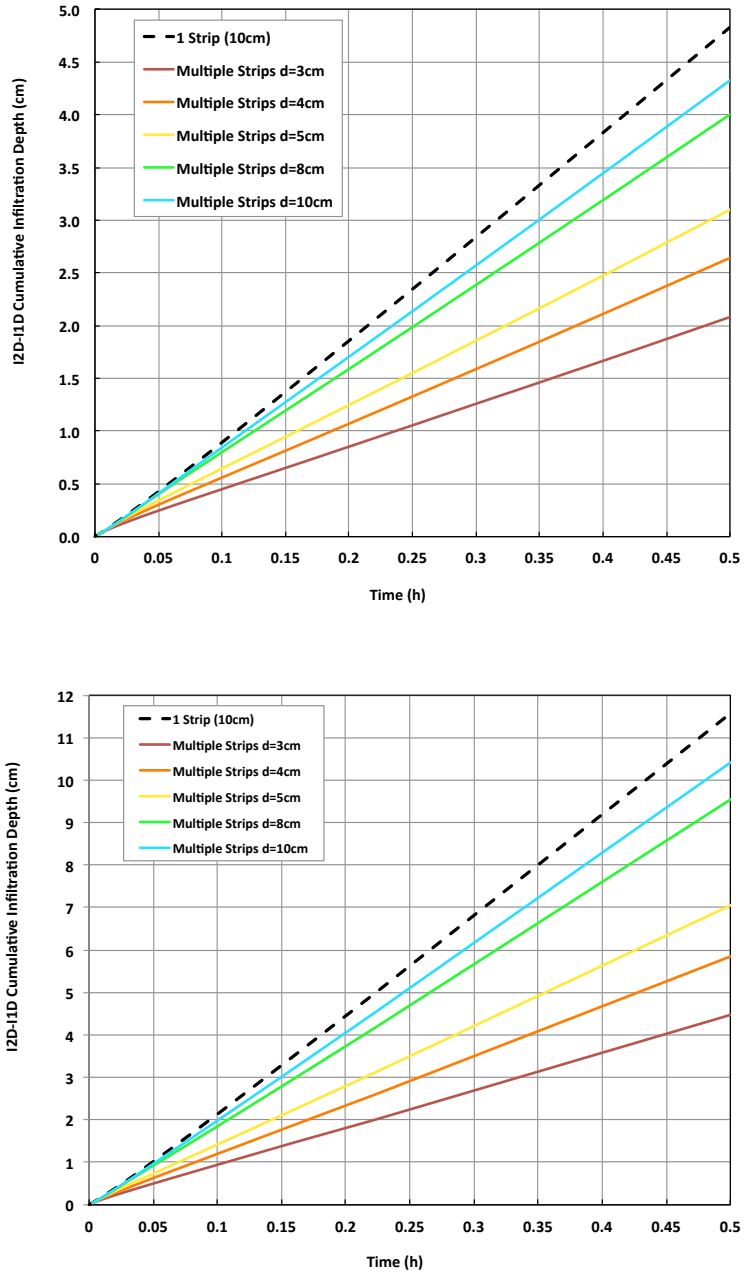

Figure 3.8 Difference in one-dimensional and two-dimensional cumulative infiltration depth over time from a 10cm width strip water source. The dashed line represents a single strip and the solid lines represent multiple equidistant strips at a distance (*d*) for loamy sand (up) and sand (down) with θ_i=0.3.

The relative edge effect ($\frac{I_{2D}-I_{1D}}{I_{1D}}$) increases over time until it reaches a constant value (Figure 3.9). At the initial time steps (Figure 3.7 left), the flow is mostly vertical in both one-dimensional and two-dimensional simulations; therefore, the

difference between one-dimensional and two-dimensional infiltration is small. For longer time periods (Figure 3.7 right), the edge effect becomes more important, and at steady state (soil column saturation), the relative edge effect reaches its maximum. For a single strip of 10cm width in a loamy sand soil, the edge effect in terms of infiltration depth ($\frac{I_{2D}-I_{1D}}{I_{1D}}$) adds 60% more infiltration to the one-dimensional infiltration depth after 15min and approximately 70% at steady state (Figure 3.9 up). The presence of parallel strips decreases this relative edge effect in a loamy sand soil to between 9% (d=10cm) and 40% (d=3cm). This relative difference between soils decreases as the distance between strips increases. For a single strip of width 10cm in a sandy soil, the edge effect in terms of infiltration depth ($\frac{I_{2D}-I_{1D}}{I_{1D}}$) adds 71% more infiltration to the one-dimensional infiltration depth after 15min and approximately 79% at steady state (Figure 3.9 down). These results imply that relative edge effect becomes less critical with finer soils and lesser times.

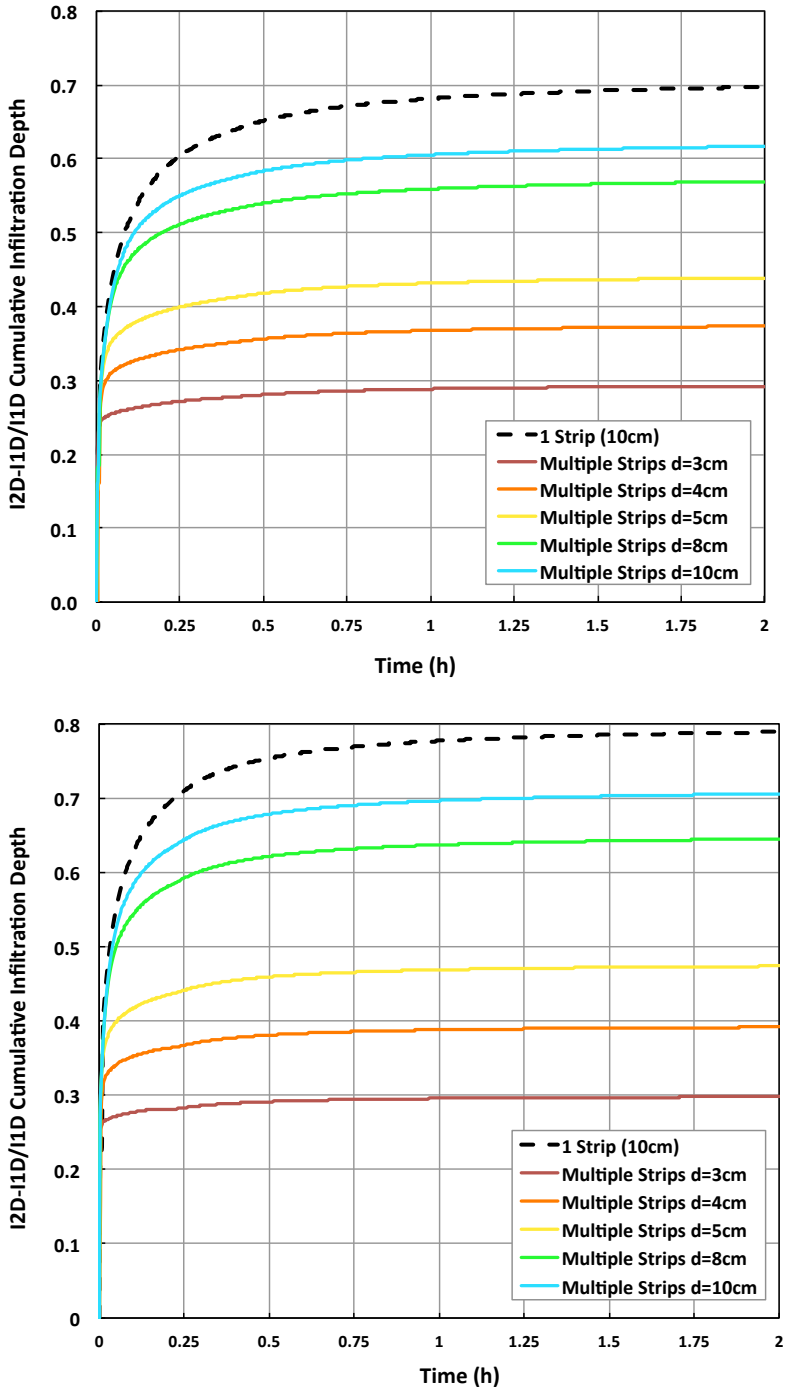

Figure 3.9 Ratio of the difference in one-dimensional and two-dimensional cumulative infiltration depth to one-dimensional cumulative infiltration over time from a strip water source (width=10cm). The dashed line represents a single strip and the solid lines represent multiple equidistant strips at a distance (d) for loamy sand (up) and sand (down) with θ_i=0.3.

4. Discussion

4.1 Analysis of results

Equations 6 and 7 provide an estimate of the infiltration edge effect for multiple equidistant strip water sources. The constant C depends on the soil type, width of the strip, and water depth at the source. For the range of soil types and widths tested, and h_0 =3mm, C [1/cm] lies in the range of 0.16 to 0.32, with an average value of 0.2; that corresponds to L_{50} and L_{90} values in the range of 2 to 4 cm and 10 to 19 cm, respectively. For greater values of h_0, the constant C decreases, as shown in Figure 3.6, and the distance between parallel strips that yields a relevant impact on edge infiltration increases. In summary, for the same distance between strips, wider strips, greater water depths, and finer soils have a greater reduction in edge effect infiltration from parallel strip water sources.

In Figures 3.10 and 3.11 the ratio of edge infiltration rate (i_{2D} - i_{1D}) to one-dimensional infiltration rate at steady state of 3 cm and 20cm wide strips in loamy sand soil are plotted as a function of water depth. For the case of a single strip without interactions with neighboring strips, the edge infiltration rate linearly increases with water depth (h_0), along with the edge infiltration depth (Bautista *et al.*, 2014). However, for the cases with parallel strip water sources, the relationship is not always linear, tending to a constant value for short distances between strips. For example, in the 3cm width simulations the edge effect linearly increases with water depth for distances between strips greater than 6 cm, though for distances of 3 and 4 cm the edge infiltration rate does not increase after h_0 = 1cm (Figure 3.11). The relative edge effects are greater than the vertical infiltration rates (i_{1D}) for the 3cm strip and lower for the 20cm strip.

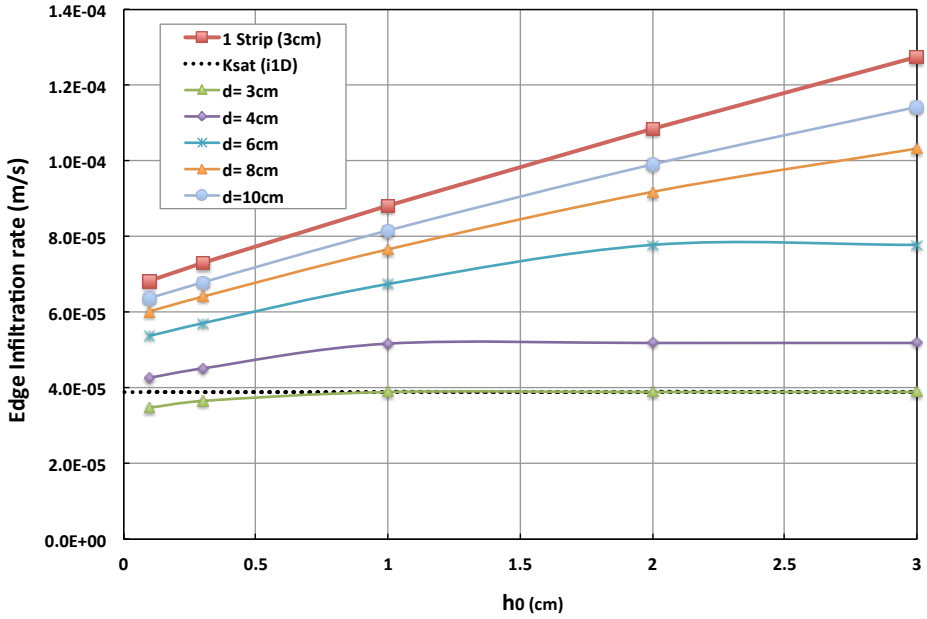

Figure 3.10 Edge infiltration rates (i_{2D}-i_{1D}) at steady state for a 3cm wide strip water source. The one-dimensional infiltration rate (K_{sat}) is given for comparison. The points represent edge infiltration rates for a single strip and multiple equidistant strips at a distance (d) for a loamy sand.

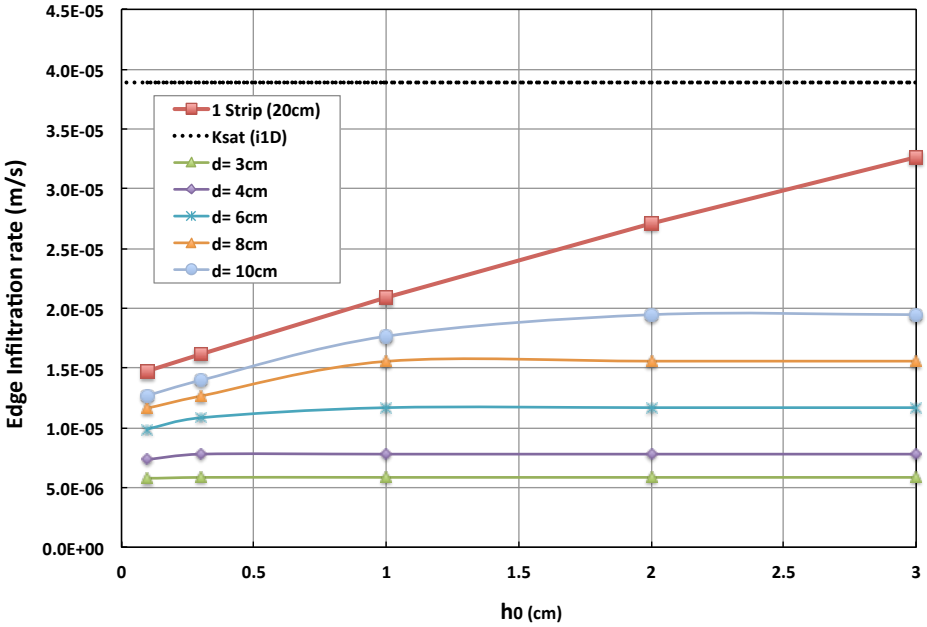

Figure 3.11 Edge infiltration rates (i_{2D}-i_{1D}) at steady state for a 20cm wide strip water source. The one-dimensional infiltration rate (K_{sat}) is given for comparison. The points represent edge infiltration rates for a single strip and multiple equidistant strips at a distance (d) for a loamy sand.

The range of γ values is greater than those previously estimated by Warrick *et al.* (2007), despite using the same method to calculate S_0, due to the shorter strip widths and shallower water depths tested in this study. Therefore, the information provided in Table 3.2 is useful to apply the Warrick and Lazarovitch (2007) equations to strips of widths shorter than 10 cm and water depths shallower than 1cm, adding a set of conditions not tested before these calculations. Bautista *et al.* (2014) suggested average values for γ of 0.85 for van Genuchten (VG) soils applicable to typical furrow geometries in mild to flat slopes. For the case of shallow concentrated overland flow we recommend using γ of 0.6 for VG soils, applicable to water depths in the order of 3 mm and strip widths of 3-10 cm.

To estimate the impact of adding the edge effect using Eq. 6 to one-dimensional infiltration calculations a relative contribution of edge effect (e_R), in terms of infiltration rate at steady state, was calculated as:

$$e_R = (1 - \frac{i_{1D}}{i1D + iEdge}) \quad (9)$$

where i_{1D} and $i_{2D} = i_{1D} + i_{Edge}$ are the one-dimensional and two-dimensional infiltration rates from a strip water source.

The fraction of relative contribution of edge effect (e_R) as a function of the distance between parallel strips is presented in Figure 3.12. Three soil types have been tested for a flow depth of 3mm. The width of the strip makes an important impact on the fraction of relative contribution of edge effect, but the soil type has a small effect. In addition, the distance between strips has the same effect on e_R for all the strip widths tested, and it tends to reach a steady value after a separation of 16 cm. For the 20 cm width strips, the fraction of relative contribution of edge effect is 0.32 or below, that means the maximum contribution of the edge infiltration, in this case, is 100 x 0.32 / (1-0.32) = 47% of the vertical infiltration rate. For the 1cm width strips, the e_R is above 0.7, so the minimum contribution of the edge infiltration is 2.33 times the vertical infiltration rate.

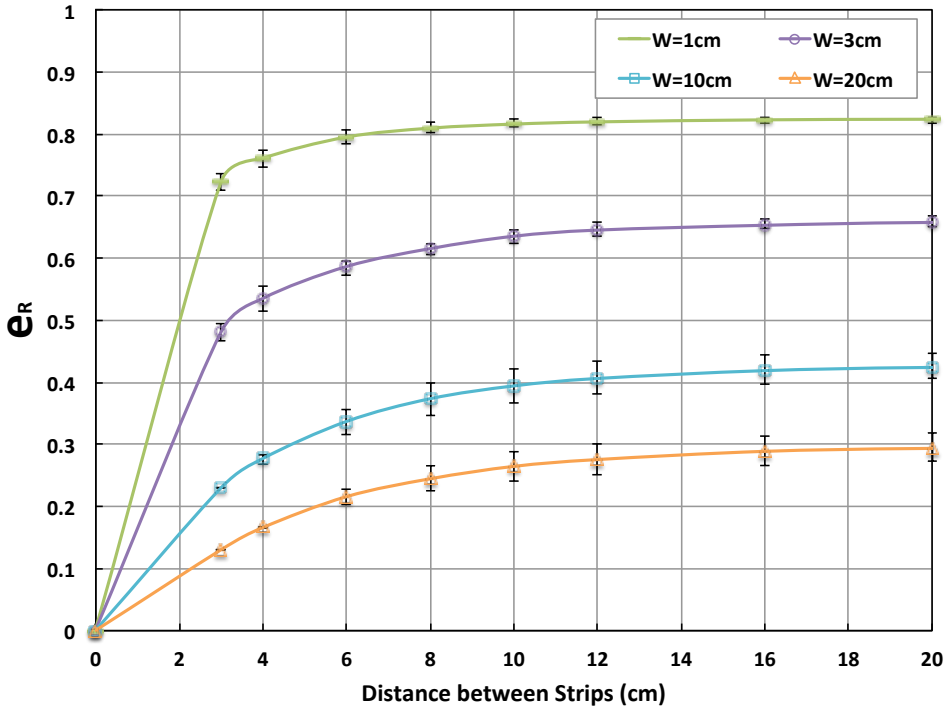

Figure 3.12 Fraction of relative contribution of edge effect as a function of the distance between parallel strips for different width strip water sources (h_0= 3mm). The values are the average for three soil types (sand, loamy sand, and sandy loam) and the error bars represent the range of values for the three soil types.

4.2 Limitations

All the numerical simulations presented in this study were based on a flat strip water source with constant pressure head over its surface. Azis *et al.* (2003) found that the distributions of the matric flux potential of parallel channels associated with a flat strip and semi-circular channel are similar. However, Bautista *et al.* (2014) determined that the geometry of the water source can influence the two-dimensional infiltration process mainly due to the change on the average pressure. In addition, the transient flow simulations are based on the assumption of a constant water depth over time. In reality, the water depth would first increase over time and then decrease as no more water is input in the system and the ponded water infiltrates. Furthermore, the soil was assumed to be homogeneous with isotropic properties, however macropores can allow

vertical bypassing (Kirkby, 1988) and the relative edge effects compared to vertical infiltration may be diminished.

4.3 Case Studies

Two different case scenarios have been analyzed for practical application of the results obtained under steady state conditions: 1) furrow irrigation, 2) concentrated overland flow on relatively smooth surfaces. For the furrow irrigation from multiple equidistant strip water sources, consider a strip width of 20cm spaced by three distances (20, 40, and 60 cm). Based on Equation 7 and the C values from Table 3.2 and Figure 3.6, the ζ value, used to calculate edge effect in Equation 6, for both loamy sand and sandy loam soils with a water depth of 3cm is 0.85 for 20 cm of spacing and 0.98 for 40 cm of spacing. This means that 20cm wide water strip sources, with 3 cm flow depth, separated 20cm will have 15% reduction in infiltration rate due to interaction with neighboring strips and negligible reduction for 40 and 60cm spacing. Increasing the flow depth to 5cm has a greater impact on loamy sand than sandy loam soils, based on the linear interpolation of the C parameter (Figure 3.7) for greater water depths. A 20 cm wide water strip source with 5cm flow depth in loamy sand, will have 54% reduction in infiltration rate due to interaction with neighboring strips at 20cm, 30% reduction at 40cm, and 16% reduction at 60 cm. For the same conditions in sandy loam, the reductions in infiltration rate at steady state are 38% (20cm), 14% (40cm), and 5% (60cm).

The case studies for concentrated overland flow are based on 1) shallow overland flow over a relatively smooth slope (flow in fingers) and 2) eroded slope containing parallel rills carrying deeper water flows. These scenarios represent, for example, overland flow over the side of a roadside drainage ditch for low flows, without and with erosion, respectively. First, for low runoff flows overland flow over a lateral slope is concentrated in fingers, instead of sheet flow, having only a fraction of the surface wetted (Garcia-Serrana *et al.*, 2017). Figure 3.13 provides the percentage difference between infiltration flux for concentrated flow

conditions and sheet flow in a 1m x 1m surface versus the fraction of wetted area. The results are based on a water flow depth of 3 mm and two strip widths, 3 and 10cm. The infiltration fluxes for concentrated flow conditions take into account edge effects, while for the sheet flow conditions there is only vertical infiltration but 100% surface coverage. In general, calculating infiltration fluxes assuming sheet flow for fractions wetted lower than 0.65 over predicts infiltration. For strip widths of 3 cm and 10 cm, above 0.65 and 0.75 fraction wetted, respectively, the infiltration flux with sheet flow conditions is comparable to the flux calculated for equidistant parallel strips with two-dimensional infiltration; for the three soil types tested. These estimations are based on the assumption of equal flow depth for sheet flow and concentrated flow conditions, however concentrated flow would have deeper water depths and higher input fluxes.

Second, a surface can develop rill erosion with parallel rill networks (McGuire *et al.*, 2013). The computational model was also used to estimate the difference between sheet flow infiltration and infiltration occurring in a surface with parallel rills. The eroded surface (1m x1m) was assumed to have 3 cm width rills, 10 cm apart with a flow depth of 1 cm. The infiltration flux of the eroded surface was 28% and 31% lower than for the sheet flow conditions, for the loamy sand and sandy loam soils respectively. This indicates that, despite the added infiltration flux per unit width due to edge effect in rills, erosion reduces infiltration capacity of surfaces due to the reduction of water coverage or concentration of flow.

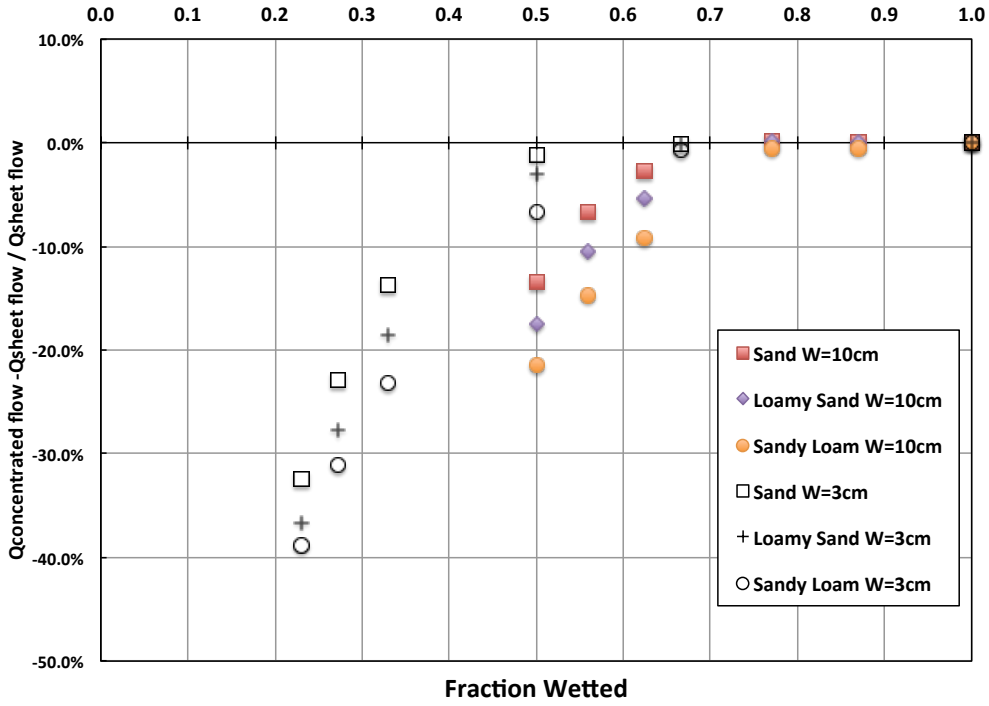

Figure 3.13 Percentage difference between infiltration flux for concentrated flow conditions and sheet flow versus the fraction of wetted area. Results based on a 1m x 1m surface, h_0= 3mm, and width of the strip (W) of 3 and 10cm.

5. Conclusions

The effect of equidistant parallel strip water sources on the lateral component of flow of the vadose zone infiltration process has been analyzed. The method of calculating two-dimensional flow from a strip water source by adding an edge effect to the one-dimensional calculations developed by Warrick and Lazarovitch (2007) has been extended to multiple strip water sources for both tilled furrow and concentrated flow on relatively smooth surface applications.

The infiltration from strip water sources was simulated with COMSOL Multiphysics® using various strip widths, spacings, flow depths, and soil textural classes. The interaction between neighboring parallel strips effectively reduces the lateral flow beneath the individual strips and this in effect reduces the infiltration through each strip. A relationship between strip water source width and distance between strips, soil texture and the infiltration from parallel strip water

sources on the soil surface was established (Equation 6 and 7). This relationship represents a modification of Warrick and Lazarovitch's equation to account for infiltration rates at steady state with multiple parallel strip water sources. In general, for the same distance between strips, wider strips, greater flow depths, and finer soils, in descending order, have a greater reduction in edge effect infiltration from parallel strip water sources. The results also show that there is a specific separation between strips, different for each soil texture class and strip width, where there is no effective interaction between them with respect to the edge effect.

The constant *C* from Equation 7 depends on the soil type, width of the strip, and flow depth at the source and it is inversely proportional to the reduction in edge infiltration for multiple strip water sources. Within the range of conditions studied, strip width has a greater impact on the value of *C* than soil type and *C* is inversely proportional to h_0. Warrick and Lazarovitch (2007) found that the cumulative infiltration depth due to the edge effect is linear over time; the case of multiple equidistant strip sources transitions to a linear relationship at larger times. For transient flow conditions, the relative edge effect increases over time until it reaches a constant value. For longer time periods, the edge effect becomes more important, and at steady state the relative edge effect reaches its maximum. The outcomes of this study have been applied to two different practical applications under steady state conditions: furrow irrigation and shallow concentrated overland flow over non-eroded and rilled surfaces. In general, calculating infiltration fluxes assuming sheet flow for fractions wetted lower than 0.65 over predicts infiltration. For strip widths of 3 cm and 10 cm, above 0.65 and 0.75 fraction wetted, respectively, the infiltration flux with sheet flow conditions is comparable to the flux calculated for equidistant parallel strips with two-dimensional infiltration; for the three soil types tested.

Acknowledgments

J.L. Nieber's effort on this project was partially supported by the USDA National Institute of Food and Agriculture, Hatch/Multistate project 12-059. The authors acknowledge the Minnesota Supercomputing Institute (MSI) at the University of Minnesota for providing resources that contributed to the research results reported within this paper. URL: http://www.msi.umn.edu.

Chapter 4

Description of Soil Micro-topography and Fractional Wetted Area under Runoff using Fractal Dimensions

Summary

Understanding the connections between the micro-topography of a surface and the patterns of shallow overland flow is important to the study of both runoff and infiltration processes. In slopes with micro-topographic features parallel to the flow, water tends to flow concentrated in channels and only a fraction of the slope contributes to the overland flow. This study aims to formulate the relevance of the fractal approach for understanding the relation of soil surface roughness to overland flow patterns. Laboratory experiments of simulated runoff over a bare soil slope at 17% were used to test the efficacy of two fractal parameters (fractal dimension (*FD*) and the vertical intercept (*VIC*) from the Fourier power spectrum

method) to describe how main surface micro-topographic features can influence runoff, infiltration and erosion processes. By defining indicators of rill erosion and associating them with flow patterns, a better description of shallow overland flow can be achieved.

The fractal parameters behaved differently for the distinctive initial surface treatments (smooth, 3 rills and 5 rills). The initially smooth surfaces had the greatest *FD* values and smallest vertical intercept (*VIC*). The minimum *FD* decreased and the vertical intercept increased with runoff time. In addition, the anisotropy of the surface was evident based on the change of the fractal parameters with direction. The rose plots of the fractal parameters provided important information about the type of erosion of a surface and its main direction; in the direction perpendicular to the rills, the *FD* values were lower and the vertical intercept greater.

A linear relationship between the volume infiltrated normalized by the length of the section of the slope studied and the percentage of wetted area was observed. Furthermore, a relationship between the fraction of wetted area and the fractal parameters has been developed, indicating that vertical variations (*VIC*) in roughness had more impact on fraction of wetted area than horizontal variations (*FD*) of the surface. Finally, a decrease in the minimum *FD* and an increase in the maximum *VIC* were related to greater scour volumes. The scour volume of an initially smooth surface seems to be well-represented by a power relationship with the maximum vertical intercept. Fractal parameters based on the Fourier power spectrum method were good indicators of runoff, infiltration and erosion of a surface with predominant roughness features parallel to the flow direction.

1. Introduction

There are several components of soil roughness associated to scale, from higher order roughness related to slope with its curvature at the field scale, to micro-relief, related to variations due to the spatial distribution of individual grains and micro-aggregates (Römkens and Wang, 1986). Soil roughness can be random (not directional) or oriented (predominant in one direction). Oriented roughness can be caused by tillage practices or erosion creating rills and gullies (Paz-Ferreiro *et al.*, 2008). A rill is an incision on the soil surface as a consequence of erosion that acts like a channel concentrating the water flow. Assuming uniform sheet flow, which is flow that has constant or irregular depth over the entire width of a hillslope, is not applicable when the micro-topography of a surface presents important spatial variations, (Parsons *et al.*, 1990; Hairsine and Rose, 1992; Cerdà, 1995; Bergkamp *et al.*, 1996). Instead, water tends to flow concentrated in rills so that only a fraction of the hillslope surface contributes to overland flow and the infiltration of overland flow. It is therefore important to analyze the effect that flow patterns generated by erosion processes have on overland flow and infiltration processes.

In the past, the development of methods for quantifying soil surface roughness was limited by the ability to obtain accurate data sets (Huang, 1998). Currently, however, point elevation readings can be taken with millimeter resolution to evaluate soil surface micro-topography within a meter scale area (Paz-Ferrreiro *et al.*, 2008). Fractal analysis, popularized by Mandelbrot (1982), has been used to describe the spatial complexity of soil surfaces. Previous studies on fractal analysis of soil surfaces focused on tilled surfaces and evolution of surfaces with cumulative rainfall (Vázquez *et al.*, 2005, 2007; Vermang *et al.*, 2013), and surfaces with random roughness and depressions (Chi *et al.*, 2012). Fractal surfaces that are invariant under a change of length scales are called *self-similar* fractals. However, soil elevation profiles are *self-affine* rather than *self-similar* (Huang *et al.*, 1992; Anguiano, 1993; Vázquez *et al.*, 2005, 2007; Abedini and

Shaghaghian, 2009), that means that the fractal model is only suitable within a limited range of scale and at least two parameters are required to describe roughness. The concept of fractal within a limited range or distance has also been defined as *pseudofractal* (Orford and Whalley, 1983; Whalley and Orford, 1989), where variations at small scales do not scale up proportionally when the areal scale is increased (Huang, 1992).

Different methods have been proposed to estimate fractal parameters from Digital Elevation Models (DEM): Fourier power spectrum (Russ, 1994), variogram (Klinkenberg and Goodchild, 1992; Paz-Ferreiro *et al.*, 2008), box counting, triangular prism (Clarke, 1986 Vermang, 2013), isarithm method (Shelberg *et al.*, 1983), Kolmogorov (Rawers and Tylczak, 1999), root mean square (Vázquez *et al.*, 2005), along with others. Russ (1994) and Rawers and Tylczak (1999) reported that the resulting fractal value is a function of the surface and the technique used for the analysis, however they found a correlation between the relative ranking of fractal values obtained from different fractal measuring techniques. In this study, the Fourier power spectrum method has been used. This method has several advantages (Russ, 1994; Zhang, 2006): 1) the fractal dimensions are a function of surface orientation and anisotropy can be captured; 2) the method is relatively insensitive to the presence of noise; 3) it offers computational efficiency due to the possibility of applying the Fast Fourier Transformation (FFT) algorithm; 4) the method is sensitive to both horizontal and vertical variations by calculating the fractal Dimension (*FD*) and the ordinate intercept or vertical intercept (*VIC*); 5) Finally, the Fourier power spectrum method is based on an explicit formula and potentially more accurate computationally.

The three roughness parameters computed and evaluated in this study are the fractal parameters *FD* and *intercept* or *VIC*, and the statistical parameter random roughness (*RR*). *RR* is related to the standard deviation of elevations from a mean surface (Kuipers, 1957; Allmaras et al, 1966) and has been widely used to

quantify soil surface roughness. These three parameters have been used to measure the roughness of a surface, but according to Abedini and Shaghaghian (2009) more research needs to be done to link the self-similarity behavior of a surface, captured by fractal parameters, to physical processes like erosion. The organization of a surface micro-topography is affected by the presence of rill networks. By defining indicators of rill erosion and associating them with flow patterns, a better description of shallow overland flow can be achieved. Fractal parameters may be potential indicators of both flow patterns and erosion of a surface.

There can be dominant contrasts in surface elevation parallel to the flow direction or perpendicular to it. A wide range of results has been obtained regarding overland flow and infiltration with rough surfaces. When defining a rough surface, authors do not always specify if the roughness is random or contains a predominant direction. In some cases, a rough soil surface is associated with larger surface depression storage, however rilled surfaces have high relative roughness but cannot retain large amounts of water. Chi *et al.* (2012) performed an overland flow experiment conducted on rough (dominated by depressions) and smooth field plots under natural rainfall. Relationships were established between fractal dimension (*FD*), derived from the variogram method, overland flow and hydrologic connectivity. Dominant surface roughness existed along the directions of smaller *FD* values. Along those directions, surface runoff was prone to be hindered or blocked by continuously distributed ridges. Therefore, a surface with a smaller *FD* in a direction parallel to the flow had the potential to retain more water on the surface, which in turn redistributed surface water, enhanced infiltration in the depressions, and delayed surface runoff generation. In the present study, fractals parameters have been used to evaluate surfaces with predominant roughness features parallel to the flow direction (rills), instead of perpendicular (depressions).

The distribution of water on surfaces is controlled by the micro-topographic

conditions. Previous research on fractal descriptors of micro-topography has mainly focused on depressions and tilled surfaces; the characterization of flow concentration due to rills needs further research. The impact of rill erosion on overland flow and infiltration is important for better understanding the effects on the performance of stormwater management practices that utilize these processes, such as filter strips and roadside swales. This study aims to formulate the relevance of the fractal approach for understanding soil surface roughness and overland flow patterns. The objective was first to determine the impact that fractional wetting of the slope surface has on infiltration rates and runoff generation; second, establish a relationship between the fractal dimensions *FD* and vertical intercept *(VIC)* and flow concentration over a surface as fraction of wetted area; and finally, find connections between the evolution of the fractal parameters over time and erosion processes.

2. Method

2.1 Experimental Settings and Procedure

Laboratory Flume Components

A full-scale physical model of a road embankment built at the St. Anthony Falls Laboratory was used for the laboratory experiments. The model consisted of a wooden flume (Figures 4.1 and 4.2) with a soil bed of a total length of 6 m representing the cross section of a roadside swale, with a 2% slope pervious shoulder and a 17% side slope (Figure 4.3). The shoulder consisted of the same soil as the slope of the swale. The width of the flume was approximately 0.91m. On the side slope, the soil depth was 0.3m. There was a suppressed rectangular weir, horizontal crest that crosses the full channel width, at the transition from the road section to the shoulder. A series of eight perforated drainpipes were located below the soil layer to measure infiltrated water (Figure 4.2). These drainpipes were covered with a permeable geotextile to keep soil from entering.

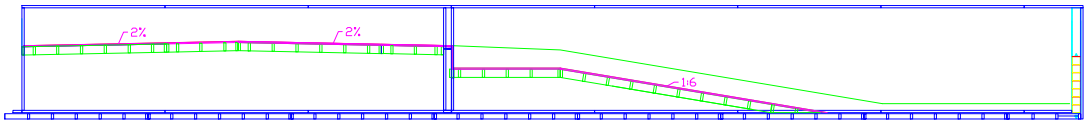

Figure 4.1 Flume cross-sectional profile with the road and the side slope.

Figure 4.2 Image of four of the perforated drain pipes underneath the soil in the flume.

Figure 4.3 Flume view from the downstream end with a smooth soil surface.

Soil Characteristics

The soil was loamy sand consisting of a mixture of 4% gravel, 88% sand, 6% silt, and 2% clay (Figure 4.4). The soil was compacted before each experiment with a 5.4 kg, 25.4 cm x 25.4 cm tamper. Three soil cores of 13 cm length from the surface were collected, using a cylindrical core sampler and a metalhammer and

driver. A bulk density of 1.44g/cm^3 value was obtained, following the procedure described by ASTM D2937-10. From those core samples, the porosity was calculated to be 40%. The flume was saturated with water 24 hours before each experiment and allowed to drain, so the soil could be considered at field capacity when the experiments began. The initial soil moisture content was approximately 12% in all of the tests. The Green Ampt (1911) parameters, saturated hydraulic conductivity (K_{sat}) and wetting-front suction (ψ) in the upper 25 cm were estimated at the end of all the tests using the MPD infiltrometer method (Asleson *et al.* 2009; Olson *et al.*, 2013; Ahmed *et al.* 2014). Nineteen measurements of falling head were taken in areas without eroded channels and utilized in the MPD spreadsheet to compute the saturated hydraulic conductivity and the capillary suction of the soil ahead of the wetting front. The saturated hydraulic conductivities obtained with this technique had a geometric mean of 12.8 cm/h with a standard deviation of 5.5 cm/h, and the average effective wetting front suction was 3.5 cm with a standard deviation of 4.6 cm.

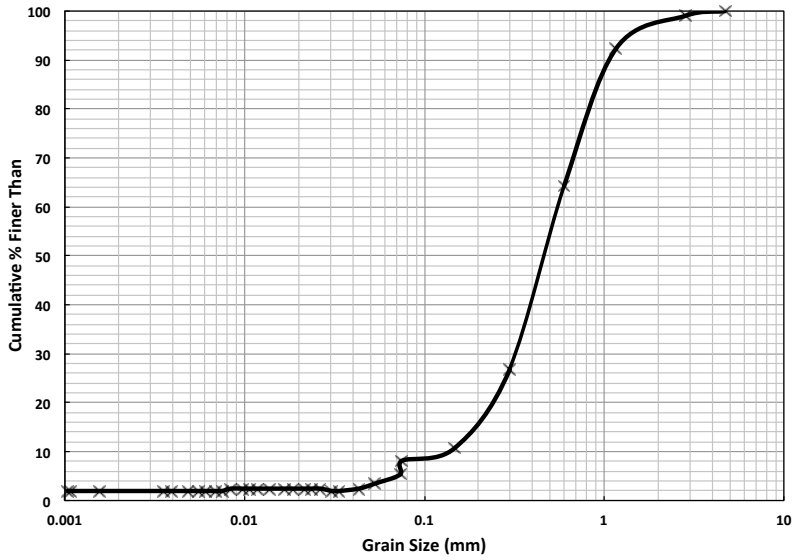

Figure 4.4 Particle Size Analysis of the laboratory soil (ASTM D422; ASTM D6913).

Soil Surface Data Acquisition

A custom laboratory data acquisition system with automated three-dimensional

control of all sensor positions with high accuracy (tenth of a millimeter precision), was used in the experiments. The laser elevation scanner, attached to a mobile cart, was employed to scan the soil surface several times during the tests. The data acquisition system software generated a Digital Elevation Model (DEM), which is a representation of the surface of the slope, with a 1mm x 1mm cell size. To enable visualization of the flow patterns, the water was mixed with titanium dioxide (TiO_2) (particle size less than 44 μm), which allows the laser light to be reflected on the water surface (Legout *et al.*, 2012), using a paint mixer to achieve a uniform concentration. Three different micro-topographies were tested over the bare loamy sand soil: a smooth surface (Figure 4.3), a surface with three parallel rills, and a surface with five parallel rills (Figure 4.5). For each experiment, the soil was prepared by compaction with a tamper and smoothed with a plastering trowel. For the treatments with rills, longitudinal channels were produced in the compacted soil using a 4.6 cm diameter steel pipe. Each of the scenarios was repeated three times, for nine total number of tests.

Figure 4.5 Left: Surface with 5 initial rills. **Right:** Surface with 3 initial rills.

Water Supply

Water supply was regulated with a valve and connected to a rectangular constant

head tank located on the impervious area closer to the side slope. The input water flux was 7.06×10^{-5} m^2/s, equivalent to a uniform rainfall intensity of 2.54 cm/h over a 10 m wide impervious area connected to the pervious side slope. Each experiment lasted for one hour with a total volume of 234 L applied over the surface for each experiment. The water infiltrated was collected by the drainpipes, transported out of the flume by gravity and measured in buckets located underneath the exit of the pipes. The runoff water, or water that was not infiltrated, was collected at the bottom of the flume and discharged into an outflow channel. Titanium dioxide was added to the box where the water was pumped and mixed with a paint mixer. An electronic metering pump was used to add a slurry of water and TiO_2 to the main flow of water (Figure 4.6). Tests indicated that a 13 g/L concentration of TiO_2 was required for the water surface elevation to be measured by the data acquisition system.

Figure 4.6 Injection of the mix of titanium dioxide and water into the pooled water upstream of the sloped surface. Picture by David Bauer.

2.2 Data Collection

The following data were collected for each experimental run:

- Volume of water infiltrated in each drain pipe over time,
- Total volume of runoff (water not infiltrated),

- Micro-topography of the surface, and
- Wetted surface area.

The first 1.5 meters of the slope were not included in the analysis due to the difference in the slope; the rest of the surface was divided into seven different sections, each of them linked to an underdrain. The topographic information collected with the data carriage was processed using MATLAB R2016a. The micro-topography of the soil surface was scanned four times, at 0, 20, 40 and 60 minutes after the beginning of each experiment. After the second and third scanning, a mix of TiO_2 and water was added to the inflow with a pump and two more readings of the surface were completed, although only the second reading was used due to the surface changing more rapidly (due to erosion) during the first scan. The wetted area was calculated as the points where there was a positive difference in elevation between the dry surface reading and the reading with input of water and titanium dioxide. An example can be seen in Figure 4.7. The scour volume was calculated as the difference in elevation between the dry surface reading and the initially scanned surface.

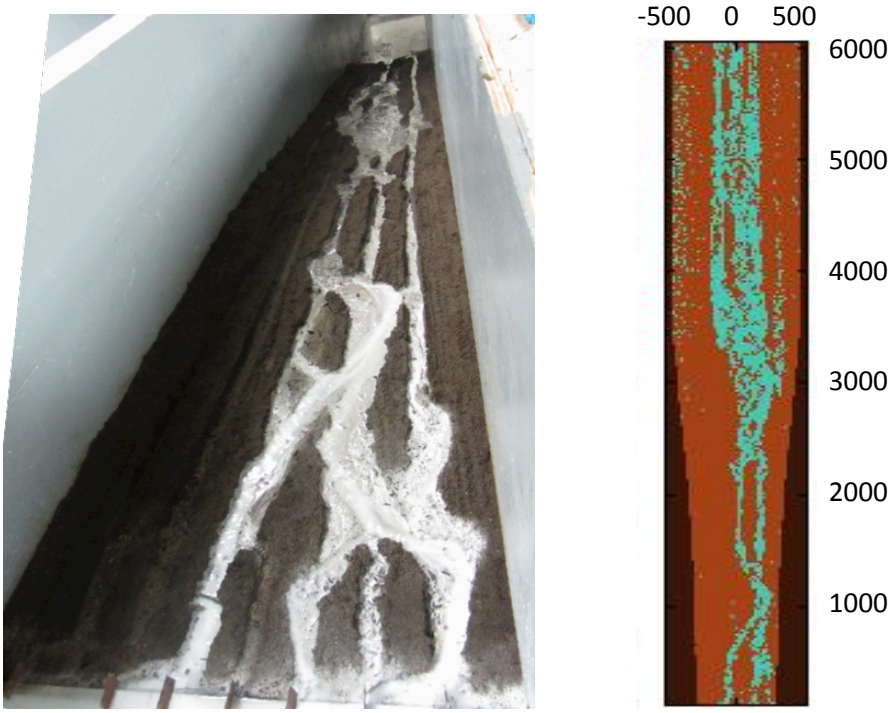

Figure 4.7 Left: TiO_2 mixed with water flowing over the side slope of the slope surface in the laboratory, 3 rills surface treatment. **Right:** Computational representation of the wetted areas, reading performed 10 minutes after the picture on the left was taken. Units in mm.

2.3 Roughness Parameters

Before the calculation of the roughness parameters, the micro-topographic data sets were detrended or corrected for slope (17% bottom slope). This operation consisted of subtracting the plane of best fit to the surface, calculated using linear multiple regression, from the soil profile data (Currence and Lovely, 1970; Vázquez *et al.*, 2005, Paz-Ferreiro *et al.*, 2008)). Trend removal is necessary to obtain reliable roughness estimates (James *et al.*, 2007; Zhang *et al.*, 2016).

Fractal Dimensions

There are multiple methods to calculate the fractal dimension *FD*, as mentioned in the introduction, but they follow similar procedures in that they use some version of the statistical relationship between the measured quantities of an object and a spatial scale to derive the estimates of the fractal dimensions (Sun *et al.*, 2006). In this study the Fourier power spectrum method was applied

(Pentland, 1984, Burrough, 1981). First, the two-dimensional Fast Fourier transform (FFT) $F(i, j)$ of the surface $S(x, y)$ (Figure 4.8a) is computed; where u and v are the spatial frequencies (number of waves per unit wavelength) in the x and y directions respectively. Second, the power spectral density function, $P(i, j)$ is estimated from $F(i, j)$:

$$P(i,j) = |F(i,j)|^2 \quad (1)$$

The magnitude of $P(i, j)$ at an angle θ is converted to the polar coordinate system $P(f)$, where $f = \sqrt{i^2 + j^2}$ and $\theta = \tan^{-1}(j/i)$. The values of $P(f)$, at each radial frequency f, are averaged over angular distributions. A fractal surface shows the following relationship:

$$P(f) = c|f|^{-\beta} \quad (2)$$

where c is a constant and β is a spectral exponent. Taking the logarithm of both sides of equation (2):

$$log(P(f)) = log(c) - \beta * log(|f|) \quad (3)$$

The slope (β) of the fitted linear regression line (Figure 4.8 c and d) is related to the fractal dimension FD by (Turner *et al.*, 1998; Zhang, 2006; Ahammer, 2011):

$$FD = \frac{3*D_T+2-\beta}{2} \quad (4)$$

where D_T is 2 for a surface; therefore $FD = (8 - \beta)/2$. For a two-dimensional profile, FD is expected to lie in the range of $2 < FD < 3$. The vertical intercept ($VIC = \log(c)$) is also derived from the least squares fit to equation 3. The fractal dimension FD and the VIC are computed as a function of direction by using all of the points within a pie-shaped wedge in the transform image (Russ, 1990). Due to the symmetry of the $P(i, j)$, the angle only needs to be varied from $0 \leq \theta \leq \pi$ (Zhang, 2006). Plotting the FD and VIC values on polar coordinates (a rose plot) (Figure 4.9) shows the directionality of the values and the anisotropy of the surface (Russ, 1990). In this study, the frequency space is uniformly divided in twenty-four directions, 15° wedges, and each one is uniformly sampled at thirty

points. Then, the phase values (Figure 4.8c) for the terms in the Fourier transform of the surface are checked for randomness to consider the original surface a fractal (Russ, 1990). To compute *FD* and *VIC* for all directions, the Zhang (2006) implementation of the Russ (1990) procedure was used. Both *FD* and *VIC* were used as fractal descriptors to characterize each surface.

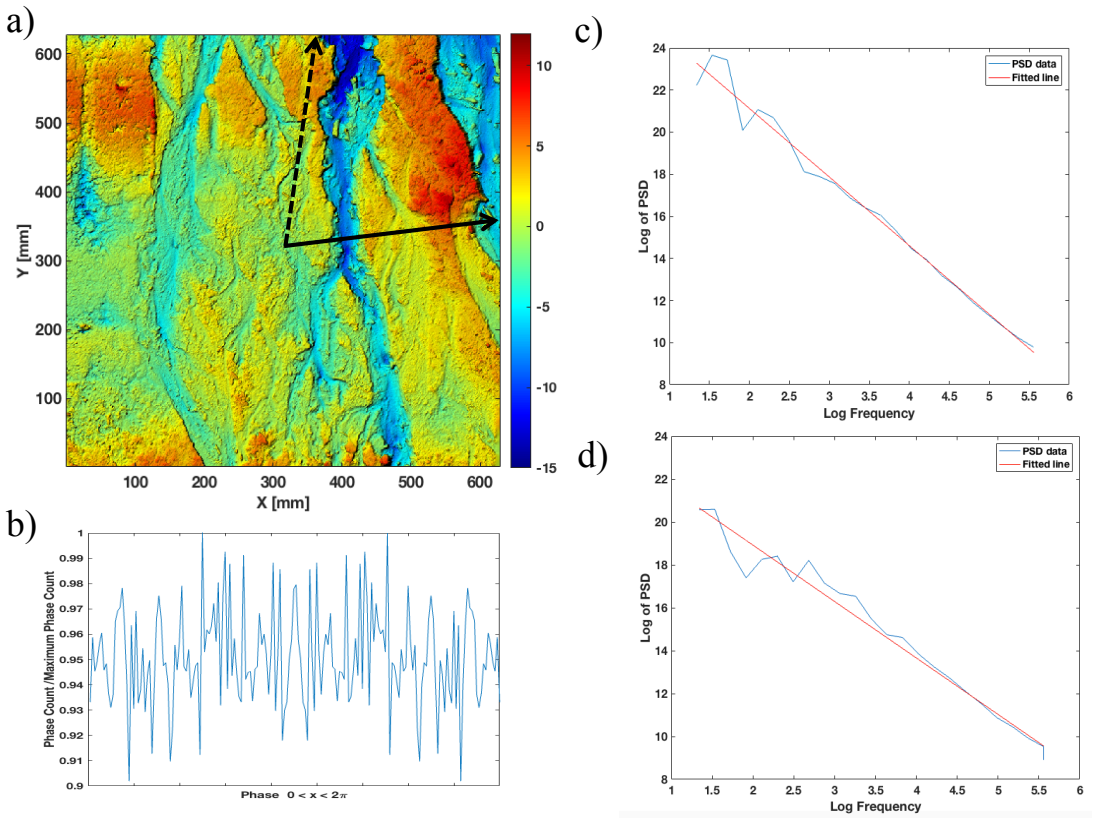

Figure 4.8 a) Hillshade map from the DEM of Section 1 of the slope (corrected for slope) initially smooth after 20 minutes of simulated runoff, colorbar heights in mm; the solid line arrow represents direction of *θ=7.5°* and the dashed line arrow represents direction of *θ=82.5°;* **b)** Phase distribution of the terms in the Fourier series corresponding to surface in Figure 4.8a; **c)** Power spectral density for surface in Figure 4.8a along the radial line *θ=7.5°* and least squares fit line with slope=3.26*;* **d)** Power spectral density for surface in Figure 4.8a along the radial line *θ=82.5* and least squares fit line with slope=2.63.

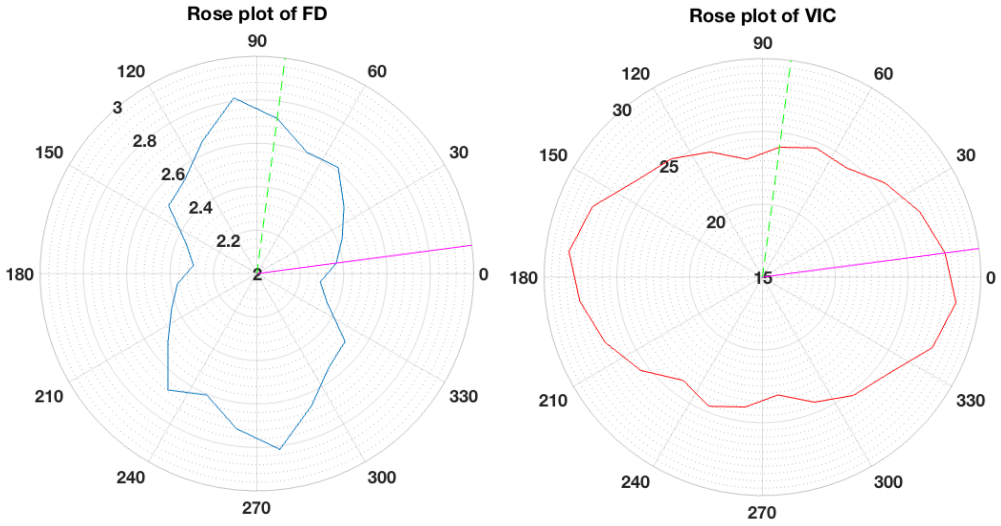

Figure 4.9 Left Rose plot of the fractal dimension (*FD*) of surface in Figure 4.8a **Right** Rose plot of the vertical intercept (*VIC*) of surface in Figure 4.8a. The solid magenta line represents θ=7.5° and the dashed green line represents θ=82.5° (the angles represented in Figure 4.8c and 4.8d, respectively).

Random Roughness

The third roughness parameter calculated was the random roughness (RR), which reveals the vertical variability in surface elevations (Yang and Chu, 2013) after detrending for slope. Each surface was divided into 24 directions and the RR was calculated for each cross section at a specific direction as (Allmaras *et al.* 1966):

$$RR = \sqrt{\frac{\Sigma(z - z_{mean})^2}{N}} \tag{5}$$

where z is the elevation at a given point, z_{mean} is the mean elevation of a cross section, and N is the number of points in a cross section.

3. Results and Discussion

The three initial surfaces were smooth and three and five artificially generated rills. The artificially rilled surfaces were developed to initiate rill formation in given locations. In all three surfaces, erosion in upslope positions and deposition in downslope positions was observed over time (Figure 4.10). Therefore, despite

referring to those tests as “smooth” “three rilled” and “five rilled” surfaces, this qualification only defines their initial condition. Finer soil particles were observed on the slope surface after the start of the simulated runoff due to erosion and deposition processes; the deposition of fine particles on the surface caused the formation of surface sealing in some areas.

Figure 4.10 Initially smooth surface at t=0 min and after 60 min of simulated runoff.

3.1 Infiltration Volume and Impact of Wetted Area

Figure 4.11 presents the percentage infiltration results of all tests by initial surface treatment. The average percentage of water infiltrated was 45.1% (2.4% st. dev.) for the initially smooth surfaces, 34.4% (3.9% st. dev.) for the surface with three rills, and 34.7% (4.6% st. dev.) for the surface with five rills. Although all surfaces experienced erosion over time, the initially rilled surfaces had less infiltration overall; the relative difference between an initially smooth surface and both cases with rills was around 30% more water infiltrated. The difference between the scenarios with 3 and 5 initial rills was insubstantial. Additionally, the time when runoff first reached the bottom of the slope was affected by the surface treatment. No runoff reached the outlet of the slope for the initially smooth surface until the erosional features developed after 19 minutes of simulated runoff; while for the cases with rills runoff reached the bottom of the slope after 2 minutes of simulated runoff.

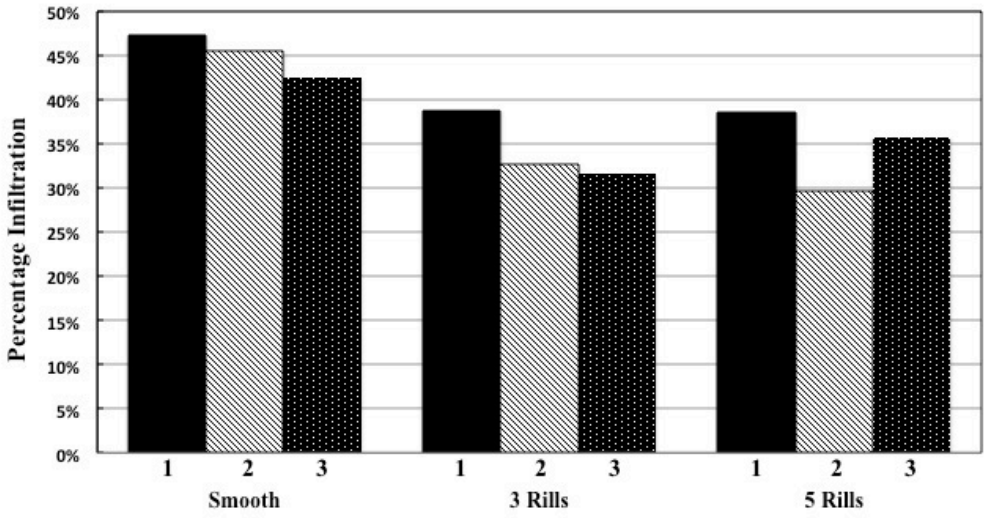

Figure 4.11 Percentage of water infiltrated in each of the experiments for the three surface treatments. Three tests were performed for each surface. The total input of water was 234 liters (61.82gal).

To compare the volume infiltrated in each of the sections, the following representative dimensionless parameter has been defined, since not all the areas draining to the underdrains had the same size:

$$Normalized\ Vol_{Inf}i\ =\ \frac{{}^{Vol\ _{Inf}i}/_{L_S}}{{}^{Total\ Vol_{Inf}}/_{L_T}} \tag{6}$$

where *Normalized Vol$_{inf}$ i* is the normalized volume infiltrated in a specific section *i; Vol$_{inf}$ i* is the volume infiltrated in a specific section *i* of the slope (corresponding to the water collected in a particular underdrain); *Total Vol$_{inf}$* is the total volume infiltrated in the slope (corresponding to the water collected in all the underdrains); L_S is the length of the section; and L_T is the total length of the slope.

A linear relationship between the normalized volume infiltrated parameter and the percentage of wetted area was observed (Figure 4.12). A possible source of error in the infiltration data was related to water leaking from upstream underdrains to the last underdrain located on a flat surface. For this reason, from the seven sections that the slope was divided, the last section was not included in this analysis. Concentrated flow was observed over the slope, with a maximum

percentage of wetted area of 42% for the flux tested. Concentrated flow took place in all the tests and sections, and uniform sheet flow (or 100% of wetted area) was not observed. The values of percentage of wetted area are based on a particular boundary flux of 7.06×10^{-5} m^2/s; larger wetted areas would be expected for greater boundary fluxes (Garcia-Serrana *et al.*, 2017).

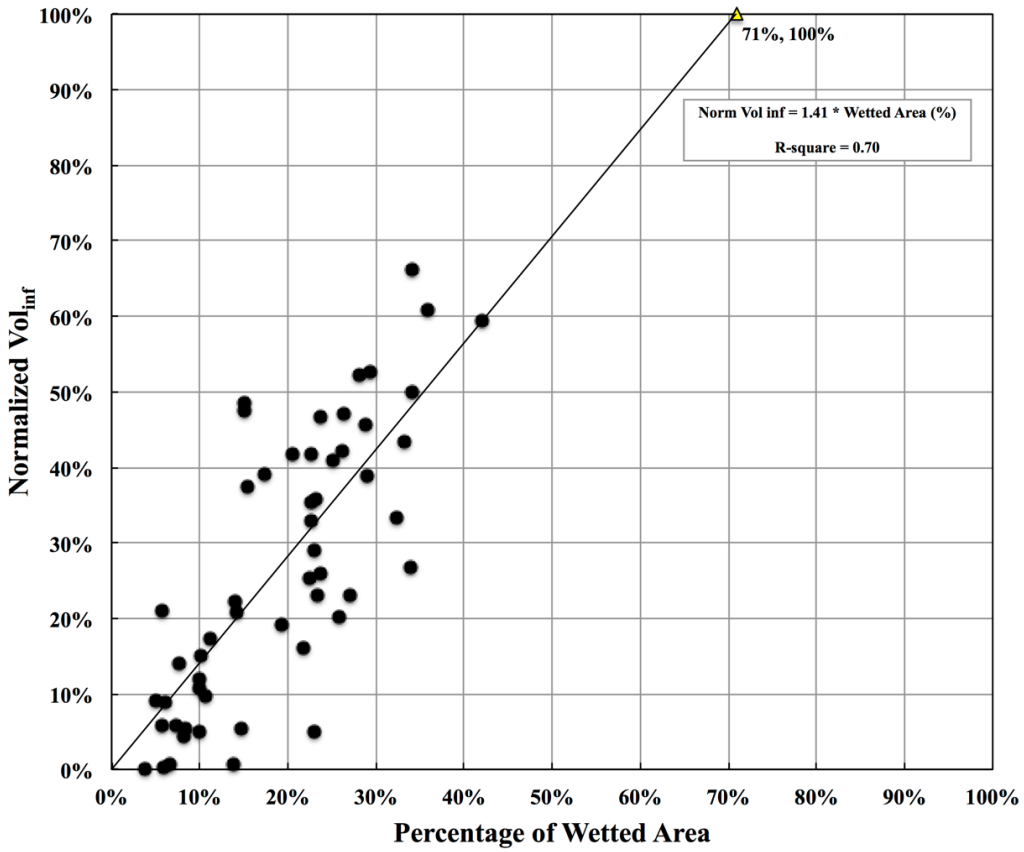

Figure 4.12 Normalized volume infiltrated versus percentage of wetted area for a boundary flux of 7.06×10^{-5} m^2/s.

3.2 Micro-topography: Parameters and Evolution

A summary of all the surface roughness parameters evaluated with minimum or maximum, and average for all directions and sections is presented in Table 4.1 for all the surface treatments and the three repetitions. The fractal dimension (*FD*), associated with the slope of the fitted line of the Fourier power spectrum, characterizes the heterogeneity of spatial variation of a surface, i.e. *FD* describes

the horizontal variations of a surface (Huang, 1998). Furthermore, the vertical intercept (*VIC*) of the power spectrum is associated with the magnitude of the roughness vertical component (Russ, 1994). Random roughness (*RR*), the standard deviation of the surface elevation, is another descriptor of vertical variations. A relationship between *RR* and the fractal vertical intercept has been observed (Figure 4.13), a weak correlation was found between *FD* and *RR*. According to Sung *et al.* (1998), surfaces with higher *FD* values appear to have rapid changes in a short distance, however these surfaces present small variability at a large distance or overall gradual changes in surface elevations (Huang, 1998). On the other hand, surfaces with lower *FD* have greater elevation differences; for example Chi *et al.* (2012) associated lower *FD* values to surfaces containing larger and deeper depressions. Both, *FD* and *VIC* should be used to describe horizontal variations and the range of the vertical variations of a surface (Huang, 1998; Vazquez *et al.*, 2006). For two surfaces with the same *FD*, the rougher surface is associated with greater vertical intercept (Russ, 1994; Eltz and Norton, 1997).

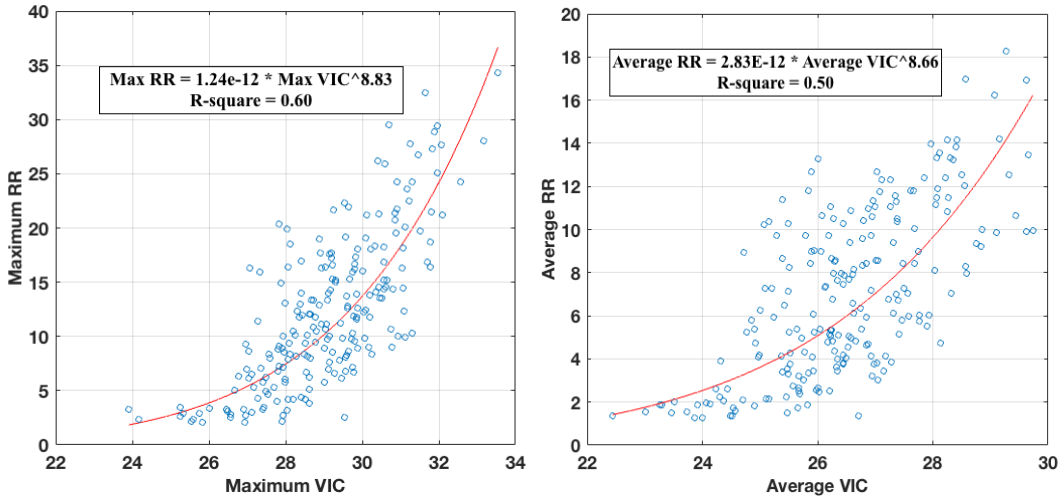

Figure 4.13 Left - Maximum random roughness (RR) versus maximum power spectrum intercept (Int or *VIC*) **Right -** Average random roughness (RR) versus average power spectrum intercept (Int or *VIC*). The red line represents the fitted equation.

Table 4.1 Summary of the average surface micro-topography parameters (fractal D [FD], fractal vertical Intercept [Int] or *VIC*, and Random Roughness [RR]) and their standard deviation.

		Time	FD Min	St. dev.	FD Ave.	St. dev.	VIC Max	St. dev.	VIC Ave.	St. dev.	RR Max.	St. dev.	RR Ave.	St. dev.
Initially Smooth	Test 1	t=0 min	2.52	0.09	2.71	0.03	25.75	1.36	23.87	0.81	3.74	1.58	2.08	0.55
		t=20 min	2.38	0.06	2.57	0.05	27.09	1.22	24.98	0.74	3.95	1.35	2.21	0.55
		t=40min	2.29	0.05	2.46	0.05	28.54	1.49	26.75	1.36	10.35	7.35	4.64	2.41
		t=60min	2.25	0.06	2.44	0.05	29.22	1.64	27.17	1.29	12.39	6.76	5.94	2.40
	Test 2	t=0 min	2.56	0.07	2.72	0.06	24.67	1.03	23.01	0.90	2.83	0.78	1.57	0.40
		t=20 min	2.47	0.09	2.64	0.06	25.71	1.37	23.86	1.02	3.32	1.61	1.81	0.60
		t=40min	2.34	0.12	2.57	0.08	27.49	1.83	25.08	1.33	4.86	2.63	2.56	1.02
		t=60min	2.25	0.10	2.50	0.07	29.16	2.01	26.42	1.78	10.95	8.11	5.01	3.51
	Test 3	t=0 min	2.52	0.07	2.67	0.05	24.89	1.34	23.32	1.29	3.41	1.30	2.07	0.66
		t=20 min	2.32	0.09	2.53	0.07	27.54	1.58	25.26	1.33	3.32	1.61	1.81	0.60
		t=40min	2.23	0.12	2.44	0.09	29.11	1.93	26.85	1.57	11.34	8.43	5.41	2.79
		t=60min	2.18	0.10	2.40	0.07	30.16	1.88	27.69	1.19	17.48	8.44	8.62	2.85
3 Initial Rills	Test 1	t=0 min	2.27	0.06	2.56	0.03	28.92	0.67	25.64	0.69	10.56	2.00	7.34	1.27
		t=20 min	2.31	0.07	2.56	0.05	29.02	0.62	25.89	0.88	10.76	3.24	7.24	1.93
		t=40min	2.29	0.08	2.50	0.07	29.02	1.12	26.48	1.36	11.19	5.40	6.81	2.91
		t=60min	2.29	0.11	2.49	0.07	29.10	1.60	26.69	1.57	11.91	6.64	7.01	3.25
	Test 2	t=0 min	2.31	0.07	2.57	0.06	28.65	1.24	25.36	0.97	10.92	1.66	6.94	1.10
		t=20 min	2.34	0.06	2.56	0.05	28.58	0.83	25.80	0.65	10.09	1.91	6.13	1.54
		t=40min	2.28	0.11	2.51	0.07	29.32	1.45	26.63	1.29	12.36	7.13	7.18	3.70
		t=60min	2.27	0.09	2.47	0.05	29.71	1.49	27.35	1.24	17.65	7.46	9.71	3.61
	Test 3	t=0 min	2.32	0.08	2.58	0.04	28.80	1.06	25.61	0.72	13.23	1.94	8.37	1.43
		t=20 min	2.33	0.06	2.54	0.03	29.27	0.97	26.45	1.07	15.68	5.25	8.96	2.57
		t=40min	2.29	0.07	2.52	0.05	29.89	1.11	26.91	1.28	16.10	7.72	9.63	4.10
		t=60min	2.31	0.07	2.49	0.07	29.71	1.38	27.37	1.19	18.25	7.63	10.71	4.15
5 Initial Rills	Test 1	t=0 min	2.31	0.03	2.59	0.03	29.08	1.07	25.70	0.77	11.97	2.27	8.40	1.35
		t=20 min	2.33	0.03	2.58	0.06	29.31	0.85	26.12	0.68	10.76	3.24	7.24	1.93
		t=40min	2.31	0.05	2.52	0.03	29.41	0.92	26.71	0.77	11.19	5.40	6.81	2.91
		t=60min	2.31	0.04	2.51	0.05	29.13	1.25	26.76	0.94	11.91	6.64	7.01	3.25
	Test 2	t=0 min	2.30	0.12	2.55	0.08	29.40	1.70	26.34	1.10	13.52	1.75	9.08	1.24
		t=20 min	2.28	0.10	2.53	0.07	29.89	1.55	26.74	1.19	14.48	2.35	9.19	1.44
		t=40min	2.29	0.08	2.53	0.07	29.89	1.80	26.94	1.44	15.39	5.64	9.26	3.65
		t=60min	2.29	0.08	2.52	0.10	30.04	1.60	27.19	1.49	16.74	7.57	9.72	4.81
	Test 3	t=0 min	2.27	0.07	2.54	0.04	30.08	0.84	26.76	0.69	16.15	1.70	11.48	1.13
		t=20 min	2.28	0.06	2.52	0.04	30.17	0.91	27.00	0.89	16.68	2.15	10.69	1.87
		t=40min	2.32	0.07	2.54	0.06	29.63	1.21	26.84	0.91	14.33	5.23	8.39	4.11
		t=60min	2.30	0.07	2.52	0.06	29.56	1.44	26.95	1.01	14.37	6.35	8.40	4.28

For initial conditions, before the start of the simulated runoff, most indexes were different for the distinctive surface treatments. The initially smooth surfaces had the greatest *FD* values and smallest *VIC* and *RR*, as expected. Based on the *FD* values, the three and five rilled surface could not be differentiated, however, both the *VIC* and *RR* show a small difference in the values for these two surface treatments. Paz-Ferreiro e*t al.* (2008) suggested that the fractal crossover length calculated by the semivariogram method was more sensitive to changes in micro-topography than *FD.* Similarly, the results presented in Table 4.1 show that the vertical intercept estimated with the Fourier power spectrum method was more sensitive to roughness differences than the *FD*.

Other studies have analyzed the effect of rainfall on roughness parameters (Paz-Ferreiro *et al.*, 2008; Vermang *et al.*, 2013; Zhang *et al.*, 2016). In this study, the effect of simulated runoff on roughness parameters was evaluated. All of the roughness parameters changed over time due to the erosion and deposition processes that took place during the one hour of simulated runoff. The evolution of the initially smooth surface is presented in Figures 4.14 and 4.15. The minimum *FD* noticeably decreased and the vertical intercept increased with runoff time, for all the time intervals. However, the *RR* did not capture the variation from t=0 to t=20 min as satisfactorily as the other two parameters. In addition, *RR* cannot always provide the predominant direction of the roughness elements, while *FD* and *VIC* can, as described below.

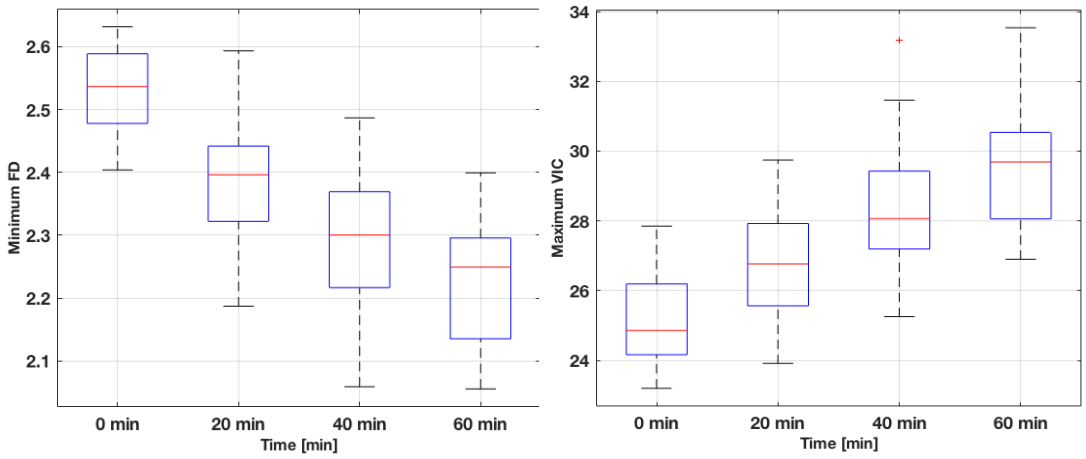

Figure 4.14 Box plots of the evolution of the fractal dimensions (Left-Minimum *FD* and Right-Maximum vertical intercept (*VIC*)) over time for the three tests with initially smooth surface. The red line represents the median of the tests, the error bars the minimum and maximum values, and the red crosses are outliners.

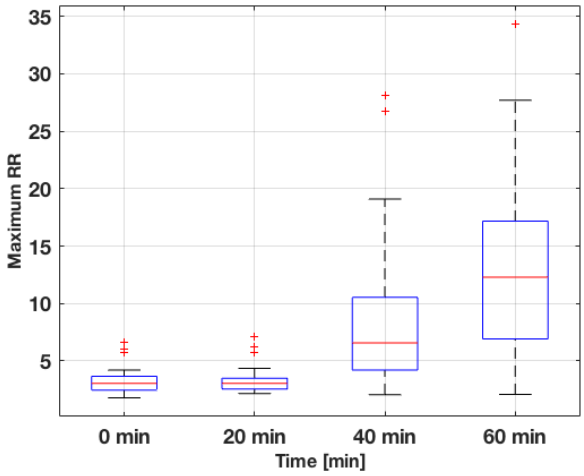

Figure 4.15 Box plots of the evolution of the random roughness (*RR*) over time for the three tests with initially smooth surface. The red line represents the median of the tests, the error bars the minimum and maximum values, and the red crosses are outliners.

An analysis of directional fractal dimension *FD* and vertical intercept has been performed based on initially smooth surfaces that evolved to the surfaces in Figure 4.16 after 40 minutes of simulated runoff. Different fractal parameter values were found depending on the direction, showing the anisotropy or heterogeneity of the surface (Zhang *et al.*, 2016) (Figures 4.17 and 4.18). For the initial conditions, the slight anisotropy could be due to the concavity of the surfaces and irregularities in the smoothing process. The anisotropy of the fractal

dimensions became more pronounced over time. Sung *et al.* (1998) suggested that, at a topographic scale, the main direction of the fractal dimensions follows the major features in an area. In general agreement with Sung *et al.* (1998), the values of the fractal dimensions *FD* were the highest in the direction of the rills (main direction) and lowest perpendicular to them (Figure 4.17 – center and right). Similarly, Vazquez *et al.* (2005) observed that a decrease in directional fractal dimension revealed the presence of oriented roughness features, in this case related to tillage. Fractal dimensions along the tillage direction were higher and in the direction perpendicular to the tillage the *FD* values were lower. These observations are different from the results obtained by Chi *et al.* (2012) for a surface dominated by depressions, where the fractal dimension rose plot was much more isotropic compared to the rose plot with surfaces with rills or tillage marks (Figure 4.18). The anisotropy coefficients ($a = 10^{St.Dev.(FD)}$) (Green and Erskine, 2004) of the three surfaces represented in in Figure 4.18 are: 1.09, 1.47, and 1.55, for the surface with depressions, rills, and tillage marks, respectively. Furthermore, the vertical intercept (*VIC*), after 40 and 60 minutes of flow, was highest in the direction perpendicular to the rills, where the maximum elevation changes existed (Figure 4.19 – center and right). Therefore, the trend was to see increasing values of the vertical intercept and decreasing values of *FD* in the direction perpendicular to the rills. Finally, the increase of the *FD* and the decrease of *VIC* over time in the direction of the flow in sections 3 and 5 could be due to the surface sealing process that made certain parts of the surface smoother (decrease in local roughness).

Wider and deeper rills were developed in sections 1 and 7, while sections 3 and 5 had multiple shallow and narrow rills (Figure 4.16). The minimum *FD* values and the *VIC* values were observed for sections 1 and 7 (Figures 4.17 and 4.19). On the other hand, sections 3 and 5 exhibited greater values of *FD* and lower vertical intercept values. It can be concluded, that the rose plots of the fractal parameters can provide important information about the type of erosion of a surface and its main direction.

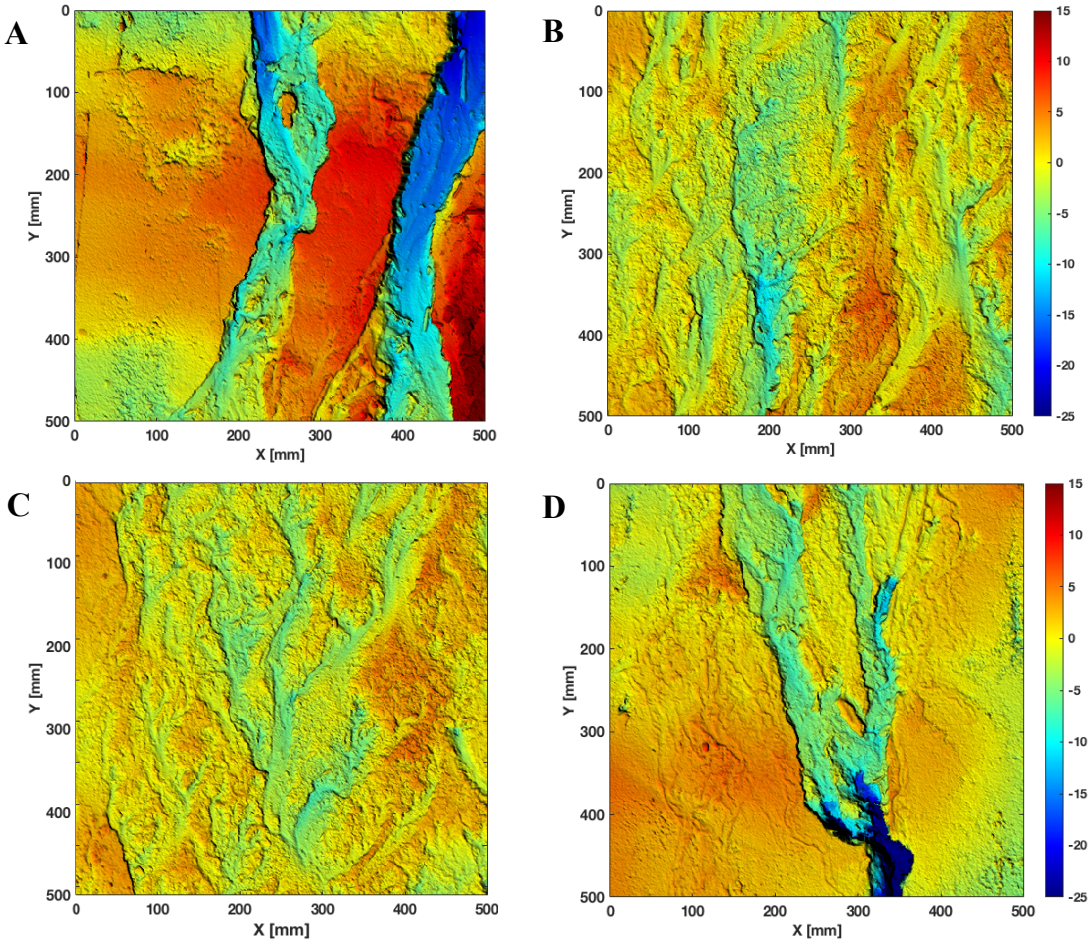

Figure 4.16 Hillshade map from the DEM of sections 1 (A), section 3(B), section 5(C), and section 7(D) of the slope (corrected for slope) initially smooth after 40 minutes of simulated runoff. The color bar represents elevation in mm.

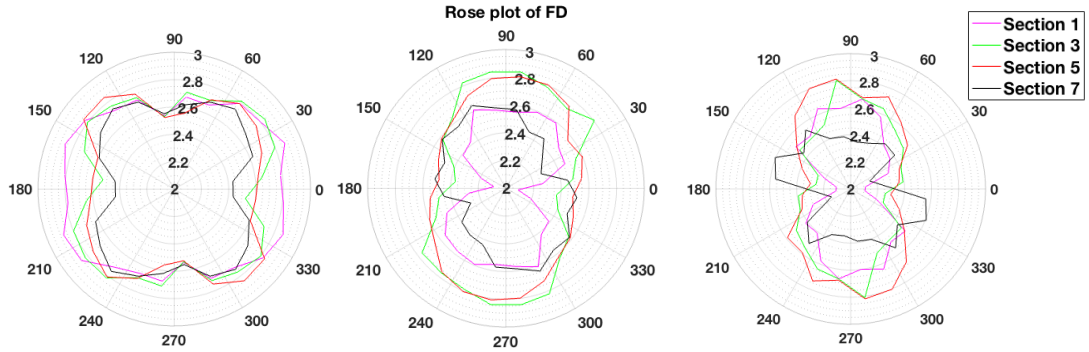

Figure 4.17 Rose plots of the fractal dimension (*FD*) of four sections of the slope surface (corresponding to A, B, C and D in Figure 4.16). Parameters (in 24 directions) calculated based on an initially smooth test after: **Left**- time=0 min; **center-** time=40 min; and **right-** time=60 min of simulated runoff.

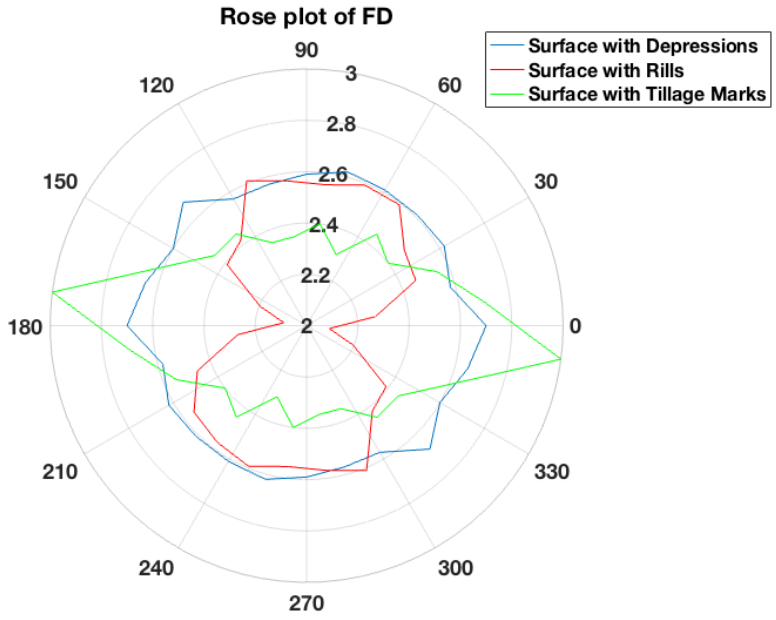

Figure 4.18 Rose plots of the fractal dimension (*FD*) of three surfaces: 1) Surface with depressions (adapted from Chi *et al.*, 2010), fractal dimension calculated using the variogram method; 2) Surface with rills (corresponding to A in Figure 16); 3) Surface with tillage marks (adapted from Vázquez *et al.*, 2005), fractal dimension calculated using the variogram method.

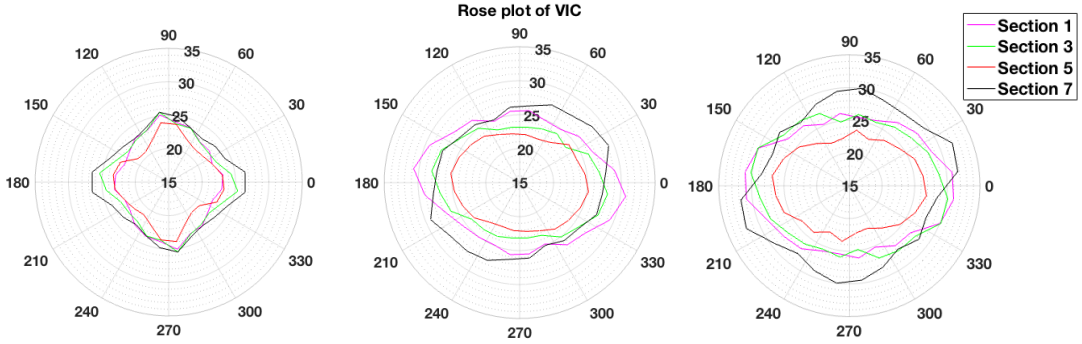

Figure 4.19 Rose plots of the fractal vertical intercept (*VIC*) of four sections of the slope surface (corresponding to A, B, C and D in Figure 4.16). Parameters (in 24 directions) calculated based on an initially smooth test after: **Left**- time=0 min; **center-** time=40 min; and **right-** time=60 min of simulated runoff.

3.3 Micro-topography and Wetted Area

Wetted area is an important parameter for both runoff and infiltration. The fraction of the surface area that is wetted, for example, is proportional to infiltration and inversely proportional to runoff. The previous section shows a connection between the micro-topographic features of a surface and the fractal

parameters *FD* and *VIC*. In this section, relationships between the two fractal parameters and the fraction of wetted area are presented. The fractal parameters were calculated after 40 and 60 minutes of runoff and the fractions of wetted area were estimated after 45 to 50 minutes of runoff. Table 4.2 shows the total fraction of wetted area of the overall slope, the low values in all tests show evidence of flow concentration for the three surface treatments.

Table 4.2 Percentage of water infiltrated during the one hour tests (Volume of water infiltrated/ Total volume of input water) and fraction of wetted area (over the total slope) after 45 minutes of simulated runoff.

Initial Surface	Test #	%Water Infiltrated	Total Fraction of Wetted Area
Smooth	Test 1	47.3%	0.22
	Test 2	45.6%	0.17
	Test 3	42.5%	0.16
3 Rills	Test 1	38.8%	0.12
	Test 2	32.7%	0.13
	Test 3	31.6%	0.17
5 Rills	Test 1	38.6%	0.21
	Test 2	29.7%	0.13
	Test 3	35.8%	0.18

The relationships between the fraction of wetted area and the minimum *FD* and the maximum *VIC* for the initially smooth sections are illustrated in Figures 4.20 and 4.21, respectively. From Figure 4.20 it can be concluded that the fraction of wetted area increases as the minimum *FD* increases; it should be highlighted that the minimum *FD* took place in directions approximately perpendicular to the flow. Figure 4.21 indicates that the fraction of wetted area tends to decrease as the maximum vertical intercept increases with an exponential relationship; again, the maximum *VIC* took place in directions approximately perpendicular to the flow. In addition, a better correlation was found between fraction wetted and maximum *VIC* (R^2 = 0.69) than when using minimum *FD* (R^2 = 0.60); this means that

vertical variations in roughness have more direct impact on shallow overland flow patterns (due to the flow distribution over the surface blocked by the rills) than horizontal variations of the surface. Finally, a relationship between the fraction of wetted area, for the three surface treatments evaluated, and maximum *VIC* was established (Figure 4.22).

It should be noted that no correlation was observed between the minimum *FD* of the initially rilled surfaces and the fraction of wetted area. We hypothesize that the better correlation between the fractal parameters and the fraction of wetted area for the initially smooth surface is because of the erosion in these cases was solely caused by the flow and not artificially generated micro-topography. In the initially rilled surface, the flow patterns did not necessarily follow the preexisting micro-topographic features.

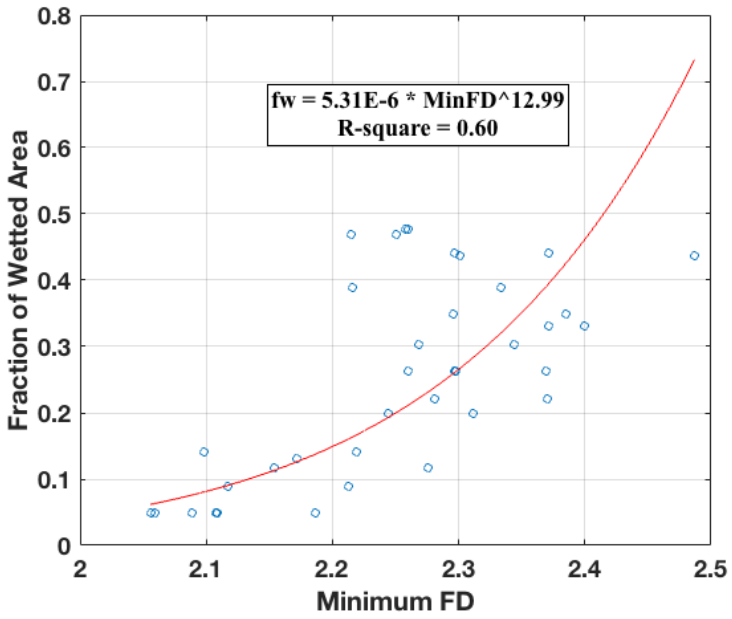

Figure 4.20 Fraction of wetted area versus minimum fractal dimension (*FD*). The data represents three tests with initially smooth surfaces, seven sections of the slope and two surface micro-topography readings (t=40 and t=60min).

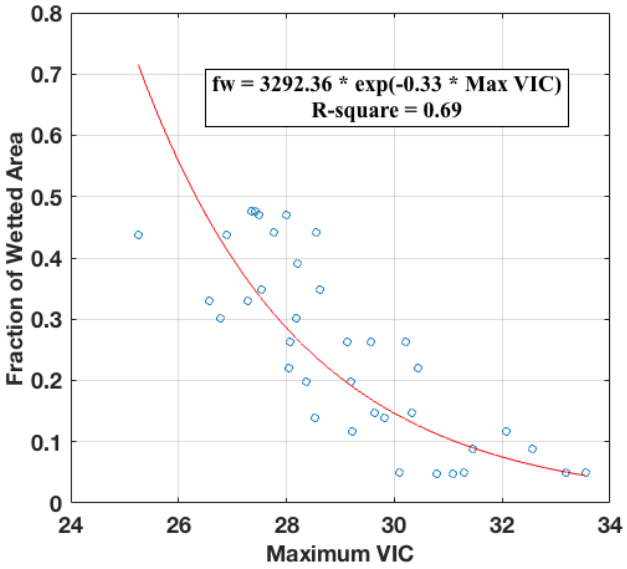

Figure 4.21 Fraction of wetted area versus maximum fractal vertical intercept (*VIC*). The data represents three tests with initially smooth surfaces, seven sections of the slope and two surface micro-topography readings (t=40 and t=60min).

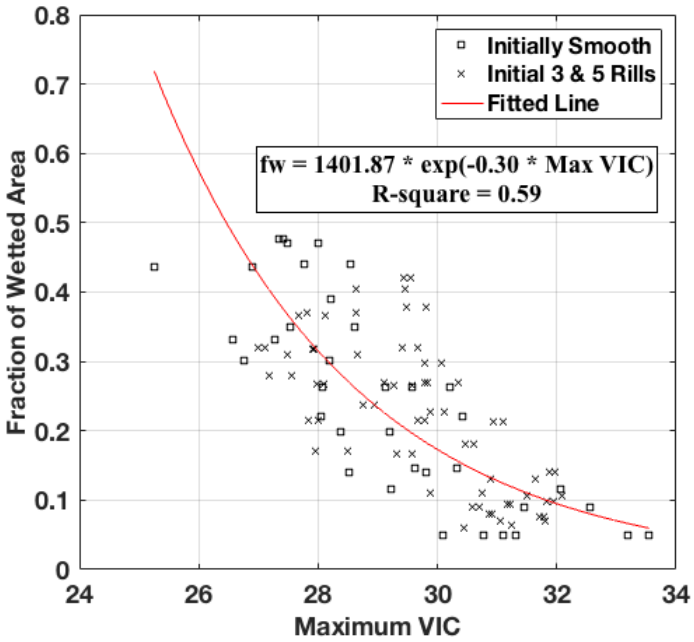

Figure 4.22 Fraction of wetted area versus maximum fractal vertical intercept (*VIC*). The data represents each of the three tests for initially smooth surfaces, three rills and five rills. The slope was divided into seven and two surface micro-topography readings (t=40 and t=60min) were used to calculate the fractal parameters.

The previous relationships were developed for a specific input flux of 7.06×10^{-5} m^2/s, however, the fraction of wetted area would vary if the boundary flux

changes. To adjust the fraction wetted area to other input fluxes, assuming that the surface topography follows a relationship of: *fw* = *a**exp(-*b**Maximum *VIC*), the Abbott-Firestone curve or the Bearing Area Curve (BAC) of the surface topography, in addition to Manning's equation, were employed. Manning's equation related the flux with the water depth:

$$q = \frac{1}{n}\sqrt{S_o}\, h^{\frac{5}{3}} \tag{7}$$

where S_0 is the slope of the bottom surface, n is Manning's roughness coefficient, h is the water depth, and metric units (m, s) are used for all the variables. The manning coefficient was assumed to be 0.25 s/m^3.

Kanafi and Tuononen (2017) defined the BAC as the curve formed by cutting the surface topography at different depths from the highest elevation to the bottom of the deep valleys and then calculating the percentage of the surface area that intersects with the cut plane. The BAC was estimated for a selection of five surfaces with different values of maximum *VIC*, based on the procedure described by Kanafi and Tuononen (2017). The estimations of the curves in Figure 4.23 consisted of an iterative process where, first, the water depth was estimated for a specific boundary flux using Manning's equation and an initial guess of fraction wetted. Second, using the BAC curve, the water depth was correlated with a fraction of wetted area, assuming that the water would flow on the deeper points of the surface first. This assumption is more probable for a surface with rills, as the surfaces observed in these experiments, because water would tend to fill in the rills or deepest points of the surface first. However, in a surface dominated by non-rilled depressions, this assumption would not be as valid, since all the depression (low points of the surface) may not be connected. If the fraction of wetted area obtained from the BAC curve was different from the value initially guessed, the first step was repeated using the new value of fraction wetted. This iteration was continued until the fraction wetted used in Manning's equation and the value obtained from BAC were approximately equal (+/- 0.001 difference). The fraction wetted results and corresponding values of maximum

VIC, were fitted to four additional exponential curves presented in Figure 4.23. These curves are important because they can be used to determine the wetted area of a surface based on the runoff boundary flux and the soil surface characteristics.

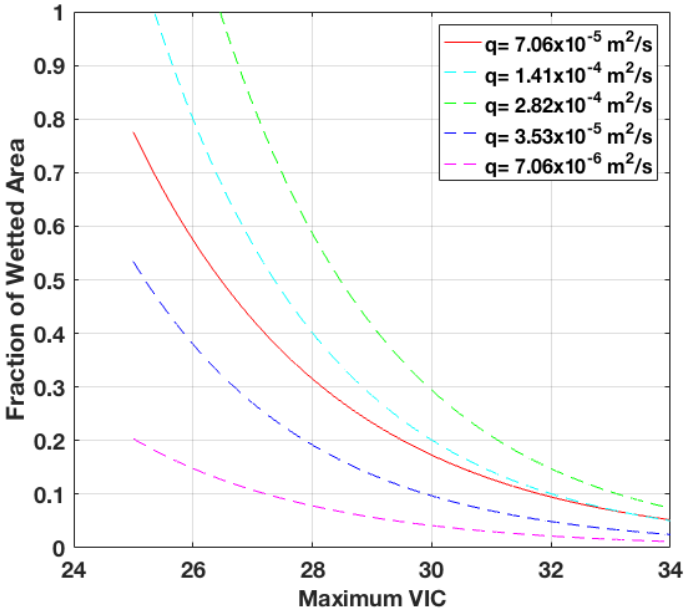

Figure 4.23 Fraction of wetted area versus maximum fractal vertical intercept (*VIC*) for five different rainfall intensities over an impervious area of 10m long.

3.4 Roughness Parameters and Scour Volume

The evolution of surface scouring, based on the total volume scoured for these experiments during the three simulated runoff tests with initially smooth surface, is evaluated in this section. In addition, the relationships between roughness parameters and scour volumes for each of the slope sections were analyzed using two fractal roughness parameters: *FD* and *VIC*. Figure 4.24 shows the effect of runoff duration on the total volume scoured for an input flux of 7.06×10^{-5} m^2/s. During the first 20 minutes of runoff, the scour volume slightly increased with runoff time. For the following 20 minutes, after 40 minutes of simulated runoff, the scour volume increased rapidly with increased runoff time. With further duration of runoff the scour volume continued to increase, this time at a lesser

rate. Based on the experimental observations, most of the erosion on the slope surface was rill erosion of two different types: shallow rill networks with multiple channels and a few number of deeper and wider rills, as shown in Figure 4.16. When the concentrated water increased enough, the deeper and wider rills were formed. Moreover, the sections with maximum erosion corresponded to the first and last sections (1 and 7), while the central part of the slope had both deposition and erosion processes, decreasing the volume of scour observed.

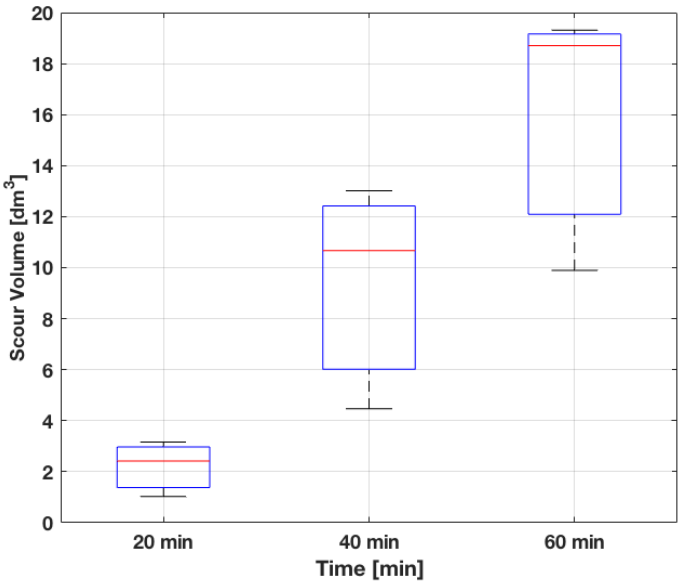

Figure 4.24 Box plots of the evolution of the total scour volume over time for the three tests with an initially smooth surface. The red line represents the median of the tests and the error bars the minimum and maximum values.

Figures 4.25 and 4.26 show the correlations between the scour volume for each slope section and the two fractal roughness parameters investigated, at three different times after the start of the simulated runoff. The relationship between scour volumes and the roughness parameters are opposed to the ones observed for fraction of wetted area: an increase in the minimum *FD* and a decrease in the maximum *VIC* correspond to lower scour volumes. The maximum *VIC* (R^2 = 0.69) is a more meaningful parameter to quantify erosion over time than minimum *FD* (R^2 = 0.62). Although scour volume depends upon many parameters specific to the experiment, this analysis indicates that the scour volume of an initially smooth

surface seems to be better represented by a power relationship with the maximum vertical intercept calculated based on the Fourier power spectrum method.

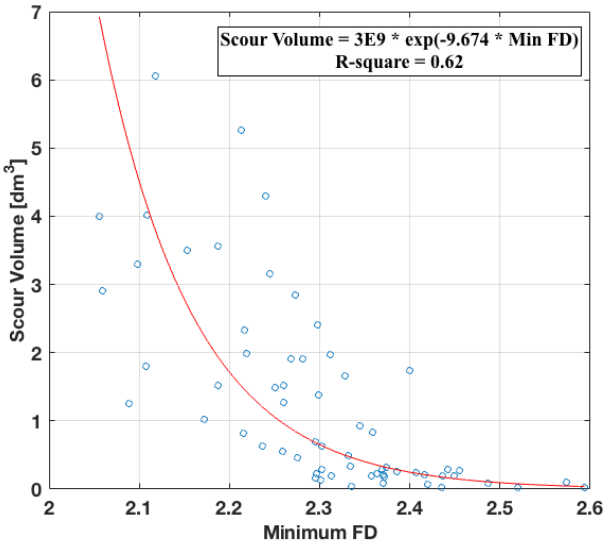

Figure 4.25 Total scour volume [dm^3] after 20, 40, and 60 minutes of simulated runoff (for each of the seven slope sections) versus minimum *FD* for the three tests with initially smooth surfaces.

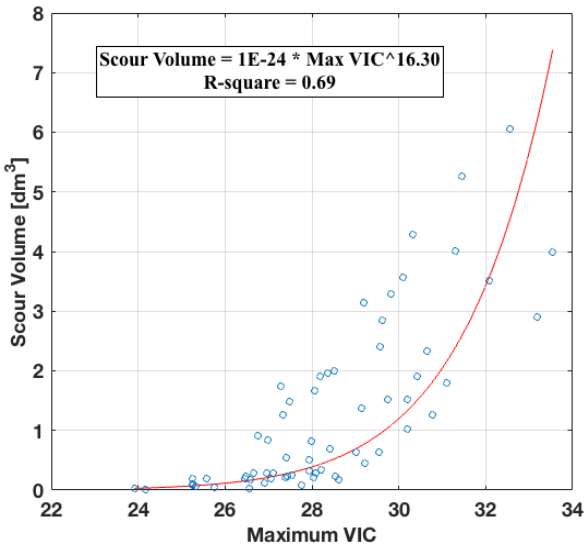

Figure 4.26 Total scour volume [dm^3] after 20, 40, and 60minutes of simulated runoff (for each of the seven slope sections) versus maximum vertical intercept (*VIC*) for the three tests with initially smooth surfaces.

4. Conclusions

Shallow overland flow over a slope with micro-topographic features parallel to the flow tends to concentrate in channels so that only a fraction of the slope surface contributes to the overland flow and infiltration processes. It is therefore important to analyze the effect that flow patterns affected by erosion processes have on infiltration. This study aims to formulate the relevance of the fractal approach for understanding soil surface roughness and overland flow patterns. The Fourier power spectrum method has been used to determine two fractal parameters describing *self-affine* surfaces obtained from simulated runoff tests in a laboratory setting: fractal dimension (*FD*) and the ordinate intercept or vertical intercept (*VIC*).

A 17% side slope of bare soil receiving simulated runoff from an upstream impervious area was monitored over time to determine infiltration volume (captured by underdrains), surface micro-topography, and water patterns. A linear relationship between the volume infiltrated normalized by the length of the section of the slope studied and the percentage of wetted area was observed. Concentrated flow was observed over the slope in all the tests and the sections that the slope was divided, with a maximum percentage of wetted area of 42% for the boundary flux tested (7.06×10^{-5} m^2/s).

The fractal parameters behaved differently for the distinctive initial surface treatments (smooth, 3 rills and 5 rills). The initially smooth surfaces had the greatest *FD* values and smallest vertical intercept (*VIC*) and random roughness (*RR*), as expected. The vertical intercept was more sensitive to roughness differences than the *FD*. The minimum *FD* noticeably decreased and the vertical intercept increased with runoff time. The fractal parameters were dependent on the direction, showing the anisotropy of the surface. The trend was to see increasing values of the vertical intercept and decreasing values of *FD* in the direction perpendicular to the rills. Surfaces with wider and deeper rills had

different fractal parameters than surfaces with shallow and narrow rills. In conclusion, the rose plots of the fractal parameters can provide important information about the type of erosion of a surface and its main direction.

In addition, the fraction of wetted area increased with the minimum *FD* and decreased as the maximum vertical intercept increased; the minimum *FD* and maximum *VIC* took place in directions approximately perpendicular to the flow. However, vertical variations in roughness had more impact on shallow overland flow patterns than horizontal variations of the surface. By relating fractal parameters to fraction of wetted area, linearly correlated to infiltration, the infiltration efficiency of filter strips can be estimated based on the micro-topography of its surface.

A decrease in the minimum *FD* and an increase in the maximum *VIC* were related to greater scour volumes. The maximum *VIC* is the most meaningful parameter to quantify erosion over time. The scour volume of an initially smooth surface seemed to be well-represented by a power relationship with the maximum vertical intercept. By defining indicators of rill erosion and associating them with flow patterns, a better description of shallow overland flow can be achieved. Fractal parameters based on the Fourier power spectrum method are good indicators of both flow patterns and erosion of a surface with predominant roughness features parallel to the flow direction.

Acknowledgments

The writers are grateful to the Minnesota Department of Transportation and Minnesota Local Road Research Board for funding this research under Contract No. 99008- 97, with Barbara Loida as Technical Liaison. J.L. Nieber's effort on this project was partially supported by the USDA National Institute of Food and Agriculture, Hatch/Multistate project 12-059.

Chapter 5

Infiltration Capacity of Roadside Filter Strips with Non-Uniform Overland Flow

Summary

The side slope to a roadside swale (drainage ditch) constitutes a filter strip that has potential for infiltration of road runoff, thereby serving as a stormwater quantity and quality control mechanism. A total of thirty-two tests were performed during three seasons in four different highways located in the Minneapolis-St. Paul metropolitan area, MN to analyze the infiltration performance of roadside filter strips and the effect of fractional coverage of water on infiltration. Three different application rates were used in the experiments. All the tests showed that water flow on the lateral slope of a roadside swale is concentrated in fingers, instead of sheet flow, at the typical road runoff intensities for which infiltration practices are utilized to improve surface water quality. A linear relationship between flux of water from the road and fraction of wetted surface was observed, for the intensities tested.

The average percentage infiltration of the medium road runoff rate ($1.55x10^{-4}$ m^2/s, without direct rainfall) experiments performed in fall was 85% and in spring 70%. For the high road runoff rate ($3.1x10^{-4}$ m^2/s, without direct rainfall) tests the average amount of water infiltrated was 47% and for the low road runoff rate ($7.76\ x10^{-5}$ m^2/s, without direct rainfall) tests it was 69%, both set of tests performed in spring and summer. The saturated hydraulic conductivity of swale soil was high, relative to the values typical of laboratory permeameter measurements for these types of soils. This is believed to be due to the macropores generated by vegetation roots, activity of macrofauna (e.g. earthworms), and construction/maintenance procedures. The trend was to have more infiltration when the saturated hydraulic conductivity was higher and for a greater side slope length, as expected. The vegetation, type of soil and length of the side slope are important to consider for constructing and maintaining roadside swales that will be efficient as stormwater control measures. These measurements indicate that the filter strip portion of a roadside swale typically infiltrates a substantial fraction of road runoff. However, the measurements do not incorporate the influence of direct rainfall upon the infiltration into filter strips.

1. Introduction

A growing trend in stormwater management is to include techniques that reduce runoff volumes and improve runoff water quality in addition to reducing the peak flow rate. Such techniques are called low impact development (LID) practices or Green Infrastructure (GI) and are typically designed to reduce runoff and to mimic a site's predevelopment hydrology. These practices include filter strips and vegetated drainage ditches (grassed swales), among others. They improve water quality by infiltration, filtration, and sedimentation. For roadway runoff flowing into a grassed swale, volume reduction occurs primarily through infiltration into the soil, either as the water flows over the side-slope in a direction perpendicular to the roadway into the swale or down the length of the swale channel parallel to the roadway. Most of the prior research on swales was on the channel portion, not the side slope. According to Barrett *et al.* (1998), as long as the road runoff is allowed to flow directly down the side slope into the swale, the side slope acts as a filter strip. Pollutant removal can occur by sedimentation of solid particles onto the soil surface, filtration of solid particles by vegetation, or infiltration and adsorption/degradation of pollutants dissolved in the runoff (Abida and Sabourin*,* 2006). The infiltration capacity of each swale will depend on many variables and each swale should be examined individually (Ahmed *et al.,* 2015).

Using synthetic runoff, Deletic and Fletcher (2006) studied a 5m long grass strip with a 7.8% average longitudinal slope and found 33% of average infiltration rates (as a percentage of the inflow) for the tests where the inflow water was mixed with sediment and 56% where the inflow was clean. A study by Liu *et al.* (2016) analyzed the synthetic runoff from 5m long loamy hillslopes (15º and 30º slopes) with different vegetation treatments on a newly built unpaved road. The mean runoff coefficient for the grassed side slopes was less than 0.1. The runoff coefficient was found to be correlated with the saturated hydraulic conductivity, vegetation cover, root weight density, and root length density.

Multiple studies have monitored volume reduction with swales subject to natural storm events. For example, Lancaster (2005) monitored infiltration along roadside swales in Washington, and reported 100% infiltration within the first two meters from the edge of pavement in one site (36 precipitation events). At another site, 67% of the events (18 precipitation events) had no observed runoff. Ahearn and Tveten (2008) investigated the performance of four 41 year-old, unimproved roadside swales. The results from the monitoring station located at 4 meters from the edge of pavement showed 66% to 94% runoff volume reduction.

The main difference between the side slope to a roadside grassed swale and traditional filter strips is the slope, the former having much greater incline. Hunt *et al.* (2010) investigated the volume reduction capability of a 44.8 m (147 ft) vegetative filter strip with a 1.25% slope over a 16-month period and 23 rainfall events. Total volume reduction over the monitoring period was 85% and the 3 events that produced runoff at the base of the swale had total rainfall depths greater than 40 mm (1.6 inches). Knight *et al.* (2013) monitored different vegetative filter strips with a level spreader. The strips had 1% slope, sandy loam/clay loam soils, and an estimated 0.1 cm/h hydraulic conductivity. The 8m long strip had an average runoff reduction of 36% while the 20 m long strip had a 59% average volume reduction.

Barrett (1998) indicated that in practice, flow in swales tends to concentrate in small, incised channels that reduce their effectiveness in removing constituents dissolved in highway runoff. Le Bissonnais *et al.* (2004) reported a reduction in the efficiency of grassed strips when the runoff was concentrated in rills and the surface was not completely covered by sheet flow. Poletika *et al.* (2009) investigated the effect of upper boundary application flow rate and flow concentration on percentage volume reduction of a vegetative filter strip. An application flow rate of approximately 2.09×10^{-4} m^2/s had a mean volume reduction of 41% and an application flow rate of 4.78×10^{-4} m^2/s had a 34%

volume reduction. The plot with concentrated flow (covering 10% of the surface width) had a volume reduction of 16%.

Results from previous research on infiltration performance of swales and filter strips have great variability on percentage of water infiltrated, probably because they have a wide range of inputs, use different methods to apply the water, and have different extents of concentrated flow. They generally vary in location, swale characteristics and type of soil, precipitation intensity and duration, drainage area, and whether the water is input as natural or artificial rain, or concentrated runoff. Based on previous studies, it is believed that the infiltration performance of swales is linked to infiltration capacity of the soil, initial soil moisture content, ratio of impervious drainage area-swale area, length and width of the vegetated area, slope, type of flow down the side slope of the swale (sheet or concentrated flow), and total depth and intensity of precipitation. Consequently, the experiments presented in this research take into account the most important factors for typical roadside swales side slopes. According to Asleson *et al.* (2009), monitoring the performance of full-scale stormwater treatment devices during real storm events is difficult to do with accuracy; alternatively performance tests of field installation using simulated rainfall events is a more reliable approach. In this research, the effect of non-uniform overland flow under a range of generated runoff fluxes on infiltration rates is tested. The goal is to analyze the volume reduction achieved by roadside filter strips (side slope of the swale) under different rainfall regimes using simulated runoff.

2. Method

2.1 Site Selection and Preparation

The four highways selected for this study were analyzed previously in field infiltration measurements study by Ahmed *et al.* (2015): Hwy 13 (Hwy 13 and Oakland Beach Ave. SE, Savage, MN), Hwy 47 (University Ave. NE and 83rd Ave. NE, Fridley MN), Hwy 55 (Snelling Ave. and County Rd. E, Arden Hills, MN),

and Hwy 77 (Cedar Ave. and E 74th St. North of Hwy 494, Bloomington, MN). These swales are between 30 and 50 years-old, constructed by the Minnesota Department of Transportation. Two locations were tested in each highway, 6-10 m apart, chosen to assure safety and ease of access. All of the side slopes had 90% or more vegetation cover, which is sufficient to consider these vegetated. For water quality purposes, for example, CALTRANS (2003) found that "a minimum vegetative cover of about 65% is required for pollutant concentration reduction to occur, and a rapid decline in performance occurs below about 80%." The soil types studied (loam, loamy sand, sandy loam, and sandy clay loam) correspond to hydrologic soil groups A, B and C (NRCS, 2009).

For the field tests, the grass was mowed with a lawn mower and shears were used to finish cutting the surface vegetation to a height of approximately 1 cm. The grass clippings were collected in the lawn mower bag and the remainder was cleared with a bamboo rake (Figure 5.1). The water depths during the tests were lower than the height of the remaining vegetation. The roots of the vegetation were not modified, leaving the existing soil matrix and soil macroporosity in the original state. Surface roughness data was collected using a pin meter operated on a fixed frame. Cross-sectional pin meter measurements were documented with a camera, collecting the relief every 10.2 cm (4 in) along the entire length of the swale side slope.

Figure 5.1 Grassed roadside swale at Hwy 77 after cutting and raking the surface vegetation.

2.2 Experimental Procedure

Three different boundary flux rates (q_b) were used (Table 5.1), equivalent to a uniform rainfall intensity of 2.8 cm/h, 5.6 cm/h, and 11.2 cm/h intensity over a 10 m wide road and shoulder, assumed typical for a road with 2 lanes. Water equivalent to the road runoff intensity from each of these events was applied to a strip width of 0.9 m at the top of the slope along the edge of the shoulder of the road. The water was pumped with a hose from a reservoir with a submersible pump. Discharges were adjusted with a valve, volumetrically calibrated before every experiment to 4.3, 8.5, and 17 L/min. The water was pumped to a plastic box with a rectangular weir (Figure 5.1). To enable visualization of the flow patterns, the water was mixed with industrial kaolin (median particle size 0.5 µm), a clay mineral, using a paint mixer to achieve a 13 g/L uniform concentration. The total volume of water for each experiment was 255 L. The water patterns were recorded by installing a camera with a mounting pole set in the channel of the swale; the pole had an adjustable height and the average height at which the

camera was set was 2.5 - 3 m. The camera was programmed to take one picture every five seconds. A 1x1m mesh frame was installed on the swale to facilitate corrections of angle distortions in the pictures taken (Figure 5.2a).

Table 5.1 Boundary flux (q_b), intensity (I), assumed width of the road (W_r), and duration of the test corresponding to the low, medium and high flux experiments.

Flux Type	q_b **(m²/s)**	I **(cm/h)**	W_r **(m)**	**Duration (min)**
Low flux	7.76×10^{-5}	2.79	10	60
Medium flux	1.55×10^{-4}	5.59	10	30
High Flux	3.10×10^{-4}	11.18	10	15

The water not infiltrated by the swale was collected from a clay lined trench dug at the bottom of the side slope connected to a receiving bucket. The total volume of water that was not infiltrated (runoff) was recorded, as well as the runoff rate when the system reached steady state, or when the volume collected over 30 second intervals was constant by the end of the tests. The following data were collected:

- Micro-topography of the surface,
- Total volume of runoff water (water not infiltrated in the side slope of swale),
- Intensity of runoff flow,
- Wetted surface area over time,
- Soil texture and bulk density,
- Initial soil moisture content, and
- Saturated hydraulic conductivity and effective wetting front suction.

For each highway, two soil cores of 13 cm length from the surface were collected

during fall 2014, using a cylindrical core sampler to examine bulk density and porosity (ASTM D2937-10). Those cores were used to investigate soil texture; the soil samples were processed using the wet sieving analysis (ASTM D6913) and hydrometer analysis (ASTM D422) to determine % clay, % silt and % sand in each sample. Before each test, three soil samples were collected to determine initial soil moisture content (ASTM D2216). The Green Ampt (1911) parameters, saturated hydraulic conductivity and wetting-front suction (ψ) in the upper 25 cm were estimated at the end of the field tests using the MPD infiltrometer method (Asleson *et al.* 2009; Olson *et al.*, 2013; Ahmed *et al.* 2014). For this, twenty measurements of falling head were taken per highway and utilized in the MPD spreadsheet to compute the saturated hydraulic conductivity and the capillary suction of the soil ahead of the wetting front.

To evaluate the wetted area, images were processed following a five step procedure using the software ImageJ, an image processing and analysis software. First, based on the frame positioned in the field, the image (Figure 5.2a) was orthogonally projected (Figure 5.2b), using the ImageJ plugin Projective_Mapping with a bilinear approximation. Second, the picture was transformed into an 8-bit grey scale. Afterwards, a study area was selected and cropped based on the spread of the water along the slope. Then, a Fuzzy Contrast Enhancement (Figure 5.2c) plugin (Alestra and Battiatto, 2008) was used to differentiate the wetted from the dry area. Finally, a thresholding method that binarises 8-bit images was implemented to select the wetted area. The preferred technique was the “Intermodes” method (Prewitt *et al.*, 1966), which assumes a bimodal histogram (Figure 5.2d). Verification of the images was made by visually observing the locations of the water on the slope and comparing them to the information taken from the photographs; the results were similar.

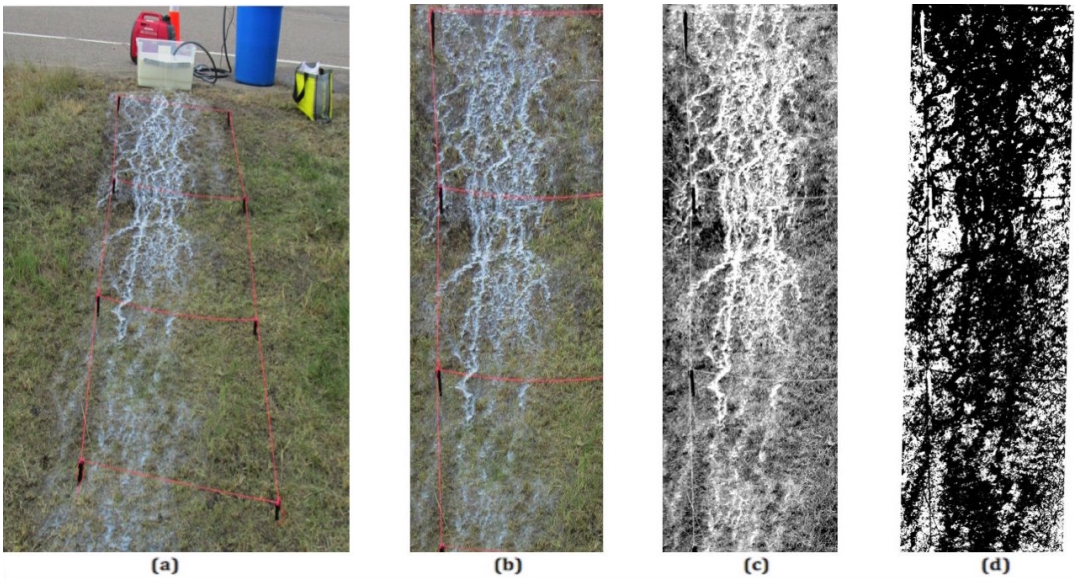

Figure 5.2 Original and processed images of the water pattern flowing down the side slope of swale during a simulated a 1.1in-30min storm. a) Original picture b) crop and orthogonal projection c) Projection with Fuzzy Contrast Enhancement applied d) Final selection of the wetted area (in black).

3. Results and Analysis

The analysis is based on a total of 32 tests performed during fall 2014, spring 2015, and summer 2015 on highways: 51, 77, 47, and 13 in the Minneapolis-St. Paul, USA metropolitan area. The duration of the low, medium, and high application rates was 60, 30 and 15 minutes, respectively.

3.1 Dimensionless Infiltration Parameters

Infiltration measurements were made at two strips in each of four sites. Representative dimensionless parameters will be used to generalize the results. These were chosen from knowledge of the physical processes. The first parameter is a relative volume of infiltration:

$$V_i^* = \frac{V_{inf}}{V_{in}} \quad (1)$$

where V_{inf} is the volume infiltrated and V_{in} is the input volume. When V_i^* is equal to one, all of the runoff from the road has infiltrated in the side slope of the swale. The second parameter is a relative saturated hydraulic conductivity:

$$K_s^* = \frac{K_{sat}}{I}\frac{W_S}{W_R} \quad (2)$$

where K_{sat} is a representative saturated hydraulic conductivity for the side slope, I is average rainfall intensity, W_S is the width of the swale perpendicular to the road, and W_R is the width of the road draining into the swale. Infiltration fraction will typically increase with K_s^*. In a sheet flow, K_s^* equal to one will result in complete infiltration of the water. This factor does not take into account concentrated flow, which would reduce V_i*, or soil moisture deficit, which would increase V_i*. The field experiments results presented show the relationship between K_s* and V_i*, taking into account concentrated flow and initial soil moisture content.

3.2 Characteristics of the Roadside Filter Strips

Table 5.2 provides information about the sections of the roadside filter strips examined during the field experiments. Using the percentages of clay, silt and sand in a textural triangle (USDA, 2014) the soil texture class in the upper 13 cm was determined. Rows with two soil textures (Hwy 51, 47, and 13) indicate that among the eight soil cores samples, there were both textural classes of soil. The slope and length of the side slope perpendicular to the road were measured at each site. The values of K_{sat} were adjusted to 20°C by multiplying the measured K_{sat} at a given temperature (T) by the viscosity correction factor $\eta_T / \eta_{20°C}$; where η_T is the viscosity of water at a certain temperature.

The representative saturated hydraulic conductivity for infiltration given in Table 5.2 is computed as:

$$K_{sat} = \beta\, K_{sat\ Arithmean} + (1-\beta)\, K_{sat\ Geomean} \quad (3)$$

,where the arithmetic ($K_{sat\ Arithmean}$) and geometric ($K_{sat\ Geomean}$) mean values were calculated from 20 measurements of saturated hydraulic conductivity using the MPD infiltrometer (Ahmed *et al.*, 2015) performed on the strips tested. Equation 3, with β = 0.32, was derived by fitting to a simulation that used 268 K_{sat} measurements at 12 sites by Weiss and Gulliver (2015). They found that a linear combination of K_{sat} arithmetic and geometric mean values more accurately represented the observed aggregated infiltration in the soil of stormwater treatment practices, including swales.

Table 5.2 Characteristics of the swales studied based on soil cores samples, estimations of saturated hydraulic conductivity (at 20ºC), and length and slope of the sections used in the experiments. *Coefficient of variation in parenthesis.

	Soil Texture	**Arithmetic mean of K_{sat} (cm/h)**	**Geometric mean of K_{sat} (cm/h)**	**K_{sat} (cm/h) (based on Eq. 3)**	**HSG (based on Eq. 3)**	**Bulk Density (g/cm^3)**	**Porosity (%)**	**Mean θ_i (Fall) (%)**	**Mean θ_i (Spring) (%)**	**Slope**	**Length studied (cm)**
Hwy 51	Loam /sandy loam	5.1 (1.44)*	2.8	3.5	B	1.1	0.56	0.15	0.30	5:1	406
Hwy 77	Loamy sand	7.5 (0.94)*	4.9	5.7	A	1.2	0.56	0.15	0.20	5:1	407
Hwy 47	Loamy sand /sandy loam	4.9 (1.29)*	2.8	3.5	B	1.2	0.54	0.12	0.27	5:1	779
Hwy 13	Loam /sandy clay loam	6.1 (1.87)*	3.2	4.1	A	1.1	0.58	0.13	0.29	4:1	422

3.3 Infiltration Volume

Table 5.3 summarizes the results of the different experiments performed at the highway 51, 77, 47, and 13 sites during fall 2014, and spring and summer 2015, with percentage of volume infiltrated, start time of runoff (flow not infiltrated entering the channel) and approximate runoff rate (at the bottom of the side slope) after steady state in runoff was approached for the different cases studied. The field tests were performed in this order: medium flux (fall 2014), medium flux, low flux, and high flux (spring and summer 2015).

Table 5.3 Results of the field experiments in chronological order at the four highways selected during the three different seasons using three different intensities of boundary flux. The fall experiments were performed in 2014 and the spring and summer tests in 2015. The (-) indicates no runoff generation. *Tests affected by construction and**Site with plains pocket gopher holes.

	Season	Boundary Fluxes	Site	Runoff start time (min)	Rate runoff (L/min)	Wetted Area (%)	% Infiltrated
Hwy 51	Fall	Medium Flux	Site 1	17	2.75	84%	86.5%
			Site 2	9	3.1	69%	74.1%
	Spring	Medium Flux	Site 1	11.6	5.5	61%	61.4%
			Site 2	12	4.2	69%	72.4%
		Low Flux	Site 1*	8.8	3.1	67%	59.2%
			Site 2*	5.6	3	77%	62.1%
		High Flux	Site 1*	1.7	16.25	79%	32.2%
			Site 2*	1.4	16.5	90%	32.7%
Hwy 77	Fall	Medium Flux	Site 1	6.3	3.75	64%	64.8%
			Site 2	15	4.2	70%	76.6%
	Spring	Medium Flux	Site 1	9	4.85	66%	61.8%
			Site 2	8.8	4.75	54%	65.9%
		Low Flux	Site 1	17.6	2.5	85%	68.9%
			Site 2	28.8	2.5	66%	72.9%
		High Flux	Site 1	2	16.25	82%	20.6%
			Site 2	3.3	15	88%	37.5%
Hwy 47	Fall	Medium Flux	Site	-	-	75%	100%
			Site 2	27.6	0.04	83%	100%
	Spring	Medium Flux	Site	25	1	70%	98.0%
			Site 2	9.8	4.4	77%	72.7%
	Summer	Low Flux	Site	-	-	70%	100%
			Site 2	14.8	2.5	57%	65.0%
	Summer	High Flux	Site	10	2.8	80%	95.0%
			Site 2	5.9	8	81%	74.9%
Hwy 13	Fall	Medium Flux	Site 1	18.5	2.5	77%	88.4%
			Site 2	18.25	2.6	72%	87.0%
	Spring	Medium Flux	Site 1	10.9	4.5	75%	68.4%
			Site 2	9.2	6.9	70%	59.1%
	Summer	Low Flux	Site 1	11.8	2.82	58%	60.7%
			Site 2	13	2.8	57%	60.7%
	Summer	High Flux	Site 1	1.5	13	85%	41.8%
			Site 2	1.6	13.2	80%	42.2%

During spring 2015, before the low flux tests, the roadside swale of Hwy 51 (both sites) was impacted by the placement of fiber optic cable across the ditch and the nearby construction of County Road E bridge. The surface of the swale had vegetation losses and compaction due to truck and excavation operations, however these factors did not noticeably affect the results. At highway 47, plains pocket gopher (*Geomys bursarius*) holes were observed at site 1, and the infiltration rates at this site were high, with almost 100% infiltration for all intensities. This is presumed to be a special case due to the plains pocket gopher holes, and will not be included in the analysis. Figure 5.3 displays the average infiltration percentage for the different intensities. The total equivalent simulated rainfall depth (assumed to be applied over the road) was 2.8 cm in all tests. The average percentage of water infiltrated during the medium flux experiments performed in fall (8 tests) was 85%, or 2.4 cm of rain on the road with a 13% standard deviation. This value is higher than the results observed during spring, with 70%, or 1.95 cm of rain on the road with a 12% standard deviation. During the high flux experiments (8 tests) the average of water infiltrated was 47%, or 1.3 cm of rain on the road with a 25% standard deviation. The average water infiltrated during the low flux experiments was 69%, or 1.93 cm of rain on the road with a 14% standard deviation.

Figure 5.4 provides the mean and standard deviation of the runoff coefficient (ROC) at the end of the experiment, or the rate of runoff at the end of the experiment divided by the boundary flux rate, for each set of tests. The medium flux fall tests had a lower ROC than in the spring, probably because of the low initial soil moisture content for those tests. The infiltration data collected from the medium flux experiments (spring tests) was similar to the low flux tests. These results imply that either there was a reduction in the saturated hydraulic conductivity or an increase of the soil moisture content in the experiments carried out after the first tests (medium flux) in spring. The similar start time of runoff

(Figure 5.5) and greater ROC (Figure 5.4) confirm this observation. In the spring tests at highway 13 (Figure 5.5), the ROC of the low flux test was 0.66, higher than the medium flux test 0.53; both had similar start times of runoff generation. The possible causes of the relative infiltration reduction are addressed in the Discussion, section 4.2.

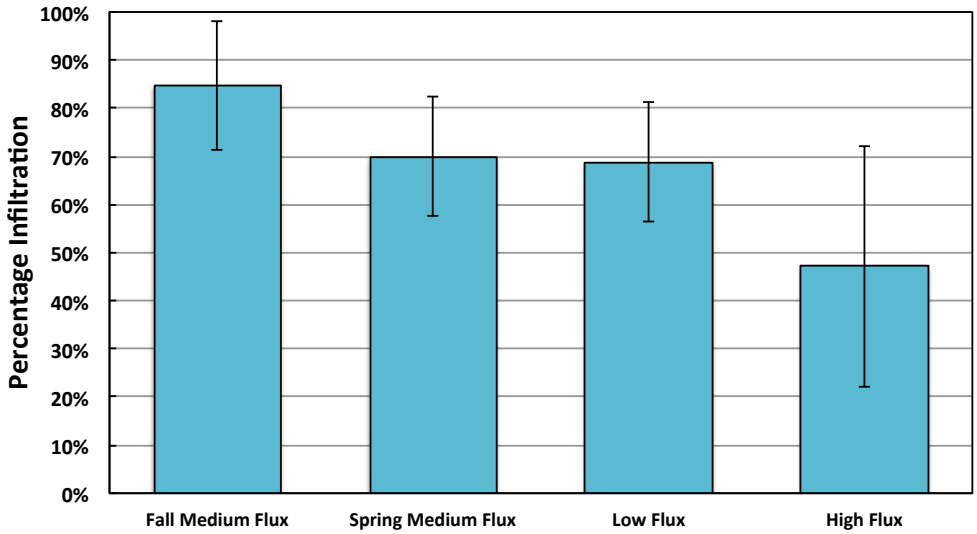

Figure 5.3 Average percentage of water infiltrated in the field experiments, in chronological order of tests. Two sites were tested for each of the four highways. Three boundary fluxes were applied, corresponding to: low, medium, and high boundary flux tests. The error bars represent the standard deviations.

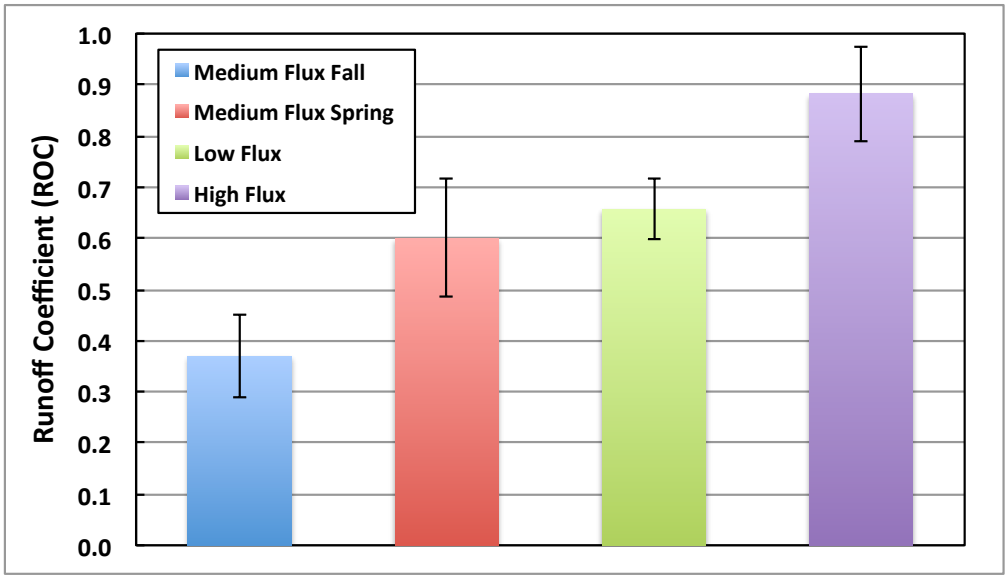

Figure 5.4 Average of runoff coefficients the field experiments, in chronological order of tests. Three boundary fluxes were applied, low, medium and high. The error bars represent the standard deviations.

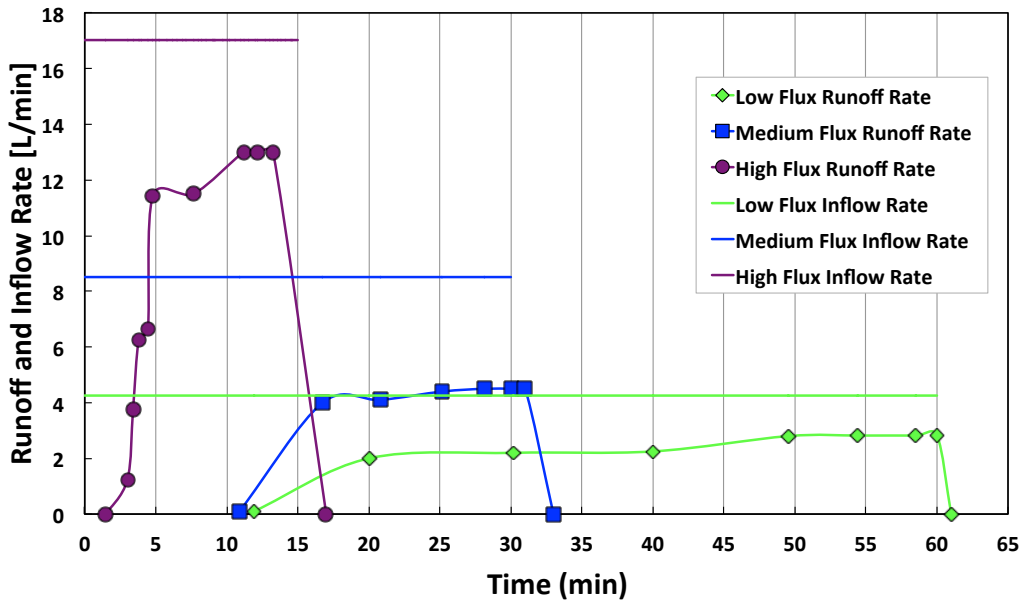

Figure 5.5 Runoff rates measured in the field (points) and inflow rates (lines) of three tests in the spring and summer on highway 13, corresponding to simulated runoff of low (green diamonds), medium (blue squares), and high (purple circles) boundary fluxes.

3.4 Roughness and Wetted Area

The surface of the swales studied neither showed signs of previous erosion nor experienced erosion during the experiments. The measurements taken with the pin meter were translated into a random roughness factor (RR) (Allmaras *et al.*, 1966), which is the standard deviation of surface elevations. The RR reveals the vertical variability in surface elevations (Yang *et al.*, 2013) and was found to be close to the same value for all sites. The average RR (perpendicular to the flow) for all the swales was 4 mm with a standard deviation of 1mm. The average RR (parallel to the flow), corrected for slope, was 5 mm, with a standard deviation of 3 mm. For these swales, the variation in RR was minor, and a correlation of RR and wetted area was not attempted.

The wetted area appears to be related to the rainfall intensity over the road (Figure 5.6). A greater intensity, results in more area covered by water. The mean value of percentage wetted area was 72%, with a 9% standard deviation for the selected intensities among the four sites. The maximum percentage wetted area was 90% and minimum 54%. An empirical relationship between fraction of wetted area and intensity is given in the following equation, fitted to the field data:

$$\textit{Fraction of Wetted Area} = 0.00225 \times \textit{Intensity [mm/h]} + 0.581 \quad (4)$$

Roughness measurements showed that there were minimal preferential pathways in the micro-topography. We hypothesize that the sensitivity of wetted area to intensity is due to the absence of preferential flow features. We also hypothesize that if there were structured micro-topography, oriented in the downslope direction, there would be smaller sensitivity to intensity. The side slopes of the swales were relatively smooth, indicating that the Minnesota Department of Transportation's maintenance procedures were effective.

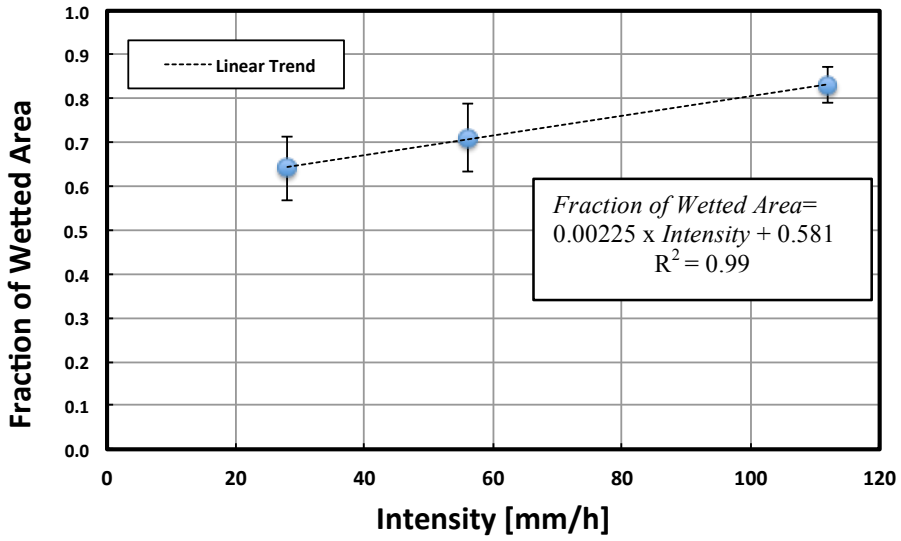

Figure 5.6 Fraction of the side slope wetted versus rainfall intensity over the road during the field experiments, for three different intensities. The error bars represent the standard deviation and the line is the linear trend.

3.5 Saturated Hydraulic Conductivity and Infiltration

As expected, the saturated hydraulic conductivity of the soil is observed to be an important factor for infiltration rates. Figure 5.7 displays the relationship between the percentage infiltrated (V_i^*) and dimensionless parameter K_s^*, which is a function of the saturated hydraulic conductivity, rainfall intensity, width of the swale perpendicular to the road, and width of the road. The soil moisture deficit was higher in Test 1 than in the three other tests. The results indicate that V_i^* rises sharply below a K_s^* of 0.3. For K_s^* greater than 0.3, other factors seem to influence the percent infiltrated in the tests. The influence of soil moisture content, for example, can be seen in the high percent of V_i^* values measured in Test 1. This influence is discussed in the next subsection.

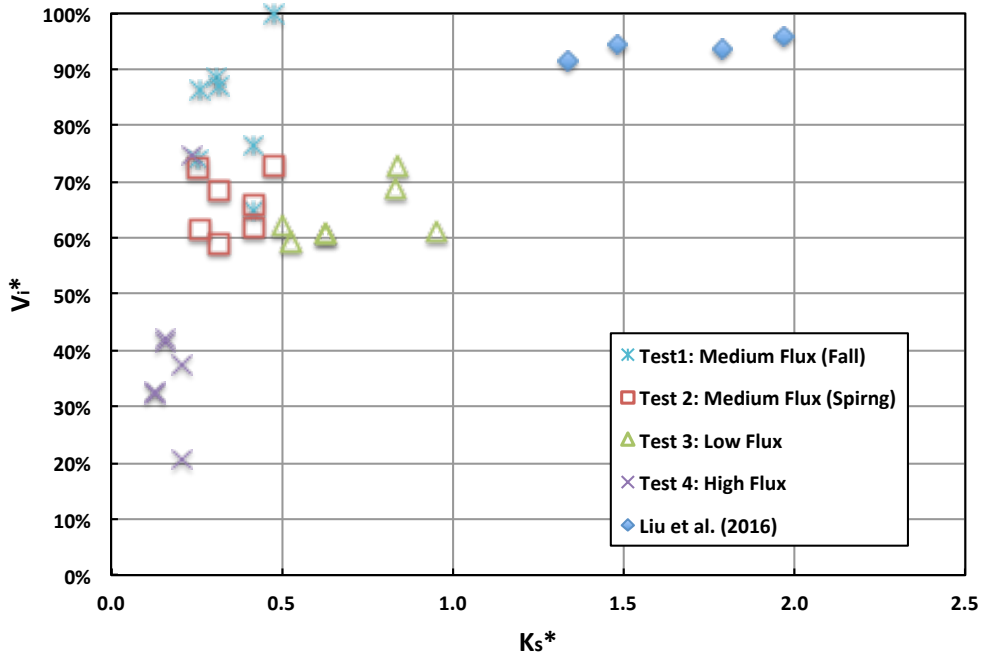

Figure 5.7 Infiltration percentage (V_i^*) versus saturated hydraulic conductivity dimensionless parameter K_s^*. Tests from highways: 13, 51, 77, and 47 (site 1 not included) (N= 28). The assumed road and shoulder width was 10 m. The experiments of Liu *et al.* (2016) are given for comparison.

3.6 Initial Soil Moisture Content Effect on Infiltration

The initial soil moisture content during the spring experiments was higher than the previous fall, for the same boundary flux. Subsequently, the volume of water infiltrated during the spring experiments was lower than during the fall tests. Figure 5.8 shows the relationship between the percentage of water infiltrated and the soil moisture deficit (computed as the difference between the porosity of the soil and initial soil moisture content). The trend is to see a lower volume infiltrated for initially wetter conditions. Figure 5.8 indicates there is lower sensitivity of infiltration capacity to soil moisture deficit reduction, which is also linked to a decrease in sorptivity. The data seemed to be relatively constant until a soil moisture deficit of 0.35, then it rises rapidly at higher soil moisture deficits. For a soil moisture deficit above $\Delta\theta$ = 0.35 the percentage of water infiltrated appears to follow a linear relationship.

To relate the dimensionless parameter K_s^* and soil moisture deficit to percentage infiltration (V_i^*) a log-log multiple regression equation has been developed using the field data, excluding the data from for Site 1 at Hwy 47, where pocket gopher holes were observed:

$$V_i^* = \beta_0 K_s^{*\beta 1} \Delta\theta^{\beta 2} \quad (5)$$

where $\beta_0 = 1.79$, $\beta_1 = 0.25$, and $\beta_2 = 0.68$, $\Delta\theta$ is the fraction soil moisture deficit, and $V_i^* \leq 1$ Figure 5.9 shows the goodness of fit of the equation. A correlation coefficient of 0.47 (n = 28) and a slope significantly different from zero (α =0.05) were observed.

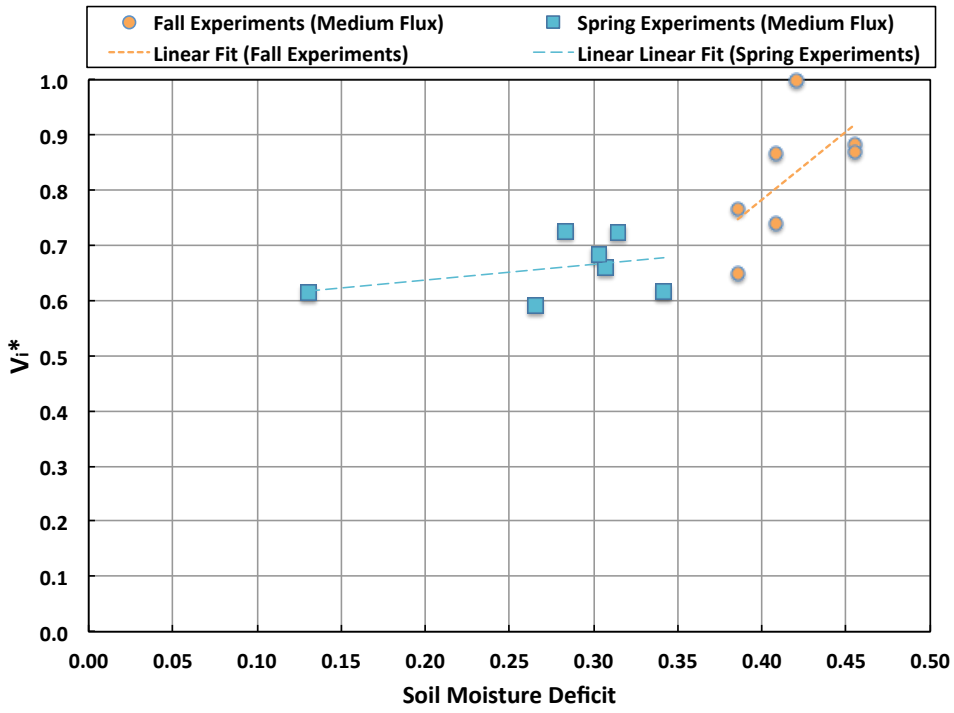

Figure 5.8 Percentage of water infiltrated versus soil moisture deficit. Soil moisture deficit is defined as the difference between porosity and initial moisture content. The Hwy 47 (Site 1) where gopher holes were observed is not included.

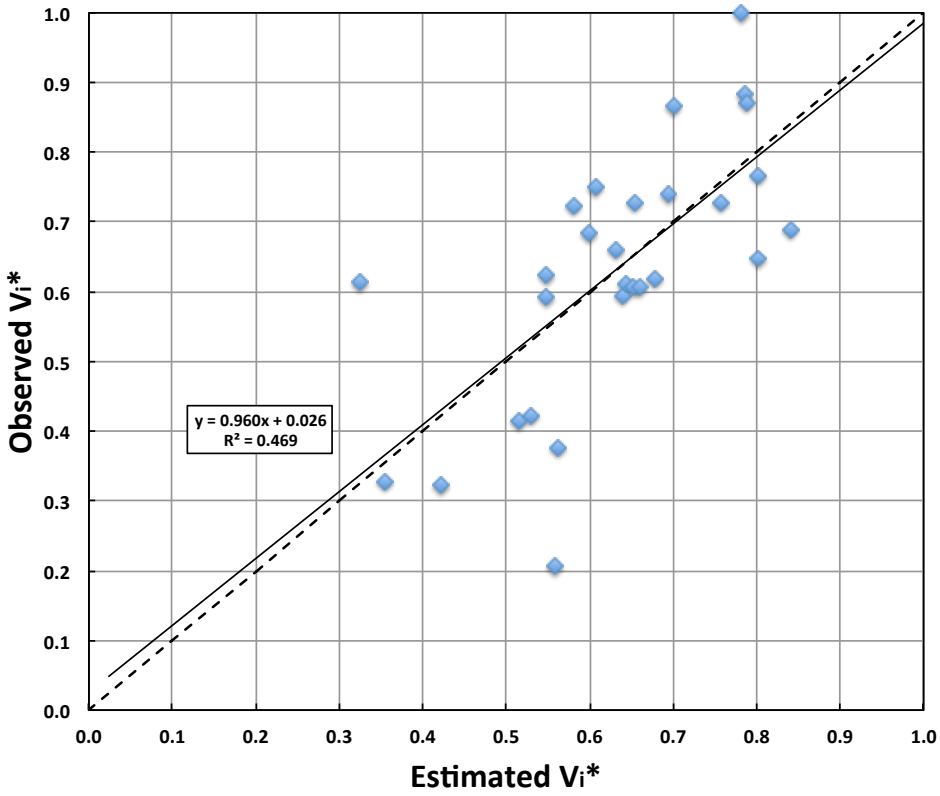

Figure 5.9 Observed infiltration percentage versus estimated infiltration percentage with the log-log regression equation. RMSE= 0.15 (N=28). The solid line represents the log-log regression linear fit and the dashed line the 1:1 ratio of observed versus estimated V_i^*.

4. Discussion

4.1 Analysis of the Experimental Design Parameters

The three different boundary flux rates used (Table 5.1), were based on the correspondent return periods (T) of 1-year, 2-year and 10-year in the Minneapolis-St. Paul metropolitan area, Minnesota, USA (Perica *et al.*, 2013). Additionally, the field tests were designed to investigate the processes that are believed to be the most significant in infiltration and runoff. There are differences in conditions between what could occur during a real storm event and what occurred in the controlled field tests. A list of those differences is given below.

• The rainfall that would be occurring on the side slope in a real event was not

considered in the field tests. The initial soil moisture deficit is overestimated because of the lack of pre-wetting of the soil by rainfall incident directly on the side slope surface. Additionally, the added volume due to direct rainfall could spread the fingers and consequently reduce the concentration of flow on the side slope, increasing the fraction of wetted area over time. This effect would be greater downslope and for high flows. Overall, the direct rainfall would be expected to decrease the volume of road runoff infiltrated.

- The water supply container was placed downslope of the shoulder. However, many shoulders consist of gravel and compacted soil, and some water will infiltrate into the shoulder material. This effect will reduce the actual intensity of flow entering the side slope to a value below the intensities associated with the given event return periods, and will increase the fraction of infiltrated road runoff.
- The initial abstraction of water that would be retained on the surface of the road is not taken into account. Again, this effect will reduce the actual intensity of flow entering the side slope below the intensities associated with the given event return periods and will increase the fraction of infiltrated road runoff.
- Natural decaying organic matter on the side slope surface will absorb some fraction of the direct precipitation and road discharge. The presence of organic matter would decrease the amount of road runoff that reaches the bottom of the filter strip.
- The rainfall intensity over the road surface and runoff from the road was assumed to be constant and to flow directly to the side slope without a lag time (the time of concentration was assumed to be zero). Incorporating a lag time would increase the fraction of infiltrated road runoff.
- The road discharge was imposed as a uniform sheet flow at the location where

it entered the side slope. In the actual field situation it is likely that runoff from the road will not enter uniformly onto the side slope. This will have a variable impact on runoff.

These effects are not being considered because the focus of this research was on infiltration of road runoff into the slope. Based on our results, we believe that this infiltration is a significant portion of the infiltration into most roadside swales.

4.2 Importance of Soil Moisture and K_{sat} Measurements

The soil textures (Table 5.2) of the roadside filter strips soils correspond to hydrologic soils groups (HSGs) A, B and C; however, the K_{sat} values estimated correspond to values close to or above the lower end of HSG A, 3.6 cm/h (NRCS, 2009) with a small variance. Lee, *et al.* (2016) have found that soil texture is a "poor" predictor of infiltration performance. It is particularly interesting that at Hwy 13, with a loam/sandy clay loam soil texture type corresponding to an HGA B/C soil, measured K_{sat} corresponds to a HSG A soil. In the field, it was observed that the clay did not exist as a layer within the soil profile, but was heterogeneously distributed in aggregates, allowing infiltration around the clay. Furthermore, it is important to highlight that after 30 years receiving road runoff these roadside filter strips were not clogged with sediment. The high K_{sat} of the soil was probably high due to the macropores generated by vegetation roots, activity of macrofauna (e.g. earthworms), and roadside construction/maintenance procedures.

The behavior in Figure 5.8, where percentage infiltration rises rapidly at higher soil moisture deficits, is not consistent with a sorptivity-based infiltration model from infiltration theory. That theory shows that as the moisture deficit increases, the infiltration capacity approaches a maximum value asymptotically. Instead, the plot shows the infiltration capacity increasing without apparent bound as the moisture deficit increases. The high soil moisture deficit values occurred in fall 2014, and the percentage infiltration difference between seasons (fall and spring), for the same boundary flux, might be explained by a series of factors related to soil structure, changes in macropores and temperature, and surface

sealing. Each of these factors has been analyzed taking into account the measured and observed characteristics of the sites studied. Soil cracking due to aggregate formation during wet-dry cycles takes place in soils containing high percentage of clay (Beven and German, 1982; Preston *et al.*, 1997). Soils with more than 15% of clay content exhibit aggregate structure (Horn *et al.*, 1994, Jarvis, 2007), however the soils in this study had 5% or less percentage of clay content. In addition, no surface cracks were observed in the field. Freeze-thaw cycles would not explain the observed decreased percentage infiltration during spring since these would likely increase the hydraulic conductivity after winter (Chamberlain and Gow, 1979: Zimmie and LaPlante, 1990). The temperature during the spring tests was higher (an average of 13.5F higher) than in the fall tests. Therefore the viscosity of water was lower in spring, which would result in higher infiltration rates; this effect does not justify the trends seen on Figure 5.8. There are two phenomena that might explain the decrease in infiltration percentage during spring: seasonal changes in roots and surface sealing. During fall with drier weather conditions roots are dying, leaving voids in the soil (Fisher *et al.*, 2015); therefore, infiltration capacity could have been increased (Gish and Jury, 1983; Mitchel *et al.*, 1995; Beven and German, 2013) during the fall tests. On the other hand, during spring, the new fine growing roots can clog soil pores and decrease infiltration capacity (Fisher *et al.*, 2014; Barley, 1954). Finally, the reduction of infiltration capacity after the fall tests may be due to surface sealing (Moore, 1981; Singer and Le Bissonnais, 1998; Gomez and Nearing, 2005). There are two types of rainfall-induced surface seals: structural seals (related to raindrop impact and sudden wetting), and sedimentary seals (result from settling of fine particles carried by runoff). Dense vegetation protects the surface of the swales from structural seals, since raindrop energy is mitigated before impacting the soil surface. However, during the fall experiments the vegetation was cut, and the slope surface was exposed to rain drop impact afterwards, increasing the possibility of surface sealing development.

The lack of a substantial percentage infiltration difference between the medium flux and low flux experiments in the spring implies a change in the soil condition in the latter of the two experiments. There are two hypotheses to explain this outcome. First, the kaolinite particles suspended in the water could have precipitated and clogged soil pores. The latter tests would have started with an initially partially sealed surface, causing the infiltration rates to be lower than in the first experiment. A similar situation was previously observed in filter strip field tests by Deletic and Fletcher (2006) with sediment with a median diameter of 50 µm. However the particle size of 0.5 µm in the present study is likely too small to clog the larger and more influential pores.

Second, an incomplete drainage could have occurred between experiments. Typically, two days of drainage occurred between the tests at each site. On swale side slopes the soil is compacted at a depth of 20-30 cm during construction so that the saturated hydraulic conductivity is significantly smaller than at the surface. Water draining from a given infiltration experiment will be impeded by the lower permeability layers, with an increase soil moisture and thereby increase the wetting front potential (decrease the wetting front suction) at depth. Per infiltration theory, such as with the Green and Ampt model, this will then reduce the infiltration capacity of the soil for subsequent infiltration tests. In the experiments conducted we measured the initial water content of only the surface layer of soil and therefore do not have evidence for this reduction in wetting front suction. Although the saturated hydraulic conductivity would be unchanged, the soil moisture would have needed further characterization at depth due to the two-layer impact on soil moisture content. We believe that the second hypothesis is the more likely explanation for the reduction on infiltration.

4.3 Comparison to Previous Research

The results of this study are best compared with filter strip studies. The differences would be the higher slope of the side slopes in a roadside swale and the attention to the measurement of K_{sat} in this study, without the need for

calibration. Deletic and Fletcher (2006) used synthetic runoff applied upslope of a grass strip that was 5m long, (comparable to the 4 m side slopes considered in this study) with a 7.8% average longitudinal slope, and 0.3 m width. The initial soil moisture content was not measured and the tests were classified as initially wet or dry. A simplified double-ring infiltrometer test was used to get an estimation of the saturated hydraulic conductivity (0.72-3.6 cm/h). However, after calibration to match the measured infiltration at the plot scale, the K_{sat} values were assumed to be in the range of: 3.6-27 cm/h. The range and magnitude of K_{sat} values were greater than the ones observed in the roadside swales of this study (3.47-5.74 cm/h). The boundary fluxes utilized by Deletic and Fletcher were $3.3x10^{-4}$, $6.7x10^{-4}$, and 1 $x10^{-3}m^2/s$, the first being similar to the high flux in this study ($3.1x10^{-4}$ m^2/s), corresponding to a 10-year storm; the other two fluxes were two and three times greater, possibly because they were designed to simulate a more concentrated flow. The runoff coefficients (ROCs) obtained in the cases where the inflow water was mixed with sediment were 0.38 (dry conditions) and 0.67 (wet conditions); these results are lower than the 0.88 ROC values observed in the field experiments presented here for a similar flux. The difference in K_{sat} is the main reason for the dissimilar results obtained.

In the experiments by Liu *et al.* (2016) two newly constructed sloped grassed field scale plots with 17% and 33% slopes, 5m long were studied applying water from an upstream water distributor. The soil moisture content was not reported. K_{sat} values were measured using the constant head method (16.1 and 17.7 cm/h for each slope, respectively). The boundary fluxes applied were $1.3x10^{-4}$and $1.7x10^{-4}$ m^2/s, similar to the medium flux used in this study ($1.55x10^{-4}$ m^2/s). These parameters correspond to a K_s^* in the range of 1.34-1.97, which is approximately 2 to 13 times greater than the K_s^* observed in this study (Figure 5.7). In addition, they found saturated hydraulic conductivity and the ROC had a -0.97 correlation coefficient, which indicates the importance of K_s^*. The average ROC for both side slopes was 0.07, five to nine times lower than the ROC values of 0.37 (fall) and 0.6 (spring) observed in the field tests presented in this study.

These results are not surprising since the K_{sat} values estimated by Liu *et al.* were approximately three times greater than the ones estimated in the highways studied in this research.

In contrast to the other studies presented using synthetic runoff, the field tests reported in this study show the response to a wide range of boundary fluxes, including both high and low flows, representing typical intensities for which roadside filter strips in swales are designed and utilized to improve surface water quality. Measurement of the initial soil moisture has been found to be important to compare the soil's infiltration performance. In addition, the percentage of wetted area was estimated in all tests, providing information about flow concentration in grassed roadside swales under different runoff fluxes. Furthermore, measuring K_{sat} in the field is essential since the soil texture is not a good proxy (Lee *et al.*, 2016). Multiple measurements of K_{sat} are necessary due to its spatial variability (Asleson *et al.*, 2009; Olson *et al.*, 2013; Ahmed *et al.*, 2015); and 10 measurements per site were taken in these field tests. Finally, these experiments were performed in roadside swales that are 30-50 years-old, therefore the infiltration capacity estimated corresponds to the long-term infiltration of these stormwater control measures.

5. Conclusions

A total of thirty-two tests were performed during three seasons on four different highways located in the Minneapolis-St. Paul metropolitan area, Minnesota, USA to analyze the infiltration performance of roadside filter strips and the effect of fractional coverage of water on infiltration. This study assists the evaluation of vegetated roadside filter strips located on the side slope of swales as stormwater control measures. The channel portion of a roadside swale has typically been the main element believed to control and reduce stormwater runoff, however the side slope shows great potential for runoff infiltration.

All the tests indicated that water flow on the lateral slope of a roadside swale is

concentrated in fingers, instead of sheet flow, at the typical rainfall/runoff intensities for which infiltration practices are utilized to improve surface water quality. The minimum fraction wetted detected was 54% and maximum 88%, with an average of 72% and standard deviation of 9%. A linear relationship between flux of water from the road and fraction wetted was observed, for the intensities tested. Due to the maintenance procedures followed by the Minnesota Department of Transportation, the surface of the side slopes was relatively smooth with no prominent topographical features or signs of erosion; this was supported by low random roughness (RR) measurements.

Despite the initial compaction during construction, the saturated hydraulic conductivity of the swales soil was high, relative to the values typical of laboratory permeameter measurements for the type of soil. This is believed to be due to the macropores generated by vegetation roots, activity of macrofauna (e.g. earthworms), and construction/maintenance procedures. An average of 1.9 cm of runoff from a typical two-lane highway was infiltrated during the experiments, indicating a high potential for side slope infiltration in these swales.

The trend was to have more infiltration when the saturated hydraulic conductivity was higher and for a greater side slope length, as expected. The vegetation cover, type of soil and length of the side slope would be important to consider for constructing roadside swales that will be efficient in stormwater management. The volume infiltrated during spring for the same intensity (medium flux) was on average 12% lower than in fall due to the larger initial soil moisture content in the spring. Finally, a log-log regression equation has been developed that relates percentage of water influx infiltrated with a dimensionless saturated hydraulic conductivity parameter (K_s^*) and soil moisture deficit. This equation can provide an estimate of percentage infiltration in the side slopes of roadside swales, which is often the most important means of infiltration because of their area relative to the channel of the swales.

Acknowledgments

The writers are grateful to the Minnesota Department of Transportation and Minnesota Local Road Research Board for funding this research under Contract No. 99008- 97, with Barbara Loida as Technical Liaison. We also thank David Liddell for his help on the field experiments. J.L. Nieber's effort on this project was partially supported by the USDA National Institute of Food and Agriculture, Hatch/Multistate project 12-059.

Chapter 6

Non-Uniform Overland Flow-Infiltration Model for Roadside Swales

Summary

There is a need to quantify the hydrologic performance of vegetated roadside swales (drainage ditches) as stormwater control measures (SCMs). To quantify their infiltration performance in both the side slope and the channel of the swale, a model has been developed for coupling a Green-Ampt-Mein-Larson (GAML) infiltration submodel with kinematic wave submodels for both overland flow down the side slope and open channel flow for flow in the ditch. The coupled GAML submodel and overland flow submodel has been validated using data collected in twelve simulated runoff tests in three different highways located in the Minneapolis-St. Paul metropolitan area, MN.

The percentage of the total water infiltrated into the side slope is considerably greater than into the channel. Thus, the side slope of a roadside swale is the main component contributing to the loss of runoff by infiltration and the channel primarily conveys the water that runs off the side slope, for the typical design found in highways. Finally, as demonstrated in field observations and the model, the fraction of the runoff/rainfall infiltrated (V_i^*) into the roadside swale appears to increase with a dimensionless saturated hydraulic conductivity (K_s^*), which is a function of the saturated hydraulic conductivity, rainfall intensity, and dimensions of the swale and contributing road surface. For design purposes, the relationship between V_i^* and K_s^* can provide a rough estimate of the fraction of runoff/rainfall infiltrated with the few essential parameters that appear to dominate the results.

1. Introduction

Non-point source pollution in urban watersheds is an important cause of surface water quality degradation (Novotny and Olem, 1994). High levels of pollutants, including suspended solids, toxic metals, and nutrients, are present in stormwater runoff from highway pavements (Asplund *et al.,* 1980; Wu *et al.,* 1998; Barrett *et al.,* 1998a, Kayhanian *et al.*, 2012). To mitigate the environmental impacts of highway runoff, state departments of transportation and other public agencies have been required to put in place stormwater control measures (Han *et al.,* 2005), also called best management practices.

Grassed roadside drainage ditches are a common feature of highways. For example, there are approximately 0.9 million hectares of grassland in the right-of-way (ROW) of the National Highway System (NHS) in the United States (USDOT-FHWA, 2010). Properly maintained, grassed roadside drainage ditches act as swales with a filter strip over the side slope and a grassed channel because they convey and treat water by sedimentation and filtration of solid particles (sediment-bound nutrients), and infiltrate stormwater and dissolved pollutants (Abida and Sabourin, 2006). Grassed roadside swales receive road runoff directly and water is infiltrated over the swale side slope, perpendicular to the road (Figure 6.1). Water that runs off the side slopes then has a further opportunity to infiltrate as it flows down the length of the channel parallel to the roadway.

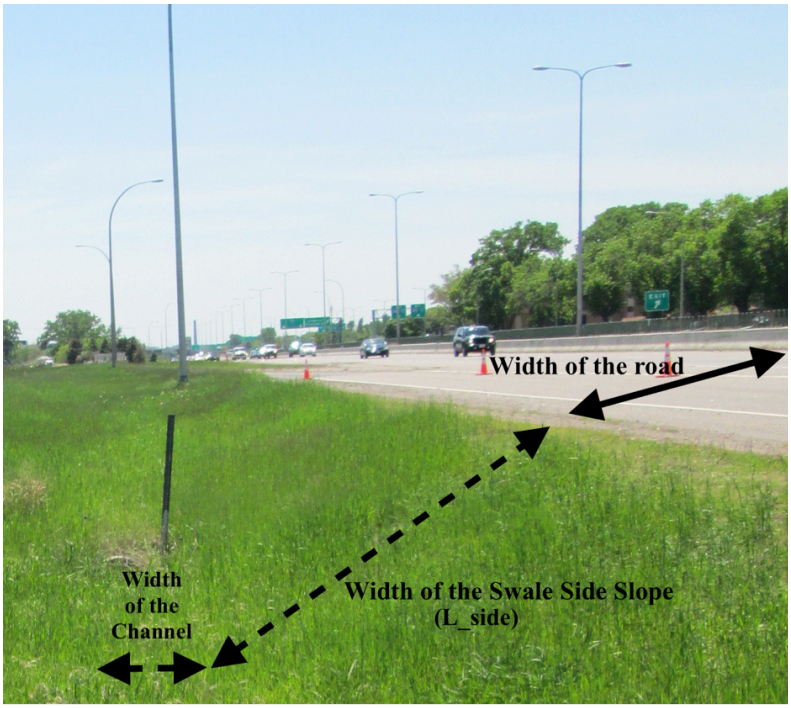

Figure 6.1 Roadside Swale on Hwy 77 in Richfield, MN.

Most of the prior interest in modeling roadside swales has been on the channel portion, not the side slope (Fassman and Liao, 2009; Grinden, 2014). However, in most roadside grassed swales the side slope is an important component when calculating the volume reduction. According to Barrett et *al.* (1998b), as long as the road runoff is allowed to flow directly down the side slope into the swale, the side slope acts as a filter strip (Figure 6.1); in addition, the infiltration performance increases with the cumulative length of infiltrating surface (Caltrans, 2003). Most vegetated filter strip (VFS) models have focused on the sediment removal efficiency in agricultural field applications (Hayes *et al.*, 1984; Muñoz-Carpena *et al.*, 1999; Helmers *et al.*, 2005). The design characteristics of the filter strip in roadside swales and water application conditions differ from agricultural settings. First, the characteristics of the catchment or drainage area discharging to the filter are different in agricultural filter strips. Typically, the filter strip to contributing area ratio is smaller in agricultural fields than in roadside filter strips; furthermore, the area draining to the roadside is impervious. The flow entering

the filter strip from an agricultural field is not uniform and does not spread over the whole width of the filter, instead substantial concentration of flow occurs (Dosskey *et al.*, 2002). In roadside swales the water coming from the road is more uniform and can often be assumed as sheet flow. If the flow rate is low enough the overland flow transitions into fingers of flow on the swale side slope (Garcia-Serrana *et al.* 2017). Second, the design characteristics of agricultural filter strips differ from roadside swale side slopes in slope, width, and construction process. Agricultural filter strips have 1-4% slopes whereas roadside side slopes have 17-25% slopes and their width is generally shorter, constrained by the width of right-of-way. In addition, the construction and maintenance procedure of roadside swales is consistent; the slopes are smooth with uniform vegetation type and height, undergoing routine maintenance.

The return periods tested for validation of existing filter strip models are based on erosion control scenarios due to the interest in sediment trapping performance. Usually a 10-year storm return period event is selected (Larson *et al.* 1997; Haan *et al.*, 1994). However, concerns about water quality impairments are usually associated with lesser events than the 10-year storm, in general smaller than the two-year storm. Flow rates associated with these events are smaller, and flow depths are shallower. Infiltration is more significant under these conditions, and the estimation of soil hydraulic parameters becomes essential to successfully validate the model results.

While there has been extensive research on the sedimentation achieved by vegetated filter strips (Hayes *et al.*, 1984; Muñoz-Carpena *et al.*, 1993; Deletic *et al.*, 2001), relatively little research has been conducted on the modeling of the infiltration performance of roadside grassed swales. In 1999, Muñoz-Carpena *et al.* (1999) presented VFSMOD, a single event model for simulating the hydrology and sediment filtration in buffer strips. This model has been validated mainly for sediment trapping efficiency; some predictions of infiltration-runoff volumes with uncalibrated parameters did not satisfactorily simulate the field-measured values (Han *et al.*, 2005; Poletika *et al.*, 2009). Abu-Zreig *et al.* (2001) tested and

validated VFSMOD under high runoff boundary flux conditions (2.5 $x10^{-4}$, 5.4 $x10^{-4}$, and 8.3 $x10^{-4}$ m^2/s). However, to validate the infiltrated volume simulated by the model, the saturated hydraulic conductivity was estimated from the observed inflow and outflow rates in the experiments. Deletic (2001) created TRAVA, a mathematical model of sediment transport in runoff over grass filters. Only the sediment submodel was verified with laboratory and field experiments (Deletic, 2005; Deletic *et al.*, 2006). The runoff submodel of TRAVA was calibrated (adjusting saturated hydraulic conductivity, initial soil moisture content, and Manning's n) to simulate the water runoff rates measured in the field.

The flows tested for validation in previous models were relatively high, with sheet flow predominant, compared to the flows typically observed to occur in roadside swales, and the characteristics of the land surface (slope and width) in most cases were representative of agricultural filter strips. There is a need for testing overland-infiltration models for roadside swale side slopes using Green-Ampt parameters measured in the field with infiltration devices. Previous models have focused on modeling either agricultural filter strips or in the case of swales only the channel portion of the swale. In addition, these models have simulated the flow of runoff water generated on impervious areas as sheet flow over the pervious areas. The model reported in the present study simulates a coupled filter strip and channel, the two components of a roadside swale, and takes into account the fractionally wetted surface occurring over the side slope. Furthermore, the necessity of a calibration for the infiltration parameters is evaluated by using field infiltration measurements in the swales and comparing the results obtained by the model without calibration.

The main objective of this paper is to determine whether the kinematic wave submodel incorporating fractional wetted surface on the side slope and a Green-Ampt-Mein-Larson (GAML) infiltration submodel are sufficient to model the observed roadside swale results from the field; in essence testing whether the fractional wetted surface is an important hydrologic phenomenon in the process of overland flow on slopes. More specific goals are as follows:

(1) to develop a coupled overland flow-infiltration model for roadside swale side slopes that accounts for fractional wetted surface on the side slope and couple it with a channel model,
(2) to validate the accuracy of the side slope model and the measured infiltration parameters with monitored field data generated using simulated runoff tests,
(3) to evaluate the infiltration performance of the side slope and channel of a roadside swale, and,
(4) to further assess the sensitivity of volume reduction to the hydraulic properties of roadside swales.

2. Description of the mathematical model

To simulate the hydrology of a vegetated roadside swale, the flow over and infiltration into the two land surface components involved in the process, need to be coupled. Those two land surface components are the swale side slope filter strip and the flat bottomed open channel at the base of the slope. Two main submodels, used in both components, are free surface flow and infiltration. These submodels are linked together to develop a one-dimensional field-scale model for single storm events. The presented model includes the option of routing the road runoff over only a fraction of the side slope surface, instead of assuming sheet flow. The Green-Ampt-Mein-Larson (Green and Ampt, 1911; Mein and Larson, 1973) assumptions were implemented to calculate infiltration along with a kinematic wave model for overland flow that accounts for concentration of flow. The model has been established in the MATLAB programming language and allows for a wide range of user inputs such as: rainfall intensity, initial moisture content of the soil, saturated hydraulic conductivity, wetting-front suction of the soil, and the geometry of the side slope.

2.1 Overland Flow

Lighthill and Whitham (1955) developed an approximation of the Saint-Venant's

equations to model overland flow in 1-D, the kinematic wave approximation. The equation is based on the assumptions that the acceleration term and the pressure gradient term in the momentum equation are negligible, so that the slope of the energy grade line is equal to the slope of the overland flow plane or the channel. For shallow overland flow, neglecting the velocity and pressure head gradients in the momentum equation is an adequate approximation (Woolhiser and Liggett, 1967; Singh, 2001; Singh, 2002). The kinematic wave equation is a first-order hyperbolic partial differential equation (continuity equation):

$$\frac{\partial A}{\partial t} + \frac{\partial Q}{\partial x} = i_e b \quad (1)$$

where A is the wetted cross section for plane flow (A [m^2]=h [m]*b [m]); h is the mean depth of flow [m]; b is the lateral extent of the flow [m]; Q is the discharge [m^3/s]; i_e is the rainfall excess [m/s] (that which does not infiltrate); t is time [s]; and x is the downslope distance [m].

Garcia-Serrana *et al.*, (2017) observed that water flow on the lateral slope of a roadside swale is concentrated in fingers, instead of sheet flow. When there is shallow concentrated flow, the width of the flowing water depends on the fraction of the area that is wetted (fw [-]). That fraction wetted changes with time and space, until it reaches steady state and it becomes only a function of space ($fw(x)$). In this model we have assumed that the fraction wetted is steady, and the lateral extent of the channel is:

$$b = fw * w \quad (2)$$

where w is the lateral extent of the study area [m] (channel or slope) and b the total lateral extent of the wetted surface calculated as the sum of the width of individual fingers of wetted surface.

If we substitute $A = b*h$ and $Q = q$ [m^2/s]$* b$ in equation (1):

$$\frac{\partial b*h}{\partial t} + \frac{\partial q*b}{\partial x} = i_e b \tag{3}$$

Dividing by b and recognizing that b is independent of time:

$$\frac{\partial h}{\partial t} + \frac{1}{b}\frac{\partial q*b}{\partial x} = i_e \tag{4}$$

Substituting Eq. (2) into Eq. (4):

$$\frac{\partial h}{\partial t} + \frac{1}{fw}\frac{\partial q*fw}{\partial x} = i_e \tag{5}$$

In this model, Manning's equation, suitable for fully rough, turbulent flows, is used to relate q and h assuming the energy gradeline slope is equal to the bottom slope and with a depression storage term:

$$q = \frac{1}{n}\sqrt{S_o}(h - d_s)^{\frac{5}{3}} \tag{6}$$

where S_0 is the slope of the bottom surface [m/m], n is Manning's roughness coefficient [s/m$^{1/3}$], and d_s is the depression storage [m].

An explicit numerical scheme with forward differences for time and space has been used to obtain the non-iterative numerical solution of Eq. (5). The initial and boundary conditions can be summarized as:

- Initial condition for the side slope ($t = 0$):

  $h = 0$, $0 \le x \le L$; where L [m] is the width of the side slope perpendicular to the road.

- The upstream boundary is the specified influx from the road:

  $q_{in} = q_0$ [m^2/s] at $x = 0$; $t > 0$

where q_0 is the runoff flux from the road per unit longitudinal length of the road.

Therefore, the i_e of the first cell is equal to: $q_0/\Delta x + i_r - f$; where i_r is the rainfall intensity, and f [m/s] is the infiltration rate. For the remaining cells the i_e is equal to: $i_r - f$.

When the Froude Number ($Fr = \frac{v}{\sqrt{gh}}$, where v is the flow velocity [m/s] and g the acceleration of gravity [m/s^2]) is less than 2, kinematic waves dominate and dynamic wave fronts dissipate rapidly (Lighthill and Whitham, 1955). All of the Froude numbers computed herein were lower than 2. Additionally, Woolhiser and Liggett (1967) showed that the dynamic component can be neglected if $k = \frac{S_0 L}{hFr^2} > 10$. This condition was met too.

2.2 Infiltration

The infiltration model, which is coupled to the overland flow model, is based on the Mein and Larson (1973) modification of the Green and Ampt (1911) method to account for the time to surface ponding. This model was selected due to its simplicity and robustness (Fiedler and Ramirez, 2000; Esteves *et al.*, 2000) and the convenient estimation of the necessary input data from physical soil characteristics (Kale and Sahoo, 2011). To model unsteady rainfall, we utilized Chu's (1978) adaptation of the Mein and Larson algorithm:

$$F(t) - F(t-\Delta t) = \Delta F = \xi ln(\frac{F(t)+\xi}{F(t-\Delta t)+\xi}) + K_{sat}\Delta t = \xi ln(1 + \frac{\Delta F}{F(t-\Delta t)+\xi}) + K_{sat}\Delta t \quad (7)$$

where F is the infiltration depth [m]; K_{sat} is the field-measured saturated hydraulic conductivity [m/s]; $\xi = \psi_f(\theta_s - \theta_i)$, ψ_f is the soil matric suction head at the wetting front [m], and θ_s, θ_i are the saturated and initial soil moisture content [-], respectively.

To compute actual infiltration rate (f), infiltration depth over one time step (ΔF) is compared to the available water depth (ΔF_P) that can potentially be infiltrated. There are two conditions to calculate infiltration rate:

- If $\Delta F_P = (q_{in}/\Delta x + i_r)\ \Delta t < \Delta F$ then:

$$f = \frac{q_{in}}{\Delta x} + i_r \text{ and } F(t) = F(t - \Delta t) + \Delta F_P \quad (8)$$

where q_{in} is the discharge per unit width entering the cell [m^2/s], Δx is the length of the cell [m], and i_r is the rainfall intensity [m/s].

- If $\Delta F_P = (q_{in}/\Delta x + i_r)\,\Delta t > \Delta F$ then:

$$f = K_{sat}\frac{\xi + F}{F} \text{ (Green Ampt equation) and } F(t) = F(t - \Delta t) + \Delta F \quad (9)$$

When $h \leq d_s$ and there is still ponded water i.e. $h > 0$, the ponded water will infiltrate and the two conditions to calculate infiltration rate would be:

- If $\Delta F_P = h < \Delta F$ then:

$$f = h/\Delta t \text{ and } F(t) = F(t - \Delta t) + \Delta F_P \quad (10)$$

- If $\Delta F_P = h > \Delta F$ then:

$$f = K_{sat}\frac{\xi + F}{F} \text{ (Green-Ampt equation) and } F(t) = F(t - \Delta t) + \Delta F \quad (11)$$

2.3 Numerical Solution

The model flow chart is presented in Figure 6.2. The model equations were discretized and solved using an explicit scheme for the overland flow submodule. The infiltration submodule based on the Green-Ampt equation was solved with a fully implicit scheme. The infiltration submodel Eq. (7) was solved using the Li *et al.* (1976) simple two-step method to estimate infiltration depth after surface saturation for a Green-Ampt profile. The first step calculates ΔF using a truncated series expansion:

$$\Delta F_0 = \frac{1}{2}\left[K_{sat}\Delta t - 2F + \sqrt{K_{sat}\,\Delta t(K_{sat}\,\Delta t + 4F + 8\xi) + 4F^2}\,\right] \quad (12)$$

where ΔF_0 is the initial estimate of the increment of infiltration depth during the time increment.

The second step uses a second-order Newton method to determine ΔF, the infiltration depth within the time increment.

$$\Delta F = -F - \frac{(F+\Delta F_0)^2}{\xi} + \left(\frac{F+\xi+\Delta F_0}{\xi}\right)\sqrt{(F+\Delta F_0)^2 + 2\xi\left(\xi ln\left(1+\frac{\Delta F_0}{F+\xi}\right) + K_{sat}\,\Delta t - \Delta F_0\right)} \quad 13)$$

For the overland flow submodel, the forward differences representation of a finite difference method over time (*k*) and space (*j*) was used to solve Eq. (5):

$$\frac{\partial h}{\partial t} = \frac{h_k^{j+1} - h_k^j}{\Delta t} \tag{14}$$

$$\frac{1}{fw}\frac{\partial q * fw}{\partial x} = \frac{q_k^j * \frac{fw_k + fw_{k+1}}{2} - q_{k-1}^j * \frac{fw_k + fw_{k-1}}{2}}{\Delta x\, fw_k} \tag{15}$$

Additionally, the rainfall excess has been averaged between time steps:

$$ie = \left(ie_k^j + ie_k^{j+1}\right)/2 \tag{16}$$

Then, an explicit numerical scheme is used to obtain the numerical solution of the first-order partial differential equation:

$$\frac{h_k^{j+1} - h_k^j}{\Delta t} + \frac{q_k^j * \frac{fw_k + fw_{k+1}}{2} - q_{k-1}^j * \frac{fw_k + fw_{k-1}}{2}}{\Delta x\, fw_k} = \left(ie_k^j + ie_k^{j+1}\right)/2 \tag{17}$$

Once the water depth (h_k^{j+1}) is calculated, the discharge (q_k^{j+1}) is determined using Eq. (6) with the condition that water depth must be greater than the depression storage to have discharge from a cell.

Explicit numerical algorithms require the Courant number, *Cr* [-], to have a value less than 1 for numerical stability:

$$C_r = C_k \frac{\Delta t}{\Delta x} < 1 \tag{18}$$

$$C_k = amh^{m-1} \tag{19}$$

where C_k [m/s] is the kinematic wave speed. In this case, based on Manning's equation, $a = \frac{1}{n}\sqrt{S_0}$ and m = 5/3. The maximum Courant number was calculated

at the end of the workflow, reducing the time step (Δt), if necessary, to satisfy the Cr<1 condition for the whole simulation.

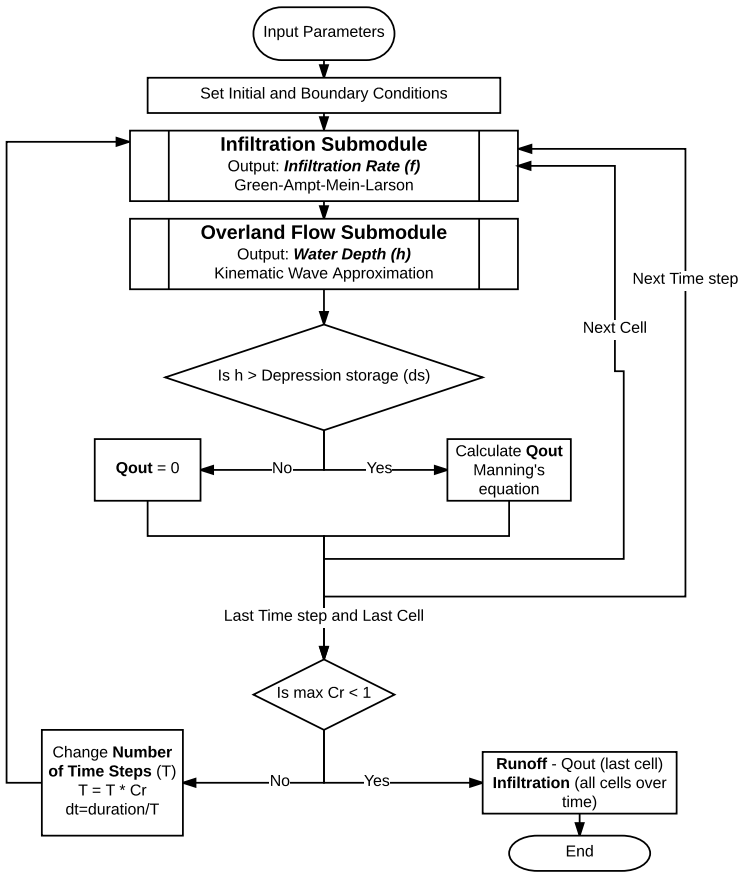

Figure 6.2 Flow chart of the infiltration-overland flow model for the swale side slope.

2.4 Input Parameters

The input parameters of the side slope model are presented in Table 6.1:

Table 6.1 Side slope model input parameters

Feature	Parameter	Symbol	Units	Values used for Validation
Rainfall	Rainfall Intensity	i	[L/T]	2.8 / 5.6 / 11.2 cm/h
	Duration of Storm Event	$duration\_storm$	[T]	0.25/ 0.5 /1 h
Soil	Effective Wetting Front Suction	ψ	[L]	Different by location. Range [1.8 – 6.4] cm
	Soil Moisture Deficit	$\Delta\theta=\theta_s-\theta_i$	[-]	Different by test. Range [0.15 - 0.45]
	Saturated Hydraulic Conductivity	K_{sat}	[L/T]	See Table 6.2
Flow	Fraction Wetted	fw	[-]	Different by test. Range [0.54 – 0.88]
	Manning's n	n	$[T/L^{1/3}]$	0.25 $s/m^{1/3}$
	Width of the road perpendicular to traffic	w_{road}	[L]	10 m
Swale	Width of the Side Slope	L_{side}	[L]	See Table 6.2, Figure 6.1
	Lateral Extent of the Side Slope (or length of the channel connected to filter strip)	w_{side}	[L]	0.914 m
	Slope	S	[-]	See Table 6.2
	Depression Storage	d_s	[L]	1mm
Model	Total Time Simulated	$duration$	[T]	1.6 h
	Number of sections down slope	$rows$	[-]	101
	Number of Time Steps	T	[-]	10,000

2.5 Coupled Side Slope Model

To model both the runoff water from the road that is routed to only a fraction of the slope (*fw*) and the rainfall over both the concentrated flow area (*fw*) and non-concentrated flow area (*1- fw*), the side slope is divided into two parallel sections (Figure 6.3):

i. **Side slope where road runoff is routed**: this submodel calculates the runoff from the side slope applying a "fraction wetted" parameter, *fw*, that simulates the concentration of the road runoff into a fraction of the surface. The submodel receives the water from the road as an upslope boundary condition, and applied rainfall onto the area: (*Area of side slope) * fw*.

ii. **Side slope without road runoff**: this submodel calculates the runoff from the remaining part of the side slope that does not receive runoff from the road. This submodel only receives direct rainfall, not road discharge, over: (*Area of side slope) * (1-fw).* Runoff is generated from this submodel only if rainfall intensity exceeds infiltration capacity.

The result of coupling these two submodels is discharge from the side slope of the swale and volume of water infiltrated over time.

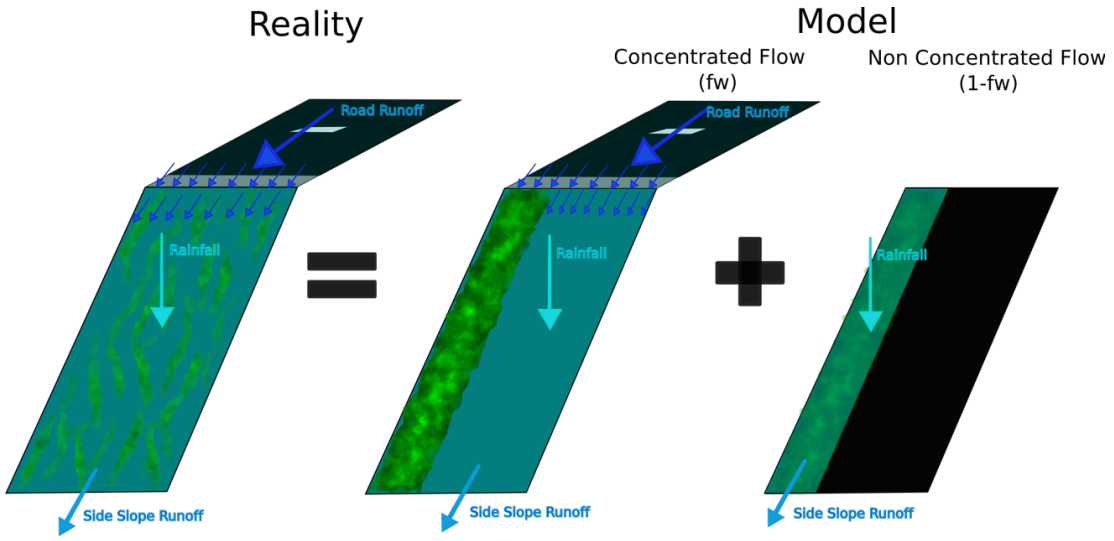

Figure 6.3 Layout of reality (left) versus modeled side slopes (right). In order to simulate reality, the model combines two modules or concentrated flow from the road and rainfall over the area where water from the road does not concentrate.

2.6 Roadside Swale Model

In a roadside swale, the runoff from the side slope enters a channel and the discharge of the system is the runoff from the channel section. A model of the

swale channel has been developed, representing a rectangular channel and accounting for rain falling over its entire surface with the additional input of water coming from the side slopes (Figure 6.4). The model has independent temporal loops for each submodule (side slope and channel). The groundwater level is assumed to be low in the channel section. The model is based on the same overland flow and infiltration submodels described in Sections 2.1, 2.2, and 2.4 with the following differences:

- Initial and boundary conditions:
    - At $t = 0$: $h = 0$, $0 \leq x \leq L_{\text{channel}}$; where $L_{channel}$ is the length of the channel
    - At $x = 0$ (k=1, first cell) the boundary condition is no-flow; there is no upstream flow coming into the system.
- The effective intensity applied on the channel cells is calculated using three terms: 1) water coming from the last cell of the side slope normalized over the surface of the channel cell ($\frac{Q_{side}}{B\, w_{side}}$); 2) rainfall intensity (i_r); and 3) infiltration rate (f). Therefore, i_e of all the channel cells is equal to: ($\frac{Q_{side}}{B\, w_{side}}$) + i_r - f; where Q_{side} is the discharge coming from the side slope, B is the width of the channel, and w_{side} is the width of the side slope cell.
- Finally, the fraction wetted in the channel is 1.

The coupled model (Figure 6.4 and 6.5) consists of a combination of the side slopes and channel of the drainage ditch. The final volume infiltrated is the result of adding the volume infiltrated on the side slope and the channel, over the system length, $L_{channel}$. The model code is presented in Appendix A.

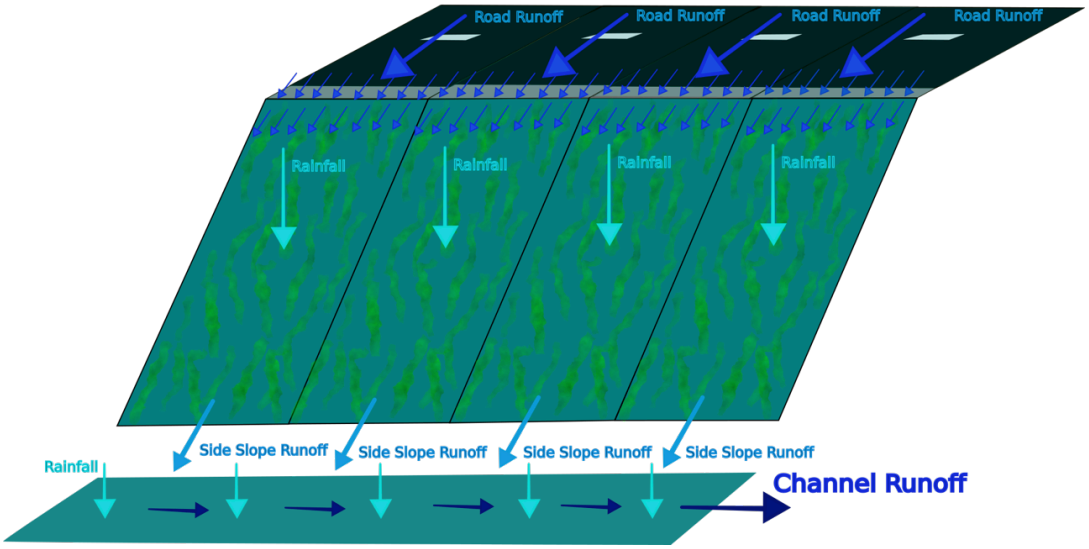

Figure 6.4 Layout of the coupled model: side slope and channel.

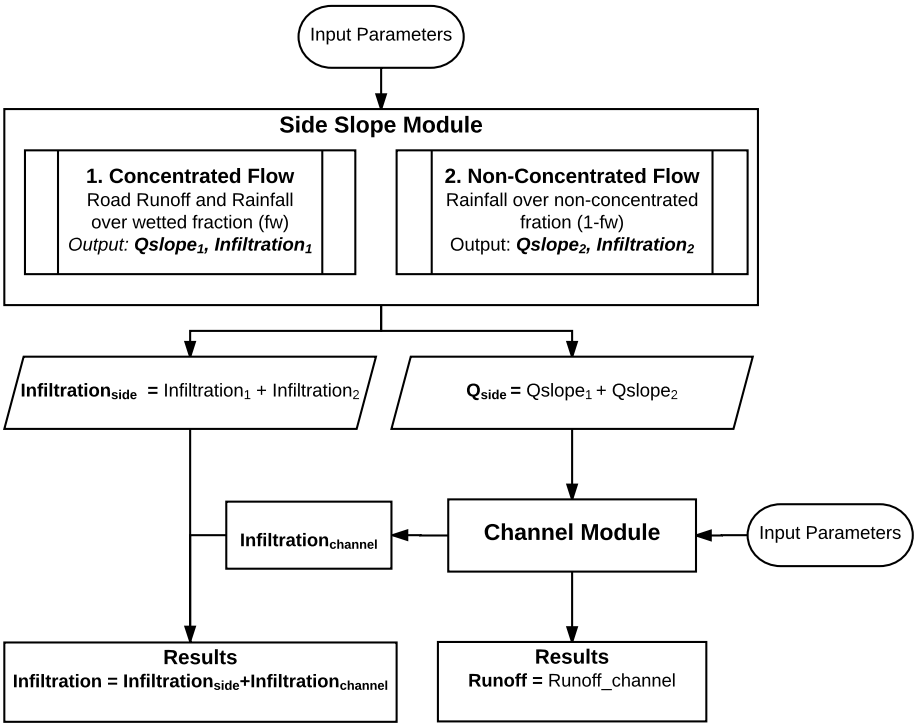

Figure 6.5 Flow chart of the infiltration-overland flow model for the coupled side slope and channel of the swale.

3. Results

3.1 Validation of the model

The side slope model of a vegetated swale has been tested using the data collected in twenty-four simulated runoff tests in three different highways (Hwy 51, 77, 13) located in the Minneapolis-St. Paul metropolitan area, MN (Garcia-Serrana *et al.*, 2016, 2017). These tests were performed during two seasons (spring and summer), using three different application rates, and testing two sites per highway. The predicted infiltration loss on the side slope and runoff rate using the parameterized coupled infiltration-overland flow model has been compared with the actual infiltration loss and runoff rate determined from the monitored field tests. In this manner, the accuracy of the model can be estimated. The flow over the channel of the roadside swale was not evaluated in the field tests.

The road runoff tests that have been simulated with the model used three different application rates or boundary fluxes: low (7.76×10^{-5} m^2/s), medium (1.55×10^{-4} m^2/s), and high flux (3.10×10^{-4} m^2/s); these rates are equivalent to a uniform rainfall intensity of 2.8 cm/h, 5.6 cm/h, and 11.2 cm/h over a 10 m wide road and shoulder, assumed typical for a road with 2 lanes. A total volume of 255 L of water was applied, for all experiments (for a duration of 60 minutes for low, 30 minutes for medium, and 15 minutes for high), to a strip width of 0.9 m at the top of the slope along the edge of the shoulder of the road. The total volume of water that was not infiltrated (runoff) was collected from a clay lined trench dug at the bottom of the side slope connected to a receiving bucket. The runoff rate when the system reached steady state was recorded for all the tests. For Hwy 13, measurements of runoff over time were taken for the three application rates for the two sites (Figure 6.7). For Hwy 77, measurements of runoff over time were taken for two (low and medium flux) of the three application rates. For Hwy 51, the only data recorded was the runoff rate when the system reached steady state. The Green-Ampt (1911) parameters, saturated hydraulic conductivity (K_{sat})

(Table 6.2) and wetting-front suction (ψ) (Table 6.1) in the upper 25 cm were estimated at the end of the field tests using the MPD infiltrometer method (Asleson *et al.*, 2009; Olson *et al.*, 2013; Ahmed *et al.*, 2014; Ahmed *et al.*, 2015). For this, twenty measurements of falling head were taken per highway and utilized in the MPD spreadsheet to compute the saturated hydraulic conductivity and the capillary suction of the soil ahead of the wetting front. The representative field-scale saturated hydraulic conductivity for infiltration given in Table 6.2 is computed as:

$$K_{sat} = \beta\ K_{sat\ Arithmean} + (1-\beta)\ K_{sat\ Geomean} \quad (20)$$

where $\beta = 0.32$ (Weiss and Gulliver, 2015), and $K_{sat\ Arithmean}$ and $K_{sat\ Geomean}$ are the arithmetic and geometric mean values, respectively. The parameters used in the model (Table 6.1 and 6.2) were estimated and measured in the field by Garcia-Serrana, *et al.* (2017) (Chapter 5); there was no calibration of any of the values. In this manner, the validity of the model as well as the associated soil hydraulic and surface geometry parameters has been evaluated. The field tests were used to validate the most important functions of the model, e.g. runoff and infiltration from road runoff onto the side slope. Although the rainfall over the side slope was not incorporated in the field tests as described earlier, the model has the capacity to simulate rainfall over the side slope and channel.

Table 6.2 Characteristics of the swales studied based on soil cores samples, estimations of saturated hydraulic conductivity (at 20ºC) from the MPD measurements and range of values measured in the field in brackets, and width (perpendicular to the road) and slope of the sections used in the field experiments.

	K_{sat} (cm/h)	Porosity (%)	Slope	Width studied (cm)
Hwy 51	3.54 [0.5-33.2]	0.56	20%	406
Hwy 77	5.74 [0.5-26.8]	0.56	20%	407
Hwy 13	4.14 [0.4-53.1]	0.58	25%	422

The sequence of the tests and saturated hydraulic conductivity measurements is important to understand the results obtained from the simulations. The first tests were performed in Fall 2014 (all at medium flux). During the spring and summer of 2015, three tests were performed in the following order: medium flux, low flux, and finally high flux tests. Each test was performed on different days, with a time separation between tests of three to seven days. The Green-Ampt parameters were estimated using the MPD measurements one to two days after the last test (high flux).

A summary of the predicted and observed values of percentage infiltration (volume infiltrated over total input volume), total volume of runoff and runoff rate at steady state for the twelve tests using low and high fluxes is presented in Table 6.3, in addition to some of the measured parameters used for validation (K_{sat}, $\Delta\theta$, and fw). The saturated hydraulic conductivity, as well as the other nine model parameters, were not calibrated. The percentage infiltration (with respect to the total volume input in the system) measured in the low and high flux tests (N=12) are compared with the predictions from the model (Figure 6.6).

Statistics of the goodness-of-fit obtained for all the tests in Table 6.3 combined are summarized in Table 6.4. These statistical values indicate a good match between the runoff rates, total runoff volume and infiltration losses estimated by the model and the field measurements in the field.

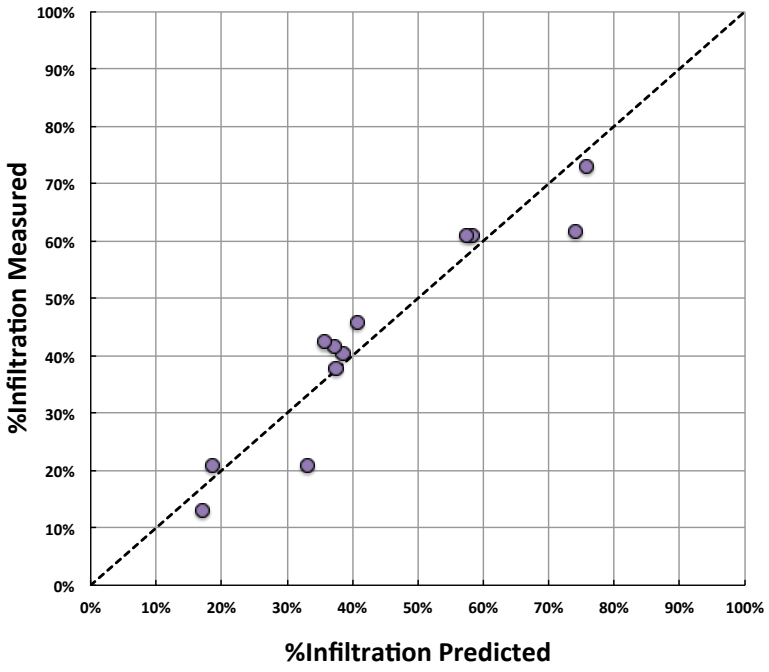

Figure 6.6 Percentage of infiltration measured versus predicted by the combined infiltration-overland flow model of the side slope of a swale for the low and high flux tests. The line represents the area where predicted equals measured percentage infiltration.N=12.

Table 6.3 Field testing of the model for three highways, two sites per highway, and two application fluxes (low and high). The predicted and observed values of runoff rate at steady state (Q_{out}), total runoff volume and percentage of the total volume infiltrated are presented.

Hwy	Site	Q_{in} [L/min]	K_{sat} [cm/h]	$\Delta\theta$	fw	Q_{out} [L/min]			Runoff Volume [L]			% Infiltration		
						Pred.	*Obs.*	*%Error*	*Pred.*	*Obs.*	*% Error*	*Pred.*	*Obs.*	*%Diff.*
13	1	4.3	4.14	0.266	0.58	2.3	2.82	-18%	106.8	100	7%	58%	61%	-3%
	2	4.3	4.14	0.271	0.57	2.43	2.8	-13%	108.9	100	9%	57%	61%	-3%
	1	17	4.14	0.313	0.85	13.1	13	1%	160.2	149	8%	37%	42%	-4%
	2	17	4.14	0.325	0.80	13.4	13.2	2%	164.4	147	12%	36%	42%	-7%
51	1	4.3	3.54	0.172	0.67	2.9	3	-3%	157.1	152.4	3%	39%	40%	-2%
	2	4.3	3.54	0.226	0.77	2.65	3.1	-15%	83.2	76	9%	41%	46%	-5%
	1	17	3.54	0.198	0.79	15.1	16.5	-8%	208.1	202	3%	19%	21%	-2%
	2	17	3.54	0.145	0.90	14.82	16.25	-9%	211.5	222	-5%	17%	13%	4%
77	1	4.3	5.74	0.347	0.67	2.62	2.5	5%	66.4	98	-32%	74%	62%	12%
	2	4.3	5.74	0.297	0.66	2.61	2.5	4%	61.8	69	-10%	76%	73%	3%
	1	17	5.74	0.316	0.82	13.2	16.25	-19%	170.8	202	-15%	33%	21%	12%
	2	17	5.74	0.318	0.88	12.8	15	-15%	159.5	159	0.3%	38%	38%	-0.2%

Table 6.4 Measures of goodness-of-fit of the model predictions shown in Table 6.3 (N=12).

	MSE	RMSE	St. Dev of Obs.	Normalized MSE	Modeling Efficiency (Loague and Green, 1991)	Normalized mean error
Q_{out} [L/min]	1.7	1.3	6.5	4%	96%	12%
Runoff Volume [L]	254	16.0	51.5	10%	90%	3%
Infiltration [%]	0.004	0.1	19%	12%	88%	-2%

The hydrographs obtained from the model were compared with the runoff rates measured in the Hwy 13 tests (sites 1 and 2) for three different intensities (Figure 6.7). The hydrographs for Hwy 77 are presented in supplemental information. The hydrographs for the low and high flux represent the field observations well. The start time for those cases is overestimated, but the shapes of the hydrographs were comparable to the observed. On the other hand, the model overestimates the runoff rates from the medium flux test.

Figure 6.8 presents the comparison between the measured and the predicted percentage infiltration for all the medium flux tests (N=12), all of which took place prior to conducting the tests using the low and high flux rates in both seasons. All the infiltration losses of the medium flux tests are under-predicted. In Chapter 5, where the field tests are analyzed in great detail, data regarding runoff fluxes and volume infiltrated in the medium and low flux tests support the idea that there was a reduction of the infiltration capacity in the consecutive tests. For example, despite reducing the magnitude of the input flux by half, the same volume of water was infiltrated in the consecutive tests; the first tests (medium flux) manifesting a higher infiltration capacity than the rest (low and high flux). This observation will be addressed further in the discussion section.

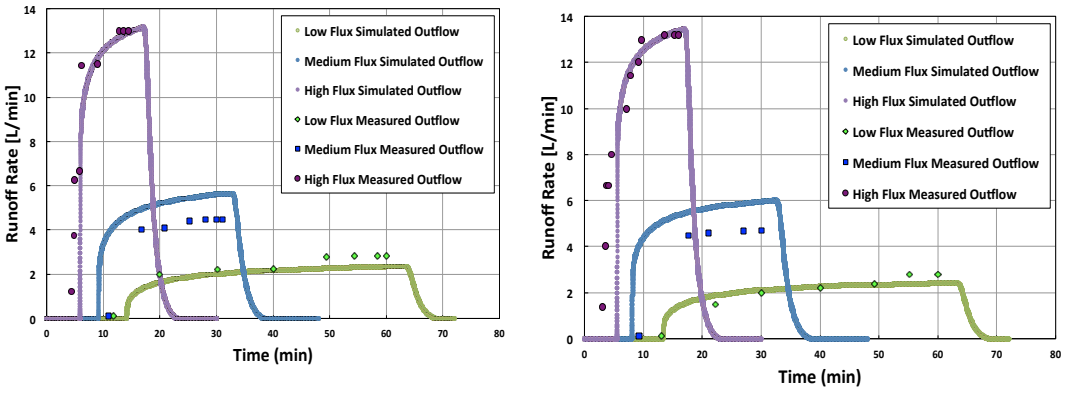

Figure 6.7 Hydrographs simulated by the model for the low, medium, and high flux tests at Hwy 13 site 1 (left) and site 2 (right) and runoff rate values measured during the field tests.

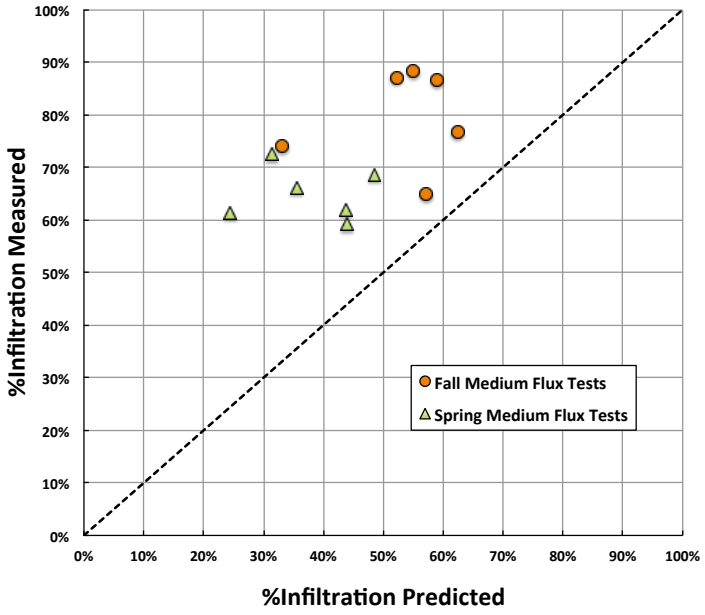

Figure 6.8 Percentage of infiltration measured versus predicted by the combined infiltration-overland flow model of the side slope of a swale for the medium flux tests in fall and spring. The line represents the area where predicted equals measured percentage infiltration. N=12.

3.2 Infiltration in Side Slope and Channel of Roadside Swale

To understand the infiltration partitioning between the side slope and the channel of a roadside swale, two K_{sat} values (0.51 and 5.1 cm/h, from Hydrologic Soil Group (HSG) C and A, respectively) and three side slope to road width ratios ($W_{side\ slope\ swale}/W_{road}$ = 0.2, 0.4, and 0.6) have been tested with the model using five different rainfall intensities (from 0.25 – 10.16 cm/h) (Figures 6.9 and 6.10). The width of the channel (perpendicular to the road traffic) in all the cases was 0.5 m, the widths of the side slopes were: 2, 4, and 6 m, the slope of the side slope was 25% and the length of the swale parallel to the road was 10 m. The simulation results are given in Figures 6.9 and 6.10.

The results indicate that the percentage of the total water infiltrated into the side slope is considerably greater than into the channel, despite the difference in slope (25% versus 2%). While the maximum percentage infiltrated by the channel is around 25%, for the cases simulated, the corresponding percentage infiltrated in the side slope ranges from 74% to 97%. Varying the saturated hydraulic conductivity does not significantly alter the partitioning results. The percentage infiltration into the side slope is greater for wider side slopes, as would be expected. Some guidelines to insure the performance of swales with respect to stormwater treatment focus on the swale channel (parallel to the road) (Ferguson, 1998; Yu *et al.*, 2001). However, for the typical design where the side slope is greater than the width of the channel, the percentage of water infiltrated in the side slope of a swale is greater than in the channel. Therefore, attention should be given to the design of roadside swales side slopes.

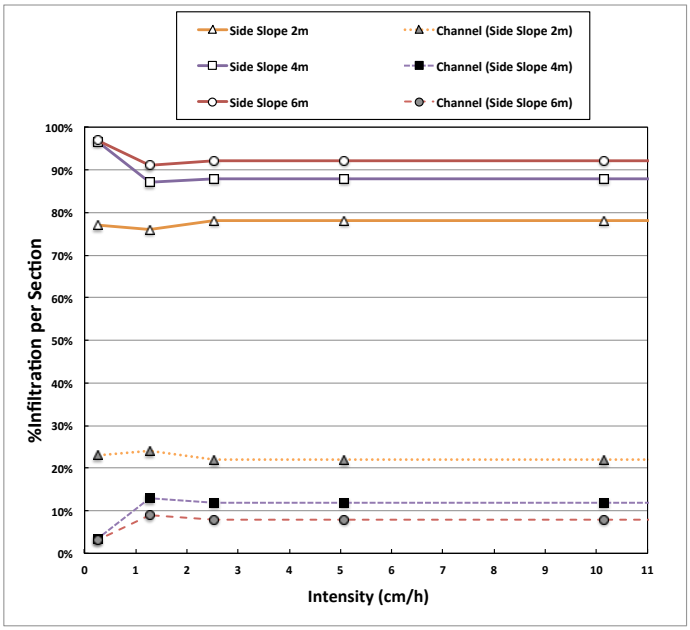

Figure 6.9 Percentage infiltrated into the side slope or channel of a swale versus the rainfall intensity applied over road and swale. The K_{sat} of the soil is 0.51 cm/h. The width of the channel was 0.5 m in all the cases and the width of the side slope varied (2, 4, and 6m).

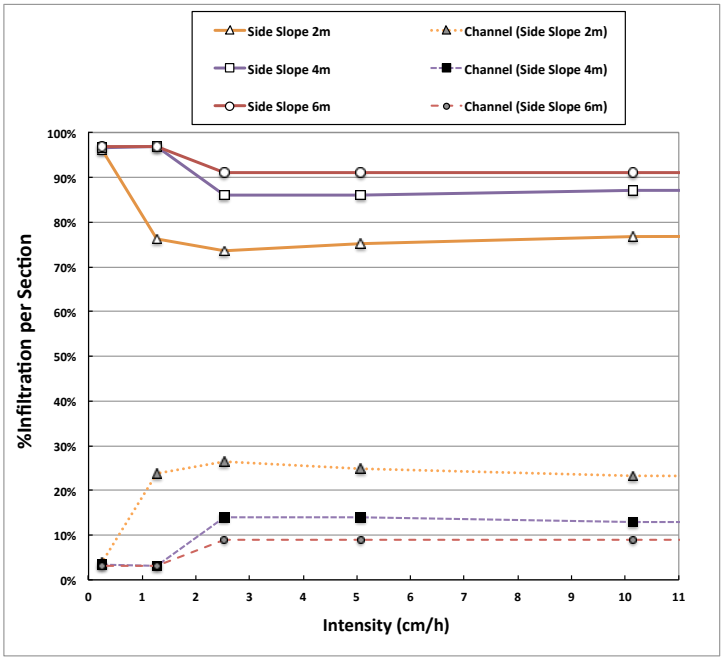

Figure 6.10 Percentage infiltrated into the side slope or channel of a swale versus the rainfall intensity applied over road and swale. The K_{sat} of the soil is 5.1 cm/h. The width of the channel was 0.5 m in all the cases and the width of the side slope varied (2, 4, and 6m).

3.3 Relative Volume of Infiltration and Relative Saturated Hydraulic Conductivity

Two parameters, previously used in Chapter 5 to analyze the field tests, have been used to relate infiltration performance with the main characteristics of the side slope of a swale. The first parameter is a relative volume of infiltration:

$$V_i^* = \frac{V_{inf}}{V_{in}} \quad (21)$$

where V_{inf} is the volume infiltrated and V_{in} is the input volume. A value of V_i^* equal to one means that all the runoff from the road has infiltrates into the side slope of the swale. The second parameter is a relative saturated hydraulic conductivity:

$$K_s^* = \frac{K_{sat}}{I}\frac{W_S}{W_R} \quad (22)$$

where K_{sat} is a representative saturated hydraulic conductivity for the side slope, I is average rainfall intensity, W_S is the width of the swale perpendicular to the road, and W_R is the width of the road draining into the swale.

The model was applied to simulate three different soil moisture deficits (0.1, 0.2, and 0.3) and their corresponding wetting front suctions, based on the van Genuchten (1980) parameters of a loamy sand (Carsel and Parrish, 1988), and the results are plotted in Figure 6.11 in terms of the variables Vi* and K_s^*. To have the same conditions as the field tests condition the rainfall intensity was only applied to the road, the direct rainfall over the side slope was not included. The results indicate that the model is sensitive to the typical range of soil moisture deficit and their corresponding wetting front suction, for the cases studied. In addition, V_i^* appears to increase linearly for both field tests (Garcia-Serrana *et al.*, 2017 - Chapter 5; Liu *et al.*, 2016) and the model. The field tests from Liu *et al.* (2016) indicated that even for K_s^* values greater than 1, the infiltration performance of the side slope was above 90% but not 100%; the model does not capture this reduced efficiency at high K_s^* values. This could be due to heterogeneous conditions of the surface vegetation and soil characteristics (K_{sat} or $\Delta\theta$), inaccuracies inherent to the field data collection, or low fractions of wetted area. Knowing the

relationship between V_i^* and K_s^* has advantages for application in order to obtain an estimated value of percentage infiltration using only those few parameters that appear to dominate the response of the swale.

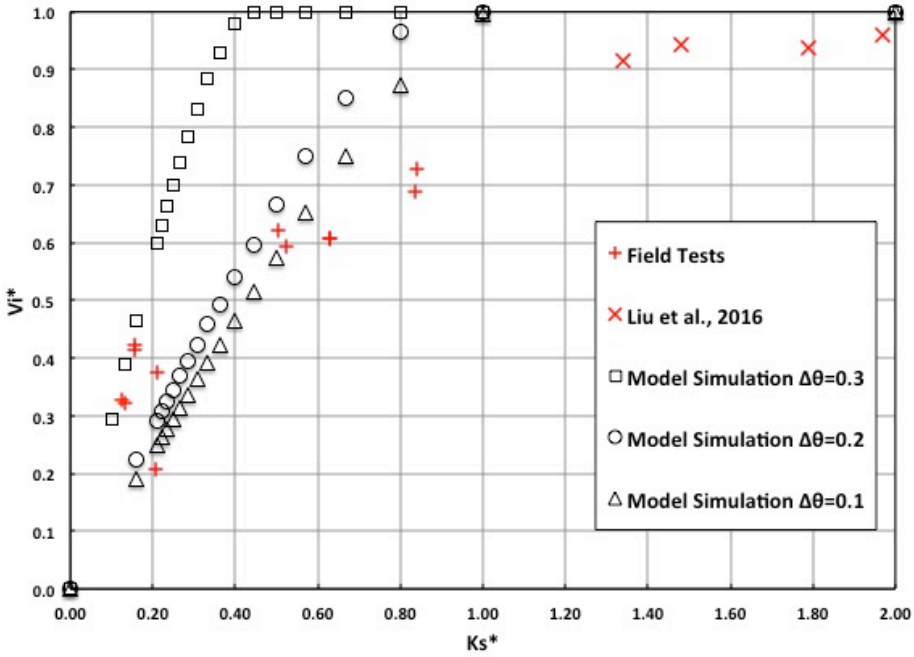

Figure 6.11 Relative volume of infiltration versus relative saturated hydraulic conductivity based on field tests and model simulations. For the model simulations, three typical soil moisture deficits were tested: 0.1, 0.2, and 0.3; with corresponding ψ of 7.5, 14.4, and 40.4 cm, respectively (based on van Genuchten parameters of α=12.4 m^{-1} and n=2.3 (Carsel and Parrish, 1988)). The following parameters were constant for all the simulations (obtained from the average values measured in the field): fw = 0.7, S_0= 25%, and ds = 1mm.

4.Discussion

4.1Assumptions and Implications of the Model

There are some processes that the model does not take into account when simulating overland flow and infiltration in a roadside swale. The limitations of the model are listed below:

- The shoulder of the road is assumed to be impervious, which is a conservative assumption. Many shoulders consist of gravel and compacted soil, and some water will infiltrate into the shoulder material.

Again, this effect will reduce the actual boundary flux entering the side slope to a value below the input intensity.

- The rainfall interception by the side slope and channel grass is assumed to be negligible. This effect will reduce the actual rainfall intensity applied over the swale.
- The concentrated flow in the side slope is assumed to occur in a fraction of the area, calculated as the sum of all the channels where water is concentrated. In reality, each channel will be independent. In addition, the fraction wetted is assumed to be steady.
- The road discharge is imposed as a uniform sheet flow at the location where it enteredthe side slope. In the actual field situation it is possible that runoff from the road will not enter uniformly onto the side slope.

Furthermore the validation of the model has been performed on the side slope part of the model, not the channel. The field tests did not include the channel section of the roadside swale; consequently there is no data to validate this part of the model. However, existing models – such as HEC-1 (USACE, 1990) and PRMS (Leavesley *et al.*, 1983) – have been widely used to simulate channel flow, using similar overland flow-infiltration assumptions. Despite these limitations, the focus of this model was on infiltration of the water into the slope and channel.

4.2 Effective K_{sat} Estimation for the Medium Boundary Flux Tests

The model has been validated with the low and high boundary flux tests. However, the model underestimated the infiltration performance of the side slope of the swales for the medium boundary flux tests, the first tests in the series. The same saturated hydraulic conductivity, estimated in the field after the completion of the high flow tests, was input in all the test simulations, however we hypothesize there was a reduction in the infiltration capacity in the consecutive tests. This hypothesis is further explained in Chapter 5, where the field test results are analyzed in fine detail. The effective K_{sat} values observed in the

medium flux tests were estimated using the coupled infiltration-runoff model presented. The model was run inputting different values of K_{sat}, while keeping all other parameters fixed, and matching the runoff volume simulated with the actual runoff volume measured in the tests. The K_{sat} values were estimated to have diminished by a factor of between1.2 and 3, with an average of 2.1; the calibrated K_{sat} values (for each strip) during the first fall and spring tests were: 10.6 and 10.6 cm/h (Hwy 51), 6.9 and 9.2 cm/h (Hwy 77), and 9.1 and 7.0 cm/h (Hwy 13).

4.3 Infiltration Performance of Roadside Swales

To address the roadside swales design implications of the model presented, repeated simulations of the model were run to quantify the relationship between rainfall depth and percentage infiltration for four different K_{sat} values and three ratios of width of the roadside filter strip over width of the road (W_{swale}/W_{road}). A rainfall duration of one hour and a constant intensity were assumed for the simulations. Average values observed in the field were used for the rest of the input parameters. Figure 6.12 presents the model results of infiltration performance of twelve different roadside swale design scenarios. The parameters changed were the width of the side slope (W_s) (2, 4 and 6 m) and the K_{sat} of the soil (0.5, 1.1, 4.1, and 16 cm/h); the road width (W_r) was assumed to be 10 m.

Several conclusions can be implied from Figure 6.12 results. First, for a K_{sat} of 0.5cm/h the swale side slope would infiltrate completely only small storms and would yield excess water to the channel for greater storms. Furthermore, a width ratio of the side slope to road of 0.2, despite being small, can be sufficient if K_{sat} was high enough; this case would apply specifically to a situation where the space for the swale is restricted. For example, there are two scenarios that, despite having different design characteristics, the infiltration performance is equivalent. A roadside swale with a K_{sat} of 1.1 cm/h and W_{swale}/W_{road} of 0.2 is equivalent to a swale with Ksat=0.5 cm/h and W_{swale}/W_{road} =0.4. Similarly, a K_{sat}

of 1.1 cm/h and W_{swale}/W_{road} of 0.6 is equivalent to a swale with Ksat=4.1 cm/h and W_{swale}/W_{road} =0.2. Finally, the relationship between percentage infiltration and the values of K_{sat} and W_{swale}/W_{road} is not linear, therefore the roadside swale design could be optimized by applying the information obtained from Figure 6.12, and finding the best conditions to infiltrate the rainfall depths required.

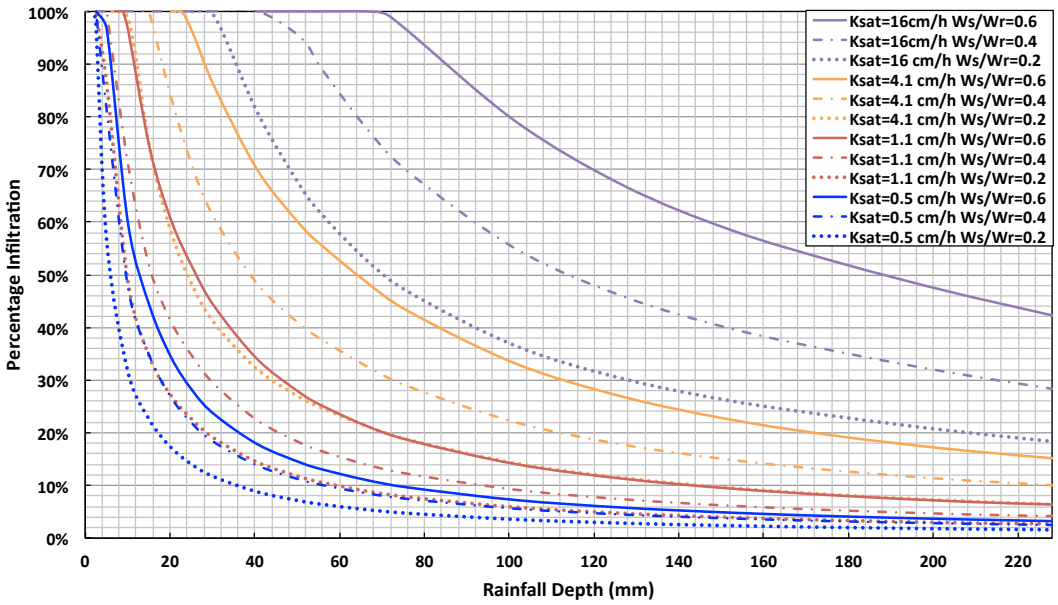

Figure 6.12 Rainfall depths versus percentage infiltration for three different ratios of swale side slope width (W_s) to road width (W_r) and four different saturated hydraulic conductivities. The channel width, perpendicular to the road, was assumed to have a length of 0.5m.

5. Conclusions

Properly maintained, grassed roadside swales (drainage ditches) can be considered stormwater control measures. This research provides the means to accurately determine the volume infiltrated by swales in both the side slope and the channel without calibration. To quantify infiltration performance of grassed roadside swales, a coupled overland flow-infiltration model that accounts for shallow concentrated flow in the side slope has been developed. Two submodels have been generated, a Green-Ampt-Mein-Larson infiltration submodel along

with a kinematic wave model for overland flow that accounts for concentration (fingering) of flow. These submodels are linked to develop a one-dimensional field-scale model for a single storm event.

The side slope model of a grassed swale has been validated using the data collected in twelve simulated runoff tests in three different highways located in the Minneapolis-St. Paul metropolitan area, MN. The model was successfully validated without any calibration required; the modeling efficiency (Loague and Green, 1991) for runoff rates, volume of runoff and percentage of infiltrated water over total input water predictions are 96%, 90%, and 88%, respectively. Specifically, saturated hydraulic conductivity is the most sensitive parameter to accurately estimate infiltration in filter strips (Fox *et al.*, 2010; Deletic, 2001), and it was measured in the field using an MPD infiltrometer. Other filter strip models calibrated the K_{sat} (Deletic, 2001) or used the observed inflow and outflow rates to estimate K_{sat} (Abu-Zreig *et al.*, 2001), which would not be reproducible in another location unless the same tests are performed. The model presented confirms that, if representative K_{sat} values, among other parameters, are measured in the field and input into the model, the infiltration performance of roadside filter strips can be estimated without any calibration.

The results indicate that the percentage of the total water infiltrated into the side slope is considerably greater than into the channel. For the cases simulated, the percentage infiltration in the side slope ranged from 74% to 97% of the total water infiltrated. Thus, the side slope of a roadside swale is typically the primary contributor to the loss of runoff by infiltration and the channel mainly conveys the water that runs off the side slope.

The model is sensitive to the typical range of wetting front suction and soil moisture deficit values, for dry and wet conditions. Finally, percentage infiltration (V_i^*) appears to increase linearly with K_s^*, which is a function of the saturated hydraulic conductivity, rainfall intensity, width of the swale perpendicular to the road, and width of the road, until V_i^* reaches a maximum. For design purposes, the relationship between V_i^* and K_s^* can help estimate percentage infiltration with

essential parameters that appear to dominate the results. In addition, the developed relation between rainfall depth, effective K_{sat} and road/swale side slope geometry can be used to determine infiltration effectiveness of a given swale.

Acknowledgments

The writers are grateful to the Minnesota Department of Transportation and Minnesota Local Road Research Board for funding this research under Contract No. 99008- 97, with Barbara Loida as Technical Liaison. J.L. Nieber's effort on this project was partially supported by the USDA National Institute of Food and Agriculture, Hatch/Multistate project 12-059.

Chapter 7

Calculator to Estimate Annual Infiltration Performance of Roadside Swales

Summary

Roadside swales or drainage ditches are low impact development (LID) practices for stormwater treatment and control, and there is a need to quantify their infiltration performance for design and planning purposes. A roadside swale calculator has been developed where only the main design parameters that have a significant impact on the runoff volume output are required, in addition to the rainfall distribution of the study site. The inputs of the calculator are the saturated hydraulic conductivity of the soil, width of the swale, width of the road, and the location's rainfall frequency or volume percentile. The calculator and the ancillary information provided can be used to determine: 1) the total percentage of annual volume infiltrated 2) the percentage of events entirely captured by a roadside swale in a year, and 3) the percentage of road runoff infiltrated by a roadside swale with a specific swale width to road width ratio and saturated hydraulic

conductivity for a given rainfall depth event.

1. Introduction

Traditionally, the main purpose of roadside drainage ditches or swales has been to convey stormwater runoff to prevent road flooding. However, previous research confirms that roadside swales also provide water quality benefits (Barrett *et al.*, 1998; Davis *et al.*, 2012; Abida and Sabourin, 2006). Roadside swales improve water quality by infiltration and filtration of stormwater, and by sedimentation of suspended sediment. Road runoff volume reduction through infiltration occurs as the water flows over the side slope (which acts as a filter strip) in a direction perpendicular to the roadway and/or along the swale channel parallel to the roadway. Therefore, roadside swales are low impact development (LID) practices or green infrastructure (GI) and there is a growing interest in stormwater calculators that quantify reductions in runoff using these systems.

Previous Roadside Swale or Filter Strip Field Studies

Multiple studies have monitored volume reduction achieved by roadside swales subject to natural storm events. Yonge (2000) studied vegetated roadside filter strip plots constructed on native soil and topsoil. Highway runoff data was collected over an 18-month period. An average infiltration percentage of 70% and 47% was observed in plots of 4.6 m length with native soil and local site fill material, respectively. CALTRANS (2003) performed a 2-year study where the infiltration performance of roadside grassed swales was evaluated. The percentage infiltration, based on all events during the study period, was on average: 85% for the 13 m length side slopes, 73% for the 9 – 10 m side slopes and 60% for the 7 – 8 m side slopes. Lancaster (2005) monitored infiltration along roadside swales and reported 100% infiltration within the first two meters from the edge of pavement in one site (36 precipitation events). At another site, 67% of the events (18 precipitation events) had no observed runoff at the base of the swale. Ahearn and Tveten (2008) investigated the performance of four forty-one year-old roadside swales, with a monitoring station located at 4 meters from

the edge of pavement. The percentages of runoff volume reduction observed ranged from 66% to 94%. Davis *et al.* (2012) investigated the hydraulic performance of four grassed roadside swales in Maryland over 4.5 years, with a total of 52 rainfall events. Based on the results, they concluded that the swales would capture 0.56 cm of rain through initial abstractions and completely capture runoff when infiltration rates were greater than 0.3–1.5 cm/h. It was predicted that similarly designed swales would capture 59% of storm events during an average year in Maryland. Furthermore, Davis *et al.* (2012) concluded that, hydraulically, the swales studied operated in three categories: completely infiltrating the smallest 40% of storm events, reducing the total runoff volume for an additional 40% of events, and performing simply as flow conveyance with negligible volume attenuation for the largest 20% of events. The variability in runoff reduction by roadside swales will be investigated in this paper, and used to develop a simplified model that utilizes the most important independent variables.

Previous Simplified Swale and Filter Strip Models

The main disadvantage of physically and process-based models for filter strips and swales (Muñoz-Carpena *et al.*, 1999; Deletic, 2001; Garcia-Serrana *et al.*, 2017b – Chapter 6; USDA, 1980) is they require specification of numerous parameters. Simplified vegetative filter strip models have been developed from more comprehensive models to obtain easy and fast approximations of the performance of these runoff management practices. Most of the simplified models or design aid tools, however, focus on sediment trapping, not runoff volume reduction. Flanagan *et al.* (1989) developed simplified equations from the CREAMS model (USDA, 1980) to predict sediment delivery ratios from filter strips. Dosskey *et al.* (2011) created a design aid for sizing agricultural filter strips based on the process-based VFSMOD model (Muñoz-Carpena *et al.*, 1999). This graphical design aid was used to assess the relationship between pollutant and water trapping efficiency and ratio of filter strip area to contributing area. The graphic aid consisted of seven lines, obtained by fitting a nonlinear regression of

an exponential equation simulating different scenarios based on filter slope, soil texture, and agricultural field cover management practice. A simplified model to estimate sediment reduction in grassed swales and vegetative filter strips was developed by Winston and Hunt (2016); however, infiltration was not considered. Akan (2014) developed a mathematical model for filter strips that incorporates infiltration, based on the kinematic wave and the Green-Ampt equations (Green and Ampt, 1911). The model required calibration and was verified with a set of laboratory experiments (Stomph *et al.*, 2002), although none of the soil infiltration parameters were measured. Using the principle of hydrologic similarity and neglecting direct rainfall over the filter strip, Akan developed generalized charts that helped determine reductions in runoff volume and peak discharge from filters; however more than five input parameters are required to apply the charts to obtain a percentage runoff reduction from a specific storm event.

Objectives

The purpose of the research presented in this manuscript was to develop an easy-to-use calculator that can estimate annual infiltration performance of roadside swales. The mathematical model used in developing the simplified calculator is presented in Chapter 6. The objectives of this paper are as follows:

(1) Perform a sensitivity analysis of the input variables in a coupled overland flow-infiltration model for roadside swales that accounts for shallow concentrated flow in the side slope,

(2) Determine the most important input variables needed to estimate infiltration performance of roadside swales and establish a relationship between these variables and percentage infiltration,

(3) Simplify the comprehensive model (Chapter 6) into an easy-to-use Excel spreadsheet that can be used to answer the following questions: 1. What percentage of the annual rainfall (in volume) does a roadside drainage ditch infiltrate in a specific location? 2. What percentage of all possible storm events is entirely captured by roadside swales at a specific

location? 3. What percentage of road runoff is infiltrated by a roadside swale with a specific swale width to road width ratio and saturated hydraulic conductivity for a given rainfall depth?

(4) Test the roadside swale calculator in two case studies.

(5) Provide guidance for roadside swale design optimization for runoff volume reduction.

2.Description of the Mathematical Model

A coupled overland flow-infiltration model that incorporates fractional wetted surface over the side slope of a roadside swale has been developed by Garcia-Serrana *et al.* (2017b) (Chapter 6). This numerical model was used to estimate the infiltration performance of roadside swales (both side slope and channel) using the Green-Ampt-Mein-Larson assumptions to calculate infiltration along with a kinematic wave model for overland flow that accounts for concentrated flow. The swale model was validated using the data collected in twelve simulated runoff tests for three different highways located in the Minneapolis-St. Paul metropolitan area, MN USA. The model was established in MATLAB programming language and allows for a wide range of user inputs such as: rainfall intensity, initial moisture content of the soil, saturated hydraulic conductivity, wetting-front suction, and the geometry of the side slope, channel, and road.

3. Sensitivity Analysis

A sensitivity analysis aims to characterize the change in the response of a model to changes in the input parameters of a model; thereby identifying the main parameters that contribute to variations in the response of a model (Iman and Helton, 1988). The goals of the sensitivity analyses presented here are: 1) parameter prioritization – to rank the input parameters according to their relative contribution to the model output variability and 2) parameter fixing – to identify

the input parameters that have a minor effect on output variability and fix them at some mean value (Saltelli *et al.*, 2008).

Two global sensitivity analyses have been performed that consider variation of the input parameters within the entire space of their variability, considering them as stochastic variables. The first sensitivity analysis, the screening method of Morris (1991), was used as a qualitative analysis for parameter prioritization of eight input parameters (Table 7.1). The second analysis, density-based PAWN method (Pianosi and Wagener, 2015), was performed (using the first five parameters of the ranking) to quantify the sensitivity of the input parameters and select the parameters with negligible impact on the model outputs. The calculations of the Morris and PAWN methods were carried out using the Safe Matlab toolbox (Pianosi *et al.*, 2015). Both sensitivity analyses start by: a) choosing the input variables and assigning them probability distribution functions (PDFs), b) setting the fixed values of the remaining input variables, and c) defining the output value of the model to be used in the analysis. The input variables, their respective PDFs and associated parameters are presented in Table 7.1; these are based on values observed in a roadside swale field study performed at four different highways in the Twin Cities metropolitan area in MN, USA (Garcia-Serrana *et al.*, 2017a) and a previous filter strip model sensitivity study (Muñoz-Carpena *et al.*, 2010). An example of a probability distribution function (PDFs) and field measurements of K_{sat} is given in Figure 7.1. The fixed variables were: rainfall intensity (2.54 cm/h), width of the road (10m), width of the side slope (4m), length of the swale (10m), and slope of the channel (0.02). The selected model output to perform the sensitivity was the runoff volume of the roadside swale (in liters).

For the Morris method, a Latin-Hypercube Sampling (LHS) (Iman and Conover, 1982) method was used where one input parameter was varied at a time, keeping all the others fixed (Pianosi *et al.*, 2016). The number of total elementary effects (*EE*) (relative model output differences when changing parameters one-

at-a-time) calculated was 300 for eight input parameters (*M*) and the convergence criterion was the ranking (Sarrazin *et al.*, 2016); the ordering between the parameters must remain stable with the number of EE calculated. The results of the Morris sensitivity analysis with the absolute mean ($|\bar{x}|$) and standard deviation (σ) of the *EE* are presented in Figure 7.2. The absolute mean of *EE* (Campolongo and Saltelli, 2007) was used to assign the rankings presented in Table 7.1. The top five parameters (K_{sat}, *Ψ, Δθ, B,* and *fw*) were used in the second sensitivity analysis, the PAWN analysis, for further examination.

For the PAWN method, the Latin-Hypercube Sampling (LHS) method was used where all the input parameters were varied simultaneously and the interactions between parameters are taken into account; this method requires a higher number of model evaluations than the Morris method. As described in Pianosi and Wagener (2015), "the sensitivity to input x_i is measured by the distance between the unconditional probability distribution of the model output (y) that is obtained when all inputs vary simultaneously, and the conditional distributions that are obtained when varying all inputs but x_i". The conditional and unconditional distributions are characterized by their cumulative distribution functions (CDFs) and the measure used for distance between distributions is the Kolmogov–Smirnov statistic (*KS*), which varies between 0 and 1. The PAWN index T_i was computed as the maximum of all the *KS* calculated for each parameter. The number of output evaluations to calculate the unconditional CDF (N_u) was 300, the number of output evaluations to calculate the conditional CDF (N_c) was 150, and the number of conditioning values (n_c) was set to be 10. The criterion for convergence was the stabilization of the sensitivity indexes (T_i) (Sarrazin *et al.*, 2016; Herman *et al.*, 2013); the convergence was considered acceptable if the 95% confidence interval (CI) of all the sensitivity indexes was less than 15% of the highest T_i value. The results of the PAWN T_i indices and CI are presented in Table 7.1 and Figure 7.3; the 95% confidence intervals (5%

significance level) of the index were obtained by employing a bootstrapping procedure (Efron and Tibshirani, 1993). Figure 7.4 displays the *KS* indexes for all the conditioning values (*nc*) sampled for each of the five parameters studied. To determine non-influential input parameters, the two-sample Kolmogov–Smirnov test was used; the critical value (CV) of *KS* with a 0.05 confidence level (α) was 1.14.

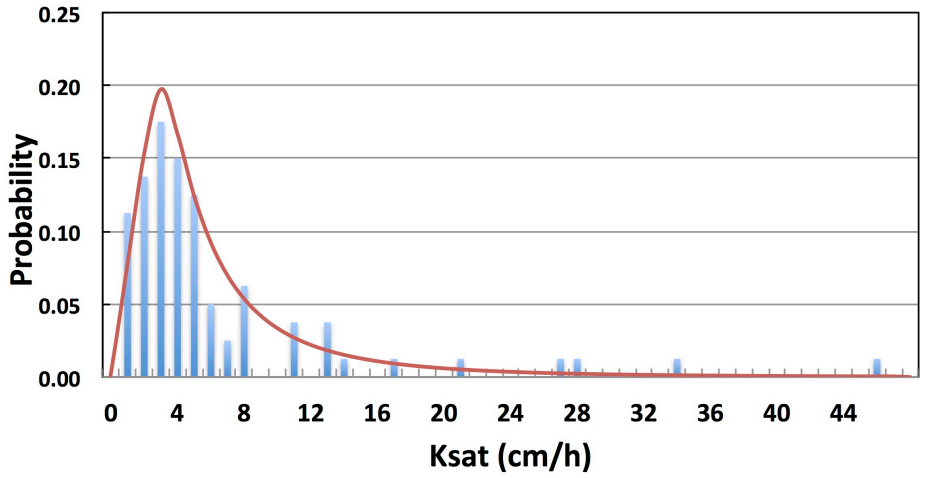

Figure 7.1 PDF of saturated hydraulic conductivity based on field measurements; Line: Log-normal distribution PDF based on these measurements.

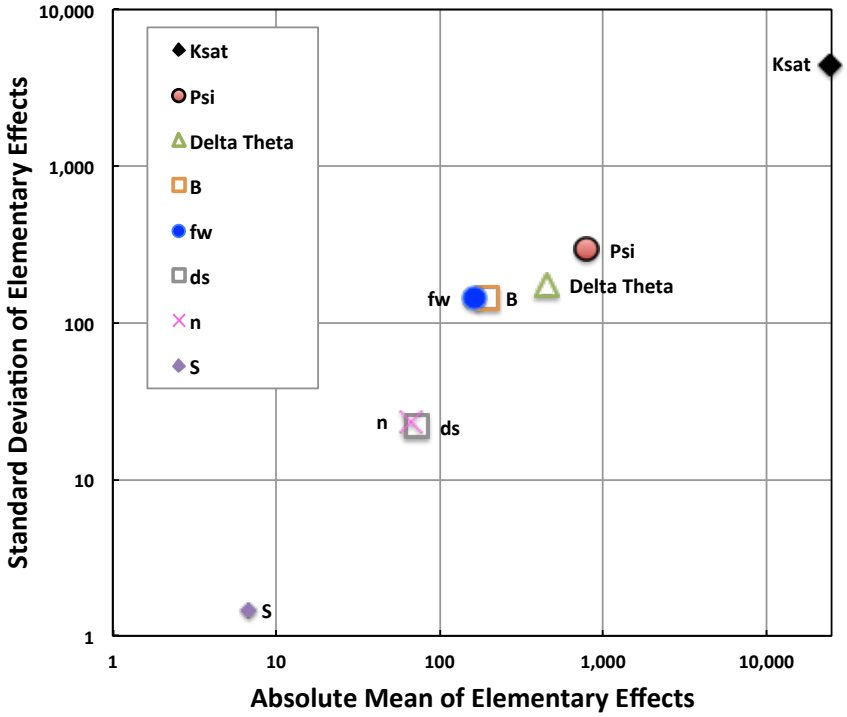

Figure 7.2 Global sensitivity analysis results of the infiltration-runoff model for roadside swales obtained using the Morris (1991) method.

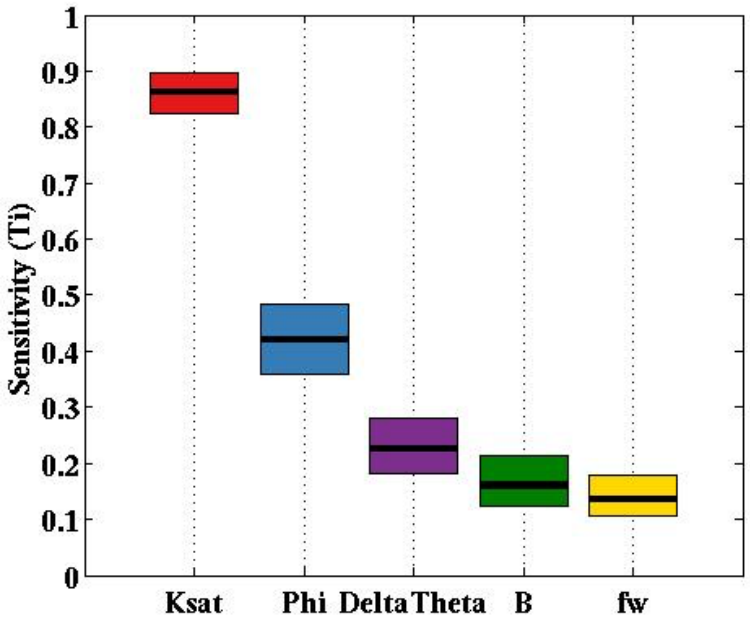

Figure 7.3 PAWN sensitivity indices (T_i) of the infiltration-overland flow model for roadside swales. Boxes represent 95% confidence intervals obtained by bootstrapping; black lines indicate the mean index estimate.

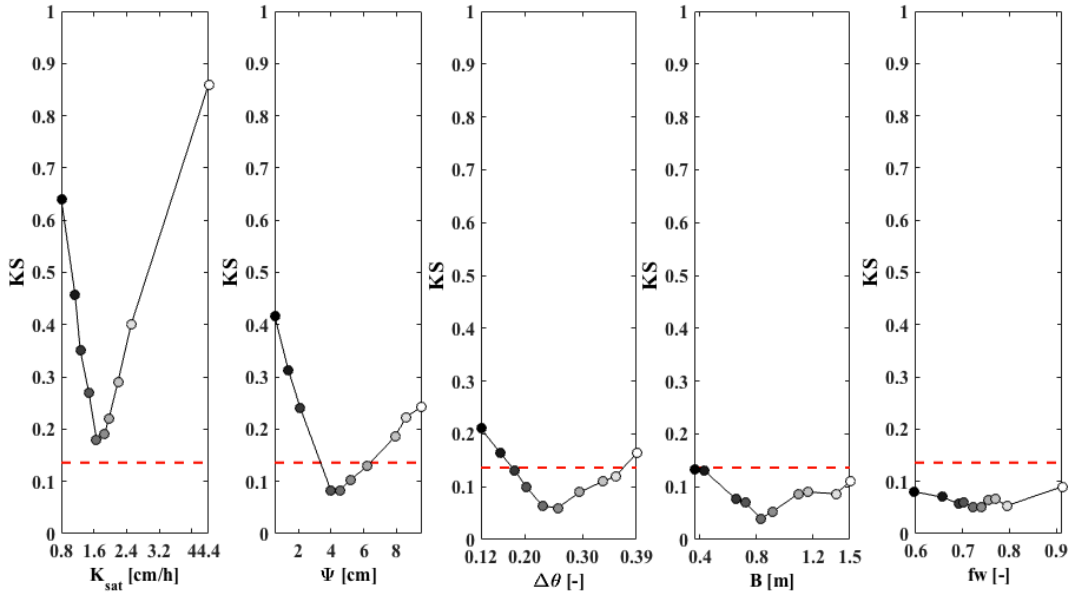

Figure 7.4 Kolmogorov Smirnov-statistic (*KS*) at different conditioning values (n_c=10) of each input parameter. The red dashed horizontal line is the critical value of the KS statistic at confidence level of 0.05.

Based on both Morris and PAWN methods, the model outputs are most sensitive to anticipated variations in K_{sat} (Table 7.1). According to the Morris sensitivity analysis, the five most important parameters are K_{sat}, *Ψ, Δθ, B,* and *fw* since they have the higher absolute mean ($|\bar{x}|$) of EE and are separated from the origin of the $|\bar{x}|$-σ plane (Figure 7.2). In the second sensitivity analysis, using the PAWN method, the same ranking was maintained based on all the PAWN T_i. All the *KS* values of K_{sat} were above the critical value, therefore it is confirmed that this parameter is influential. On the other hand, all the *KS* values of *B,* and *fw* are below the critical value, meaning that their conditional and unconditional CDFs do not differ and these two parameters can be considered non-influential. Finally, 60% and 30% of the *nc* values corresponding to upper and lower limits of *Ψ* and *Δθ*, respectively, are above the critical level; consequently these two parameters are somewhat influential and should be studied further.

These results are in agreement with other sensitivity analyses of two vegetated filter strips models conducted in previous studies, the TRAVA and VFSMOD models. Deletic (2001) performed a local sensitivity analysis in the TRAVA model and determined that the most dominant parameters were the filter length, K_{sat}, and saturated soil water content (θ_s); in addition, the model was not sensitive to the filter slope (*S*), Manning's n, and depression storage (*ds*). Muñoz-Carpena *et al.* (2007) performed a global sensitivity analysis in the VFSMOD model and also concluded that K_{sat} was the most influential input parameter.

Table 7.1 Results and data used for the global sensitivity analyses, illustrating the sensitivity of swale runoff volume to the various system parameters. Statistics of the distributions used as inputs or each of the parameters are: uniform (min, max); triangular (min, mean, max); log normal (μ_{log_y}, σ_{log_y}); normal (μ_x, σ_x). The Morris Ranking provides a qualitative ranking of the importance of individual parameters among a parameter set, and this ranking is used to select parameters for the PAWN test. The PAWN test provides a quantitative test of the significance of a given parameter on runoff volume

Parameters	Units	Distribution	Morris Ranking	PAWN T_i	95% CI PAWN T_i	% n_c > Crit.Value	PAWN Ranking	Fixed values
Saturated hydraulic conductivity (K_{sat})	cm/h	Lognormal (0.52, 0.46)	1	0.86	(0.82,0.90)	100%	1	*
Soil wetting front suction (Psi)	cm	Uniform (0.1, 10)	2	0.42	(0.36,0.48)	60%	2	5
Soil moisture deficit (DeltaTheta)	-	Uniform (0.1, 0.4)	3	0.23	(0.18,0.28)	30%	3	0.3
Channel width (B)	m	Uniform (0.3, 1.5)	4	0.16	(0.13,0.22)	0%	4	0.5
Fraction wetted (fw)	-	Normal (0.73, 0.07)	5	0.14	(0.11,0.18)	0%	5	0.7
Depression Storage (ds)	mm	Triangular (0.1, 1.55, 3)	6	-	-	-	-	0
Manning's n (n)	$s/m^{1/3}$	Triangular (0.1, 0.3)	7	-	-	-	-	0.25
Side slope (S)	-	Triangular (0.2, 0.25, 0.3)	8	-	-	-	-	0.2

* K_{sat} was found to be the most significant parameter affecting runoff volume and the only parameter not fixed in the simplified model.

4. Model Simplification

4.1 Parameter Simplification and Assumptions

Based on the sensitivity analysis, and previous studies on filter strip models, the infiltration percentage is most sensitive to the saturated hydraulic conductivity. The infiltration percentage is also somewhat sensitive to soil wetting front suction pressure (Ψ) and soil moisture deficit ($\Delta\theta$). The saturated hydraulic conductivity does not substantially change with season (Ahmed *et al.*, 2015). However, effective wetting front suction changes with soil moisture content and week-to-week the soil moisture content fluctuates (dry and wet conditions). The computations of percent infiltrated, however, will be based upon the hydrology of many seasons. In each of these seasons there will be wetter and dryer periods of variable duration. Soil moisture content changes with time depending upon precipitation patterns, and soil wetting front suction changes with soil moisture content. For this reason, the two parameters (Ψ, $\Delta\theta$) have been fixed to a representative value observed in the field during fall and spring (Garcia-Serrana *et al.*, 2017a). The rest of the parameters: Manning's n, channel width, slope, fraction wetted, and depression storage, have been shown above to be non-critical for calculating infiltration performance of roadside swales. The small effect these parameters have on the output of the model justifies assigning average values to those parameters in the simplified model. The average values of: Ψ, $\Delta\theta$, S, fw, and B are presented in Table 7.1. In addition, the depression storage (ds) was assumed to be 0 mm in the model simulations, the slope of the swale channel was fixed to 0.02, the fraction wetted in the channel was assumed to be 1, and the Manning's n was assumed to be 0.25 (Minton, 2005).

The runoff coefficient is a dimensionless coefficient relating the magnitude of runoff to the magnitude of input rainfall. The length of the system (parallel to the road) was compared to the runoff coefficient, with all the rest of the parameters equal. As the length of the roadside swale increases, the residence time of the water in the channel increases, therefore decreasing the runoff coefficient. However, the differences are not important; for example, using a design length of 100m versus 10m would reduce the runoff coefficient 3%, and using 300m or 500m versus 10m would mean a decrease of 6% and 8%, respectively. For the simplified calculation, a conservative approach has been considered and a length of 10m has been used to perform all the model simulations.

The modeled infiltration-overland process is simplified by assuming the rainfall intensity remains constant over the rain event duration. In a real rainfall event the rain intensity varies over time and the duration of rainfall events are variable. The Soil Conservation Service (SCS) intensity curve for a Type II 24-hour rainfall distribution (USDA, 1986), where the peak intensity takes place in one hour in the middle of the storm event, 45% of the rainfall occurs in 1 hour and 60% occurs in 3 hours (Figure 7.5). Instead, in our analysis the storm event is assumed to take place in one hour in the middle of the storm event. Setting the duration of the storm event to one hour, and therefore the intensity, is a conservative assumption.

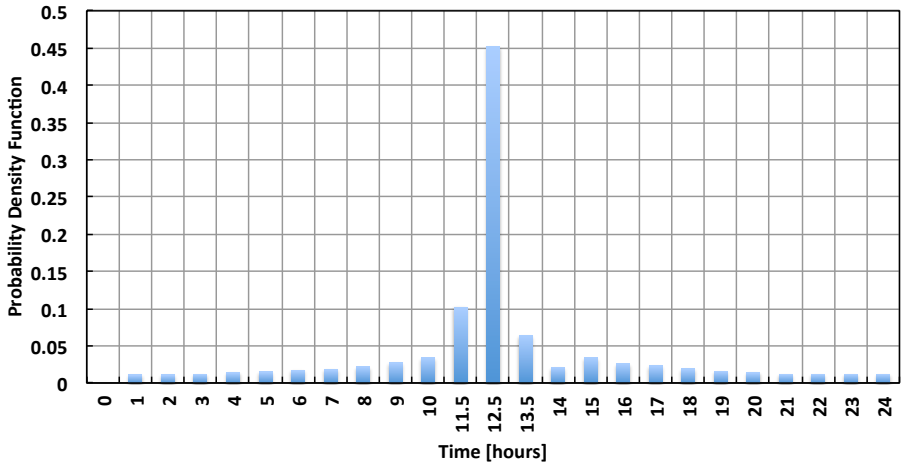

Figure 7.5 Probability Density Function of a 24-hour rainfall event based on an SCS Type II storm (USDA, 1986).

With the considerations given above, the simplified model consists of specified fixed values for soil wetting front suction pressure, soil moisture deficit, channel width, side slope, fraction wetted, Manning's *n*, and depression storage; variable K_{sat}, variable uniform rainfall intensity, and variable road width (W_{road}) and swale side slope width (W_{swale}).

4.2 Model Simulations

To create the simplified calculator, repeated simulations of the model, with the above assumptions and simplifications, were run to quantify the relationship between rainfall depth and percentage infiltration for different K_{sat} values and ratios of width of the roadside filter strip over width of the road (W_{swale}/W_{road}). The simulation results were used to develop a set of curves for eight different K_{sat} values from 0.15 to 16 cm/h and eighteen rainfall depths, from 0.25 to 22.9 cm. Nine graphs representing different width ratios, from 0.1 to 1.4 have been created. Figure 7.6 is an example of the nine graphs. The remaining graphs are presented in Appendix B. These model simulation results are essential to

generate the swale calculator. All the resulting percentage infiltration amounts are stored in performance tables for variable width ratios (W_{swale}/W_{road}).

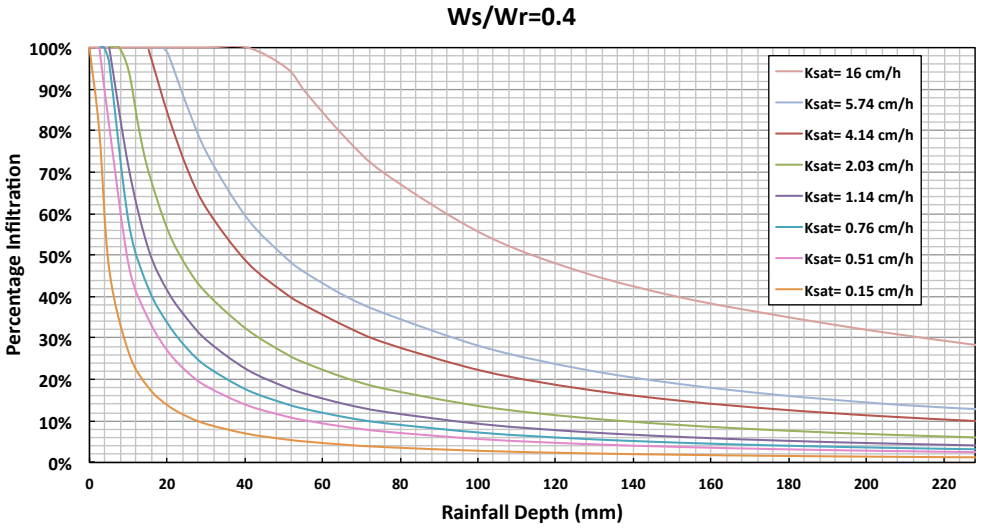

Figure 7.6 Rainfall depths versus percentage infiltration for a ratio of swale side slope width (W_s) to road width (W_r) of 0.4. The eight curves represent different saturated hydraulic conductivities.

5. Roadside Swale Calculator Results

5.1 Annual Infiltration Performance of Swales

In order to estimate annual infiltration performance of roadside swales, the distribution of the annual rainfall of the site is needed. Percentile rainfall frequency curves represent the percentage exceedance in terms of total number of rainfall events (USEPA, 2009). Percentile rainfall volume curves represent the percentage exceedance in terms of total annual rainfall volume (Young, 2006) (Figure 7.7).

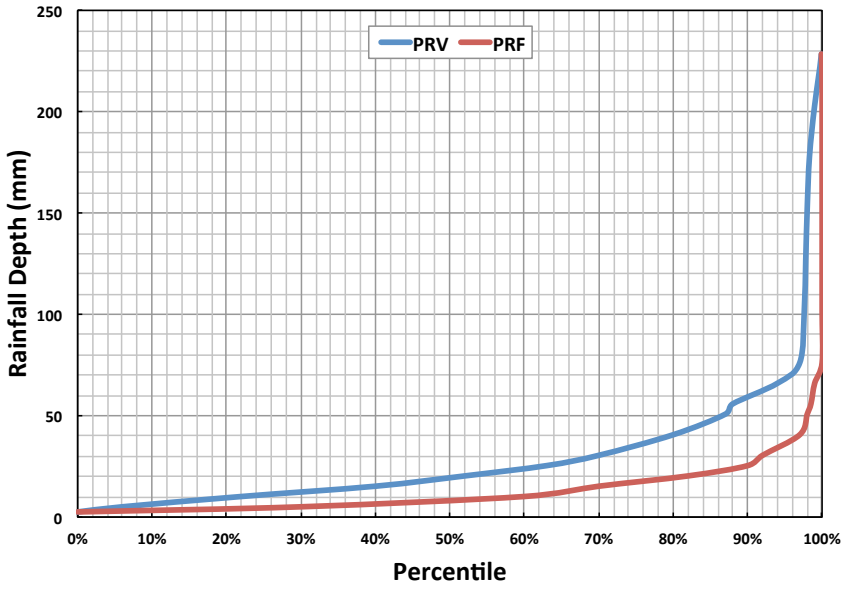

Figure 7.7 Percentile Rainfall Frequency (PRF) and Percentile Rainfall Volume (PRV) for the Minneapolis – St. Paul International Airport Station, MN. PRF is the percentile of the number of storms and PRV is the percentile of the total rainfall volume. (Emmons & Olivier Resources, 2005).

The probability distribution function of annual rainfall in a site, obtained from the percentile rainfall volume, represents the probability of a rainfall event of a specific depth to occur in a given year. The percentage of total annual precipitation that will be infiltrated in a particular roadside swale can be calculated as:

$$Annual\ Infiltration\ (\%) = \sum(Pv_i x \frac{Inf_{K_{sat}W_{ratio},i} + Inf_{K_{sat}W_{ratio},i+1}}{2}) \text{ x } 100 \qquad (10)$$

where Pv_i is the probability of a certain rainfall event in a given range between *i and i+1* rainfall depths will happen, based on total volume; $Inf_{K_{sat}W_{ratio},i}$ is the fraction infiltrated for the specific rainfall depth (*i*) based on a particular combination of K_{sat} and W_{swale}/W_{road}. Since the values of $Inf_{K_{sat}W_{ratio},i}$ are based on model simulations based on discrete parameters, the annual infiltration is interpolated based on the user's input of K_{sat} and W_{swale}/W_{road}. First, the annual

infiltration is linearly interpolated based on the input K_{sat} and a second interpolation is performed based on the input width ratio.

An example calculation of this procedure is given in Table 7.2, where the percentage of the annual rainfall (at the Minneapolis–St. Paul airport, MN station) infiltrated into a vegetated roadside swale (with a K_{sat} = 2 cm/h and W_{swale}/W_{road} = 0.4) is calculated. The result is 70% of the total annual volume is infiltrated at this particular roadside swale.

Table 7.2 Example of swale annual infiltration performance for the parameters: W_{swale}/W_{road} = 0.4 and K_{sat} = 2 cm/h, at Minneapolis-St. Paul, MN. Percentile Rainfall Volume (PRV) and Probability Distribution Function (Pv_i).

Rainfall Depth (mm)	PRV (Annual Rainfall Volume)	Pv_i	$Inf_{K_{sat}W_{rati}}$	Annual Infiltration
203	99%	1.0%	6.8%	0.07%
178	98%	0.7%	7.7%	0.06%
152	98%	0.3%	9.0%	0.03%
127	97.8%	0.2%	10.8%	0.02%
102	97.6%	0.2%	13.4%	0.03%
76	97%	0.6%	17.7%	0.11%
66	94%	3.0%	20.4%	0.66%
56	88%	6.0%	23.9%	1.59%
46	84%	5.0%	29.1%	1.47%
36	75%	9.0%	36.3%	3.52%
26	63%	12.0%	46.6%	6.13%
20	52%	11.0%	55.6%	6.91%
16	40%	12.0%	70.0%	9.85%
10	22%	18.0%	94.1%	17.47%
6	6%	16.0%	100.0%	16.00%
3	0%	6.0%	100.0%	6.00%
				Σ=70%

Following the same procedure, the percentage of storm events totally captured by roadside swales can be estimated by calculating the probability distribution function of annual rainfall in a site based on the percentile rainfall frequency,

instead of the percentile rainfall volume. The percentage of total storm events totally captured in a given year by a roadside swale can be calculated as the Σ Pf_i at which $Inf_{K_{sat}W_{ratio},i}$ =1; where *Pf* is the probability of a certain rainfall event in a given range between *i and i+1* rainfall depths will happen, based on total number of events. For the conditions of Table 7.2 (W_{swale}/W_{road} = 0.4 and K_{sat} = 2 cm/h), this calculation would result in 60% of the total number of storm events entirely captured (100% infiltrated) by the roadside swale.

5.2 Calculator Operation

The simplified model, or calculator, is in an Excel spreadsheet where the user inputs: 1) location's percentile rainfall volume or frequency, 2) width of the swale side slope, 3) width of the road, and 4) K_{sat} of the roadside swale's soil. The minimum K_{sat} value that the user can input is 0.15 cm/h, which corresponds to the upper limit of a hydrologic soil group D; the maximum value of K_{sat} that the user can input is 16 cm/h. The range of values of W_{swale}/W_{road} that the user can input is 0.1 to 1.4; values below or above those limits are approximated by the limit values. The result is the percentage of the annual rainfall infiltrated by the roadside swale or percentage of events captured. The calculator will also display a figure representing annual infiltration performance, corresponding to a specific location based on historical rainfall data, versus saturated hydraulic conductivity; each line is a different ratio of side slope and road width (Figure 7.8). Finally, a summary table of infiltration performances for eight different saturated hydraulic conductivities and six ratios of width of the swale over width of the road is generated.

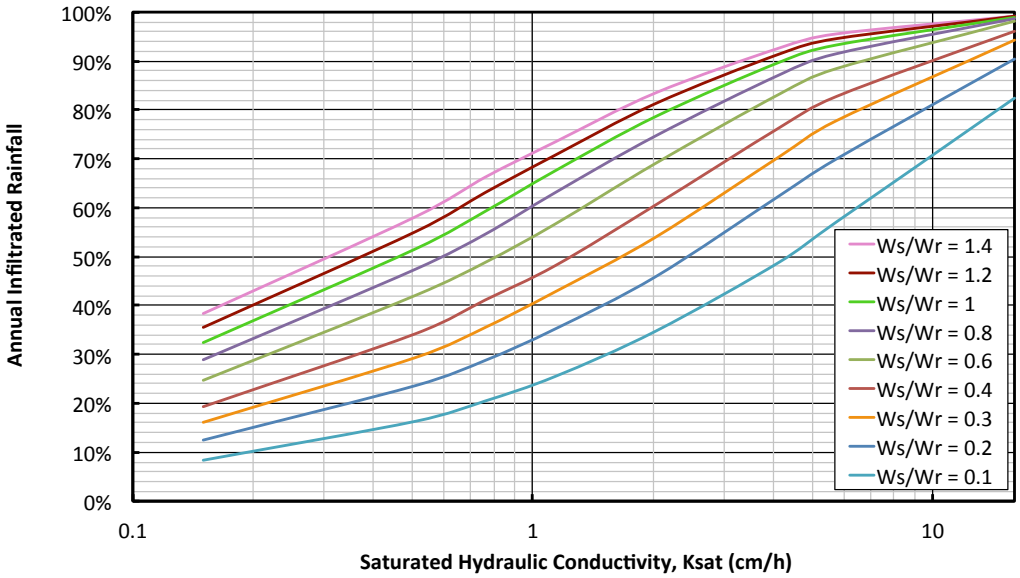

Figure 7.8 Annual infiltration performances versus saturated hydraulic conductivity (K_{sat}) based on the Minneapolis - St. Paul, MN International airport rainfall station.

6. Case Studies

6.1 California

The Sacramento and Moreno Valley, California, USA site in the CALTRANS (2003) study were selected to perform a comparison of the calculator predictions and the field monitoring results of a roadside swale. These locations were chosen because no gopher holes were present and the infiltration data provided could be fit to Philip's equation (Philip, 1957) to estimate K_{sat}. First, the percentile rainfall volume (PRV) curve from the site was estimated based on the rainfall data, depths and total volumes of twenty-one and ten rainfall events, from 2001-2002 between October and April (wet season) provided in the study report for Sacramento and Moreno Valley respectively. The width of the road was estimated to be 15–16 m, based on the reported drainage area and length. Four different filter widths: 1.1, 4.6, 6.6, and 8.4 m were tested in Sacramento and three in Moreno Valley (2.6m, 4.9m, and 9.9m). A Turf-Tec Infiltrometer was used

to perform infiltration rate measurements, with a total of three measurements per filter. The infiltration depth over time data was fitted to Philip's equation to calculate three values of K_{sat} per filter. A calibration coefficient of 0.231 was used for the Turf-Tec K_{sat} estimations (Houle, 2017) and the average value of the three measurements was obtained following the equation described by Weiss and Gulliver (2015). The K_{sat} values were 4.08, 2.41, 2.17, and 2.39 cm/h, from shorter to longer width in Sacramento and 0.22, 0.3, and 1.03cm/h in Moreno Valley. Each roadside swale infiltration performance was evaluated based on all the events during the study period. The percentile rainfall curve, widths of the road and swale, and K_{sat} were input in the swale calculator and the results obtained are presented in Table 7.4. On average, the calculator estimated the percentage of annual water infiltrated with an error of -3.75%. These results show that the calculator is capable of providing a reasonable estimation of annual infiltration performance based on a few key parameters.

Table 7.3 Infiltration performance of roadside swales in Sacramento and Moreno Valley, CA based on CALTRANS (2003) observations and the calculator predictions.

Location	Filter Width [m]	K_{sat} [cm/h]	CALTRANS (2003) Observations	Calculator Predictions
Sacramento	1.1	4.08	68%	59%
	4.6	2.41	66%	67%
	6.6	2.17	72%	72%
	8.4	2.39	84%	79%
Moreno Valley	2.6	0.22	0%	7%
	4.9	0.3	0%	12%
	9.9	1.03	38%	34%

6.2 Maryland

The same procedure described above was used to test the calculator with Maryland roadside swales data collected by Davis *et al.* (2012). In this case, the percentile rainfall frequency (PRF) curve based on average Maryland values (Kreeb and McCuen, 2003) was used to analyze annual rainfall distribution. The width of the road and the swale were estimated to be 16.4m and 15.2m, respectively, based on the roadway and swale areas and longitudinal length. The saturated hydraulic conductivity (0.12cm/h), or steady state infiltration rate, was estimated by Davis *et al.* from the slope of the capture line fitted to the total rainfall depth captured during of all monitored events. The analysis using the swale calculator was based on a W_{swale}/W_{road} = 0.93 and K_{sat} = 0.15 cm/h. The calculator predictions are presented in Table 7.4; similar volume attenuation results were estimated by Davis *et al.* (2012) for two swale designs.

Table 7.4 Infiltration performance of roadside swales in Maryland based on Davis *et al.* (2012) observations and the calculator predictions. The percentage of events that have reduction of total runoff volume is based on the criteria of infiltrating more than 10% of the volume and flow conveyance is based on less than 10% infiltration.

Infiltration Performance	Davis *et al.* (2012) Observations	Calculator Predictions
Complete infiltration	57%	33%
Reduction of total runoff	29%	67%
Flow conveyance	14%	0%
Percentage of events captured in a year	59%	67%

7. Discussion

Both the roadside swale characteristics and the location's rainfall distribution are important factors to determine infiltration performance of swales. Roadside swales manage to infiltrate almost 100% of small rainfall events, reduce runoff volumes for medium events, and simply convey water for large

events (Figure 7.6; Table 7.2; Davis *et al.*, 2012). Similarly to other Low Impact Development (LID) practices, roadside swales work well as stormwater management practices for water quality designed rainfall events. During flood events roadside swales should convey and transport water from the road quickly due to safety requirements.

The calculator results confirm that the infiltration performance of roadside swales improves with increasing side slope width and hydraulic conductivity of the soil. Furthermore, the ratio of width of the swale over width of the road is not linearly related to annual infiltration performance; the greater the magnitude of W_{swale}/W_{road}, the less sensitive the system to an increase in this parameter. For example, for a roadside swale located in the Minneapolis-St. Paul, MN area (Figure 7.8) increasing W_{swale}/W_{road} from 0.2 to 0.3 increases annual percentage infiltration up to 8%. On the other hand, the maximum the percentage of annual infiltration increases when changing W_{swale}/W_{road} from 1.2 to 1.4 is 3%. In addition, the relationship between K_{sat} and annual percentage infiltration is approximately logarithmic between an annual percent infiltration of 30% and 80%. Thus, increasing K_{sat} has different effects on the improvement of annual infiltration percentage depending on the location in the curve.

Calculator limitations

The limitations of the roadside swale calculator are linked to the assumptions of the extended roadside swale model. A list of the extended model assumptions is described in Chapter 6 (Garcia-Serrana *et al.*, 2017b). One of the assumptions of the extended model is that groundwater level does not restrict infiltration and that infiltration is not constrained by an impervious layer close to the surface. In addition, the accuracy of the roadside swale calculator is lower than the extended model because further assumptions are needed to simplify the input parameters. The swale calculator assumes rainfall events last for one hour at constant

intensity, which is a conservative assumption. In reality, the rainfall intensity will progressively increase over time until the peak intensity is achieved. Furthermore, a number of swale parameters have been fixed and set to average parameters observed specifically in roadside swales; similarly, Dosskey *et al.* (2011) based their simplified filter strip model on agricultural site soils with slopes of 2 or 10%.

The most important parameter of the swale calculator is K_{sat}. As such, a satisfactory estimation of this parameter in the field is necessary to obtain a suitable estimation of the annual infiltration performance of a swale. Ahmed *et al.*, (2015) found that 10 measurements are required to result in a mean K_{sat} that has a 95% confidence interval within a factor of 3 and 20 measurements are required to get that interval within a factor of 2. For a pre-construction estimation of the roadside swale, K_{sat} at a nearby reference site should be analyzed, where the soil and vegetation of the new swale are consistent with the reference site. Finally, the swale calculator assumes that there is no erosion in the side slope of the drainage ditch. Having an eroded surface would increase flow concentration and decrease infiltration performance, causing the roadside swale calculator to overestimate infiltration.

Comparison to other Simplified Models

The vegetated filter strip model by Akan (2014) required more than five input parameters to derive estimates of runoff from filter strips. Typically limited input data is available from field measurements, so generally it would be difficult to assign all five parameters in a practical application. The sensitivity analyses herein verified that not all values are needed to obtain a rough estimation of infiltration performance of roadside swales. Moreover, Akan's model predicts volume reduction, peak flow and residence time of a single storm event; the

model presented here focuses on estimating the annual percentage of volume infiltrated and individual events captured by a roadside swale.

The graphical design aid of Dosskey *et al.* (2011) is also based on a nonlinear regression that relates trapping efficiency of water or sediments with the ratio of filter strip area over contributing area. However, the tool is designed for agricultural buffers and the inputs are: filter slope (2 or 10%), soil texture (not hydraulic properties of the soil), and agricultural field cover management practice. Finally, their results are based on a single design storm, 61mm in one hour (10-year return period across multiple regions in the US); the roadside swale calculator provides infiltration performance information for an annual distribution of storm events and also any storm depth in one hour.

Calculator Applications

There are two main applications that make this calculator practical for design and planning purposes. First, the total percentage of annual volume infiltrated or the percentage of events captured by roadside swales can be estimated using a calculator based on three parameters (W_{swale}, W_{road}, and K_{sat}) and the percentile of rainfall volume or frequency at a specific site. Second, the curves (Figures 7.6 and Appendix B) that relate percentage infiltration of a rainfall event of a given depth with K_{sat} can be used to determine the percentage infiltration achieved by a roadside swale with a specific W_{swale}/ W_{road} ratio for a design objective. For example a roadside swale with a K_{sat} of 1.14 cm/h and a W_{swale}/ W_{road} of 0.8 infiltrates more than 50% of a 25.4 mm rainfall event. This calculator enables designers and planners to directly determine a W_{swale}/ W_{road} ratio that will achieve a desired level of infiltration efficiency for a design storm.

8. Conclusions

Roadside grassed swales are stormwater control measures (SCMs) that

reduce the volume of road runoff. Their infiltration performance as a function of design variables and rainfall distribution is necessary to assign the appropriate pollution prevention credits for roadside swales. A roadside swale calculator, based on the Garcia-Serrana *et al.* (2017b) infiltration-overland flow model, has been developed where only the main design parameters that have a significant impact on the model results are required. The inputs of the calculator, after the simplifications, are the saturated hydraulic conductivity of the soil, width of the swale, width of the road, and the location's rainfall volume or frequency percentile as a function of rainfall depth. The calculator provides good predictions for two case studies based on field observations in California and Maryland, and is available for download at stormwater.safl.umn.edu.

The calculator and ancillary figures and tables are useful for design and planning purposes providing: 1) the total percentage of annual volume infiltrated or the percentage of events captured by roadside swales, and 2) the percentage infiltration achieved by a roadside swale with a specific W_{swale}/ W_{road} ratio and K_{sat} for a given rainfall depth. The results confirm that the infiltration performance of roadside swales improves with increasing side slope width and hydraulic conductivity of the soil. Moreover, the ratio of width of the swale to width of the road is non-linearly related to annual infiltration performance. Finally, the relationship between K_{sat} and annual percentage infiltration is approximately logarithmic.

Provided that there is a satisfactory estimation of the saturated hydraulic conductivity in the field, and the side slope does not show signs of erosion, the roadside swale calculator can be used to provide an estimation of the water captured by the channel and side slope of a roadside swale.

Acknowledgments

The writers are grateful to the Minnesota Department of Transportation and Minnesota Local Road Research Board for funding this research under Contract No. 99008- 97, with Barbara Loida as Technical Liaison. J.L. Nieber's effort on this project was partially supported by the USDA National Institute of Food and Agriculture, Hatch/Multistate project 12-059.

Chapter 8

Conclusions

Roadside grassed swales or drainage ditches are low impact development (LID) practices for stormwater treatment and control that reduce the volume of road runoff by infiltration. Infiltration takes place over the side slope, acting like a filter strip, and over a grassed channel parallel to the road. Their infiltration performance as a function of design variables and rainfall distribution is necessary to assign the appropriate pollution prevention credits for roadside swales.

This thesis has advanced the understanding of how water flows on a fraction of the lateral slope of a roadside swale, how surface roughness parameters are related to the fraction of wetted area, and what is the effect of equidistant parallel strip water sources on the lateral component of infiltration. Furthermore, a coupled overland flow-infiltration model that accounts for shallow concentrated flow in the side slope has been developed and, finally, a roadside swale

calculator has been generated with a reduced set of input parameters that estimates their infiltration performance for design and planning purposes.

Simulated runoff tests have been performed in the laboratory with a field-scale model and on four different highways. All the tests indicated that water flow on the lateral slope of a roadside swale is concentrated in fingers, instead of sheet flow, at the typical rainfall/runoff intensities for which infiltration practices are utilized to improve surface water quality. A linear relationship between flux of water from the road and fraction of wetted area was observed. In addition, fractal parameters based on the Fourier power spectrum method are good indicators of both flow patterns and erosion of a surface with predominant roughness features parallel to the flow direction.

To quantify infiltration performance of grassed roadside swales, two submodels have been generated and validated; a Green-Ampt-Mein-Larson infiltration submodel along with a kinematic wave model for overland flow that accounts for concentration of flow. The research presented confirms that both the model and the measuring technique (MPD infiltrometer) can be used to quantify infiltration losses in swales. It has been concluded that the side slope of a roadside swale is the main feature contributing to the loss of runoff by infiltration, and that the channel primarily conveys the water. Based on this model, a roadside swale calculator has been developed with a reduced set of input parameters: the saturated hydraulic conductivity of the soil, width of the swale and width of the road, and the location's rainfall frequency or volume percentile. The results can be used to determine: 1) the total percentage of annual volume infiltrated 2) the percentage of events totally captured by a roadside swale in a year, and 3) the percentage of road runoff infiltrated by a roadside swale with specific design characteristics for a given rainfall depth event.

Finally, roadside swales are on-site infiltration practices that require low maintenance and their performance has been tested decades after their

construction. Therefore, roadside swales are a practical solution to mitigate the impact of road runoff on water bodies, and this research supports informed decision-making on how to account for their infiltration benefits.

References

Abedini, M. J., and Shaghaghian, M. R. (2009). Exploring scaling laws in surface topography. *Chaos, Solitons, and Fractals*, 42(4): 2373–2383.

Abida, H. and Sabourin, J.F. (2006). Grass swale-perforated pipe systems for stormwater management. Journal of Irrigation and Drainage Engineering, 132(1): 55–63.

Abrahams, A. D., Parsons, A. J., and Hirsch, P. J. (1992). Field and laboratory studies of resistance to interrill overland flow on semi-arid hillslopes, southern Arizona. Overland flow, A. J. Parsons and A. D. Abrahams, ed., *UCL Press, Univ. College London*, London, 1–23.

Abu-Zreig, M., Rudra, R. P., and Whiteley, H. R. (2001). Validation of a vegetated filter strip model (VFSMOD). *Hydrological Processes*, *15*(5): 729–742.

Ahammer H. (2011) Higuchi Dimension of Digital Images. *PLoS ONE*, 6(9): e24796.

Ahearn, D. and Tveten, R. (2008). Legacy LID: Stormwater Treatment in Unimproved Embankments Along Highway Shoulders in Western Washington, *International Low Impact Development Conference*, November 16-19, 2008, Seattle, WA.

Ahmed, F., Gulliver, J. S., and Nieber, J. L. (2015). Field Infiltration Measurements in Grassed Roadside Drainage Ditches: Spatial and Temporal Variability. *Journal of Hydrology,* 530(11): 604–611.

Ahmed, F., Nestingen, R., Nieber, J. L., Gulliver, J. S., and Hozalski, R. M. (2014). A modified Philip-Dunne infiltrometer for measuring the field-saturated hydraulic conductivity of surface soil. *Vadose Zone Journal*, 13 (10).

Akan, A. O. (2014) Hydrologic Modeling of Urban Vegetative Filter Strips. *Journal of Hydrologic Engineering*, 19 (1): 188–195.

Alestra, S. and Battiatto, S. (2008). Fuzzy Image Processing. Implementazione di plug-in per l'ambiente ImageJ. Universita di Catania, Departimento di Matematica e Informatica. Internet, url: http://svg.dmi.unict.it/iplab/imagej/Plugins/Fuzzy%20Image%20Processing/downloads/Fuzzy%20Image%20Processing%20-%20Implementazione%20di%20plug-in%20per%20l'ambiente%20ImageJ.pdf (accessed April 6, 2016).

Ali, M., Sterk, G., Seeger, M., and Stroosnijder, L. (2012). Effect of flow discharge and median grain size on mean flow velocity under overland flow. *Journal of Hydrology*, 452-453: 150–160.

Allmaras, R. R., Burwell, R. E., Larson, W. E., and Holt, R. F. (1966) Total porosity and random roughness of the interrow zone as influenced by tillage. *USDA Conservation Research Report* 7, USDA, Washington, DC.

Anguiano, E., Pancorbo, M., and Aguilar, M. (1993). Fractal characterization by frequency analysis. I. Surfaces. *Journal of Microscopy*, 172: 233–238.

Antoine, M., Javaux, M. and Bielders, C. L. (2011). Integrating subgrid connectivity properties of the micro-topography in distributed runoff models, at the interrill scale. *Journal of Hydrology*, 403(3-4): 213–223.

Antoine, M., Javaux, M. and Bielders, C., (2009). What indicators can capture runoff-relevant connectivity properties of the micro-topography at the plot scale? *Advances in Water Resources* 32 (8): 1297–1310.

Appels, W. M., Bogaart, P. W. and van der Zee, S. E. T. M. (2011). Influence of spatial variations of microtopography and infiltration on surface runoff and field scale hydrological connectivity. *Advances in Water Resources*, 34(2): 303–313.

Appels, W. M., Bogaart, P. W., van der Zee, S. E. A. T. M. (2016). Surface runoff in flat terrain: how field topography and runoff generating processes control hydrological connectivity. *Journal of Hydrology*. 534: 493–504.

Asleson, B. C., Nestingen, R. S., Gulliver, J. S., Hozalski, R. M. and Nieber, J. L. (2009) Performance Assessment of Rain Gardens, *Journal of the American Water Resources Association*, 45: 1019–1031.

Asplund, R., Ferguson, J. F., and Mar, B. M. (1980) Characterization of Highway Runoff in Washington State. *Washington State Department of Transportation*, Olympia, WA.

ASTM D2216-10 (2010), Standard Test Methods for Laboratory Determination of Water (Moisture) Content of Soil and Rock by Mass, *ASTM International*, West Conshohocken, PA.

ASTM D2937-10 (2010), Standard Test Method for Density of Soil in Place by the Drive-Cylinder Method, *ASTM International*, West Conshohocken, PA.

ASTM D422-63 (2007)e2, 2007. Standard Test Method for Particle-Size Analysis of Soils. ASTM International, West Conshohocken, PA.

ASTM D6913 (2009). Standard test methods for particle size distribution (Gradation) of soils using sieve analysis, D18.03. *ASTM International*, West Conshohocken, PA.

Azis M.I., Clements D.L., and Lobo M. (2003) A boundary element method for steady infiltration from periodic channels. *ANZIAM Journal*, 44(E): C61–C78.

Barley, K. P. (1954). Effects of root growth and decay on the permeability of a synthetic sandy loam. *Soil Science*, 78: 205–210.

Barrett, M. E., Irish, L. B., Malina, J. F., and Charbeneau, R. J. (1998a) Characterization of Highway Runoff in Austin, Texas, Area. *Journal of Environmental Engineering,* 124(2): 131–137.

Barrett, M. E., Keblin, M. V., Walsh, P. M., Malina, J. F., and R. B. Charbeneau, (1998). Evaluation of the performance of permanent runoff controls: summary and conclusions, *Center for Transportation Research,* University of Texas at Austin, TX.

Barrett, M. E., Zuber, R. D., Collins, E. R., Malina, J. F., Jr., Charbeneau, R. J. and Ward, G. H. (1995). A Review and Evaluation of Literature Pertaining to the Quantity and Control of Pollution from Highway Runoff and Control of Pollution from Highway Runoff and Construction. *Center for Research in Water Resources,* Bureau of Engineering Research, University of Texas at Austin.

Barrett, M.E., Walsh, P.M., Malina, J.F., and R.B. Charbeneau, (1998b). Performance of vegetative controls for treating highway runoff, *Journal of Environmental Engineering*, 124(11): 1121–1128.

Bautista, E. (2016) Effect of infiltration modeling approach on operational solutions for furrow irrigation. *Journal of Irrigation and Drainage Engineering*, 142(12): 06016012.

Bautista, E., Warrick, A.W., and Strelkoff, T.S. (2014). New results for an approximate method for calculating two-dimensional furrow infiltration. *Journal of Irrigation and Drainage Engineering*, 140(10): 04014032.

Bergkamp, G., Cammeraat, L. H., and Martinez-Fernandez, J. (1996). Water movement and vegetation patterns on shrubland and an abandoned field in two desertification threatened areas in Spain. *Earth Surface Processes and Landforms,* 21: 1073–1090.

Beven, K. J. and Germann, P. F. (2013). Macropores and water flow in soils revisited. *Water Resources Research*, 49: 3071–3092.

Beven, K. J., and P. F. Germann (1982). Macropores and water flow in soils, *Water Resources Research*, 18(5): 1311–1325.

Booth, D. B. and C. Rhett Jackson, C.R. (1997). Urbanization of aquatic systems: degradation thresholds, stormwater detection, and the limits of mitigation. *JAWRA Journal of the American Water Resources Association,* 33(5): 1077–1090.

Bracken, L. J., and Croke, J. (2007). The concept of hydrological connectivity and its contribution to understanding runoff-dominated geomorphic systems, *Hydrological Processes,* 21(13): 1749–1763.

Bracken, L. J., Wainwright, J., Ali, G. A., Tetzlaff, D., Smith, M. W., Reaney, S. M., Roy, A. G. (2013). Concepts of hydrological connectivity: Research approaches, pathways and future agendas. *Earth-Science Reviews*, 119: 17–34.

Bresson, L. M., and Boiffin, J. (1990). Morphological characterization of soil crust development stages on an experimental field. *Geoderma*, 47(3-4), 301–325.

Burrough, P. A. (1981). Fractal dimensions of landscapes and other environmental data. *Nature*, 294: 240–242.

Caltrans (2003) Roadside Vegetated Treatment Sites (RVTS) Study Final Report, Report # CTSW-RT-03-028, *California Department of Transportation*, 1120 N St., Sacramento, CA., Nov. 2003.

Cammeraat, L. H. (2002). A review of two strongly contrasting geomorphological systems within the context of scale. *Earth Surface Processes and Landforms* 27: 1201–1222.

Campolongo, F., Saltelli, A. (1997) Sensitivity analysis of an environmental model: an application of different analysis methods. *Reliability Engineering and System Safety*, 57 (1): 49–69.

Carsel, R. F., and Parrish, R. S. (1988) Developing joint probability distributions of soil water retention characteristics. *Water Resources Research*, 24(5): 755–769.

Cea, L., Legout, C., Darboux, F., Esteves, M., and Nord, G. (2014). Experimental validation of a 2D overland flow model using high resolution water depth and

velocity data. *Journal of Hydrology*, 513: 142–153.

Cerdà, A. (1995). Factores y Variaciones Espacio-Temporales de la Infiltración en los Ecosistemas Mediterráneos. *Editorial Geoforma, Logrofio,* 159 pp.

Chabaeva, A., Civco, D. L., Hurd, J. D. (2009). Assessment of impervious surface estimation techniques. *Journal of Hydrologic Engineering*, 14(4): 377–387.

Chamberlain, E. J., and Gow, A. J. (1979). Effect of freezing and thawing on the permeability and structure of soils. *Engineering Geology*, 13: 73-92.

Chen, L., Sela, S., Svoray, T. and Assouline, S. (2013). The role of soil-surface sealing, microtopography, and vegetation patches in rainfall-runoff processes in semiarid areas. *Water Resources Research*, 49(9): 5585–5599.

Chi, Y., Yang, J., Bogart, D. and Chu, X. (2012). Fractal Analysis of Surface Microtopography and its application in understanding hydrologic problems. *American Society of Agricultural and Biological Engineers*, 55(5): 1781–1792.

Chu S. T. (1978). Infiltration during unsteady rain. *Water Resources Research 14(3): 461–466.*

Chu, X., Nelis, J. and Rediske, R. (2013a). Preliminary Study on the Effects of Surface Microtopography on Tracer Transport in a Coupled Overland and Unsaturated Flow System, *Journal of Hydrologic Engineering,* 18: 1241–1249.

Chu, X., Yang, J., Chi, Y. and Zhang, J. (2013b). Dynamic puddle delineation and modeling of puddle-to-puddle filling-spilling-merging-splitting overland flow processes. *Water Resources Research*, 49(6): 3825–3829.

Clarke, K. C. (1986). Computation of the fractal dimension of topographic surfaces using the triangular prism surface area method. *Computers and Geosciences*, 12: 713–722.

COMSOL Multiphysics (2016). Documentation for COMSOL Release 5.2. *COMSOL, Inc.*, MA, USA, http://www.comsol. com.

COMSOL Multiphysics®, version 5.2, www.comsol.com.

Cooper, J. R., Wainwright, J., Parsons, A. J., Onda, Y., Fukuwara, T., Obana, E. and Hargrave, G. H. (2012). A new approach for simulating the redistribution of soil particles by water erosion: A marker-in-cell model. *Journal of Geophysical Research: Earth Surface*, 117(4): 1–20.

Currence, H. D. and Lovely, W. G. (1970). The analysis of soil surface roughness, *Transactions of American Society of Agricultural Engineering*, 13: 710–714.

Darboux, F. and Huang, C. (2003). An instantaneous-profile laser scanner to measure soil surface microtopography. *Soil Science Society of America Journal*, 67: 92–99.

Darboux, F., Davy, P., Gascuelodoux, C. and Huang, C. (2001). Evolution of soil surface roughness and flowpath connectivity in overland flow experiments, *Catena*, 46 (2-3): 125–139.

Davis, A.P., Stagge, J.H., Jamil, E., and Kim, H. (2012). Hydraulic performance of grass swales for managing highway runoff. *Water Research*, 46(20): 6775–6786.

De Lima, J. L. M. P., and Abrantes, J. R. C. B. (2014). Can infrared thermography be used to estimate soil surface microrelief and rill morphology? *Catena*, 113: 314–322.

Deletic, A. (2001). Modelling of water and sediment transport over grassed areas. *Journal of Hydrology*, *248*(1-4): 168–182.

Deletic, A. (2005). Sediment transport in urban runoff over grassed areas. *Journal of Hydrology*, *301*: 108–122.

Deletic, A. and Fletcher, T. D. (2006). Performance of grass filters used for stormwater treatment—a field and modelling study. *Journal of Hydrology*, *317*(3-4): 261–275.

Dosskey, M. G., Helmers, M. J., and Eisenhauer, D.E. (2011) A design aid for sizing filter strips using buffer area ratio. *Journal of Soil and Water Conservation,* 66(1): 29–39.

Dosskey, M. G., Helmers, M. J.,Eisenhauer, D. E., Franti, T. G., and Hoagland, K. D. (2002) Assessment of concentrated flow through riparian buffers. *Journal of Soil and Water Conservation*, 57(6): 336–343.

Dupuis, T. V. and Kobriger, N. (1985). Effects of Highway Runoff on Receiving Waters - Vol. IV: Procedural Guidelines for Environmental Assessments, *Federal Highway Administration*, Office of Research and Development Report No. FHWA/RD-84/065.

Ebrahimian, A., Gulliver, J. S., Bruce, B. N. (2016). Improved methods to estimate the effective impervious area in urban catchments using rainfall-runoff data, *Journal of Hydrology*, 536(2): 109–118.

Efron, B. and Tibshirani, R. (1993) An Introduction to the Bootstrap. *Chapman & Hall/ CRC.*

Eltz, F. L. F. and Norton, L. D. (1997). Surface roughness changes as affected by rainfall erosivity tillage and canopy cover. *Soil Science Society of America Journal*, 61: 1746–1755.

Emmet, W. (1970). The hydraulics of overland flow on hillslopes. *US Geological Survey Professional Paper, 662A, 68pp.*

Emmons & Olivier Resources (2005) Issue Paper “B”, Precipitation Frequency Analysis and Use. Prepared for the Minnesota Stormwater Manual Sub-Committee.

Esteves, M., Faucher, X., Galle, S. and Vauclin, M. (2000). Overland flow and infiltration modelling for small plots during unsteady rain: numerical results versus observed values. *Journal of Hydrology*, 228(3-4): 265–282.

Fassman, E. A., Liao, M. (2009) Monitoring of a Series of Swales within a Stormwater Treatment Train. *In Proceedings of the 32nd Hydrology and Water Resources Symposium, Newcastle, Australia,* 30 November–3 December 2009; Engineers Australia: Barton, Australia, 2009; pp. 368–378.

Feddes, R. A., Kabat, P., Vanbakel, P. J. T., Bronswijk, J. J. B., and Halbertsma, J. (1988) Modelling soil water dynamics in the saturated zone—State of the art, *Journal of Hydrology*, 100: 69–111.

Ferguson, B. K. (1998) Introduction to stormwater: concepts, purpose, design. *John Wiley & Sons, Inc.*, New York, NY.

Fiedler F. R., Ramirez J. A. (2000) A numerical method for simulating discontinuous shallow flow over an infiltrating surface. *International Journal of Numerical Methods in Fluids,* 32: 219–240.

Fischer, C., Roscher, C., Jensen, B., Eisenhauer, N., Baade, J., Attinger, S., Scheu, S.,

Weisser, W. W., Schumacher, J., Hildebrandt, A. (2014). How do earthworms, soil texture and plant composition affect infiltration along an experimental plant diversity gradient in grassland? *PLoS One* 9(6): e98987.

Fischer, C., Tischer, J., Roscher, C. *et al.* (2015). Plant species diversity affects infiltration capacity in an experimental grassland through changes in soil properties. *Plant Soil*, 397: 1–16.

Flanagan, D. C., Foster, G. R., Neibling, W. H., and Burt, J. P. (1989). Simplified equations for filter strip design. *Transactions of the American Society of Agricultural and Biological Engineers*, 32(6): 2001–2007.

Fletcher, T. D., Andrieu, H., and Hamel, P. (2012). Understanding, management and modelling of urban hydrology and its consequences for receiving waters: A state of the art, *Advances in Water Resources*, 51(9): 261–279.

Fox, D. M., Le Bissonnais, Y. and Quétin, P. (1998a). The implications of spatial variability in surface seal hydraulic resistance for infiltration in a mound and depression microtopography. *Catena*, 32: 101–114.

Fox, D.M., Le Bissonnais, Y., and Bruand, A. (1998b). The effect of ponding depth on infiltration in a crusted surface depression. *Catena*, 32(2): 87–100.

Fox, G., Muñoz-Carpena, R., and Sabbagh, G. J. (2010). Influence of flow concentration on parameter importance and prediction uncertainty of pesticide trapping by vegetative filter strips. *Journal of Hydrology*, *384*(1–2): 164–173.

Freebairn, D. M., and Gupta, S. C., (1990). Microrelief, rainfall and cover effects on infiltration. *Soil and Tillage Research,* 16: 307–327.

Frei, S., and Fleckenstein, J. H. (2014). Representing effects of micro-topography on runoff generation and sub-surface flow patterns by using superficial rill / depression storage height variations. *Environmental Modelling & Software*, 52: 5–18.

Garcia-Serrana, M., Gulliver, J. S., Nieber, J. L. (2016) Enhancement and Application of the Minnesota Dry Swale Calculator, Final Report 2016-15. *Research Services and Library, Office of Transportation System Management, Minnesota Department of Transportation, April 2016.*

Garcia-Serrana, M., Gulliver, J. S., Nieber, J. L. (2016) Roadside swale calculator. *Stormwater Research at St. Anthony Falls Laboratory*. Retrieved from: http://stormwater.safl.umn.edu/resources/roadside-swale-calculator (accessed 10 January 2017).

Garcia-Serrana, M., Gulliver, J. S., Nieber, J. L. (2017) Infiltration Capacity of Roadside Filter Strips with Non-Uniform Overland Flow, *Journal of Hydrology*, 545 (2): 451–462.

Garcia-Serrana, M., Gulliver, J. S., Nieber, J. L. (2017b) Non-Uniform Overland Flow-Infiltration Model for Roadside Swales. *Journal of Hydrology* (under revision).

Ghimire, S. R. and Johnston, J. M. (2017). A modified eco-efficiency framework and methodology for advancing the state of practice of sustainability analysis as applied to green infrastructure. Integrated Environmental Assessment and Management. Accepted Author Manuscript. doi:10.1002/ieam.1928

Gilley, J..E. and Kottwitz, E.R. (1995). Darcy–Weisbach roughness coefficients for surfaces with residue and gravel cover. *Transactions American Society of Agricultural Engineers,* 38: 539–544.

Gish T. J, Jury, W. A. (1983). Effect of plant root channels on solute transport. Transactions of the American Society of Agricultural Engineers, 26: 440–444.

Gómez, J. A. and Nearing, M. A. (2005). Runoff and sediment losses from rough and smooth soil surfaces in a laboratory experiment. *Catena*, 59(3): 253-266.

Gómez, J. A., F. Darboux, and M. A. Nearing (2003). Development and evolution of rill networks under simulated rainfall, *Water Resources Research,* 39(6): 1–14.

Goodrich, D. C., Woolhiser, D. A., and Keefer, T. O. (1991). Kinematic routing using finite elements on a triangular irregular network, *Water Resources Research*, 27: 995–1004.

Govers, G., Takken, I., and Helming, K. (2000). Soil roughness and overland flow. *Agronomie*, 20(2): 131–146.

Green, T. R., and Erskine, R. H. (2004). Measurement, scaling, and topographic analyses of spatial crop yield and soil water content. Hydrologic Processes, 18(8): 1447–1465.

Green, W. H. and Ampt, G. (1911) Studies of soil physics, part I – the flow of air and water through soils. *Journal of Agricultural Science*, 4:1–24.

Grinden, A. (2014). Numerical Modeling of Combined Hydraulics and Infiltration in Grassed Swales. Master's Thesis, Norwegian University of Science and Technology, Trondheim, Norway.

Haan, C. T., Barfield, B. J. and Hayes, J.C. (1994) Design Hydrology and Sedimentology for Small Catchments. *New York: Academic Press*.

Hairsine, P. B. and Rose, C. W. (1992). Modeling Water Erosion Due to Overland Flow Using Physical Principles 2. Rill Flow. Water Resources Research, 28(1): 245–250.

Han, J., Wu, J. S., Allan, C. (2005) Suspended Sediment Removal by Vegetative Filter Strip Treating Highway Runoff. *Journal of Environmental Science and Health*, 40: 1637–1649.

Harel, M. A. and Mouche, E. (2014). Is the connectivity function a good indicator of soil infiltrability distribution and runoff flow dimension? *Earth Surface Processes and Landforms*, 39 (7): 1514–1525.

Haverkamp, R., Ross, P. J. ,Smettem, P. J., and Parlange, J. Y. (1994) Three-dimensional analysis of infiltration from the disc infiltrometer: 2. Physically based infiltration equation, *Water Resources Research*, 30: 2931–2935.

Hayes, J.C., Barfield, B.J., and Barnhisel, R.I. (1984). Performance of grass filters under laboratory and field Conditions, *Transactions of the American Society of Agricultural Engineers,* 27(5): 1321–1331.

Helmers, M. J. and Eisenhauer, D.E. (2006). Overland flow modeling in a vegetative filter considering non-planar topography and spatial variability of soil hydraulic properties and vegetation density. *Journal of Hydrology*, 328(1–2): 267–282.

Helmers, M. J., Eisenhauer, D. E., Franti, T. G., and Dosskey, M.G. (2005) Modeling sediment trapping in a vegetative filter accounting for converging overland flow. *Transactions of the American Society of Agricultural Engineers,* 48: 541–555.

Helming, K., Romkens, M. J. M., and Prasad, S. N. (1998). Surface Roughness Related Processes of Runoff and Soil Loss: A Flume Study. *Soil Science Society of America*, 62(1-2): 243-250.

Herman, J. D., Kollat, J. B., Reed, P. M., Wagener, T. (2013) Technical Note: method of Morris effectively reduces the computational demands of global sensitivity analysis for distributed watershed models, *Hydrology and Earth System Sciences*, 17: 2893–2903.

Holman-Dodds, J., K., Bradley, A.A., and Potter. K. W. (2003). Evaluation of hydrologic benefits of infiltration based urban storm water management, Journal of the American Water Resources Association, 39(1): 205–215.

Horn, R., Taubner, H., Wuttke, M. and Baumgartl, T. (1994). Soil physical properties related to soil structure. *Soil and Tillage Research*, 30: 187–216.

Horton, R. E. (1945). Erosional Development of Streams and their Drainage Basins; Hydrophysical approach to quantitative morphology. *Bulletin of the Geological Society of America*, 56(3): 175–370.

Huang, C. (1998). Quantification of soil microtopography and surface roughness, *Fractals in Soil Science,* edited by Baveye, P., Parlange, J. Y. and Stewart, B. A., *CRC Press*, Boca Raton, FL, USA, 153–168.

Huang, C. and Bradford J. M. (1992). Applications of a Laser Scanner to Quantify Soil Microtopography. *Soil Science Society of America*, 56: 14–21.

Hunt, W. F., Hathaway, J. M., Winston, R. J., and Jadlocki, S. J. (2010). Runoff Volume Reduction by a Level Spreader–Vegetated Filter Strip System in Suburban Charlotte, N.C. *Journal of Hydrologic Engineering*, 15(6): 499–503.

Hwang, C. C. and Weng, C. H. (2015). Effect of rainfall patterns on highway runoff and pollution and its control. *Water Environment Journal*, 29(2), 214–220.

Iman RL, Conover W. (1982) A distribution-free approach to inducing rank correlation among input variables. *Communication in Statistics-Simulations and Computation*, 11 (3): 311–34.

Iman, R. L. and Helton, J. C. (1988) An investigation of uncertainty and sensitivity analysis techniques for computer models. *Risk Analysis*, 8(1): 71–90.

Imeson A. C. and Verstraten J. M. (1988). Rills on badlands slopes; a physico-chemically controlled phenomenon. *Catena Supplement 12*: 139–150.

James, T. D., Carbonneau, P. E., Lane, S. N. (2007). Investigating the effects of DEM error in scaling analysis. *Earth Surface Processes and Landforms*, 73(1): 67–78.

Jarvis, N. J. (2007). A review of non-equilibrium water flow and solute transport in soil macropores: Principles, controlling factors and consequences for water quality. *European Journal of Soil Science*, 58: 523–546.

Jester, W., and Klik, A. (2005). Soil surface roughness measurement—methods, applicability, and surface representation. *Catena*, 64(2-3): 174–192.

Kale, R. V. and Sahoo, B. (2011) Green-Ampt Infiltration Models for Varied Field Conditions: A Revisit. *Water Resources Management*, 25: 3505–3536.

Kanafi, M. M. and Tuononen, A. J. (2017). Top topography surface roughness power spectrum for pavement friction evaluation. *Tribology International*, 107(3): 240–249.

Kavvas, M. L., Chen, Z. Q., Dogrul, C., Yoon, J. Y., Ohara, N., Liang, L., and Matsuura, T. (2004). Watershed Environmental Hydrology (WEHY) Model Based on Upscaled Conservation Equations : Hydrologic Module. *Journal of Hydrologic Engineering*, 11(5-6): 450–464.

Kayhanian, M., Fruchtman, B., Gulliver, J. S., Montanaro, C., and Raniere, E. (2012). Review of Highway Runoff Characteristics: Comparative Analysis and Universal Implications. *Water Research*, 46 (20): 6609–6624.

Kirkby, M. (1988) Hillslope runoff processes and models. *Journal of Hydrology*, 100: 315–339.

Kirkby, M. J. (2014). Do not only connect: a model of infiltration-excess overland flow based on simulation. *Earth Surface Processes and Landforms*, 39(7): 952–963.

Klinkenberg, B. and Goodchild, F. (1992). The fractal properties of topography: a comparison of methods. *Earth Surface Processes and Landforms*, 17: 217–234.

Knight, E. M. P., Hunt, W. F., and Winston, R. J. (2013). Side-by-side evaluation of four level spreader-vegetated filter strips and a swale in eastern North Carolina. *Journal of Soil and Water Conservation*, 68(1): 60–72.

Kreeb, L. B., McCuen, R. H. (2003). Hydrologic Efficiency and Design Sensitivity of Bioretention Facilities. *University of Maryland*, College Park, MD.

Kuipers, H. (1957). A reliefmeter for soil cultivation studies. *Netherlands Journal of Agricultural Science,* 5: 255-267.

Lancaster, C. D. (2005). A Low Impact Development Method for Mitigating Highway Stormwater Runoff - Using Natural Roadside Environments for Metals Retention and Infiltration. Masters Thesis, *Washington State University, Department of Civil and Environmental Engineering*, Pullman, Washington, USA.

Lane, S. N. (2005). Roughness - Time for a re-evaluation? *Earth Surface Processes and Landforms*, 30(2): 251–253.

Larson, W. E., Lindstrom, M.J., Schumacher, and T.E. (1997) The role of severe storms in soil erosion: A problem needing consideration. *Journal of Soil and Water Conservation*, 52(2): 90–95.

Lassabatere, L., Angulo-Jaramillo, R., Soria Ugalde, J. M., Simunek, J., and Haverkamp, R. (2009) Numerical evaluation of a set of analytical infiltration equations. *Water Resources Research*, 45, W12415.

Le Bissonnais Y., and Bruand A. (1993). Crust micromorphology and runoff generation on silty soil materials during different seasons. *Catena Supplement* 24: 1–16.

Le Bissonnais, Y., Lecomte, V., and Cerdan, O. (2004). Grass strip effects on runoff and soil loss. *Agronomie*, EDP Sciences, 24 (3): 129-136.

Leavesley, G. H., Lichty, R. W., Troutman, B. M., and Saindon, L.G. (1983). *Precipitation-Runoff Modeling System: User's Manual.* U.*S. Geological Survey, Water-Resources Investigations* Report 83–4238.

Leconte R., Brissette F. P. (2001) Soil moisture profile model for two-layered soil based on sharp wetting front approach. *Jounal of Hydrologic Engineering, ASCE* 6(2): 141–149.

Lee, R. S., Traver, R. G. and Welker, A. L. (2016). Evaluation of soil class proxies for hydrologic performance of in situ bioinfiltration systems, *Journal of Sustainable Water in the Built Environment*, 04016003.

LeFevre, G. H., Paus, K. H., Natarajan, P., Gulliver, J. S., Novak, P. J., Hozalski, R. M. (2014). Review of dissolved pollutants in urban storm water and their removal and fate in bioretention cells, *Journal of Environmental Engineering*, *ASCE*, 141(1), 04014050.

Legout, C., Darboux, F., Nédélec, Y., Hauet, A., Esteves, M., Renaux, B., and Cordier, S. (2012). High spatial resolution mapping of surface velocities and depths for shallow overland flow. *Earth Surface Processes and Landforms*, 37(9): 984–993.

Li, R.M., Stevens, M.A., and Simons, D.B. (1976). Solutions to Green-Ampt Infiltration Equation. *Journal of Irrigation and Drainage. Division of ASCE 102(IR2): 239–248.*

Lighthill, M.J. and Whitham, G.B. (1955). On kinematic waves. I. Flood movement in long rivers. *Proceedings of the Royal Society of* London. *Series A, Mathematical and Physical Sciences.* 229 (1178): 317–345.

Liu, Y., Hu, J., Wang, T., Cai, C., Li, Z., and Zhang, Y. (2016). Effects of vegetation cover and road-concentrated flow on hillslope erosion in rainfall and scouring simulation tests in the Three Gorges Reservoir Area, China. *Catena*, 136: 118-117.

Loague, K. and R. Green (1991). Statistical and graphical methods for evaluating solute transport models: Overview and application. *Journal of Contaminant Hydrology*, 7: 51–73.

Lucke, T., Mohamed, M. A. K., Tindale, N. (2014). Pollutant removal and hydraulic reduction performance of field grassed swales during runoff simulation experiments. *Water*, 6: 1887–1904.

Magunda, M. K., Larson, W. E., Linden, D. R., and Nater, E. (1997). Changes in microrelief and their effects on infiltration and erosion during simulated rainfall. *Soil Technology*, 10(1): 57–67.

Mandelbrot, B B. (1982) The Fractal Geometry of Nature. *Freeman Press*, Oxford, 1982.

MATLAB and Statistics Toolbox Release 2016a, *The MathWorks, Inc.*, Natick, Massachusetts, United States.

Mattia, F., Davidson, M. W. J., Le Toan, T., D'Haese, C. M. F.. Verhoest, N. E. C.. Gatti, A. M.. Borgeaud, M. (2003). A comparison between soil roughness statistics used in surface scattering models derived from mechanical and laser profilers. *IEEE Transactions on Geoscience and Remote Sensing*, 41: 1659–1671.

McGuire, L. A., Pelletier, J. D., Gómez, J. A, and Nearing, M. A. (2013) Controls on the spacing and geometry of rill networks on hillslopes: Rain splash detachment, initial

hillslope roughness, and the competition between fluvial and colluvial transport. *Journal of Geophysical* Research: Earth Surface, 118: 241–256.

McKenzie, E. R., Money, J. E., Green, P. G. and Young, T.M. (2009) Metals Associated with Stormwater-Relevant Brake and Tire Samples. *Science of the Total Environment*, 407, 5855–5860.

Mein, R.G. and Larson, C.L. (1971). Modelling the infiltration component of the rainfall-runoff process, *Bulletin 43, University of Minnesota, MN, Water Resources Research Center.*

Merrill, D. (1998). Comments on the chain method for measuring soil surface roughness: use of the chain set. *Soil Science Society of America Journal,* 62: 1147– 1149

Minton, G. R. (2005) Stormwater Treatment Biological, Chemical, and Engineering Principals, *Sheridan Books, Inc.*

Mitchell A. R., Ellsworth T. R., and Meek, B. D. (1995). Effect of root systems on preferential flow in swelling soil. *Communications in Soil Science Plant Analysis*, 26: 2655–2666.

Moore, I. D. (1981). Infiltration Equations Modified for Surface Effects. *Transactions of the American Society of Agricultural Engineers*, 24:1546-1553.

Moore, I. D. and Grayson, R. B. (1989). Hydrologic and digital terrain modeling using vector elevation data. *Eos* Trans. AGU, 70, 1091.

Morgan, R. P. C., Quinton, J. N., Smith, R. E., Govers, G. Poesen, J. W. A., Auerswald, K., Chisci, G., Torri, D., and Styczen, M. E. (1998). The European Soil Erosion Model (EUROSEM): A dynamic approach for predicting sediment transport from fields and small catchments. *Earth Surface Processes and Landforms*, *23*: 527–544.

Morris, M. D. (1991) Factorial sampling plans for preliminary computational experiments. *Technometrics* 33(2): 161–174.

Muñoz-Carpena, R., Garey, F. G., and Sabbagh, G.J. (2010) Parameter Importance and Uncertainty in Predicting Runo Pesticide Reduction with Filter Strips. *Journal of Environmental Quality*, 39: 630–641.

Muñoz-Carpena, R., Parsons, J.E., and Gilliam, J.W. (1999). Modeling overland flow and sediment transport in vegetative filter strips: Model development and application. *Journal of Hydrology 214:111–129.*

Muñoz-Carpena, R., Zajac, Z., and Kuo, Y.M. (2007). Global sensitivity and uncertainty analysis of the water quality model VFSMOD-W. *Transactions of the American Society of Agricultural and Biological Engineers*, 50 (5): 1719–1732.

Muñoz-Carpena, R.,Parsons, J.E. and Gilliam, J.W. (1993). Numerical approach to the overland flow process in vegetative filter strips. *Transactions of the American Society of Agricultural Engineers*. 36(3): 761–770.

National Research Council (2009). Urban Stormwater Management in the United States. Washington, D.C., *The National Academies Press*.

Neuman, S. P. (1976) Wetting front pressure head in the infiltration model of Green and Ampt, *Water Resources Research,* 12(3): 564–566.

Nord, G. and Esteves, M. (2005). PSEM_2D: A physically based model of erosion processes at the plot scale. *Water Resources Research*, 41, W08407.

Novotny, V., Olem, H. (1994) Water quality: Prevention, Identification, and Management of Diffuse Pollution. *Van Nostrand-Reinhold*, New York, NY.

Olson, N. C., Gulliver, J. S., Nieber, J. L., Kayhanian, M. (2013). Remediation to improve infiltration into compact soils. *Journal of Environment Management*, 117: 85–95.

Orford, J. D. and Whalley, W. B. (1983) The use of the fractal dimension to quantify the morphology of irregular-shaped particles, *Sedimentology*, 30: 655–668.

Parsons, A. J., Abrahams, A. D. and Luk S-H. (1990). Hydraulics of interrill overland flow on a semi-arid hillslope, southern Arizona. *Journal of Hydrology,* 117: 255–273.

Paz-Ferreiro, J., Bertol, I., and Vazquez, E.V. (2008). Quantification of tillage, plant cover, and cumulative rainfall evects on soil surface microrelief by statistical, geostatistical and fractal indices. *Nonlinear Processed in Geophysics*. 15: 575–590.

Pentland, A. P. (1984). Fractal-based descriptions of natural scenes. *IEEE Transactions on Pattern Analysis and Machine Intelligence*, 6: 661–674.

Peñuela, A., Javaux, M., and Bielders, C. L. (2015). How do slope and surface roughness affect plot-scale overland flow connectivity? *Journal of Hydrology*, *528*: 192–205.

Perica, S., D. Martin, S. Pavlovic, I. Roy, M. St. Laurent, C. Trypaluk, D. Unruh, M. Yekta, G. Bonnin (2013). NOAA Atlas 14 Volume 8, Precipitation-Frequency Atlas of the United States, Midwestern States. NOAA, National Weather Service, Silver Spring, MD.

Philip, J. R. (1957). The theory of infiltration: 1. The infiltration equation and its solution. *Soil science*, 83(5): 345–358.

Pianosi, F. and Wagener, T. (2015) A simple and efficient method for global sensitivity analysis based on cumulative distribution functions. *Environmental Modelling & Software*, 67: 1–11.

Pianosi, F., Beven, K., Freer, J., Hall, J. W., Rougier, J., Stephenson, D. B., and Wagener, T. (2016) Sensitivity analysis of environmental models: A systematic review with practical workflow. *Environmental Modelling & Software*, 79(5): 214–232.

Pianosi, F., Sarrazin, F., and Wagener, T. (2015) A Matlab toolbox for Global Sensitivity Analysis. *Environmental Modelling & Software*, 70: 80–85.

Podmore, T. H. and Huggins, L. F. (1981). An automated profile meter for surface roughness measurements. *Transactions of American Society of Agricultural Engineers,* 24 (3): 663–665, 669.

Poletika, N., Coody, P. N., Fox, G., Sabbagh, G. J., Dolder, S. C., and White, J. (2009). Chlorpyrifos and atrazine removal from runoff by vegetated filter strips: experiments and predictive modeling. *Journal of Environmental Quality*, *38*(3): 1042–1052.

Preston, S., Griffiths, B. S. and Young, I. M. (1997). An investigation into sources of soil crack heterogeneity using fractal geometry. *European Journal of Soil Science*, 48: 31–37.

Prewitt, J. M. S. and Mendelsohn, M. L. (1966). The analysis of cell images, *Annals of the New York Academy of Sciences,* 128: 1035-1053.

Rasband W. S. (1997–2014). ImageJ, U.S. National Institutes of Health, Bethesda, MD. Internet, url: imagej.nih.gov/ij/ (accessed January 15, 2016).

Rawers, J. and Tylczak, J. (1999). Fractal characterization of wear-erosion surfaces. *Journal of Materials Engineering and Performance*, 8(6): 669–676.

Richards, L. A. (1931) Capillary conduction of liquids through porous mediums. *Physics*, 1(5): 318–333.

Rieke-Zapp, D. H., (2002). Digital close range photogrammetry for generation of digital soil surface elevation models—methodology and applications for soil erosion experiments. *Ph.D. dissertation, Purdue University, West Lafayette, Indiana*. 204 pages.

Robichaud, P. R., and Molnau, M. (1990). Measuring soil roughness changes with an ultrasonic profiler. *Transactions of American Society of Agricultural Engineers* 33 (6): 1851–1858.

Römkens, M. J. and Wang, J.Y. (1986). Effect of tillage on surface-roughness. *Transactions of the American Society of Agricultural Engineers*, 29: 429–433.

Rossi, M. J. and Ares, J. O. (2012). Close range stereo-photogrammetry and video imagery analyses in soil eco-hydrology modelling, *Photogramm*. Record, 27: 111–126.

Russ, J. C. (1994). Fractal Surfaces, *Plenum Press*, NewYork.

Saleh, A. (1993). Soil roughness measurement: chain method. *Journal of Soil Water Conservation.* 48: 527– 529.

Saltelli, A., Ratto, M., Andres, T., Campolongo, F., Cariboni, J., Gatelli, D., Saisana, M., Tarantola, S. (2008). Global Sensitivity Analysis. The Primer. *Wiley*.

Sarrazin, F., Pianosi, F., and Wagener, T. (2016) Global Sensitivity Analysis of environmental models: Convergence and validation. *Environmental Modelling & Software*, 79(5): 135–152.

Shelberg, M.C., Lam, N. S. N., and Moellering, H., (1983). Measuring the fractal dimension of surfaces. *Proceedings of the Sixth International Symposium on Computer-Assisted Cartography (*Auto–Carto 6), 319–328.

Shen, H., Zheng, F., Wen, L., Lu, J., Jiang, Y. (2015). An experimental study of rill erosion and morphology. *Geomorphology*, 231: 193–201.

Singer, M. J., and Le Bissonnais, Y. (1998). Importance of surface sealing in the erosion of some soils from a Mediterranean climate. *Geomorphology*, 24(1): 79–85.

Singh, V. and Woolhiser, D. (2002). Mathematical Modeling of Watershed Hydrology. *Journal of Hydrologic Engineering*, 7:4(270): 270–292.

Singh, V.P. (2001). Kinematic wave modelling in water resources: a historical perspective. *Journal of Hydrological Processes* 15(4): 671–706.

Singh, V.P. (2002) Is hydrology kinematic? *Hydrological Processes,* 16(3): 667–716.

Smith, M. W. (2014). Roughness in the Earth Sciences. *Earth-Science Reviews*, 136: 202–225.

Smith, M. W., Cox, N. J., and Bracken, L. J. (2011a). Modeling depth distributions of overland flows. *Geomorphology*, 125(3): 402–413.

Smith, M. W., Cox, N. J., and Bracken, L. J. (2011b). Terrestrial laser scanning soil surfaces: a field methodology to examine soil surface roughness and overland flow hydraulics. *Hydrological Processes*, 25(6): 842–860.

Smith, R. E., Goodrich, D. C., Woolhiser, D. A., and Unkrich, C. L., (1995). KINEROS: a kinematic runoff and erosion model; chapter 20. In: Singh, V.P. (Ed.), *Computer Models of Watershed Hydrology*. Water Resources Publications, Highlands Ranch, Colorado, 1130 pp.

Stagge, J. H., Davis, A. P., Jamil, E., Kim, H. (2012). Performance of grass swales for improving water quality from highway runoff. *Water Resources*, 46: 6731–6742.

Stomph, T. J., De Ridder, N., Steenhuis, T. S., and Van De Giesen, N. C. (2002). Scale effects of Hortonian overland flow and rainfall-runoff dynamics: Laboratory validation of a process-based model. *Earth Surface Processes and Landforms*, 27(8): 847–855.

Strecker, E., Poresky, A., Roseen, R., Soule, J., Gummadi, V., Dwivedi, R. and Venner, M. (2014). Volume Reduction of Highway Runoff in Urban Areas: Final Report and NCHRP Report 802 Appendices C through F (No. NCHRP Project 25-41).

Subbaiah R. (2013) A review of models for predicting soil water dynamics during trickle irrigation. *Irrigation Science,* 31(3): 225–258.

Sun, W., Xu, G., Gong, P., and Liang, S. (2006). Fractal analysis of remotely sensed images: A review of methods and applications. *International Journal of Remote Sensing*, 27(22): 4963–4990.

Sung, Q. C., Chen, Y. C., and Chao, P. C. (1998). Spatial variation of fractal parameters and its geological implications. *Terrestrial, Atmospheric, and Oceanic Sciences Journal,* 9(4): 655–672.

Tayfur, G., Kavvas, M. L., Govindaraju, R. S., and Storm, D. E. (1993). Applicability of St. Venant Equations for Two-Dimensional flows over rough infiltrating surfaces. *Journal of Hydrologic Engineering*, 119(1): 51–63.

Thompson, S. E., Katul, G. G., and Porporato, A. (2010). Role of microtopography in rainfall-runoff partitioning: An analysis using idealized geometry. *Water Resources Research,* 46(7). W07520.

Tourbier, J. T. (1994). Open-Space Through Storm water Management. *Journal of Soil and Water Conservation*, 49(1): 14–21.

Turner, M.J. Blackledge, J.M., and Andrews, P.R. (1998) Fractal Geometry in Digital Imaging, *Academic Press*, New York.

U. S. Geological Survey (2003). National Highway Runoff Water-Quality Data and Methodology Synthesis, Volume I-Technical Issues for Monitoring Highway Runoff and Urban Stormwater, *Office of Natural Environment*, FHWA-EP-03-054.

U.S. Army Corps of Engineers (1990). HEC-1 Flood Hydrograph Package, Users

Manual: July 1990. *Hydrologic Engineering Center*, Davis, CA.

U.S. Department of Agriculture (1980). CREAMS: A field scale model for chemicals, runoff, and erosion from agricultural management systems. *Conservation research report No. 26, W. G. Knisel, ed.*, USDA, Washington, DC.

U.S. Department of Agriculture (1986). Urban Hydrology for Small Watersheds. *National Resources Conservation Service.* Technical Release (TR) 55, June 1986.

U.S. Department of Agriculture (2014). Natural Resources Conservation Service Soil. Internet, url: http://www.nrcs.usda.gov/wps/portal/nrcs/detail/soils/survey/?cid=nrcs142p2_054167 (accessed December 5, 2015).

U.S. Department of Transportation - Federal Highway Administration (2010) Carbon Sequestration Pilot Program. Estimated Land Available for Carbon Sequestration in the National Highway System. Federal Highway Administration Office of Planning, Environment and Realty, Washington, DC, USA.

U.S. Environmental Protection Agency (2009). Technical guidance on implementing the stormwater runoff requirements for federal projects under Section 438 of the Energy Independence and Security Act. EPA 841-B-09-001, Washington, DC.

Valentin, C., (1991). Surface crusting in two alluvial soils of northern Niger. *Geoderma,* 48: 201–222.

van Genuchten, M. T. (1980) A closed-form equation for predicting the hydraulic conductivity of unsaturated soils. *Soil Science Society of America Journal*, 44(5): 892–898.

Vázquez, E. V., Miranda, J. G. V., and González, A. P. (2005). Characterizing anisotropy and heterogeneity of soil surface microtopography using fractal models. *Ecological Modeling*, 182(3-4): 337–353.

Vázquez, E. V., Miranda, J. G. V., and González, A. P. (2007). Describing soil surface microrelief by crossover length and fractal dimension. *Nonlinear Processes in Geophysics*, 14(3): 223–235.

Verhoest, N. E., Lievens, H.,Wagner, W., Álvarez-Mozos, J., Moran, M. S.,Mattia, F., (2008). On the soil roughness parameterization problem in soil moisture retrieval of bare sur- faces from synthetic aperture radar. *Sensors,* 8: 4213–4248.

Vermang, J., Norton, L. D., Huang, C., Cornelis, W. M., da Silva, A. M. and Gabriels, D. (2015). Characterization of Soil Surface Roughness Effects on Runoff and Soil Erosion Rates under Simulated Rainfall. *Soil Science Society of America Journal*, 78(3): 903–916.

Vermang, J., Norton, L.D., Baetens, J., Huang, C., Cornelis, W. M., and Gabriels, D. (2013). Quantification of soil surface roughness evolution under simulated rainfall. *Trans. ASABE* 56: 505–514.

Vogel, T., van Genuchten, M. Th., and Cislerova, M. (2001) Effect of the shape of the soil hydraulic functions near saturation on variably-saturated flow predictions. *Advances in Water Resources,* 24: 133–144.

Walsh, P. M., Barrett, M. E., Malina Jr., J. F., and Charbeneau, R. J. (1997). Use of vegetative controls for treatment of highway runoff. Online Rep. No. 97-5, *Center for Research in Water Resources*, University of Texas at Austin.

Warner, W. S. (1995). Mapping a three-dimensional soil surface with handheld 35 mm photography. *Soil and Tillage Research,* 34: 187–197.

Warrick, A. (2003). Soil water dynamics, Oxford University Press, New York.

Warrick, A. W., and Lazarovitch, N. (2007). Infiltration from a strip source. *Water Resources Research*, 43(3), W03420.

Warrick, A. W., Zerihun, D., Sanchez, C. A., and Furman, A. (2005). Infiltration under variable ponding depths of water. *Journal of Irrigation Drainage Engineering*, 10.1061/(ASCE)0733-9437(2005)131:4(358), 358–363.

Warrick, A.W., Lazarovitch, N., Furman, A., and Zerihun, D. (2007) Explicit infiltration function for furrows. *Journal of Irrigation and Drainage Engineering*, 10.1061/(ASCE)0733-9437(2007)133:4(307): 307–313.

Wegmann, H., Rieke-Zapp, D. and Folke, S. (2001). Digital photogrammetry for measuring soil surface roughness. *Proceedings of the American Society of Photogrammetry and Remote Sensing, 2001 Annual Conference, St. Louis, MO, USA*.

Weiss, P. T. and Gulliver, J. S. (2015). Effective Saturated Hydraulic Conductivity of an Infiltration-Based Stormwater Control Measure. *Journal of Sustainable Water Built Environment*, 10.1061/JSWBAY.0000801, 04015005.

Welch, R. T., Jordan, T. R. and Thomas, A. W. (1984). A photogrammetric technique for measuring soil erosion. *J. Soil Water Conservation,* 39: 191–194.

Western, A. W., Blöschl, G., and Grayson, R. B. (2001). Toward capturing hydrologically significant connectivity in spatial patterns. *Water Resources Research*, 37(1): 83–97.

Whalley, W. B. and Orford, J. D. (1989). The use of fractals and pseudofractals in the analysis of two-dimensional outlines: Review and further exploration. Computers and Geosciences, 15: 185–197.

Winston, R. and Hunt, W. (2016). Characterizing Runoff from Roads: Particle Size Distributions, Nutrients, and Gross Solids. *Journal of Environmental Engineering*, 10.1061/(ASCE)EE.1943-7870.0001148, 04016074.

Woolhiser, D. A. and Liggett, J. A. (1967). Unsteady one-dimensional flow over a plane – the rising hydrograph, *Water Resources Research*, 3: 753–771.

Woolhiser, D. A., Smith, R.E. and D. C. G. (1990). KINEROS, a kinematic runoff and erosion model. Documentation and User Manual. U.S. Department of Agriculture, Agricultural Research Service, ARS-77, 130 pp.

Wu, J. S, Allan, C. J. Saunders, L. and Evett, J. B. (1998). Characterization and pollutant loading estimation for highway runoff. *Journal Environmental Engineering*, 124(7): 584–592.

Yang, J. and Chu, X. (2013). Effects of DEM Resolution on Surface Depression Properties and Hydrologic Connectivity. *Journal of Hydrologic Engineering,* Vol.18 (9): 1157–1169.

Yang, J., and Chu, X. (2015). A new modeling approach for simulating microtopography-dominated, discontinuous overland flow on infiltrating surfaces. *Advances in Water Resources*, 78: 80–93.

Yonge, D. (2000). Contaminant Detention in Highway Grass Filter Strips, Report WA-RD 474.1, *Washington State Transportation Commission*, Olympia, WA.

Young, B. (2006). Mapping the rainfall event for stormwater quality control. University of Kansas, Report No. K-TRAN: KU-03-1.

Yu, S.L., Kuo, J.T., Fassman, E.A., and Pa, H. (2001) Field test of grassed swale performance in removing runoff pollution. *Journal of Water Resources Planning and Management*, 127(3): 168–171.

Zhang H., Ta, N., and Zhang, Q. (2016). Spatial heterogeneity of loess contour tilled microtopographic slope in rainfall erosion, *Soil Science and Plant Nutrition*, 62 (5-6): 409–415.

Zhang J. (2006). Detection and monitoring of wear using imaging methods. Ph.D. Thesis, University of Twente, The Netherlands.

Zhang, P., Tang, H., Yao, W., Zhang, N., Xizhi, L.V. (2016). Experimental investigation of morphological characteristics of rill evolution on loess slope. *Catena*, 137: 536–544.

Zheng, Z. C., He, S. Q., and Wu, F.Q. (2014). Changes of soil surface roughness under water erosion process. *Hydrological Processes,* 28: 3919–3929.

Zimmie T. F. and LaPlante C. (1990). The effect of freeze-thaw cycles on the permeability of a fine-grained soil. *Proceedings of the 22nd Mid-Atlantic Industrial Waste Conference*. Drexel University, Pennsylvania: 580–593.

Appendix A

Supporting information for Chapter 6

Model Code

Matlab Code of the Roadside Swale Model:

A) **General Script**
B) **Function: Runoff_sideslope**
C) **Function: Runoff_channel**
D) **Green_Ampt_rate_ML**

A) General Script

```
%Roadside swale model that couples Green-Ampt-Mein-Larson (GAML)
%infiltration submodel with kinematic wave submodels for both overland flow
%down the side slope and open channel flow for flow in the channel.

clear all % clear variables
close all % close open windows

%% Inputs%%%%%%%%%%%%%%%

%The user needs to provide values for all the following inputs:
i=4; % rainfall intensity  [cm/hr]
Ks=4; %Saturated hydraulic conductivity of the soil [cm/h]
psi=5; % Effective wetting front suction of the soil [cm]
deltheta=0.3; % Soil water deficit [-]
n=.25;% Manning's n value [SI s/m^(1/3)]
length=4; %Length of the side slope, perpendicular to the road [m]
Sside=1/5; % Side slope [-]
Channel_length=10; %Length of the channel, parallel to the road [m]
Schannel=0.02; % Channel slope [-]
w_road=10; %Length of road in direction of the swale slope (perpendicular to
%traffic) [m]
B=0.375; %Width of the rectangular channel, perpendicular to the road [m]
duration_storm=1; %Duration of the storm event [h]
duration=1.2; %Duration of the study (duration>duration_storm) [h]
ds=1; %Depression storage of the side slope [mm]
ds_ch=0; %Depression storage of the channel [mm]
w_side=0.914; % Width of the side slope study area [m]
fw=0.7; %Fraction wetted (if fw over the side slope is a constant over space)[-]
T=50000; %Number of time steps for the simulation

%%Calculations Side Slope %%%%%%%%%%%%%%%%

%% Side Slope where road runoff is routed
```

```
%Flow from the road and rainfall over the area of the side slope where flow
concentrates–Fraction of wetted area  (fw)

ir=i; % Rainfall intensity over the road
%1) Function for the side slope (fw)
[Total_Inflow_1,Runoff_1,Infiltration_1, Qslope1]=Runoff_sideslope(i,ir, fw, Ks,
Sside, length, w_side, w_road, duration,duration_storm, T, ds, psi, deltheta,n);

%% Side Slope without road runoff
% Rainfall over the “dry” area of the side slope – (1-fw)

ir=0; % No road inflow
%2) Function for the side slope (1-fw)
if fw<1
   [Total_Inflow_2,Runoff_2,Infiltration_2, Qslope2]=Runoff_sideslope(i,ir, (1-fw),
Ks, Sside, length, w_side, w_road, duration, duration_storm, T, ds, psi,
deltheta,n);
else
   Total_Inflow_2=0;
   Runoff_2=0;
   Infiltration_2=0;
    Qslope2=0;
end

%Results from the two side slope submodels
Q_side=transpose(Qslope1)+transpose(Qslope2); %From from the side
%entering the channel
Total_Inflow=Total_Inflow_1+Total_Inflow_2; %Inflow Volume
Total_Runoff=Runoff_1+Runoff_2; %Runoff Volume
Infiltration=Infiltration_1+Infiltration_2; %Infiltration Volume (side slope)

%%Calculations Channel %%%%%%%%%%%%%%%%

ds=ds_ch; %depression storage of the channel [mm]
%3)Function for the channel flow with input from the side slope
[Runoff_3,Infiltration_3,rain_3,ratio_ch_side]=Runoff_channel(i, Ks, Schannel,
Q_side, Channel_length, w_side, duration,duration_storm, T, ds, psi, deltheta,n,
B);


%%Side Slope + Channel Results %%%%%%%%%%%
```

```
TOTAL_INFLOW=Total_Inflow*ratio_ch_side+rain_3; %Total Inflow Volume
INFILTRATION=Infiltration*ratio_ch_side+Infiltration_3; %Total Infiltration
%Volume
RUNOFF=Runoff_3; %Total runoff – only from the channel
Total_PERCENTAGE_INFILT=100*(INFILTRATION/TOTAL_INFLOW);
%Percentage infiltration = infiltration volume / total input volume
Side_Slope_inf_perc=100*(Infiltration*ratio_ch_side/INFILTRATION);
%Percentage of the infiltration volume loss in the side slope
Channel_inf_perc=100-Side_Slope_inf_perc;
%Percentage of the infiltration volume loss in the channel

%%%%%%%%%Print Results %%%%%%%%%%%%%%%%
fprintf('Total Inflow Swale = %.1f L\n',TOTAL_INFLOW);
fprintf('Total Infiltration = %.1f L\n',INFILTRATION);
fprintf('Total Runoff = %.1f L\n',RUNOFF);
fprintf('Mass Balance Error = %.4f%%\n',100*(((TOTAL_INFLOW)-
(INFILTRATION+RUNOFF))/TOTAL_INFLOW));
fprintf('Percentage Infiltration %.2f%%\n',Total_PERCENTAGE_INFILT);
fprintf('Percentage Infiltration Side Slope = %.2f%%\n',Side_Slope_inf_perc);
fprintf('Percentage Infiltration Channel = %.2f%%\n',Channel_inf_perc);
```

B) Function: Runoff_sideslope

```
function [Total_Inflow,Runoff,Infiltration, Qslope]=Runoff_sideslope(i,ir,fw,Ks,
Sside, length, w_side, w_road ,duration, duration_storm, T, ds, psi, deltheta,n)

%This function uses the Kinematic wave approximation to solve for runoff rate
and infiltration for the side slope of a roadside swale

%% Inputs Definition%%%%
%i - Rainfall intensity over swale [cm/hr]
%ir - Rainfall intensity over road [in/hr]
%Ks - Saturated hydraulic conductivity [cm/h]
%length - Length of slope [m]
%duration - Duration of study [h]
%duration_storm  - Duration of storm event [h]
%T - Number of time steps
%ds - depression storage [mm]
%psi - effective wetting front suction [cm]
%deltheta - Soil water deficit
```

```
%n - Manning's n value [s/m^(1/3)]
%w_side - Width of the side-slope study area [m]
w_cell=w_side; % Width of study area [m]
S=Sside; % Side slope [-]
rows=100; % Number of sections down the slope (selected by user)
%fw - Fraction wetted (it can be a constant or a matrix of values)
fw=fw*ones(rows,1); % Fraction wetted (Option 1:constant)
%or fw= xlsread('Name of Excel file')(Option 2: matrix size [rows,1])
%   (1-fw)=ones(rows,1)- fw;


%% Unit conversions
ir=ir*10/3600; % Converts to mm/s
i=i*10/3600; % Converts to mm/s
length=length*1000; % Converts to mm
w_road=w_road*1000; % Converts to mm
w_cell=w_cell*1000; % Converts to mm
duration=duration*3600; % Converts to s
duration_storm=duration_storm*3600; % Converts to s
psi=psi*10; % Converts to mm
Ks=Ks/360; % Converts to mm/s
n=n/10; % Converts to [s/mm^(1/3)]

%%Kinematic wave Variables
m=5/3;
Beta=m-1;
a=(S^0.5)/n;
alpha=a*m;

%%Simulation Parameters
dx=length/rows; %length of each cell
dt=duration/T; %duration of each time step
T_s=round(duration_storm/dt); %last time step of the storm

%%%%%%%%%%%% Calculations %%%%%%%%%%%
max_Cou=1; %initial value of maximum Courant number

while max_Cou>=1
    % Setting up variables
    qin=zeros(T,rows);
    Volinf=zeros(rows,1);
    qout=zeros(T,rows);
```

```
Qout=zeros(T,rows);
ie=zeros(T,rows);
f=zeros(T,rows);
F=zeros(rows,1);
h=zeros(T,rows);
Cou=zeros(T,rows);
infil=0;
standing=0;
qslope=zeros(T,1);
Int_e=zeros(T,rows);
SurfaceSat=zeros(rows,1);
runoff=0;
Runoff_rate=0;
Input_road=0;

% Unsteady Input of water
ir_v=zeros(T,1);
i_v=zeros(T,1);
for j=2:T_s+1
    ir_v(j)=ir;
    i_v(j)=i;
end

%Initial condition: h=0 q=0
for j=1:(T-1) % Loop through time
  for k=1:rows % Loop through space
      if k==1 %First cell
        qin(j+1,k)=ir_v(j)*w_road/fw(k); % Inflow from road
        Input_road=Input_road+qin(j+1,k)*w_cell*fw(1)*dt; %mm3 of water input
from road
      else
        qin(j+1,k)=Qout(j+1,k-1)/(w_cell*fw(k)); % Inflow from cell above
      end
      ie(j+1,k)=qin(j+1,k)/dx+i_v(j); % Effective intensity

      %%Infiltration Submodel Green-Ampt-Mein-Larson
      if ie(j+1,k)==0
         if h(j,k)>0 %Ponded water
            ie(j+1,k)=h(j,k)/dt;
         end
      end
      [f(j+1,k),
```

```
SurfaceSat(k)]=Green_Ampt_rate_ML(psi,deltheta,Ks,ie(j+1,k),dt,F(k),SurfaceSat
(k));
        F(k)=F(k)+f(j+1,k)*dt; %infiltration depth

         %Explicit numerical solution for h
          if k==1 %first cell
              Int_e(j+1,k)=qin(j+1,k)/dx-f(j+1,k)+i_v(j);
              h(j+1,k)=h(j,k)-
(dt/dx)*(qout(j,k)*((0.5*(fw(1)+fw(2))/fw(1))))+(0.5*(Int_e(j,k)+Int_e(j+1,k)))*dt;
              if h(j+1,k)>ds
                 qout(j+1,k)=a*(h(j+1,k)-ds)^m;
              end
          else %Rest of the cells
             Int_e(j+1,k)=-f(j+1,k)+i_v(j);
          end

          if k>1 %Rest of the cells
            if j==1 %First time step
              h(j+1,k)=dt*0.5*(Int_e(j,k)+Int_e(j+1,k));
              if h(j+1,k)>ds
                 qout(j+1,k)=a*(h(j+1,k)-ds)^m;
              end
            else %Rest of time steps
               if k<rows
                  h(j+1,k)=dt*0.5*(Int_e(j,k)+Int_e(j+1,k))+h(j,k)-
((qout(j,k)*(0.5*(fw(k)+fw(k+1))))-(qout(j,k-1)*(0.5*(fw(k)+fw(k-
1)))))*(dt/(dx*(0.5*(fw(k)+fw(k-1)))));
               else
                  h(j+1,k)=dt*0.5*(Int_e(j,k)+Int_e(j+1,k))+h(j,k)-((qout(j,k)*fw(k))-
(qout(j,k-1)*(fw(k-1))))*(dt/(dx*((fw(k)))));
               end
              if h(j+1,k)>ds
                 qout(j+1,k)=a*(h(j+1,k)-ds)^m;
              end
            end

          end
          if h(j+1,k)<0
             h(j+1,k)=0;
             qout(j+1,k)=0;
          end
```

```
            if qout(j+1,k)>0
              Qout(j+1,k)=qout(j+1,k)*w_cell*fw(k);
            end
            if h(j+1,k)>0
              Cou(j+1,k)=alpha*((h(j+1,k))^Beta)*dt/dx;
            end
            if j==T-1
              Volinf(k)=F(k)*dx*w_cell*fw(k);
            end
        end
        qslope(j+1)=qout(j+1,rows);
        Qslope(j+1)=qslope(j+1)*w_cell*fw(rows);
        runoff=runoff+(qslope(j+1)*w_cell*fw(rows)*dt);
    end

    Runoff_rate=qslope(T_s)*w_cell*fw(rows)*1E-6*60; %Runoff rate at end of
%storm [L/min]

    max_Cou=max(max(Cou));
    if max_Cou>1 %Courant number condition
        T=round(T*max_Cou);
        dt=duration/T;
        T_s=round(duration_storm/dt);
    end
end

%% Results (if results of just side slope are wanted) volumes in [L]
rain=i*dx*w_cell*sum(fw)*duration_storm;
infil=sum(Volinf);
standing=h(T,:)*fw*dx*w_cell;
Volume_Runoff=(runoff)*1E-6;
Total_Inflow=(Input_road+rain)*1E-6;
Runoff=Volume_Runoff;
Infiltration=(infil+standing)*1E-6;
```

C) Function: Runoff_channel

```
function [Runoff,Infiltration,rain,ratio_ch_side]=Runoff_channel(i, Ks, Schannel,
Q_side, Channel_length, w_side, duration, duration_storm, T, ds, psi,
deltheta,n,B)
```

```
%This function uses the Kinematic wave approximation to solve for runoff rate
and infiltration for the channel of a roadside swale


%% Inputs Definition%%%%
%i Rainfall intensity over swale (cm/hr)
%Ks Saturated hydraulic conductivity (cm/h)
%Q_side Discharge from side-slope (mm3/s)
%Channel_length length of the channel
%w_side width of side slope modeled
%duration Duration of study (h)
%duration_storm Duration of storm event (h)
%T Number of time steps
%ds depression storage (mm)
%psi effective wetting front suction (cm)
%deltheta Soil water deficit
%n Manning's n value (SI s/m^(1/3))
%B width of the rectangular channel
w_cell=B; %width of cell
length=Channel_length; % Length of channel (m)
ratio_ch_side=length/w_side; %Length channel/Width side (study width)
rows=100; % Number of sections down slope channel (selected by user
fw=1*ones(rows,1); % Fraction wetted (1=whole surface channel wetted)
S=Schannel; % Slope channel


%% Unit conversions
i=i*10/3600; % Converts to mm/s
length=length*1000; % Converts to mm
w_cell=w_cell*1000; % Converts to mm
duration=duration*3600; % Converts to s
psi=psi*10; % Converts to mm
Ks=Ks/360; % Converts to mm/s
duration_storm=duration_storm*3600; % Converts to s
n=n/10; % Converts to [s/mm^(1/3)]
%%Kinematic wave Variables
m=5/3;
Beta=m-1;
a=(S^0.5)/n;
alpha=a*m;
```

```
%%%%Simulation Parameters
dx=length/rows;
dt=duration/T;
T_s=round(duration_storm/dt);

%%%%%%%%%% Calculations %%%%%%%%%%
max_Cou=1;

while max_Cou>=1
    % Setting up variables
    qin=zeros(T,rows);
    Volinf=zeros(rows,1);
    qout=zeros(T,rows);
    Qout=zeros(T,rows);
    ie=zeros(T,rows);
    f=zeros(T,rows);
    F=zeros(rows,1);
    h=zeros(T,rows);
    Cou=zeros(T,rows);
    infil=0;
    standing=0;
    qslope=zeros(T,1);
    Int_e=zeros(T,rows);
    start=0;
    SurfaceSat=zeros(rows,1);
    runoff=0;
    Runoff_rate=0;
    q_side=zeros(T,1);

    q_side=Q_side*(ratio_ch_side)/(w_cell*length); %Input Side slope

    % Unsteady Input of water
    i_v=zeros(T,1);
    for j=1:T_s
        i_v(j)=i; %L/T
    end
    i_v=i_v+q_side;

    %Initial condition: h=0 q=0

   for j=1:(T-1) % Loop through time
```

```
    for k=1:rows % Loop through space
        if k>1
          qin(j+1,k)=Qout(j+1,k-1)/(w_cell*fw(k)); % Inflow from cell above
        end
        ie(j+1,k)=qin(j+1,k)/dx+i_v(j); % Effective intensity

        %%Infiltration Submodel Green-Ampt-Mein-Larson
        if ie(j+1,k)==0
           if h(j,k)>0 %Ponded water
              ie(j+1,k)=h(j,k)/dt;
           end
        end
        [f(j+1,k),
SurfaceSat(k)]=Green_Ampt_rate_ML(psi,deltheta,Ks,ie(j+1,k),dt,F(k),SurfaceSat
(k));
        F(k)=F(k)+f(j+1,k)*dt; %infiltration depth

         %Explicit numerical solution for h
         Int_e(j+1,k)=-f(j+1,k)+i_v(j);
          if k==1 %first cell
             h(j+1,k)=h(j,k)-
(dt/dx)*(qout(j,k)*((0.5*(fw(1)+fw(2))/fw(1))))+(0.5*(Int_e(j,k)+Int_e(j+1,k)))*dt;
             if h(j+1,k)>ds
                qout(j+1,k)=a*(h(j+1,k)-ds)^m;
             end
          end

          if k>1 %Rest of the cells
            if j==1 %First time step
              h(j+1,k)=dt*0.5*(Int_e(j,k)+Int_e(j+1,k));
              if h(j+1,k)>ds
                qout(j+1,k)=a*(h(j+1,k)-ds)^m;
              end
            else %Rest of time steps
               if k<rows
                  h(j+1,k)=dt*0.5*(Int_e(j,k)+Int_e(j+1,k))+h(j,k)-
((qout(j,k)*(0.5*(fw(k)+fw(k+1))))-(qout(j,k-1)*(0.5*(fw(k)+fw(k-
1)))))*(dt/(dx*((fw(k))))));
               else
                  h(j+1,k)=dt*0.5*(Int_e(j,k)+Int_e(j+1,k))+h(j,k)-((qout(j,k)*fw(k))-
(qout(j,k-1)*(fw(k-1))))*(dt/(dx*((fw(k))))));
               end
```

```
            if h(j+1,k)>ds
              qout(j+1,k)=a*(h(j+1,k)-ds)^m;
            end
          end

        end
        if h(j+1,k)<0
          h(j+1,k)=0;
          qout(j+1,k)=0;
        end

        if qout(j+1,k)>0
          Qout(j+1,k)=qout(j+1,k)*w_cell*fw(k);
        end
        if h(j+1,k)>0
          Cou(j+1,k)=alpha*((h(j+1,k))^Beta)*dt/dx;
        end
        if j==T-1
          Volinf(k)=F(k)*dx*w_cell*fw(k);
        end
      end
      qslope(j+1)=qout(j+1,rows);
      runoff=runoff+(qslope(j+1)*w_cell*fw(rows)*dt);
  end

  max_Cou=max(max(Cou));
  if max_Cou>1
     T=round(T*max_Cou);
     dt=duration/T;
     T_s=round(duration_storm/dt);
  end
end

%% Results; volumes in [L]
rain=i*w_cell*length*duration_storm*1E-6;
infil=sum(Volinf)*1E-6;
standing=h(T,:)*fw*dx*w_cell*1E-6;
runoff_final=runoff*1E-6;
Volume_Runoff=runoff_final+standing;
Runoff=Volume_Runoff;
Infiltration=(infil);
```

```
%% Plot discharge (q)
fig1 = figure;
tt=(dt/3600):(dt/3600):(duration/3600);
figure(fig1)
plot(tt,qslope*1E-6);
title('Specific Discharge from Swale Channel Over Time');
xlabel('Time (hr)');
ylabel('Specific Discharge (m^{2}/s)');
axis auto
```

D) Function: Green_Ampt_rate_ML

```
function [ f, SurfaceSat ] = Green_Ampt_rate_ML(
psi,deltheta,Ks,ie,dt,F,SurfaceSat )

%This function uses the Green Ampt Mein Larson (GAML) assumptions to solve
for infiltration rate (f)

%%%Input definitions
%psi - Wetting front suction
%deltheta - Soil water deficit
%Ks – Saturated hydraulic conductivity
%ie – effective intensity
%dt – time step
%F – infiltration depth
%SurfaceSat  - saturation condition

X=psi*deltheta; %Wetting front suction * soil water deficit
dP=ie*dt; % rainfall depth

if SurfaceSat==1
   dF_go=0.5*(Ks*dt-2*F+sqrt(Ks*dt*(Ks*dt+4*F+8*X)+4*(F^2)));
   dF_g=-F-(((F+dF_go)^2)/X)+((F+X+dF_go)/X)*sqrt(((F+dF_go)^2)...
          +2*X*(X*log(1+((dF_go/(F+X))))+Ks*dt-dF_go));
    if dP<dF_g
       f=ie;
       F=F+dP;
    else
       F=F+dF_g;
       f=Ks*(X+F)/F;
    end
```

```
else
   if ie<Ks
      F_s=10^20;
   else
      F_s=(Ks*X)/(ie-Ks);
   end

   if F_s>F+dP
      F=F+dP;
      f=ie;
   else
       SurfaceSat=1;
       dF_go=0.5*(Ks*dt-2*F+sqrt(Ks*dt*(Ks*dt+4*F+8*X)+4*(F^2)));
       dF_g=-F-(((F+dF_go)^2)/X)+((F+X+dF_go)/X)*sqrt(((F+dF_go)^2)...
          +2*X*(X*log(1+((dF_go/(F+X))))+Ks*dt-dF_go));
        if dP<dF_g
            f=ie;
            F=F+dP;
        else
           F=F+dF_g;
           f=Ks*(X+F)/F;
        end
   end
end
```

Appendix B

Supporting information for Chapter 7

Rainfall Depths versus Percentage Infiltration

To create the simplified calculator, repeated simulations of the model were run to quantify the relationship between rainfall depth and percentage infiltration for different K_{sat} values and ratios of width of the roadside filter strip over width of the road (W_{swale}/W_{road}). The simulation results were used to develop a set of curves for eight different K_{sat} values from 0.15 to 16 cm/h and eighteen rainfall depths, from 0.25 to 22.9 cm. Nine graphs representing different width ratios, from 0.1 to 1.4 have been created.

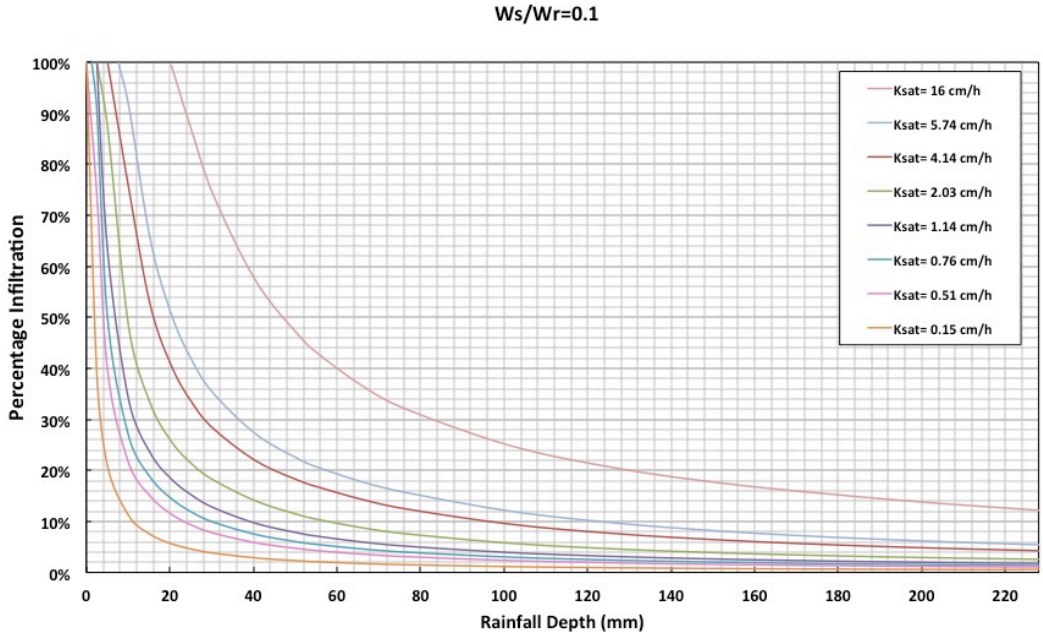

Figure AppB.1 Rainfall depths versus percentage infiltration for a ratio of swale side slope width (W_s) to road width (W_r) of 0.1. The eight curves represent different saturated hydraulic conductivities.

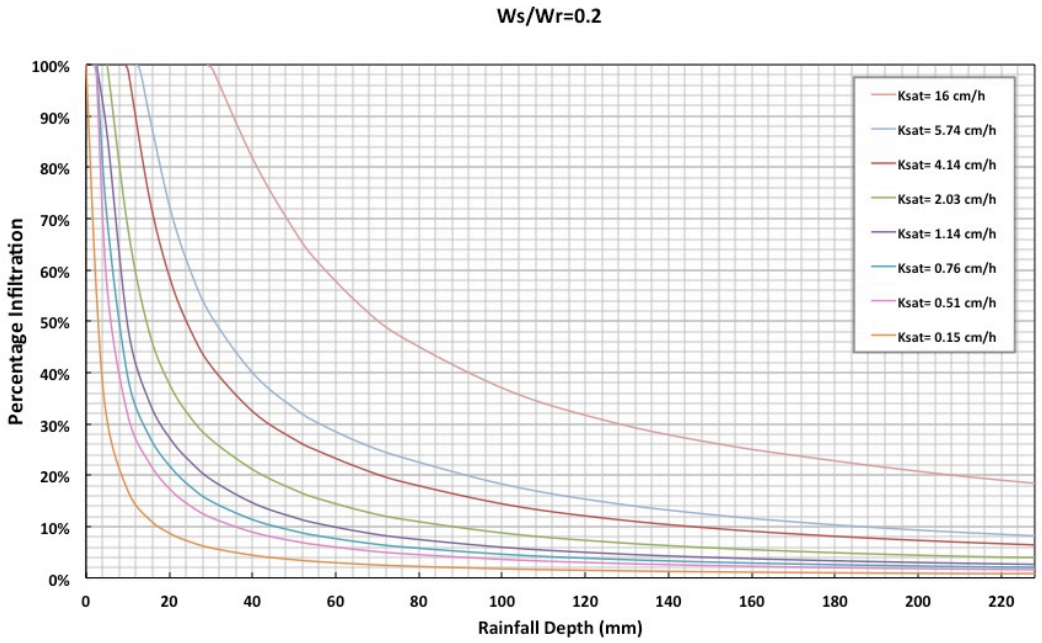

Figure AppB.2 Rainfall depths versus percentage infiltration for a ratio of swale side slope width (W_s) to road width (W_r) of 0.2. The eight curves represent different saturated hydraulic conductivities.

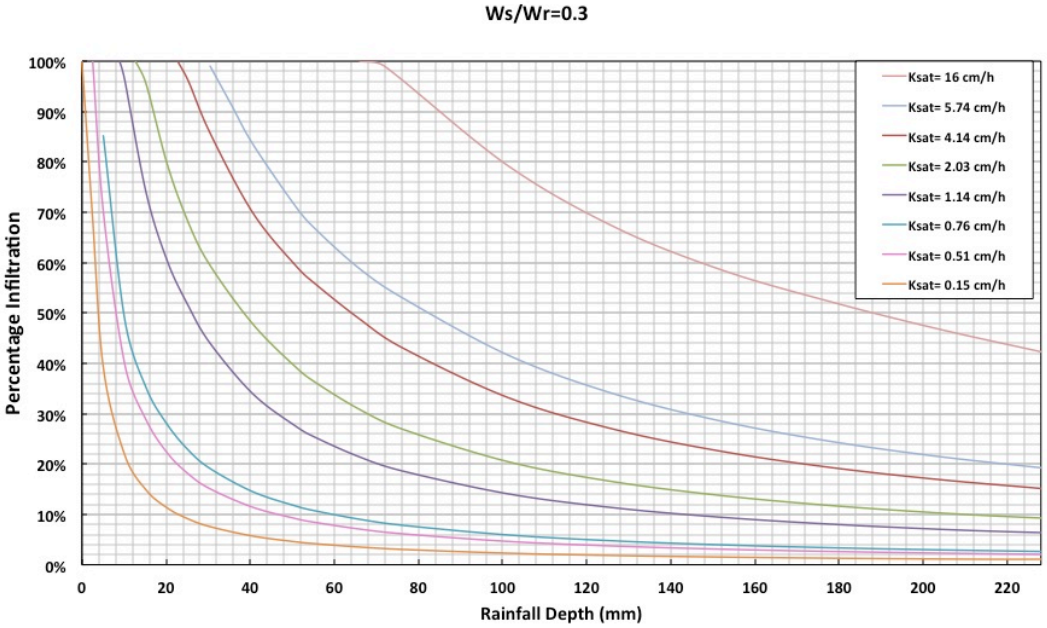

Figure AppB.3 Rainfall depths versus percentage infiltration for a ratio of swale side slope width (W_s) to road width (W_r) of 0.3. The eight curves represent different saturated hydraulic conductivities.

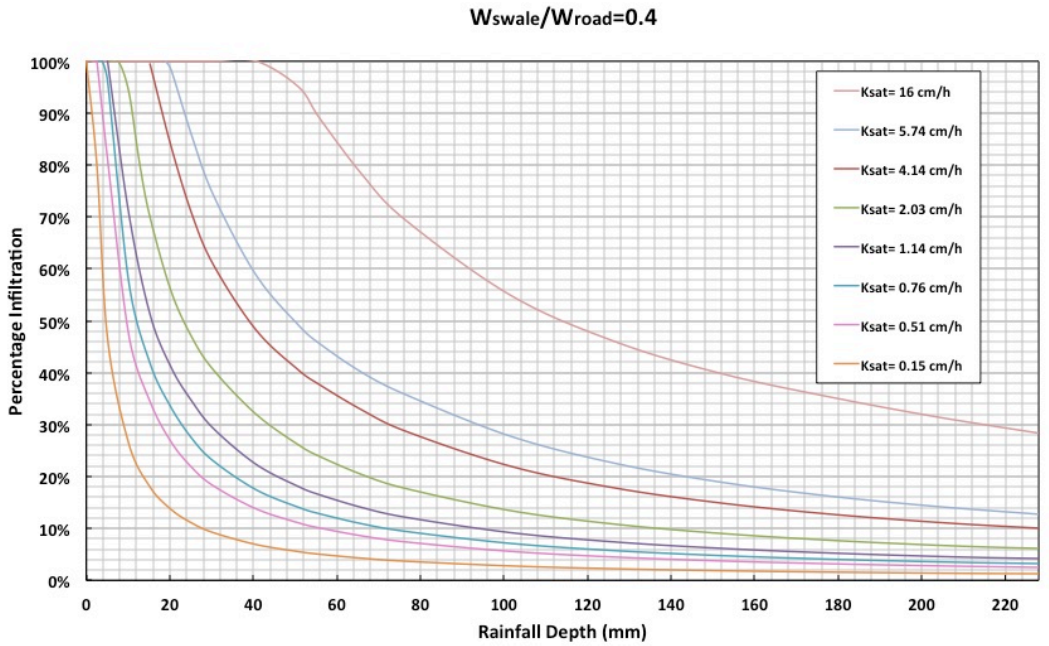

Figure AppB.4 Rainfall depths versus percentage infiltration for a ratio of swale side slope width (W_s) to road width (W_r) of 0.4. The eight curves represent different saturated hydraulic conductivities.

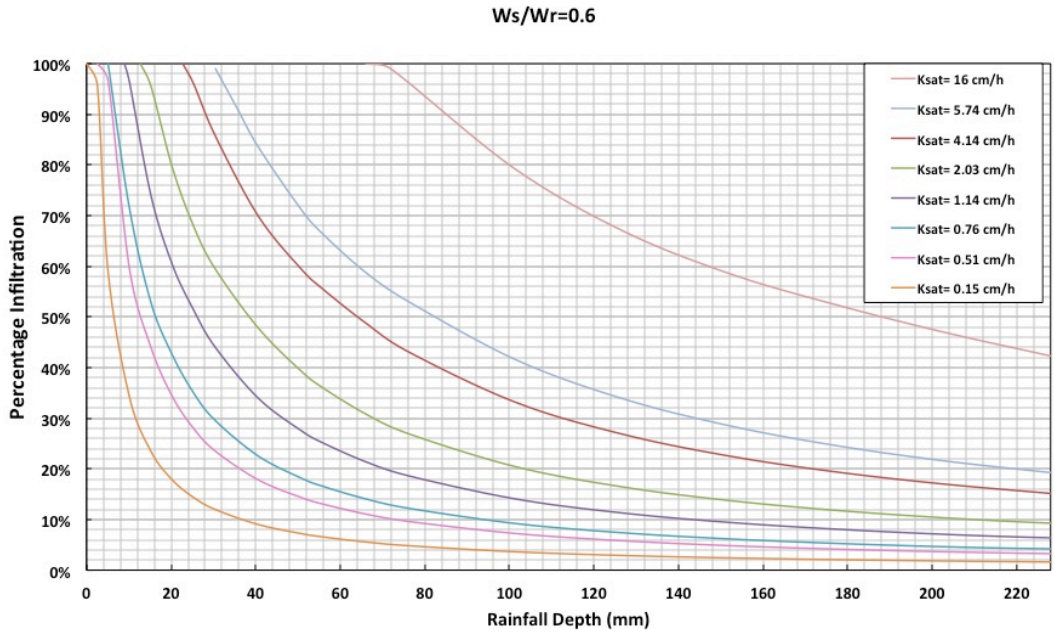

Figure AppB.5 Rainfall depths versus percentage infiltration for a ratio of swale side slope width (W_s) to road width (W_r) of 0.6. The eight curves represent different saturated hydraulic conductivities.

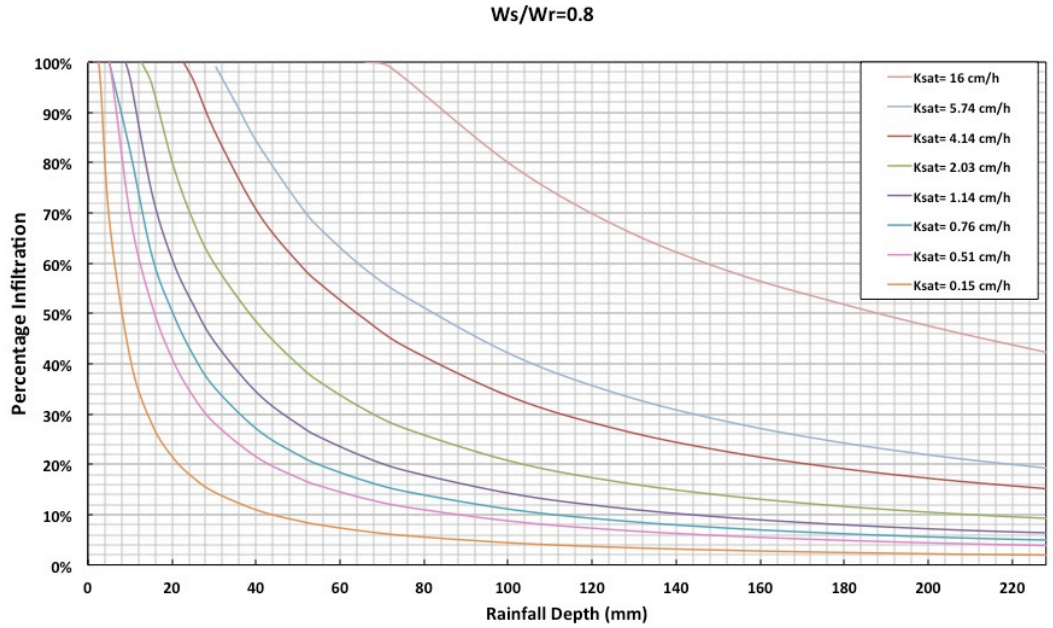

Figure App.6 Rainfall depths versus percentage infiltration for a ratio of swale side slope width (W_s) to road width (W_r) of 0.8. The eight curves represent different saturated hydraulic conductivities.

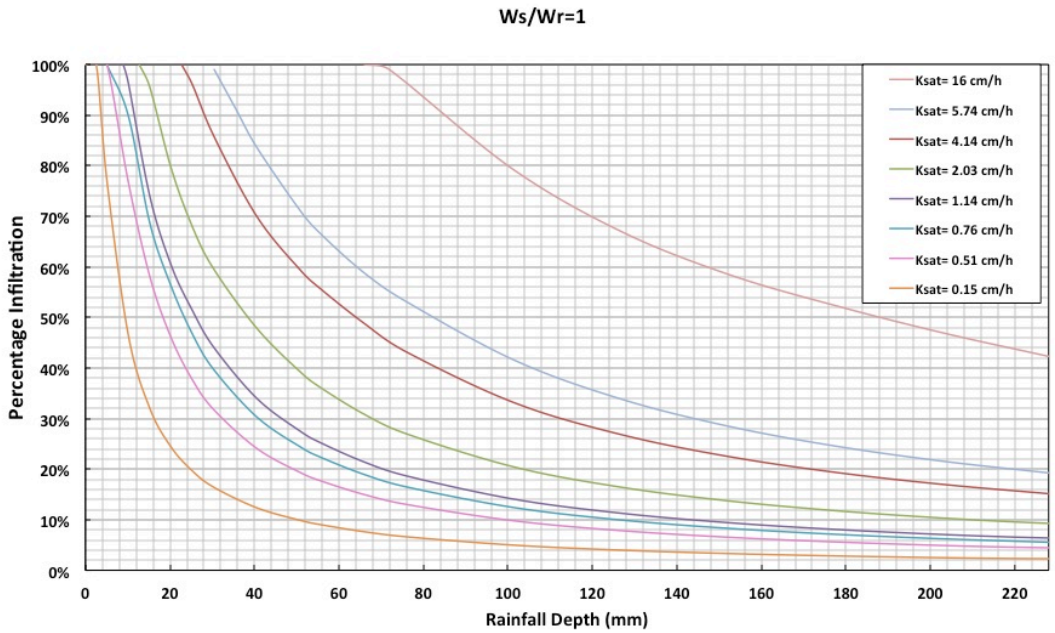

Figure AppB.7 Rainfall depths versus percentage infiltration for a ratio of swale side slope width (W_s) to road width (W_r) of 1. The eight curves represent different saturated hydraulic conductivities.

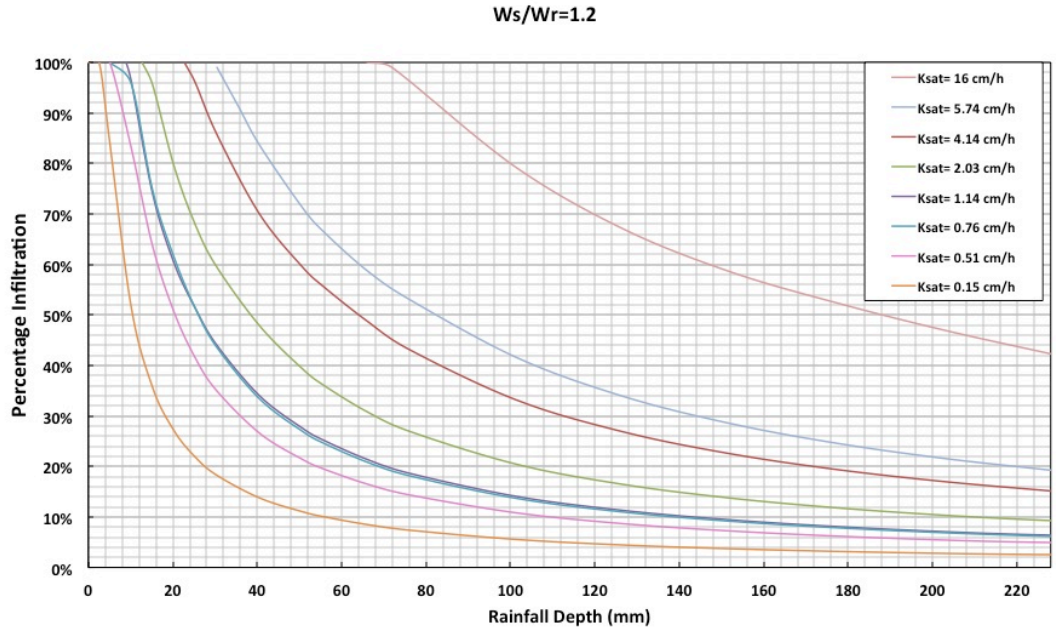

Figure AppB.8 Rainfall depths versus percentage infiltration for a ratio of swale side slope width (W_s) to road width (W_r) of 1.2. The eight curves represent different saturated hydraulic conductivities.

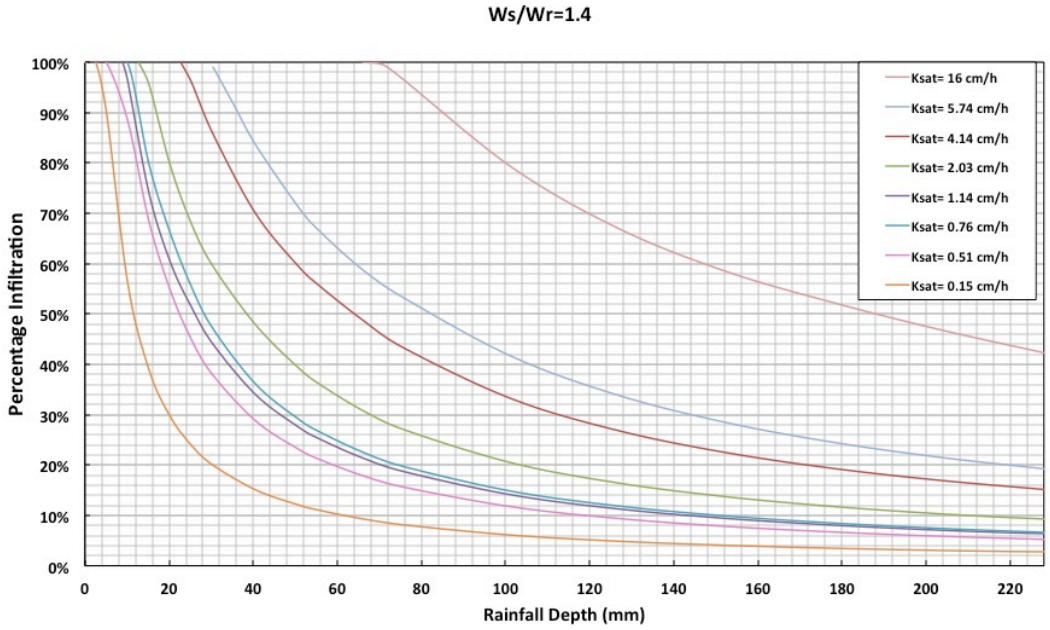

Figure AppB.9 Rainfall depths versus percentage infiltration for a ratio of swale side slope width (W_s) to road width (W_r) of 1.4. The eight curves represent different saturated hydraulic conductivities.